

# PE&RS

January 2019

Volume 85, Number 1

*The official journal for imaging and geospatial information science and technology*

**PHOTOGRAMMETRIC ENGINEERING & REMOTE SENSING**



# PECORA 21 • ISRSE 38

*Continuous Monitoring of Our  
Changing Planet:  
From Sensors to Decisions*



## Call for Abstracts

**October 6-11, 2019**

Baltimore, MD • Marriott Waterfront

<https://www.asprs.org/event/pecora21-isrse38>



The Pecora 21/ISRSE 38 Conference will be organized around four session themes spanning the Earth observations and continuous monitoring continuum. Presentations are being sought on diverse science, technology, and applications of remote sensing to understand and sustainably manage the Earth's environment and natural resources. We encourage contributions along the full value chain of Earth observation, from fundamental research on Earth system processes to operational applications, innovative techniques and future missions, as well as international programmes and coordination.

Submitted abstracts (max. 300 words) will be organized, though not exclusively, along four broad thematic areas described below:

- Understanding the Earth through continuous monitoring
- Societal benefits and empowering decision making
- Technical advances in monitoring using Earth observations
- Envisioning the future of global monitoring

Abstracts addressing the conference themes may be submitted for general consideration, or be considered for inclusion in a proposed special presentation sessions. Additional session proposals will also be accepted during the Call for Abstracts.

### Presentation Types

- **Standard presentation:** Long-format research talk (15 minutes).
- **Special presentation session:** Inclusion in one of the sessions listed to the right. For more information on the special presentations, visit <http://pecora.asprs.org/>.
- **Short presentation:** Lightning-style research talk (3 minutes)
- **Short visualization:** Lightning-style talk focused on data visualization, e.g. map products, dashboards, interactive plots, cartographic tools (3 minutes)
- **Poster:** Poster presentation. May be considered for general poster sessions or an illustrated poster sessions where posters will be grouped by topic or theme and presenters will have 1-2 minutes to introduce their poster to attendees.
- **Workshops:** 2-hour and 4-hour pre-conference workshops.

Awards will be offered in each category above, including awards for best young professional/student talk and poster. To be eligible, presenters must request to be considered for judged awards during the abstract submission process.

**Timeline** Abstracts Due—January 25, 2019

### Special Presentation Sessions

- SP1—Open Data Cube: A New Data Technology for Enhancing the use of Satellite Data to Address Sustainable Development Goals
- SP2—An Overview of the current Analysis Ready Data products, tools, applications and impacts
- SP3—New Technology and Techniques to Increase Scientific and Applications Access to Satellite Earth Observations
- SP4—Lidar Vegetation Canopy Metrics—Towards Developing Standards
- SP5—High-resolution Land Cover using NAIP
- SP6—SAR for Agriculture and Perspective Applications
- SP7—Water Colour: The Canadian Perspective
- SP8—Applications of NASA Earth Observations for Local Decision Making: 20 Years of the NASA DEVELOP Program
- SP9—How No-cost Landsat Data is Reshaping College-level Remote Sensing Courses
- SP10—Societal Benefits of Earth Observations in Natural Resource Management Decision Making
- SP11—So What, Who Cares: Linking Natural and Social Science to Understand Societal Impact and Improve Decision Making
- SP12—Importance of System Calibration and Data Quality on Earth Observation
- SP13—UAS, Changing the Future of Remote Sensing
- SP14—Satellite Interoperability
- SP15—Land Imaging Capabilities and User Needs
- SP16—Air Quality Monitoring with Earth Observations for Enhanced Decision Making and Regulatory Support
- SP17—Transitional by Nature: Leveraging Remote Sensing Technology for Continuous Monitoring of Dynamic Wetland Ecosystems
- SP18—Connecting People and Pixels through Citizen Science to Enhance Global Monitoring
- SP19—Open Civil Applications Committee Meetings
- SP20—The Next Generation of the Landsat Archive
- SP21—Space Agencies Outlook
- SP22—NASA Harvest and Other Recent Advances in Remote Sensing of Agricultural Applications and Food Security
- SP23—Sustainable Land Imaging and the Future of Moderate-Resolution Land Observation
- SP24—Geospatial Fusion: Observations, Features, Decisions
- SP25—The Challenges of Integration for Arctic Monitoring
- SP26—Remote Sensing Applications for Water Resources Management, Including Droughts, Floods and Associated Water Cycle Extremes
- SP27—Communicating Science Across the Earth Observation Life Cycle

## ANNOUNCEMENTS

Senate passes **GIS Day Resolution** following successful passage of Geospatial Data Act—Senator Orrin Hatch (R-UT) and Senator Mark Warner (D-VA) led a Senate resolution to designate 15 November 2018 as “National GIS Day.” Senators Baldwin (D-WI), Blumenthal (D-CT), Capito (R-WV), Hassan (D-NH), Inhofe (R-OK), and Wyden (D-OR) joined Hatch and Warner in submitting the resolution.

“The Senate designates November 15, 2018, as ‘National GIS Day’; encourages users of Geographic Information System technology ... [including] educators, students, and innovators to continue to employ GIS to learn and explore, to analyze and address societal challenges; and to drive economic growth for the betterment of the people of the United States and individuals around the world.” — the three-page resolution concludes.

This recognition by the Senate punctuates the passage of the Geospatial Data Act, included as a component in H.R. 302, the FAA Reauthorization Act signed into law last month.

USGS Selects **Dewberry** to Complete Lidar Mapping for State of Florida. Under an active Geospatial Products and Services contract, the U.S. Geological Survey (USGS) has selected Dewberry, a privately held professional services firm, to complete a statewide lidar mapping project for Florida. The project is funded by the Florida Division of Emergency Management and USGS as part of Hurricane Irma Disaster Recovery, Response and Preparedness measures being conducted by the state and federal agencies.

The approximately \$20 million USD project includes airborne lidar data acquisition, ground survey, and preparation of bare earth point cloud and digital elevation model (DEM) products for various applications to support response, recovery, and preparation for future storm events. The resulting quality level 1 data will be primarily used for hydrologic and hydraulic modeling and many engineering applications by the water management districts to mitigate the impacts of flooding caused by these storms. USGS and the Federal Emergency Management Agency (FEMA) will also utilize these data for various flood studies. The project encompasses an area of more than 34 000 square miles.

Dewberry has acquired and processed nearly 22 000 square miles of lidar data for various local, state, and federal agencies in Florida within the past three years. “As we continue to map the state of Florida, we’re looking forward to using the best technology and personnel to complete such a vast undertaking,” says Dewberry Vice President and Director of Remote Sensing Amar Nayegandhi, (CP, CMS, GISP.)<sup>1</sup> “Once these data are acquired and analyzed, they will be able to support USGS, FEMA, the Natural Resources Conservation Service, the Florida water management districts, and several other state and local agencies in their mission to better prepare for natural

disasters and minimize loss of life and property; and use these scientific data to enhance and protect our quality of life.”

Dewberry will serve as prime contractor for this project and will perform the majority of the data production. The firm is teaming with seven other partner firms including Woolpert, Inc., Quantum Spatial, Inc., and Digital Aerial Solutions, Inc., which will acquire and process data to support the project. Dewberry’s other subcontractors will be tasked with acquiring airborne lidar data.

“We have 11 aircraft with top-of-the-line airborne lidar sensors being deployed for data acquisition starting in early December. I’m excited to manage this project and support the needs of USGS, their partner.

## PEOPLE

**GeoCue Group, Inc.** is extremely pleased to announce that Mr. Henry “Hank” DiPietro has joined the company as Vice-President of Business Development. Hank, a civil engineer by training, brings deep experience in engineering, GIS, transportation and public safety to the company.

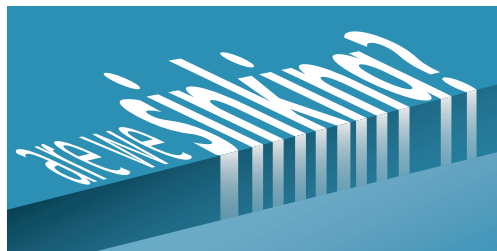
“Hank and I go way back to the mid-1990s” said Lewis Graham, President and CTO of GeoCue. “We worked together at Intergraph, bringing innovative civil engineering, photogrammetry and GIS products to market. We then formed Z/I Imaging, a joint venture company between Intergraph and Carl Zeiss of Germany. While at Z/I Imaging, we developed and brought to market the world’s first large format framing digital mapping camera. With our end-to-end sensor workflows for drone mapping, our dominance in aerial/mobile lidar scanning software and our new forays into cloud managed geospatial data systems, Hank’s expertise and market presence will be invaluable.”

“I am extremely excited to join GeoCue Group. After looking closely at the innovative products, solutions and people the company has to offer, it was an easy decision for me to join the team. GeoCue technology has a place in all the industries I have worked in over my 30 years; mapping, engineering, construction, transportation, utilities and public safety. I look forward to applying my experience in end user needs in those industries to our business development efforts.”

“Hank has always been viewed by customers as a trusted advisor,” said Jim Meadlock, Chairman of GeoCue Group. “GeoCue is a company that puts the interests of the customer ahead of all other concerns. This makes Hank the perfect executive for our new enterprise technical direction.”

\* CP- Certified Photogrammetrist, CMS - Certified Mapping Scientist, GISP - GIS Professional

## FEATURES



**5** Are We Sinking? National Geospatial-Intelligence Agency Visits LSU Campus to Measure Subsidence



**7** An Interview—Dr. David F. Maune discusses the DEM Users Manual 3<sup>rd</sup> Edition

### COLUMNS

- 11** Book Review—*GIS for Surface Water Using the National Hydrography Dataset*
- 13** Grids and Datums  
This month we look at The French Republic.
- 16** Signatures  
The Column of the Student Advisory Council.

### ANNOUNCEMENTS

- 1** Pecora 21—ISRSE 38 Conference
- 7** DEM Users Manual 3<sup>rd</sup> Edition—A Preview
- 12** Certification
- 17** Headquarters News
- 17** New ASPRS Members  
Join us in welcoming our newest members to ASPRS.

### DEPARTMENTS

- 2** Industry News
- 18** Calendar
- 18** Ad Index
- 64** ASPRS Sustaining Members

## PEER-REVIEWED ARTICLES

### 19 Simultaneous Chain-Forming and Generalization of Road Networks

*Susanne Wenzel and Dimitri Bulatov*

A well-reasoned representation of road segments by means of geometric primitives, such as straight line segments as well as circle and ellipse arcs.

### 29 Integration of Lidar Data and GIS Data for Point Cloud Semantic Enrichment

*Harith Aljumaily, Debra F. Laefer, and Dolores Cuadra*

Employing a MapReduce framework and readily available GIS data in the form of OpenStreetMap data, the proposed parallelized approach enriches large laser scanning point cloud metadata with detailed semantic information about the object type.

### 43 Assessment of Different Vegetation Parameters for Parameterizing the Coupled Water Cloud Model and Advanced Integral Equation Model for Soil Moisture Retrieval Using Time Series Sentinel-1A Data

*Long Wang, Binbin He, Xiaojing Bai, and Minfeng Xing*

Evaluating the performance of four vegetation parameters including NDVI, EVI, LAI, and FPAR for parameterizing the scattering and attenuation mechanisms of vegetation in the coupled WCM and AIEM during soil moisture retrieval over the Central Plains of the United States.

### 55 Individual Tree Detection and Crown Delineation with 3D information from Multi-view Satellite Images

*Changlin Xiao, Rongjun Qin, Xiao Xie, and Xu Huang*

A novel method to detect individual trees from orthophotos and digital surface models (DSM) derived from the multi-view satellite images with the 2D spectral and the 3D structure information.

### 65 The Potential of Multispectral Vegetation Indices Feature Space for Quantitatively Estimating the Photosynthetic, Non-Photosynthetic Vegetation and Bare Soil Fractions in Northern China

*Guoxiong Zheng, Anming Bao, Xiaosong Li, Liangliang Jiang, Cun Chang, Tao Chen, and Zhihai Gao*

The multispectral-based normalized difference senescent vegetation index (NDSVI) and brightness index (BI) were found to be combined with the selected NDVI, EVI, and OSAVI to better estimate the fractional cover of photosynthetic, non-photosynthetic vegetation and bare soil in this region.

See the Cover Description on Page 4

# COVER DESCRIPTION



As the Neuquén River winds its way from the Andes through west-central Argentina toward the Atlantic Ocean, it passes a spectacular series of rock formations in the Neuquén Basin. For paleontologists, the basin is a great place to find fossils, particularly dinosaurs. And for those in the oil business, it is fertile ground for gas and oil exploration.

The Operational Land Imager (OLI) on Landsat-8 acquired an image showing part of the basin on 3 September 2018.

From space, boundaries between some of the major groups of sedimentary rock formations are visible. In the first image, the deep reds of the Candeleros Formation—a sequence of sandstones formed roughly 90 to 100 million years ago in a braided river system—dominate the landscape. These rocks are flanked in some areas, especially near the river, by a green-yellow sequence of rocks that are part of the younger Huncical Formation, formed during drier times. The older Royosa Formation, meanwhile, peeks through in some areas where erosion has scraped away overlying rock layers. (See the cover image.)

Paleontologists have uncovered quite a menagerie of fossilized fauna in Candeleros rocks, including ancient species of fish, frogs, snakes, turtles, small mammals, and several types of dinosaurs. Few of the fossilized creatures have received the notoriety of *Giganotosaurus carolinii*—a carnivorous theropod thought to be larger and faster than *Tyrannosaurus Rex*.

Petroleum geologists are more interested in what lies beneath the Candeleros Formation. Several layers of rock, formed when the area was covered by an ocean, contain gas and oil. While drilling has been ongoing here since 1918, the recent discovery of a large deposit of shale gas and oil in the Vaca Muerta Formation has made the Neuquén Basin one of the few regions outside of the United States where companies are pursuing horizontal drilling and hydraulic fracturing.

NASA Earth Observatory images by Lauren Dauphin, using Landsat data from the U.S. Geological Survey. Story by Adam Voiland.

For more information, visit <https://landsat.visibleearth.nasa.gov/view.php?id=92908>.

## PHOTOGRAMMETRIC ENGINEERING & REMOTE SENSING

asprs THE  
IMAGING & GEOSPATIAL  
INFORMATION SOCIETY

### JOURNAL STAFF

Publisher ASPRS  
Editor-In-Chief Alper Yilmaz  
Assistant Editor Jie Shan  
Managing Editor Melissa J. Porterfield  
Assistant Director — Publications Rae Kelley  
Electronic Publications Manager/Graphic Artist Matthew Austin

*Photogrammetric Engineering & Remote Sensing* is the official journal of the American Society for Photogrammetry and Remote Sensing. It is devoted to the exchange of ideas and information about the applications of photogrammetry, remote sensing, and geographic information systems. The technical activities of the Society are conducted through the following Technical Divisions: Geographic Information Systems, Photogrammetric Applications, Lidar, Primary Data Acquisition, Professional Practice, and Remote Sensing Applications. Additional information on the functioning of the Technical Divisions and the Society can be found in the Yearbook issue of *PE&RS*.

Correspondence relating to all business and editorial matters pertaining to this and other Society publications should be directed to the American Society for Photogrammetry and Remote Sensing, 425 Barlow Place, Suite 210, Bethesda, Maryland 20814-2144, including inquiries, memberships, subscriptions, changes in address, manuscripts for publication, advertising, back issues, and publications. The telephone number of the Society Headquarters is 301-493-0290; the fax number is 301-493-0208; web address is [www.asprs.org](http://www.asprs.org).

**PE&RS.** *PE&RS* (ISSN0099-1112) is published monthly by the American Society for Photogrammetry and Remote Sensing, 425 Barlow Place, Suite 210, Bethesda, Maryland 20814-2144. Periodicals postage paid at Bethesda, Maryland and at additional mailing offices.

**SUBSCRIPTION.** For the 2019 subscription year, ASPRS is offering two options to our *PE&RS* subscribers — an e-Subscription and the print edition. E-subscribers can plus-up their subscriptions with printed copies for a small additional charge. Print and Electronic subscriptions are on a calendar-year basis that runs from January through December. We recommend that customers who choose both e-Subscription and print (e-Subscription + Print) renew on a calendar-year basis. The new electronic subscription includes access to ten years of digital back issues of *PE&RS* for online subscribers through the same portal at no additional charge. Please see the Frequently Asked Questions about our journal subscriptions.

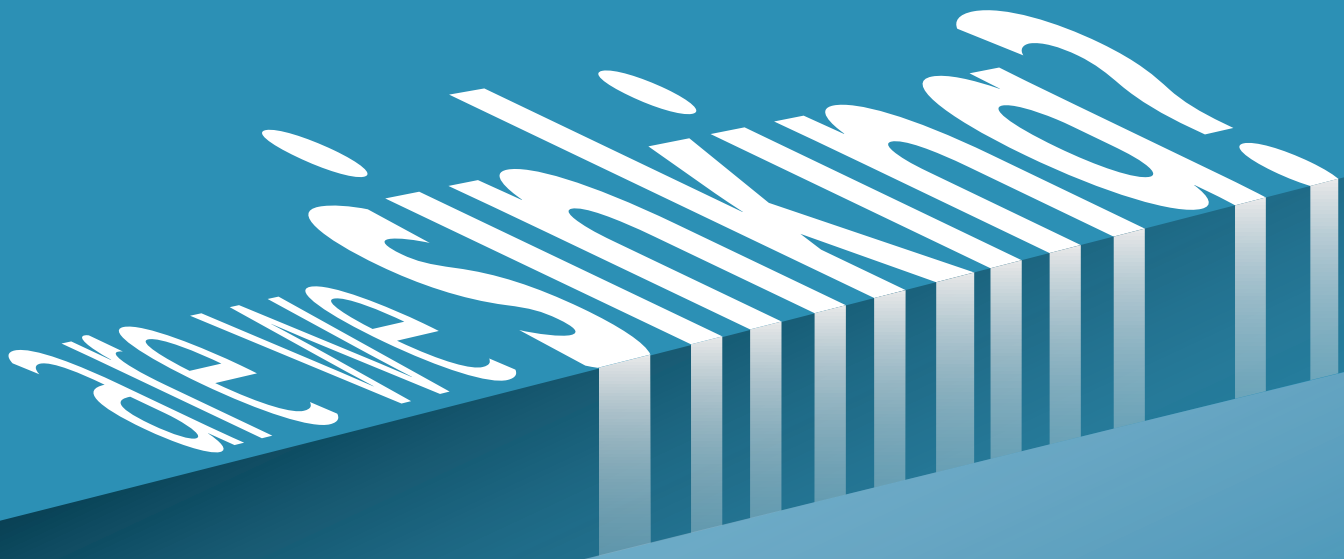
The rate of the e-Subscription (digital) Site License Only for USA and Foreign: 1000.00 USD; e-Subscription (digital) Site License Only for Canada\*: 1049.00 USD; Special Offers: e-Subscription (digital) Plus Print for the USA: 1365.00 USD; e-Subscription (digital) Plus Print Canada\*: 1424.00 USD; e-Subscription (digital) Plus Print Outside of the USA: 1395.00 USD; Printed-Subscription Only for USA: 1065.00 USD; Printed-Subscription Only for Canada\*: 1124.00 USD; Printed-Subscription Only for Other Foreign: 1195.00 USD. \*Note: e-Subscription/Printed-Subscription Only/e-Subscription Plus Print for Canada include 5% of the total amount for Canada's Goods and Services Tax (GST #135123065). **PLEASE NOTE: All Subscription Agencies receive a 20.00 USD discount.**

**POSTMASTER.** Send address changes to *PE&RS*, ASPRS Headquarters, 425 Barlow Place, Suite 210, Bethesda, Maryland 20814-2144. CDN CPM #40020812)

**MEMBERSHIP.** Membership is open to any person actively engaged in the practice of photogrammetry, photointerpretation, remote sensing and geographic information systems; or who by means of education or profession is interested in the application or development of these arts and sciences. Membership is for one year, with renewal based on the anniversary date of the month joined. Membership Dues include a 12-month electronic subscription to *PE&RS*. Or you can receive the print copy of *PE&RS* Journal which is available to all member types for an additional fee of 60.00 USD for shipping USA and or 75.00 USD for international shipping. Dues for ASPRS Members outside of the U.S. will now be the same as for members residing in the U.S. Annual dues for Regular members (Active Member) is 150 USD; for Student members 50 USD for USA and Canada 58 USD; 60 USD for Other Foreign members. A tax of 5% for Canada's Goods and Service Tax (GST #135123065) is applied to all members residing in Canada.

**COPYRIGHT 2019.** Copyright by the American Society for Photogrammetry and Remote Sensing. Reproduction of this issue or any part thereof (except short quotations for use in preparing technical and scientific papers) may be made only after obtaining the specific approval of the Managing Editor. The Society is not responsible for any statements made or opinions expressed in technical papers, advertisements, or other portions of this publication. Printed in the United States of America.

**PERMISSION TO PHOTOCOPY.** The appearance of the code at the bottom of the first page of an article in this journal indicates the copyright owner's consent that copies of the article may be made for personal or internal use or for the personal or internal use of specific clients. This consent is given on the condition, however, that the copier pay the stated per copy fee of 3.00 USD through the Copyright Clearance Center, Inc., 222 Rosewood Drive, Danvers, Massachusetts 01923, for copying beyond that permitted by Sections 107 or 108 of the U.S. Copyright Law. This consent does not extend to other kinds of copying, such as copying for general distribution, for advertising or promotional purposes, for creating new collective works, or for resale.



**National Geospatial-Intelligence  
Agency Visits LSU Campus to  
Measure Subsidence**

Throughout the month of October, ten members of the National Geospatial-Intelligence Agency (NGA) visited Louisiana State University (LSU)'s Louisiana Spatial Reference Center (LSRC) and other state wide high precision GPS continuous operation reference stations (CORS) within the LSRC's network, to take gravity measurements for a research project spearheaded by LSU Center for Geoinformatics (C4G) Chief of Geodesy, Cliff Mugnier.

Every five to ten years, the NGA takes measurements of the earth's gravity field to check for subsidence, a project Mugnier has been working on for nearly 30 years.

"LSU has the largest university-owned network of permanent GPS stations in the world, which reach from Louisiana throughout the Gulf Coast," Mugnier said. "Over the years, I have asked the military to come in to take measurements at these stations. I first go to the New Orleans Corps of Engineers, whose colonel then writes a letter to the Pentagon asking if they can come to Louisiana and observe different places where we have our GPS antennas for our research on subsidence. The idea is if you come back to the same spot over a period of years and see an increase in the strength of the earth's gravity, that means you're getting closer to the center of the earth, which equates to subsiding."

The NGA kicked off its recent Louisiana trip at LSU's Absolute Gravity Station using instrumentation similar to the FG5-X Absolute Gravity meter that C4G purchased this year. C4G also houses two CG5 relative gravity meters. From LSU, the NGA team—consisting of two groups of five trainees from New Mexico, Missouri, and both the East and West Coasts—moved on to other GPS CORS sites across south Louisiana that included Oakdale, Alexandria, New Orleans, Slidell, Boothville, Lafayette, Lake Charles, Cocodrie, and Grand Isle. The NGA will take measurements in north Louisiana this winter to conclude their 2018 Louisiana campaign.

"The reason for these gravity measurements is to have a completely independent physical measurement of vertical movement as a function of gravity, rather than readings from the GPS satellites," Mugnier said. "It all fits together for the subsidence research, but another reason is when people mortgage their homes, the banks require them to have flood insurance, which is based on elevation. The Corps [of Engineers] is also interested in subsidence

because they have the responsibility of levees and flood control."

The NGA has not visited Louisiana since 2003, shortly after Mugnier arrived at LSU. Though subsidence is of vast importance to Louisianans, the NGA does not take measurements every year because subsidence is a slow process.

"If you do it too frequently, the observations get lost in what is called white noise," Mugnier said. "Even though the instruments are super precise, you still have to have the time for the sinking to be enough for the instruments to detect."

Mugnier's research on Louisiana subsidence began when he taught at the University of New Orleans (UNO), where the first NGA measurements were taken in 1989. Since then, research has shown that UNO's campus is sinking at a rate of 9.1 mm/year, which Mugnier said is significant when you consider that equates to three feet in 100 years.

"Three feet is a whole lot when you also consider sea level is rising about two mm each year," he said.

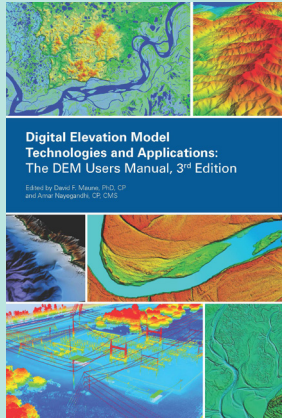
Since the first reading taken at LSU around 2003 by the National Geodetic Survey, it has been discovered that LSU's campus is subsiding around 5 mm/year near the fault line on Nicholson Drive. The campus is on the downside of the fault.

Since subsidence is an unstoppable force, Mugnier has made sure that C4G will continue his research when he is no longer at LSU. The man who started C4G, LSU Professor Roy Dokka, established the organization whose mission is in keeping with state law that says C4G is the source to keep track of elevations for the State of Louisiana.

"So, we have an organization that's going to be here long after I'm gone," Mugnier said. "And we have the perfect research project that will go on forever."

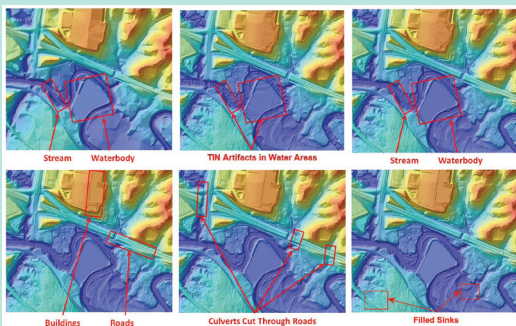
Reprinted with permission from Louisiana State University, College of Engineering. For more information, contact Libby Haydel, Communications Specialist, ehaydel1@lsu.edu.

# DR. DAVID F. MAUNE



## DEM Users Manual 3rd Edition A Preview

**Chapter 1—Introduction to Digital Elevation Models**, along with Appendix A (Acronyms) and Appendix B (Definitions), establishes the DEM vocabulary and definitions for various forms of elevation raster data, vector data, and point data (including point clouds) so that data users and producers can agree on standardized terminology. It is important that DEM users understand the concepts of mass points, breaklines, and triangulated irregular networks (TINs), for example, and how they are used to produce uniformly spaced topographic and/or bathymetric DEMs. This chapter also covers topographic and hydrologic surface modeling, e.g., hydro-flattening, hydro-enforcement and hydro-conditioning with examples at Figures 1 through 6 (below), as well as elevation derivatives and 3D terrain visualization. Definitions from this manual were also incorporated in the USGS Lidar Base Specification.



**Chapter 2—Vertical Datums** defines a vertical datum as a reference surface representing zero height—whether heights above sea level (with various tidal datums), orthometric heights (elevations) above the geoid with equal gravity potential (with various vertical orthometric datums), or ellipsoid heights above a mathematical ellipsoid that approximates the shape of the Earth as obtained from air-, land- or sea-based GPS. It is important that DEM users understand geoid undulations, how all U.S. vertical datums of the future will be geoid based vertical datums that result from the National Geodetic Survey's Gravity for the Redefinition of the American Vertical Datum GRAV-D) project, and how to transform from one vertical



*Dr. David F. Maune served 30 years of Army active duty as a commissioned officer in the U.S. Army Corps of Engineers (USACE). He specialized as a Topographic Engineer, last serving as Commander and Director, U.S. Army Topographic Engineering Center (TEC) – now the Army Geospatial Center (AGC). Today He is a Senior Project Manager for Dewberry Engineers, Inc. and currently editing the 3rd edition of “Digital Elevation Model Technologies and Applications: The DEM Users Manual.”*

*Dr. David F. Maune served 30 years of Army active duty as a commissioned officer in the U.S. Army Corps of Engineers (USACE). He specialized as a Topographic Engineer, last serving as Commander and Director, U.S. Army Topographic Engineering Center (TEC) – now the Army Geospatial Center (AGC). Today He is a Senior Project Manager for Dewberry Engineers, Inc. and currently editing the 3rd edition of “Digital Elevation Model Technologies and Applications: The DEM Users Manual.”*

### What did you learn from your active duty years in U.S. Army Corps of Engineers (USACE)?

Nearly all engineers apply the principles of science and mathematics to develop economical solutions to technical problems; their work is the link between scientific discoveries and the commercial applications that meet societal and consumer needs. Topographic engineers apply the principles of geodesy and various forms of remote sensing to map topographic and bathymetric surfaces – also to satisfy societal and consumer needs. During my Army years, most engineers in USACE built physical infrastructure; but topographic engineers built geospatial infrastructure.

### Tell us about your background that lead you to editing the DEM Users Manual?

I retired from Army active duty in 1991 and joined Dewberry in 1992 where I initially applied my expertise to floodplain mapping for FEMA; fortunately, I was able to pioneer FEMA's evaluation of lidar and IfSAR. At the ASPRS annual conference in 2000, I published a paper entitled: “Lidar and IfSAR: Pitfalls and Opportunities for our Future.” That paper was so well received that the ASPRS Executive Board asked me to write an ASPRS book on lidar and IfSAR. I replied that I would do so provided I could also include other technologies including photogrammetry, bathymetric lidar and sonar, and write it with a focus on the needs of DEM users, whether the DEM pertained to topographic or bathymetric surfaces.

The 1st edition of “Digital Elevation Model Technologies and Applications: The DEM Users Manual” was published in 2001, and the 2nd edition was published in 2007. Having almost no standard DEM products in those days, both editions included a User Requirements Menu for which users could pick and choose from a large array of choices for elevation surface types, data model types, source data, vertical and horizontal accuracy, accuracy testing and reporting, forms of hydro treatments, horizontal and vertical datums, geoid models, units, data formats, and metadata. Because technologies were immature, we had no nationwide DEM standards, guidelines and specifications, other than the FEMA guidelines that long served as a de facto lidar specification. My User Requirements Menu unknowingly demonstrated our need for standard products because all of these menu choices led to a broad assortment of nonstandard DEM products that were often incompatible with adjoining datasets.

# AN INTERVIEW

## What motivated the new edition of the “The DEM User Manual”?

Whenever I autograph a copy of the DEM Users Manual, I write “May all your DEMs come true!” This is an obvious play on words with “May all your dreams come true.” When the 2<sup>nd</sup> edition was published, I had three basic dreams:

1. Development of high-accuracy, affordable elevation technologies for the betterment of society
2. Development and update of DEM technology standards, guidelines and specifications, and
3. Implementation of a nationwide program, such as today’s 3D Elevation Program (3DEP), to produce and maintain standardized high-quality DEMs used by all.

These first three dreams have largely been realized, as documented in this 3<sup>rd</sup> edition. My future dreams include:

4. Development of a seamless 3D Nation from the tops of the mountains to the depths of the seas, to include inland bathymetry
5. Use of the latest elevation data to routinely and systematically update the National Hydrography Dataset (NHD), flood studies, forest metrics and other datasets that require up-to-date topographic and bathymetric DEMs, and
6. Development of DEM applications to fully support the dozens of business uses and hundreds of mission-critical activities (MCAs) documented in the National Enhanced Elevation Assessment (NEEA) study published in 2012 and the 3D Nation Requirements and Benefits Study being conducted in 2018-2019.

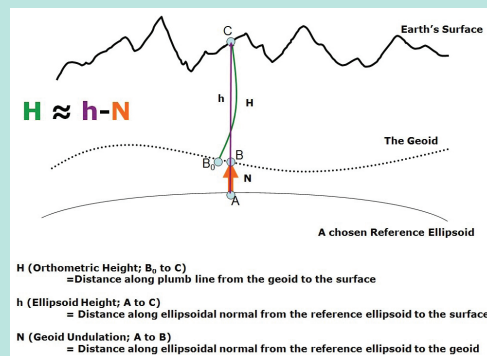
The focus of this 3<sup>rd</sup> edition of the DEM Users Manual is to help make all of these dreams come true.

## Is there recent progress in the production of digital elevation models ASPRS members should note?

Over the past decade, technologies have matured, and much progress has been made towards standardization:

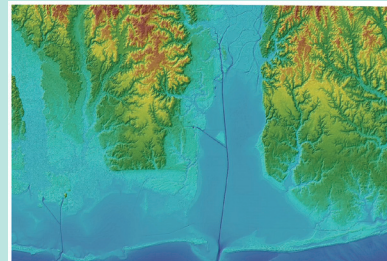
- In 2010, the U.S. Geological Survey (USGS) published its draft Lidar Guidelines and Base Specifications, V.13, which ultimately became the USGS Lidar Base Specification, V1.0.
- In 2012, the NEEA study was published that provided a comprehensive analysis of DEM user requirements and benefits for five Quality Levels (QLs) of topographic DEMs.
- In 2012, USGS published its Lidar Base Specification, V1.0.
- In 2013, based on the NEEA implementation scenario with the highest return-on-investment, USGS announced the new 3DEP to deliver QL2 lidar nationwide except for QL5 IfSAR statewide in Alaska.
- In 2013, ASPRS published its latest LAS Specification, V1.4.

datum to another. Figure 7 (right) is an image from Chapter 2 that explains the difference between orthometric heights, ellipsoid heights, and geoid undulations.

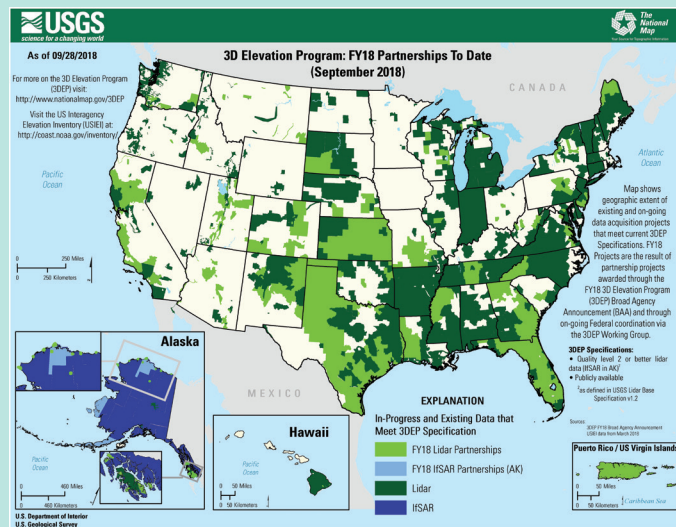


**Chapter 3—Standards, Guidelines and Specifications** introduces DEM users to the ASPRS Positional Accuracy Standards for Digital Geospatial Data v1.0, the ASPRS LAS Specifications v1.4, the USGS Lidar Base Specifications v1.3, the National Ocean Service (NOS) Hydrographic Survey Specifications based on standards of the International Hydrographic Organization (IHO), and other relevant standards, guidelines and specifications. It is important that DEM users understand these documents and how they must be rigorously enforced to achieve our vision of a seamless, consistent, high-accuracy, high-resolution 3D Nation, from the tops of the mountains to the depths of the sea.

**Chapter 4—The National Elevation Database—NED** provides the background, rationale and history of the legacy NED and how NED data were produced, quality controlled and delivered to the public. It provides information about NED specifications and production processing, accuracy and data quality. The NED was retired when the 3DEP became operational, but USGS is developing a new line of science products known as the Coastal National Elevation Database (CoNED) which integrates recent high resolution coastal lidar data (both topographic and bathymetric) and a temporal component from captures on different dates. An example of a CoNED dataset is shown at Figure 8 (right).

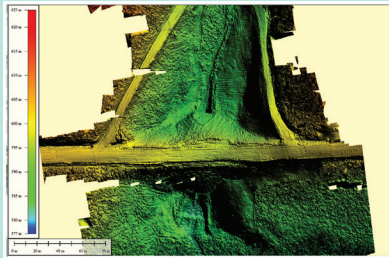


**Chapter 5—The 3D Elevation Program—3DEP** explains USGS’ national elevation initiative that forms the elevation layer of The National Map. The 3DEP resulted from analyses and vetting of the NEEA study which assessed

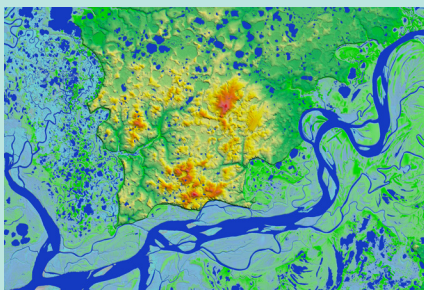


DEM user requirements and benefits and concluded that the highest return on investment would come from QL2 lidar nationwide except for QL5 IfSAR of Alaska. The chapter describes the 3DEP program; the U.S. Interagency Elevation Inventory (USIEI); the USGS Lidar Base Specifications; the Broad Agency Announcement (BAA) process; acquisition trends; 3DEP data quality assurance; 3DEP products, services and data dissemination; current developments and future directions. Figure 9 (previous page) shows 3DEP partnership awards for FY2018 alone, a major reason why the 3DEP is so popular and successful.

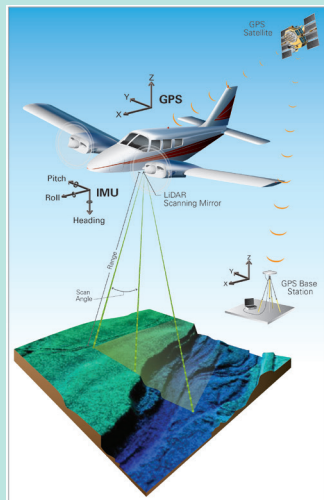
**Chapter 6—Photogrammetry** explains airborne and satellite digital imaging systems; project planning considerations; georeferencing and aerotriangulation; photogrammetric data collection methods (softcopy stereoplotters, manual and automated elevation collection); post processing; data deliverables; enabling technologies; calibration procedures; capabilities and limitations compared with competing/complementary technologies; DEM user applications; cost considerations; and technological advancements. It is important that DEM users understand the capabilities and limitations of photogrammetry compared with lidar and IfSAR, for example. Figure 10 (right) is an example of a DEM produced with Structure from Motion (SfM) photogrammetry and UAV imagery.



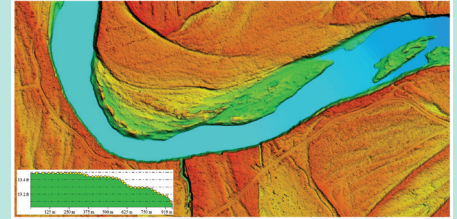
**Chapter 7—Interferometric Synthetic Aperture Radar—IfSAR** explains how interferometric synthetic aperture radar works, airborne and satellite IfSAR alternatives, how aerial IfSAR is completing the first-ever mapping of Alaska to specified accuracy standards, and how differential IfSAR/InSAR is used to monitor subsidence at the mm level. Mapping through clouds with high-resolution Ortho-rectified Radar Images (ORIs) and able to pan-sharpen low-resolution satellite imagery (with clouds), the IfSAR statewide mapping of Alaska will be completed in 2019, the first time that Alaska has ever been mapped to ASPRS accuracy standards. Figure 11 (right) shows the hydrographic feature detail of IfSAR data.



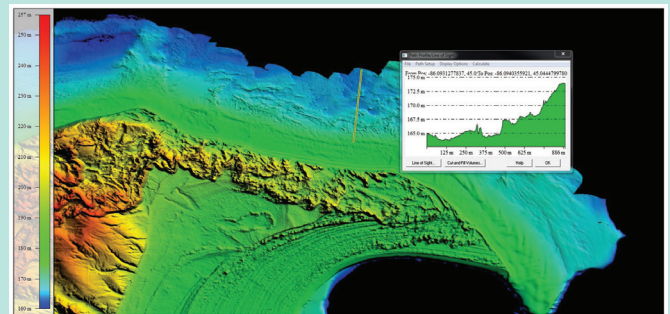
**Chapter 8—Airborne Topographic Lidar** explains the basic concepts of topographic lidar scanning and sensors; compares traditional linear-mode lidar with photon-sensitive and Geiger-mode lidar; boresight calibration; airborne lidar project planning; and the status of current lidar sensor technologies from Teledyne Optech, Leica Geosystems, Riegl, and Harris Corp. Figure 12 (right) shows a typical lidar aircraft with GPS and IMU, scanning the terrain beneath.



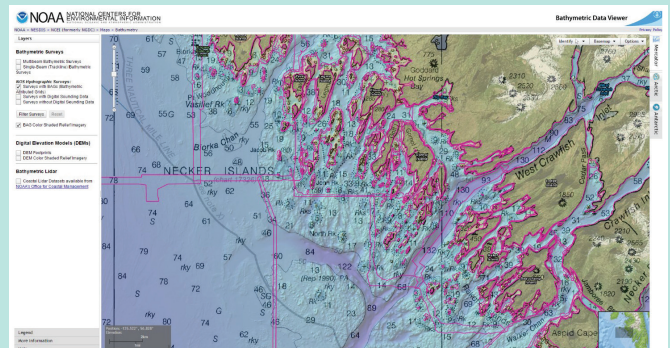
**Chapter 9—Lidar Data Processing** explains concepts and approaches to automated filtering of lidar point clouds to include ground and non-ground points, noise, vegetation, structures and other above-ground features; manual editing of lidar; breakline processing to include area and linear hydrographic features, structures, manual review and editing; elevation assignment to breakline features, to include linear and area hydrographic feature elevation assignment; DEM processing concepts and approaches, processing techniques, incorporating breaklines; DSM processing; and other derivative products including contours. Figure 13 (right) demonstrates procedures for hydro-enforcement and continuous downstream flow (monotonicity).



**Chapter 10—Airborne Lidar Bathymetry** explains the basic concepts of bathymetric lidar scanning and sensors; system design; data processing including system calibration; output formats and deliverables; and the status of current sensors including SHOALS, CZMIL, LADS, Chiroptera II/Hawk Eye III, EAARL, VQ 820/880-G, and Titan; operational and planning considerations; and comparisons with overlapping technologies. Figure 14 (below) demonstrates the bathymetric surface detail of this dataset produced by Dewberry for the NOAA Office for Coastal Management.



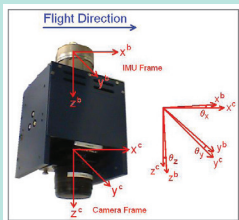
**Chapter 11—Sonar** provides a technology overview and developmental history of acoustic mapping and explains the basic principles used, to include acoustic sources and directional transmit/receive transducers. It explains the different types of sonars (vertical beam, multibeam, side scan, interferometric, focusing, and Doppler); present operating status; platforms and installation; calibration procedures; planning considerations; capabilities and limitations and comparisons with complementary and competing technologies; post processing, quality control, data deliverables, cost considerations, and technology advancements. Figure 15 (below) demonstrates a sonar product used for safety of maritime navigation.



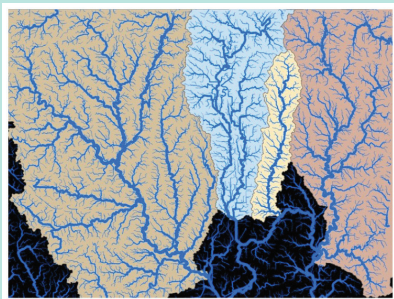
# AN INTERVIEW

- In 2014, ASPRS published its Positional Accuracy Standards for Digital Geospatial Data that included vertical accuracy classes.
- In 2014, USGS published its Lidar Base Specification, V1.2 with detailed specifications for QL0, QL1 and QL2 lidar, consistent with the ASPRS vertical accuracy classes.
- In 2015, USACE published a new EM 1110-1-1000, Photogrammetric and Lidar Mapping, endorsing both the ASPRS standards and the USGS Lidar Base Specification.
- In 2016, FEMA published its Guidance for Flood Risk Analysis and Mapping, Elevation Guidance, and it standardized on QL2 lidar as defined in the USGS Lidar Base

**Chapter 12—Enabling Technologies** explains the Global Positioning System (GPS) and other international systems that form the Global Navigation Satellite System (GNSS). It explains GNSS positioning technologies including GNSS single point positioning, differential GNSS, precise phase interferometry positioning, and precise point positioning (PPP). It explains local, regional and global differential GNSS, Continuously Operating Reference Stations (CORS), sensors and error sources. It explains inertial navigation systems (INS) and GNSS-aided inertial navigation technologies, direct georeferencing systems for airborne DEM generation, boresight calibration, post processing, and motion sensing systems for multibeam sonar bathymetry. These technologies are vital for accurate and cost-effective photogrammetry, IfSAR, lidar and sonar mapping. Although Figure 16 (right) demonstrates camera boresighting, the mounting misalignment or boresight angles between the IMU and the lidar reference frame are similarly determined through a combination of laboratory and airborne calibration.



**Chapter 13—DEM User Applications** reviews how DEMs are vital for production of digital orthophotos, topographic maps and various other types of maps (soils, geologic, wetlands, forestry, wildlife habitat, cultural resources, urban and regional planning, and flood maps); underwater and coastal mapping applications (Digital Coast, sea level rise viewing, shoreline delineation, coastal management and engineering); transportation applications (land, aviation and marine navigation and safety); military applications; technical applications (hydrologic and hydraulic (H&H) modeling [Figure 17 - below], national resources observation, water supply, subsidence, and stormwater management; commercial applications (precision agriculture, mining, renewable energy, oil and gas, telecommunications) and individual applications. It summarized the NEEA's 27 major DEM Business Uses that helped justify the 3DEP and would be relevant also to state or local initiatives seeking funding partnerships.



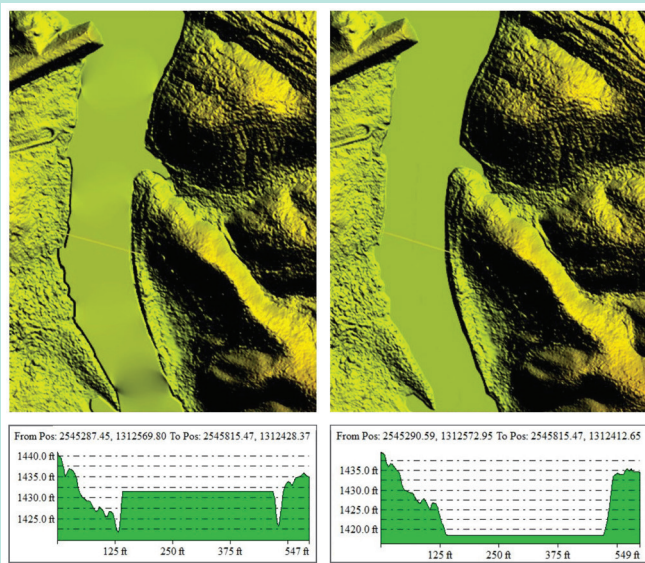
**Chapter 14—DEM User Requirements and Benefits** explains why DEM users needing lidar data should normally state their requirements for standard QL2 lidar data consistent with the 3DEP so as to receive standard raw and classified point cloud data, standard breaklines,

Specification for new lidar acquisition, consistent with the goals of the 3DEP, while also aligning with the ASPRS Positional Accuracy Standards for Digital Geospatial Data and the ASPRS LAS Specification V1.4.

- In 2017, the National Geodetic Survey (NGS) started teaming with USGS for a NEEA Update and Coastal/Offshore Elevation Requirements and Benefits Study that might establish bathymetric equivalents to the topographic data Quality Levels in the NEEA.
- In 2018, USGS published its Lidar Base Specification, V1.3, and NOAA and USGS kicked off their 3D Nation Requirements and Benefits Study.

standard metadata, and standard hydro-flattened, bare-earth raster DEMs – all with potential common data upgrades that do not compromise standardization and interoperability. The resulting benefits include: a single authoritative source of high quality and consistent 3DEP data at lower costs for all; standard 3DEP products that use common hardware/software and standard training for data users and producers; easier generation of derivative products from a standard source – all yielding a seamless, consistent elevation surface from the top of the mountains to the depths of the sea.

**Chapter 15—Quality Assessment of Elevation Data** is a 90-page tutorial with images designed to promote consistency in delivery of elevation data acceptable for the 3DEP. This chapter reviews relevant standards, guidelines and specifications; explains procedures for testing and reporting absolute and relative accuracy; and goes into great detail in addressing various forms of qualitative assessments, to include: source data QA/QC; breakline QA/QC (breakline completeness, variance and topology); macro level reviews of DEM data; and micro level reviews of topographic and topobathymetric DEMs including hydro flattening or enforcement, edge-matching, and bare-earth editing of buildings, bridges and artifacts. This chapter also includes procedures for QA/QC of contours and metadata. Figure 18 (below) shows just one of the hundreds of ways in which lidar data could fail to satisfy USGS Lidar Base Specifications.

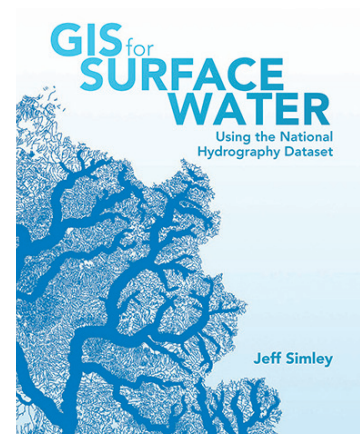


**Appendix A** is a list of approximately 500 acronyms used in the 3<sup>rd</sup> edition. **Appendix B** provides definitions for over 500 terms used in the 3<sup>rd</sup> edition. **Appendix C** explains where to download sample elevation datasets

This book introduces the audience to the National Hydrography Dataset (NHD). The book mainly targets those who study or map water features in Geographic Information Systems (GISs). It is intended to be used by users with some knowledge in both hydrography and GIS. This use of GIS in hydrography is referred to as “water GIS” by the author in his acknowledgments. The book consists of twelve chapters and is well-organized.

Chapter 1 addresses the critical role of water in civilization and what GIS is, and introduces the NHD and NHDPlus—an enhancement to the NHD. In this chapter, the author explains the major motivations behind the development of the NHD and educates the reader that the NHD is intended to be a work in progress and flexible, depending on the users’ desired level of detail and available data. Chapter 2 covers the water cycle, water budgets, the nature of water, and various water entities defined in the NHD. The author explains how various water features in the NHD can be similar to or different from those in other data sources. Chapter 3 addresses how cartographers used different methods to observe and map water on a map, and describes why the United States Geological Survey (USGS) started developing the NHD, the Watershed Boundary Dataset (WBD), and the NHDPlus. In this chapter, the author stresses the importance of the NHD in the evolution of “water GIS.” Chapter 4 discusses difficulties in identifying streams in different climates and how the NHD defines, classifies, and encodes streams and hydrology. The author summarizes different methods for classifying and coding stream networks. Also, in this chapter, he introduces Digital Flood Insurance Rate Maps (DFIRM) from the Federal Emergency Management Agency (FEMA) that the user can use as a companion dataset to the NHD to study or map floodplains inundated by extreme floods. Chapter 5 presents several hydrography datasets and looks at the issues and benefits of incorporating the datasets into the NHD.

After dedicating five chapters to addressing the basics of water and hydrography, and reviewing other datasets to better understand the needs of the users of non-NHD datasets, the book discusses the design decisions behind the NHD in Chapter 6. This chapter addresses scale issues, data accuracy and quality, and production costs. The author also discusses the role of the data model and presents the architectural concept of the NHD with its standard structure and topology that allow logical navigation and spatial interaction. Chapters 7 and 8 focus on the use of the NHD and NHDPlus in ArcGIS including how to obtain the dataset and what the data structure looks like. Chapter 7 provides an analysis exercise with step-by-step instructions that the reader can easily follow. Chapter 8 explains new capabilities in the NHDPlus such as stream order, level, and flow navigation and volume. Chapter 9 covers the use of the NHD and NHDPlus in web applications that do not require a desktop GIS or in-depth



## GIS for Surface Water Using the National Hydrography Dataset

Jeff Simley

Esri Press, Redlands, CA. 2018. xiii and 448 pp., glossary, index, about the author. Paperback. \$59.99. ISBN 978-1-58948-479-5.

**Reviewed by** Huidae Cho, Assistant Professor of Geospatial Science and Computing, Institute for Environmental and Spatial Analysis, University of North Georgia, Oakwood, Georgia.

knowledge about data analytics. Chapter 10 shows how to use Light Detection and Ranging (lidar) data and Interferometric Synthetic Aperture Radar (IfSAR) to create and attribute hydrography vector data. This chapter describes the procedure for delineating and coding stream networks using lidar and IfSAR data. Chapter 11 presents eighteen user stories where users turn the NHD into more meaningful information to help decision makers. Lastly, Chapter 12 reviews what the NHD has accomplished and discusses what the future of hydrography and “water GIS” should look like from the author’s and other researcher’s perspectives.

The author can consider following suggestions. Chapter 7 uses ArcGIS for Desktop (a.k.a., ArcMap) for an exercise, but Esri’s product line of ArcGIS for Desktop is set to enter an extended support status in 2020 and retire in 2024.<sup>1</sup> At the same time, Esri pushes ArcGIS Pro, which will eventually replace ArcMap.<sup>2</sup> I would have expected this exercise to use

Photogrammetric Engineering & Remote Sensing  
Vol. 85, No. 1, January 2019, pp. 11–12.

0099-1112/18/11–12

© 2019 American Society for Photogrammetry  
and Remote Sensing

doi: 10.14358/PERS.85.1.11

ArcGIS Pro rather than ArcMap because both industry and academia have already started adopting ArcGIS Pro or at least are planning to migrate to it. The NHD and NHDPlus are provided in Esri's proprietary geodatabase and shapefile formats, but that does not necessarily mean that these datasets cannot be used in non-Esri products. One of the import-

ant issue with this book is that it does not discuss how to use these datasets in Open Source GIS such as QGIS, which is the most popular non-commercial GIS.<sup>3</sup> The Geospatial Data Abstraction Library<sup>4</sup> provides the FileGDB<sup>5</sup> driver for read/write access to the geodatabase format and the OpenFileGDB<sup>6</sup> driver for read-only access, both of which can be used in QGIS to access this proprietary database format.<sup>7</sup> The author could have dedicated one subsection to the use of the NHD in an Open Source GIS for those without any access to Esri products.

Having said that, I still highly recommend this book to anyone who wants or needs to use the NHD to study not only hydrography but also hydrology in the United States. This book is very comprehensive and discusses many different aspects of the NHD including the history of hydrography in the United States, the structure and hierarchy of the NHD, WBD, and NHDPlus, data collection, and stream delineation and coding. The book also presents different case studies using the NHD. The material presented in this book is up to date and very useful in understanding how and why the NHD has been created. One thing I want to note is that this book is not intended to be a tutorial or user guide for NHD users. Instead, the book is more focused on introducing the NHD and educating the reader about what they can do with this dataset. It can be a good companion to the NHD User Guide published by USGS (2016).<sup>8</sup> I would say that this book is a must-have for those who have started using the NHD and want to understand the dataset better.

- 1 Esri. 2018a. ArcGIS for Desktop 10.6 Product Life Cycle. <https://support.esri.com/en/Products/Desktop/arcgis-desktop/arcmap/10-6#product-support>. Accessed on November 24, 2018.
- 2 Esri. 2018b, Migrating to ArcGIS Pro, Does ArcGIS Pro replace ArcMap? <https://www.esri.com/en-us/arcgis/products/arcgis-pro/migrate>. Accessed on November 24, 2018.
- 3 GISGeography.com. 2018. Mapping Out the GIS Software Landscape. <https://gisgeography.com/mapping-out-gis-software-landscape/>. Accessed on November 24, 2018.
- 4 GDAL. 2018a. Geospatial Data Abstraction Library. <https://www.gdal.org/>. Accessed on November 24 2018.
- 5 GDAL. 2018b. Esri File Geodatabase (FileGDB). [https://www.gdal.org/drv\\_filegdb.html](https://www.gdal.org/drv_filegdb.html). Accessed on November 24, 2018.
- 6 GDAL. 2018c. Esri File Geodatabase (OpenFileGDB). [https://www.gdal.org/drv\\_openfilegdb.html](https://www.gdal.org/drv_openfilegdb.html). Accessed on November 24, 2018.
- 7 Geospatial@UCLA, 2015. Working with File Geodatabases (.GDB) Using QGIS and GDAL. <https://gis.ucla.edu/node/53>. Accessed on November 24, 2018.
- 8 USGS. 2016. NHD User Guide., <https://nhd.usgs.gov/us-erguide.html>. Accessed on November 24, 2018.

## STAND OUT FROM THE REST

### EARN ASPRS CERTIFICATION

ASPRS congratulates these recently Certified and Re-certified individuals:

#### CERTIFIED PHOTOGRAMMETRISTS

**Nathan Litter, Certification #1642**

Effective November 1, 2018, expires November 1, 2023

**William L. Johnson, Certification #1643**

Effective November 2, 2018, expires November 2, 2023

#### CERTIFIED GEOSPATIAL INTERN GIS/LIS TECHNOLOGIST

**Jackson Ingram, Certification #GST296GI**

Effective November 20, 2018, expires November 20, 2021

#### RECERTIFIED MAPPING SCIENTIST REMOTE SENSING

**Joshua Nimetz, Certification #R206RS**

Effective August 15, 2017, expires August 15, 2022

#### RECERTIFIED MAPPING SCIENTIST GIS/LIS

**Brandon Tilley, Certification #R267GS**

Effective January 10, 2019, expires January 10, 2024

#### RECERTIFIED PHOTOGRAMMETRIST

**Barry Budzowski, Certification #R1381**

Effective November 20, 2018, expires November 20, 2023

ASPRS Certification validates your professional practice and experience. It differentiates you from others in the profession.

For more information on the ASPRS Certification program: contact [certification@asprs.org](mailto:certification@asprs.org), visit <https://www.asprs.org/general/asprs-certification-program.html>





# & GRIDS DATUMS

## THE FRENCH REPUBLIC

BY Clifford J. Mugnier, CP, CMS, FASPRS

The Grids & Datums column has completed an exploration of every country on the Earth. For those who did not get to enjoy this world tour the first time, *PE&RS* is reprinting prior articles from the column. This month's article on The French Republic was originally printed in 2001 but contains updates to their coordinate system since then.

The French Republic, originally known in the south as *Gallia Narbonensis*, was a province of the Roman Empire from 121 BC. The north and central parts, known as Gaul, were conquered by Julius Caesar from 58-51 BC. In 1789, the French Revolution overthrew the Royal government, and tumultuous times continued for over 100 years, including the reign of Napoleon Bonaparte and his First Empire. The northern part of the Republic was ravaged by fighting in World War I (1914-18), then conquered and controlled in World War II (1940-44) by the Germans. The Fourth Republic was established in 1945, and the Fifth Republic in 1958. President Charles de Gaulle resigned in 1969 following defeat of a referendum on constitutional reforms.

The Dépôt de la Guerre, established in 1688, was responsible for all military surveys. When the English scientist Sir Isaac Newton suggested that the shape of the Earth was an oblate ellipsoid, France countered that Cassini's triangulation showed that the Earth was a prolate ellipsoid. France sent expeditions to Stockholm and Quito that only served to prove the Englishman's theory correct! (See Grids and Datums of Ecuador, *PE&RS*, May 1999). The first published ellipsoid was by Bouguer and Maupertuis in 1738, as a result of their historic expeditions. During the Napoleonic Wars, Cassini was the first topographer to utilize a grid overprint on a topographic map for the "coordinated" control of artillery fire. In apparent deference to the great German cartographer, Cassini chose the Bonne equal-area projection. That projection choice, also for France's first major topographic map series of 1818-1887, influenced the rest of the world for over a century with the Carte de l'État-major au 1:80,000. The Old Triangulation of France Datum of 1818 was referenced to the DeLambre ellipsoid where the semi-major axis ( $a$ ) = 6,376,985 meters and the reciprocal of flattening ( $1/f$ )



= 308.64. The Carte de l'État-major Latitude of Origin is  $\phi_0 = 45^\circ 10' 00''$ , and the Central Meridian is  $\lambda_0 = 2^\circ 20' 13.95''$  East of Greenwich in today's convention - but was actually zero at the time. The French considered Paris as the Prime Meridian for the world, and many other countries agreed. The French Navy began publishing the *Annals Hydrographiques* in 1844 that contained latitude and longitude coordinates of stations observed astronomically worldwide, as well as details on local datums that had been established. That first tome has an amusing passage regarding the "friendly natives" encountered in an expedition to Tahiti – not all was geodesy and hydrographic surveying!

During the second half of the 19<sup>th</sup> century, France was the epicenter of mathematical cartography in the world. Tissot and Germain published their monumental works on projec-

Photogrammetric Engineering & Remote Sensing  
Vol. 85, No. 1, January 2019, pp. 13–15.  
0099-1112/18/13–15

© 2019 American Society for Photogrammetry  
and Remote Sensing  
doi: 10.14358/PERS.85.1.13

tions, and the Service Géographique de l'Armée was founded in 1887. The New Triangulation of France commenced in 1887 (NTF 1887), and the small-scale Dépôt de la Guerre (Carte de l'État-major) map series was continued until 1915 on the Bonne projection. Germain developed his Projection of Minimum Deformation, and it was chosen for the new large-scale topographic map series based on the NTF 1887. The ellipsoid of reference was the modified DeLambre 1810, or Plessis Reconstituted, where the semi-major axis ( $a$ ) = 6,376,523.994 meters and the reciprocal of flattening ( $1/f$ ) = 308.624807.

During this time, the French were developing a philosophy of categorizing map projections. This penchant, when combined with another factor, created some curious developments. Since logarithms were the universal tool for hand computations, great algebraic effort was made to simplify equations whenever possible. With numerical techniques being practically restricted to expressions in the form of infinite series, equations were always truncated to only yield the necessary computational precision. Extra digits were too expensive in terms of labor to waste on niceties. The tables of equations for the different categories of map projections showed terms only to the third power, the cubic. When Germain's Projection of Minimum Deformation was truncated to the cubic, it became identical to the Lambert Conformal Conic when truncated to the cubic. Since the late Heinrich Lambert was senior to Germain, the former's name was given to the new projection adopted for the new large-scale map series. The French tables were computed with the Lambert Conformal Conic projection of the developed meridional distance formulae truncated to the cubic term. This did not result in a strictly conformal projection, but it was deemed close enough at the time. This convention for the French Army Truncated Cubic Conic was also applied for decades to practically all of the French colonies, including Syria, the Levant or Palestine (*PE&RS* August 2000), Morocco (*PE&RS* June 1999), Algeria, Tunisia, and French Indochina (Laos, Cambodia, and Vietnam).

When the officers of the French Army fled France after the Kaiser invaded their country, they carried many of their surveys and map manuscripts to London. The United States commissioned some mathematicians and geodesists with the Coast Survey into the Corps of Engineers and sent them to London to assist the Royal Engineers and the French. Upon arrival, they noticed the scarcity of the Tables of Projection for the northern war zone (Nord de Guerre), and sent one copy back to Washington for tabular extension and duplication. In Washington, it was noticed that the documented formula was truncated at the cubic term. They apparently decided to develop tables that not only had greater latitudinal extent, but they also decided to use more terms for the developed meridional distances. Shortly after a group of mathematicians was assigned to perform the task, others at the Coast Survey decided that it was a nifty idea to use a conformal projection for a basis of survey computations. Another group was assigned to perform the same task, but instead of using

the Plessis ellipsoid for the Nord de Guerre Zone of France, they used the Clarke 1866 ellipsoid for the United States. Computations for both tables were completed at the same time, and both manuscripts were sent to the Superintendent of Documents at the same time. When the printing office sent the crates of tables back to the Coast Survey, the wrong crate was shipped to London. After some consternation, the proper crate arrived, only to cause further consternation. The fully conformal tables for the Lambert Conformal Conic would not cast a graticule to match the existing Nord de Guerre Zone sheets based on the French Army Truncated Cubic Conic. The new tables were discarded, the Royal Engineers and the French Army Engineers "made do" with what they already had. **Moral: use the same projection formulas as the originating country uses. It is not "correct" unless it matches native work.**

The French Kilometric Quadrillage (AEF) of 1918 was based on the Fully Conformal Lambert Conic where the Latitude of Origin was  $\phi_0 = 49^\circ 30' 00''$ , and the Central Meridian was  $\lambda_0 = 7^\circ 44' 13.95''$  East of Greenwich, the Scale Factor at Origin ( $m_0$ ) = 0.999509082, and both the False Eastings and False Northings were 500 km. The ellipsoid of reference was the Clarke 1866, and this Grid was never used. On the other hand, the French Nord de Guerre Zone (1914-1948) was used, and it was based on the French Army Truncated Cubic Conic where the Latitude of Origin was  $\phi_0 = 49^\circ 30' 00''$ , the Central Meridian was  $\lambda_0 = 7^\circ 44' 13.95''$  East of Greenwich, the Scale Factor at Origin ( $m_0$ ) = 0.999509082, and the False Easting was 500 km and the and False Northing was 300 km. The ellipsoid of reference was the Plessis Reconstituted.

After WWI, the French developed four Lambert zones for the country. From 1920 to 1948, Zone I (Nord) parameters were where the Latitude of Origin was  $\phi_0 = 49^\circ 30' 00''$ , the Central Meridian was  $\lambda_0 = 2^\circ 20' 13.95''$  East of Greenwich, the Scale Factor at Origin ( $m_0$ ) = 0.999877340, and the False Easting was 600 km and the False Northing was 200 km. The ellipsoid of reference was the Clarke 1880, where the semi-major axis ( $a$ ) = 6,378,249.2 meters and the reciprocal of flattening ( $1/f$ ) = 293.4660208. In France, for Zone II (Centre), the Latitude of Origin was  $\phi_0 = 46^\circ 48' 00''$ , the Central Meridian was  $\lambda_0 = 2^\circ 20' 13.95''$  East of Greenwich, the Scale Factor at Origin ( $m_0$ ) = 0.999877419, and the False Easting was 600 km and the False Northing was 200 km. In France, for Zone III (Sud), the Latitude of Origin was  $\phi_0 = 44^\circ 06' 00''$ , the Central Meridian was  $\lambda_0 = 2^\circ 20' 13.95''$  East of Greenwich, the Scale Factor at Origin ( $m_0$ ) = 0.999877501, and the False Easting was 600 km and the False Northing was 200 km. In France, for Zone IV (Corse) Corsica, the Latitude of Origin was  $\phi_0 = 42^\circ 09' 54''$ , the Central Meridian was  $\lambda_0 = 2^\circ 20' 13.95''$  East of Greenwich, the Scale Factor at Origin ( $m_0$ ) = 0.999940004, and the False Easting was 600 km and the False Northing was 200 km. All four of these zones were based on the French Army Truncated Cubic Conic projection.

In 1940, the mapping agency was renamed the Institute Géographique National (IGN). The French government de-

clared, “C’est pourquoi il fut décidé en 1948 de substituer des formules rigoureuses aux développements limités, en conservant les mêmes limites de zones et les mêmes modules d’homothétie.” In other words, France went to the rigorous fully conformal formulae in 1948 for the Lambert Conic. Since then, only Algeria has deemed to do the same in the early 1960s, according to Roger Lott, the chief surveyor of British Petroleum. The other old French colonies, although now independent, still use the French Army Truncated Cubic. Some old colonies still consider Paris as the origin of longitudes (*PE&RS* February 2000). One caution for the U.S. practitioner: the French do not use degrees-minutes-seconds for angular measurement; they use Grads where  $400^G = 360^\circ$ .

After 1948, the new French Lambert zones (I-IV) retained the same parameters as listed above for the Republic. Only the formulae changed. During that same era, the U.S. Army Map Service directed the recomputation of all the triangulations of Europe and the Mediterranean to the European Datum of 1950. Everything was sequentially tied to France (*PE&RS* October 1998, October 1999, and July 2000), and the unifying tool was the UTM Grid. France is covered by UTM zones 30-32 referenced to the EU50 Datum and the International ellipsoid where  $a = 6,378,388$  m and  $(1/p) = 297$ .

IGN currently publishes their general national 3-parameter transformation from NTF to WGS84 as:  $dX = +168$  m,  $dY = +60$  m,  $dZ = -320$  m.

## UPDATE

The IGN.FR (Institut Géographique National) now maintains a website<sup>1</sup>, which describes how the country has a complete dense coverage<sup>2</sup> of public GPS Continuously Operating Reference Station (CORS<sup>3</sup>) sites, and IGN offers a free computational web page that accepts the user’s choice of up to four National CORS sites to process with their own observations<sup>4</sup> in a manner somewhat akin to the U.S. National Geodetic Survey’s Online Positioning User Service or “OPUS”<sup>5</sup> The IGN website is well-designed and covers practically anything a potential user could ask for regarding France proper as well as for all of its Overseas Territories.

1 <http://www.ign.fr/>. Accessed 12 Decmeber 2018.

2 <http://rgp.ign.fr/>. Accessed 12 Decmeber 2018.

3 <https://www.ngs.noaa.gov/CORS/>. Accessed 12 Decmeber 2018.

4 [http://rgp.ign.fr/SERVICES/calcul\\_online.php](http://rgp.ign.fr/SERVICES/calcul_online.php). Accessed 12 Decmeber 2018.

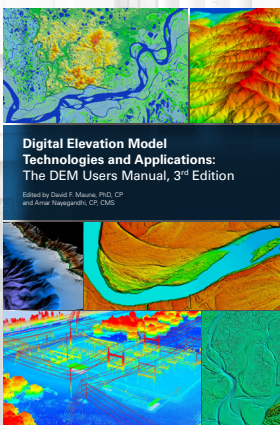
5 <https://www.ngs.noaa.gov/OPUS/>. Accessed 12 Decmeber 2018.

The contents of this column reflect the views of the author, who is responsible for the facts and accuracy of the data presented herein. The contents do not necessarily reflect the official views or policies of the American Society for Photogrammetry and Remote Sensing and/or the Louisiana State University Center for GeoInformatics (C<sup>4</sup>G).

This column was previously published in *PE&RS*.

## NEW FROM ASPRS AND DEWBERRY

# DEM Users Manual, 3<sup>rd</sup> Edition



This book is your guide to 3D elevation technologies, products and applications. It will guide you through the inception and implementation of the U.S. Geological Survey’s (USGS) 3D Elevation Program (3DEP) to provide not just bare earth DEMs, but a full suite of 3D elevation products using Quality Levels (QLs) that are standardized and consistent across the U.S. and territories. The 3DEP is based on the National Enhanced Elevation Assessment (NEEA) which evaluated 602 different mission-critical requirements for and benefits from enhanced elevation data of various QLs for 34 Federal agencies, all 50 states (with local and Tribal input), and 13 non-governmental organizations. The NEEA documented the highest Return on Investment from QL2 lidar for the conterminous states, Hawaii and U.S. territories, and QL5 IfSAR for Alaska.

Co-Editors

David F. Maune, PhD, CP and Amar Nayegandhi, CP, CMS

DEM Users Manual, 3<sup>rd</sup> Ed.

Hardback. 2018, ISBN 1-57083-102-5, Stock # 4959

Hardcopy

List Price \$100

ASPRS Member \$80

Student \$50

\*Plus shipping/handling



ORDER ONLINE [HTTPS://WWW.ASPRS.ORG](https://www.asprs.org)

## GREETINGS FROM THE STUDENT ADVISORY COUNCIL (SAC)

**A**SPRS' annual conference, the centerpiece of Geo Week 2018, will be taking place in Denver, Colorado, this month! Geo Week is an excellent opportunity for students to learn, network, and share their research. Signatures will highlight some of these exciting opportunities including the Student Advisory Council (SAC) student paper sessions, GeoLeague competition, SAC business meeting, and opportunities to become more involved in the SAC.

### STUDENT PAPER SESSION

The SAC student paper session will take place in conference room 24D at 2:00 PM on Wednesday, 30 January 2019. The student paper session is frequently a conference highlight for participants and audience members. We encourage any conference attendee to attend this session to learn more about exciting research conducted by ASPRS' student members. Paper topics include UAS calibration, UAS mapping, and novel applications in stereo pair matching. Each presentation will last approximately 15 minutes, and there will be time for questions.

### GEOLEAGUE

GeoLeague will be taking place on Monday, 28 January 2019 at 4:00 PM. The GeoLeague is a jeopardy style competition that tests the geospatial knowledge of four person teams composed of students, ILMF attendees, and ASPRS members. Teams are pitted against one another in a head to head competition. Categories can range from lidar to the history of ASPRS. Winners receive prizes, and everyone is guaranteed to have a good time.

### SAC MEETING

The SAC business meeting will take place in Granite C room at 2:00 PM on Monday, 28 January 2019. We encourage all students to attend this session. The SAC is a great way to become more involved in ASPRS. The business meeting will introduce ASPRS student members to the SAC and the what initiatives are currently in planning. Interested in learning more about these opportunities? Contact the SAC at SAC@asprs.org.

## JOIN THE SAC

Become more involved in the ASPRS apply to join the SAC at <https://www.asprs.org/councils/student-advisory-council-positions> and click apply here!

---

#### ASPRS STUDENT ADVISORY COUNCIL

JEFF PU  
COUNCIL CHAIR

BOBBY ARLEN  
EDUCATION COUNCILOR

ANTHONY CAMPBELL  
COMMUNICATIONS COUNCILOR

BRIANA WILLIAMS  
NETWORKING COUNCILOR

VICTORIA SCHOLL  
DEPUTY COUNCIL CHAIR

CORY CADDELL  
DEPUTY EDUCATION COUNCILOR

KATHERINE GATES  
DEPUTY COMMUNICATIONS COUNCILOR

GERARDO ROJAS  
DEPUTY NETWORKING COUNCILOR

## JOURNAL STAFF

### Editor-In-Chief

Alper Yilmaz, Ph.D., PERSeditor@asprs.org

### Associate Editors

Rongjun Qin, Ph.D., qin.324@osu.edu  
 Michael Yang, Ph.D., michael.yang@utwente.nl  
 Petra Helmholz, Ph.D., Petra.Helmholz@curtin.edu.au  
 Bo Wu, Ph.D., bo.wu@polyu.edu.hk  
 Clement Mallet, Ph.D., clemallet@gmail.com  
 Vasisit Sagan, Ph.D., Vasisit.Sagan@slu.edu  
 Jose M. Pena, Ph.D., jmpena@ica.csic.es  
 Xin Huang, Ph.D., huang\_w hu@163.com  
 Prasad Thenkabail, Ph.D., pthenkabail@usgs.gov  
 Ruisheng Wang, Ph.D., ruiswang@ucalgary.ca  
 Desheng Liu, Ph.D., liu.738@osu.edu  
 Valérie Gouet-Brunet, Ph.D., valerie.gouet@ign.fr  
 Yury Vizilter, Ph.D., viz@gosnias.ru  
 Dorota Iwaszczuk, Ph.D., dorota.iwaszczuk@tum.de  
 Qunming Wang, Ph.D., wqm11111@126.com  
 Filiz Sunar, Ph.D., fsunar@itu.edu.tr  
 Norbert Pfeifer, Ph.D., np@ipf.tuwien.ac.at  
 Jan Dirk Wegner, Ph.D., jan.wegner@geod.baug.ethz.ch  
 Hongyan Zhang, Ph.D., zhanghongyan@whu.edu.cn

### Assistant Editor

Jie Shan, Ph.D., jshan@ecn.purdue.edu

### Managing Editor

Melissa J. Porterfield, Ph.D., managingeditor@asprs.org

### Contributing Editors

#### Grids & Datums Column

Clifford J. Mugnier, C.P., C.M.S., cjmce@lsu.edu

#### Book Reviews

Sagar Deshpande, Ph.D., bookreview@asprs.org

#### Mapping Matters Column

Qassim Abdullah, Ph.D., Mapping\_Matters@asprs.org

#### Sector Insight

Amr Abd-Elrahman, Ph.D., sectorinsights@asprs.org  
 Lucia Lovison-Golob, Ph.D., lucia.lovison@sat-drones.com  
 William C. Wright, Ph.D., William.Wright@USMA.edu

#### Project Management Column

Raquel Charrois, PMP, CP, CMS, PMP@asprs.org

### ASPRS Staff

#### Assistant Director — Publications

Rae Kelley, rkelley@asprs.org

#### Electronic Publications Manager/Graphic Artist

Matthew Austin, maustin@asprs.org

#### Circulation Manager

Priscilla Weeks, pweeks@asprs.org

#### Advertising Sales Representative

Bill Spilman, bill@innovativemediasolutions.com

## MIKE RENSLOW RETIRES FROM ASPRS



**M**ike Renslow, Technical Editor of *PE&RS*, who has also been heavily involved in coordination and administration of ASPRS' Certification Program over the last 15 years, announced his retirement this fall from both programs.

"It has been a honor work with Mike on *PE&RS*" said Rae Kelley, Associate Director – Publications. "He has been an integral part of our production team since 2004."



Melissa J. Rura-Porterfield, Ph.D., has taken on the position Managing Editor for *PE&RS*. Melissa has work with ASPRS and *PE&RS* in various positions, including BBook Review Editor, SectorInsights Editor and on the update of The Glossary of Mapping Sciences.. "Melissa is very through and will take *PE&RS* to the next level. She is the perfect addition to our team" said Rae Kelley.

## ASPRS MEMBERSHIP

ASPRS would like to welcome the following new members!

### At Large

Adam Steer  
 Wenzong Wang  
 Ayad M. Fadhil  
 Al-Quraishi  
 Yichen Lei  
 Huan Xie  
 Gaoxiang Zhou

### Columbia River

Mischa Hey  
 Zoe Nicole Mills

### Eastern Great Lakes

Anderson Cornwall

### Florida

Scott Edenfield  
 Daniel Hutton  
 Steven Hyde, PLS  
 Joshua Misura

### Grace Plass

John (Ryan) Taylor

### Heartland

Joshua David Carron  
 Arpan Kusari

### Inter-Mountain

Ryan Howell  
 Keegan Sisroy

### Mid-South

Whitney Broussard, III  
 Kelvin Leonard Kiwale  
 Andrew N. Mindermann  
 Matthew Moudy  
 Max Pedowicz  
 George Jamal Pualwan  
 Ray D. Weger

### New England

Peter J. Cariani  
 Adam Kersnowski

### Pacific Southwest

Felicia Betancourt  
 Greald Scott Dildine  
 Michael Maier  
 Petros Maskal

### Potomac

Lisa Colson  
 Stephanie Johnson  
 Blaine Lary  
 Mike Meenehan

### Rocky Mountain

Barry Yu Miller

### Western Great Lakes

Curtis Edson

FOR MORE INFORMATION ON ASPRS MEMBERSHIP, VISIT

[HTTP://WWW.ASPRS.ORG/JOIN-NOW](http://www.asprs.org/join-now)

*Your path to success in the geospatial community*

## JOIN ASPRS IN CELEBRATING OUR NEWEST RISING STAR!

**K**ris Taniguchi-Quan is the newest ASPRS Rising Star. Kris is being sponsored by the ASPRS Pacific Southwest Region.



Kris is a research scientist at Southern California Coastal Water Research Project (SCCWRP), a leading U.S. environmental research institute that works to develop a scientific foundation for informed water-quality management in southern California and beyond. Kris received her B.S. in Environmental Science – Watershed Science in 2011 and M.S. in Geography in 2014 from San Diego State University (SDSU) and Ph.D. in Geography in 2018 from the joint doctoral program at SDSU and University of California, Santa Barbara. Kris is a fluvial geomorphologist who utilizes advanced geospatial techniques to investigate the impacts of urban development on river hydrology, stream channel erosion, and sediment transportation. During her graduate career, Kris has collaborated with the County of San Diego in using remote sensing techniques for stream channel characterization and historical time-series of channel form, and with the U.S. Environmental Protection Agency (EPA) and U.S. Department of Agriculture in utilizing unmanned aerial systems (UAS) and StructurefromMotion (SfM) photogrammetry techniques to quantify, monitor, and model erosion in Tijuana, Mexico. Her current research at SCCWRP focuses on developing and implementing a variety of watershed management tools to address the effects of hydrologic alteration on the ambient condition of streams and to develop ecohydrology targets designed to protect stream health. Kris strives to integrate geospatial sciences into watershed management and will be developing tools on the use of UAS for ephemeral and intermittent stream channel monitoring in southern California.

### CALENDAR

- 25-31 January, **GEO WEEK—ASPRS/MAPPS/ILMF**, Denver, Colorado. For more information, visit [www.lidarmap.org](http://www.lidarmap.org).
- 25-27 February, **2019 STRATUS Workshop— Systems and Technologies for Remote Sensing Applications Through Unmanned Aerial Systems**, Rochester, New York. For more information visit <http://ewh.ieee.org/r1/rochester/grss/STRATUS2019>.
- 25-28 February, **2019 GIS /CAMA Technologies Conference**, Portland, Oregon. For more information, visit [www.urisa.org/gis-cama-technologies-conference/](http://www.urisa.org/gis-cama-technologies-conference/).
- 3-7 April, **AAG 2019 Annual Meeting**, Washington, DC. For more information, visit <http://annualmeeting.aag.org/>.
- 29-30 April, **Digital Image & Signal Processing**, Oxford, United Kingdom. For more information, visit [www.disp-conference.org](http://www.disp-conference.org).
- 3-5 May, **5<sup>th</sup> International Conference on Geographical Information Systems Theory, Applications and Management**, Heraklion, Crete, Greece. For more information, visit <http://www.gistam.org>.
- 6-11 October **Pecora 21/ISRSE 387**, Baltimore, Maryland. For more information, visit <http://www.asprs.org/event/pecora21-isrse38>.

### Ad Index

Geomni, Inc.

[Geomni.net/psm](http://Geomni.net/psm)

Cover 4



**Too young to drive the car? Perhaps!  
But not too young to be curious about geospatial sciences.**

The ASPRS Foundation was established to advance the understanding and use of spatial data for the betterment of humankind. The Foundation provides grants, scholarships, loans and other forms of aid to individuals or organizations pursuing knowledge of imaging and geospatial information science and technology, and their applications across the scientific, governmental, and commercial sectors.

**Support the Foundation, because when he is ready so will we.**

[asprsfoundation.org/donate](http://asprsfoundation.org/donate)



# Simultaneous Chain-Forming and Generalization of Road Networks

Susanne Wenzel and Dimitri Bulatov

## Abstract

Streets are essential entities of urban terrain and their automatic extraction from airborne sensor data is cumbersome because of a complex interplay of geometric, topological, and semantic aspects. Given a binary image representing the road class, centerlines of road segments are extracted by means of skeletonization. The focus of this paper lies in a well-reasoned representation of these segments by means of geometric primitives, such as straight line segments as well as circle and ellipse arcs. Thereby, we aim at a fusion of raw segments to longer chains which better match to the intuitive perception of what a street is. We propose a two-step approach for simultaneous chain-forming and generalization. First, we obtain an over-segmentation of the raw polylines. Then, a model selection approach is applied to decide whether two neighboring segments should be fused to a new geometric entity. For this purpose, we propose an iterative greedy optimization procedure in order to find a strong minimum of a cost function based on a Bayesian information criterion. Starting at the given initial raw segments, we thus can obtain a set of chains describing long alleys and important roundabouts. Within the procedure, topological attributes, such as junctions and neighborhood structures, are consistently updated, in a way that for the greedy optimization procedure, accuracy, model complexity, and topology are considered simultaneously. The results on two challenging datasets indicate the benefits of the proposed procedure and provide ideas for future work.

## Introduction and Previous Work

An urban street network is an essential element of any city. Interpreting and generalizing its structure, including identification of patterns in it, not only helps to understand the structure and organization of the city, but also to interpret its historical and cultural development. How fascinating and captivating the task of description and generalization of road systems is can be visualized by several examples. Centers of many North and South American cities exhibit grid-like structures, which had been done not only for the sake of simplicity but also to impress the native inhabitants by the orderliness and civility of the conquerors. Many cities of the Middle East are characterized the labyrinth structure of paths with no visible order, which had the purpose of hiding and segregation of private aspects of life. Around many larger towns in Europe, ring roads and highways were built to organize their transportation and supply of goods as well as to avoid the traffic congestions in the inner cities, which by the way could negatively affect the city's ecology. Also in the countryside of Western European countries, such as France, there are many roundabouts which allow to regulate the traffic without necessity to mount and to maintain semaphores at every corner.

Susanne Wenzel is with the Institute of Geodesy and Geoinformation, University of Bonn, Germany. (s.wenzel@igg.uni-bonn.de)

Dimitri Bulatov is with Fraunhofer Institute of Optics, System Technologies and Image Exploitation (IOSB) in, Ettlingen, Germany (dimitri.bulatov@iosb.fraunhofer.de).

All this motivates many researchers to assess the street networks by 1) topology- and 2) geometry-based generalization methods, thus representing the main features of the road networks while suppressing their less necessary details. In the first group of methods, graph-theoretical aspects play the major part. We start the literature review by a purely topology-based method of Jiang and Claramunt (2004) who classify the road segments with respect to graph centrality properties such as degree, closeness, and betweenness. The purpose is to filter out less important road segments with respect to their topological properties. In the same category lies the work of Touya (2010), but with a stronger emphasis on the context, for example, differentiation between urban and rural road systems. An aspect interesting for us was the continuation of road strokes at the junction. The work of Mackaness and Mackechnie (1999) aims at the detection and simplification of junctions. First, without any topological context, road endpoints are clustered by a procedure that reminds of the DBSCAN algorithm. Levels of generalization are predefined using continuously increasing cluster radii. The road-net topology is then completed by rules of graph-theory: Join vertices, delete vertices, delete edge, contract edge, and add a new vertex or edge.

Many approaches strive for pattern extraction in road networks. For example, Yang *et al.* (2010) and Tian *et al.* (2016) extract grid-like patterns. Tian *et al.* (2016) recognize maximum connected components of subgraphs with similar line orientation. By finding two such dominant directions, grid cells are then easily gathered. Alternatively, Yang *et al.* (2010) developed an adaptive method for identification of grid patterns, which includes estimation of attributes of the polygons, parameter integration and identification of grid patterns; for the latter step, an automatic threshold selection module constitutes the particular innovation of the algorithm. The presented results are impressive, however, not much doubt is left that still work is to be done. For example, Tian *et al.* (2016) have stated that their method is yet to be applied to more complex data sets and that they see the system as incomplete as long as recognition of other patterns, such as rings and roundabouts, is not developed. While Sheeren *et al.* (2004) proposed a technique for recognizing roundabouts, which correspond to mathematical graph faces, Heinzle *et al.* (2006) have differentiated between grids, star, and ring patterns. To recognize star patterns, for example, a technique based on the Dijkstra minimum cost path algorithm was applied while for identification of ring structures, properties like curvature and convexity were taken into consideration.

The topology-based techniques, as the name already suggests, have the big advantage that the graph structure of the road network is retained together with its most essential properties. The main problem is that the geometrical aspects are

Photogrammetric Engineering & Remote Sensing  
Vol. 85, No. 1, January 2019, pp. 19–28.  
0099-1112/18/19–28

© 2019 American Society for Photogrammetry  
and Remote Sensing  
doi: 10.14358/PERS.85.1.19

underestimated, and therefore not always properly assessed. That similarity of the dominant directions is not always a good measure for neighbored road segments to belong together has been shown by two examples by Bulatov *et al.* (2016a). In that work, the goal was to generalize the vector data of street center-lines resulting from exploitation of airborne sensor data, for which many other excellent contributions exist (Mena, 2006; Clode *et al.*, 2007; Wegner *et al.*, 2015). The importance of these contributions is undermined by the fact that road networks are rapidly changing especially in urban environment, while in rural regions or in developing countries, merely main roads are listed in the openly available GIS data. In short, actuality, completeness and correctness of the GIS data that had been used by Yang *et al.* (2010) and other previous approaches focusing on topology only cannot always be guaranteed. However, for various time-critical applications, these missed side paths and escape ways are often essential.

Because of the variety of appearances and road types (sidewalks, tunnel entries, bridges, railways, etc.), occlusions (tree crowns or moving vehicles), shadows, etc., extraction of roads from image data is a challenging task. This is where the geometry-based generalization methods come into play. The most famous one is the Douglas-Peucker generalization method (Douglas and Peucker, 1973) which results in a representation of edges of the input polygonal chain (to be referred as a polyline in the course of this paper) by a set of straight lines. Numerous attempts have been made since then in order to improve this method. For example, Saalfeld (1999) addresses the problem of topological inconsistencies. Another area of improvement is the generalization of this approach for circle arcs, ellipses, clothoids and other geometric primitives. For example, Günther and Wong (1990) propose what they call Arc Tree, which represents arbitrary shapes in a hierarchical data structure with small curved segments at the leaves of a balanced binary tree. Moore *et al.* (2003) propose a method for polygon simplification using circles. They aim at closed polygons given by a set of 2D points. Based on the medial axis from Voronoi polygons, they propose a population of circles which they afterwards filter to get a set of circles which best approximate the given polygon. The final representation of the polygon consists of circles and tangents linking neighboring circles. Finding ellipses in images has also attracted many researchers (Porrill, 1990; Patraucean *et al.*, 2012), even though these works start from pixel-chains, which is not the case in our application. We are interested in the more general problem of describing polygonal chains by sequences of straight line, circle, and ellipse segments, a problem already addressed by Albano (1974), however, neither enforcing ellipses, nor looking for a best estimate for ellipses.

Most related to our approach is the work by Rosin and West (1995), who perform a segmentation of point sequences into straight lines and ellipses in a multistage process. They first segment a 2D-curve into straight lines. Afterwards sequences of line segments are assigned to arcs restricted to their endpoints. We might interpret this step as merging sequences of lines to elliptical arcs. Model selection is done implicitly by evaluating a significance measure to each proposed segment, which is based on its geometry, purely. However, their criteria are non-statistical, thus, cannot easily be adapted to varying noise situations. Ji and Haralick (1999) criticized this and modified their idea by a hypothesis testing framework. Starting from Rosin and West's (1995) output of arc segmentation, they merge pairs of arcs belonging to the same ellipse. Moreover, they also group non-adjacent arcs and exploit the sign of the arcs for grouping. Proposals for merging are validated using hypothesis testing. The idea of Bulatov *et al.* (2017) was to combine the *semantic* approach of fusing road segments and assuming that, being a typical

man-made object, they can be approximated by geometric primitives with the *statistical* approach of model selection to decide whether neighboring segments can be represented by a single primitive. The approach of model selection is based on information theory since not only coordinates' residuals but also model complexity is taken into consideration. One area in which this previous contribution can be improved is the way it was implemented. Basically, there were three main steps: 1) Junction-wise topological fusion using a similarity criterion, 2) Geometrical over-segmentation using the approach of Wenzel and Förstner (2013), and finally 3) Geometric generalization by means of the statistically best fitting object model and model selection. Step 1), denoted as chain forming by Bulatov *et al.* (2017), was accomplished by either comparing partial dominant directions or a RANSAC-based circle fit function. In other words, within a depth-search approach it was tested whether subsets of the road network form long straight lines or circles.

In this paper, we strive to identify the essential geometric patterns of road networks, such as long alleys and important roundabouts. Contrary to Bulatov *et al.* (2017), we wish to unify the redundant work in steps 1 and 2 into one framework containing (a breadth-first) simultaneous geometrical and topological generalization. Intuitively, the fact that merely pairwise neighbors will be considered at each step could be a disadvantage with respect to the depth search of dominant structures, since many segments are too short and do not contain too much information. It should be noted here that the initial road networks resulting from sensor data exploitation are given by a union of very short segments, from one junction to another, and not, as in case of GIS-data, by the whole entity, such as Oxford Street in London or L'Etoile in Paris. However, we expect to compensate this shortcoming by simultaneously taking into account topology, accuracy, as well as model complexity and thus to achieve a plausible solution. Even though the quality of results is expected to be below those produced by almost noise and error-free GIS data, our goal is to investigate whether the circular, linear, or elliptic structure can already be captured at the junctions within our breadth-first model selection approach and be continued in a reasonable way.

Thus, the main contribution of this work is to combine (simultaneously, within the breadth-first approach) geometrical, statistical, and semantical properties of roads. The semantical properties of roads are that they extend over a considerable distance across the images while occasionally crossing other roads in specially designed junctions. With respect to geometry, roads mostly can be represented (as typical man-made objects) by geometric primitives, like straight line segments, circle arcs, clothoids, etc. Finally, a *statistical* approach of model selection will allow us to decide whether a single primitive can represent neighboring segments. Note that after the generalization, the data is not necessarily consistent anymore; for example, a line and a circle are not guaranteed to intersect. This is a drawback at the first glance because imposing consistency on the new road system is a separate and challenging task that will not be addressed in this work. Nevertheless, the adjacency information is not lost. In the application of urban terrain simulation (Bulatov *et al.*, 2014), particularly of interest for the authors, a junction of appropriate size can be installed at the approximate intersection position of two or more roads, given the information that these roads are supposed to intersect. A virtual vehicle can then easily switch from one road to another. Conversely, wriggled, winding road segments are negatively perceived by most users of such a simulation software since they bring about jerky movements of the steering wheel.

For reasons of completeness, we provide in the following section a brief summary of methods applied in order to fit geometric primitives, such as straight lines, circles, and ellipses. Using ellipses, we strive to approximate clothoids, which are more often employed to provide a smooth transition of curvature between straight and circular road segments, especially in rural regions. The process of extracting a raw road network from the classification result is explained in Section Road Net Extraction. Afterwards, we present our approach of simultaneously forming chains and generalization such that we reach an optimal solution. Our results in the Experiments Section verify that our approach is able to generate long chains of straight as well as curved street segments, which are consistent with the initial classification result. In the last section, conclusions and ideas for future work are provided.

### Fitting Straight Lines, Circles, and Ellipses

In this section, we provide a brief summary of methods for estimating geometric entities such as straight lines, circles, and ellipses. The scope of this section is to provide the rough idea and the notation in order to allow the reader to follow the remaining procedure given at Section Merging Line Primitives Based on Model Selection. For details about the estimation procedures we refer to the literature provided below.

Given the set of  $N$  observed points  $\mathcal{X} = \{x_n\}$ ,  $n = 1 \dots N$ , we aim at the best fitting straight line, circle, or ellipse, which we represent as homogeneous elements. In each case, we look for the statistically best fitting parameter vector as well as its covariance. We need this when merging neighboring lines based on their statistical properties. A detailed discussion of uncertain homogeneous points and lines can be found in (Förstner and Wrobel, 2016) and (Meidow *et al.*, 2009). We assume i.i.d. coordinates of each point, sharing the same isotropic covariance  $\Sigma_{x_n x_n} = \sigma_n^2 \mathbf{I}_2$ .

- Straight Line:** In (Förstner and Wrobel, 2016, Sec. 9.4.2), it is shown that the statistically best fitting line passes through the centroid of given points and that its direction is given by the principal axis of their moment matrix. We obtain the estimated homogeneous coordinates of line  $\hat{\mathbf{l}}$  and the covariance matrix  $\hat{\Sigma}_{\hat{\mathbf{l}}}$ .
- Ellipse:** We use the homogeneous representation of conics to express the parameters of the ellipse. Conics are represented by a symmetric  $3 \times 3$ -matrix

$$\mathbf{C} = \begin{bmatrix} c_{11} & c_{12} & c_{13} \\ c_{12} & c_{22} & c_{23} \\ c_{13} & c_{23} & c_{33} \end{bmatrix} = \begin{bmatrix} \mathbf{C}_{hh} & c_{h0} \\ c_{0h}^T & c_{00} \end{bmatrix}. \quad (1)$$

Any point  $\mathbf{x} = [x, y, 1]^T$  on the conic fulfills  $\mathbf{x}^T \mathbf{C} \mathbf{x} = 0$ . For estimating the parameters we use the implicit polynomial representation of the conic  $\mathbf{y}^T \mathbf{c} = 0$ , with the vector of unknowns  $\mathbf{c} = [c_{11}, c_{12}, c_{22}, c_{13}, c_{23}, c_{33}]^T$  and the observations  $\mathbf{y} = [x^2, 2xy, y^2, 2x, 2y, 1]^T$ . To ensure the conic to be an ellipse,  $\det(\mathbf{C}_{hh}) > 0$  must be fulfilled. Thus, we impose the quadratic constraint  $c_{11} c_{22} - c_{12}^2 = 1$ , which is a valid choice, as the conic representation is homogeneous and all parameters can be divided by any non-zero scale factor. This leads to a non-linear Gauss-Helmert model. Using initial parameters estimated by means of the direct method of Fitzgibbon *et al.* (1999), we follow Wenzel (2016, Sec. 2.1.3, p. 47ff) to obtain the estimated parameters  $\hat{\mathbf{c}}$  of the conic and the covariance matrix  $\hat{\Sigma}_{\hat{\mathbf{c}}}$ .

- Circle:** A circle is a special regular conic for which  $\mathbf{C}_{hh}$  in Equation (1) is proportional to the  $2 \times 2$  identity matrix. Instead of using the over-parametrized conic representation, we represent circles by their implicit homogeneous

equation  $\mathbf{z}^T \mathbf{p} = 0$ , where we collect the coordinates of a point  $\mathbf{x}$  in a vector  $\mathbf{z} = [x^2 + y^2, x, y, 1]^T$  and the parameters within vector  $\mathbf{p} = [A, B, C, D]^T$ , from which we easily obtain the circle parameters,  $[x_0, y_0, r]$ . Note that setting  $A = 0$  allows us to represent circles with infinite radius, thus, straight lines. We follow Förstner and Wrobel (2016, Sec. 3.6.2.5) and derive the covariance matrix of the circle parameters  $[x_0, y_0, r]$  directly from the observed points. Finally, using variance propagation, we yield estimated parameters  $\hat{\mathbf{p}}$  and the according covariance matrix  $\hat{\Sigma}_{\hat{\mathbf{p}}}$ .

### Road Net Extraction

In this section we describe the process of extracting a raw road network from the classification result which serves as input for the simultaneous chain-forming and generalization procedure, described in the next section. The individual steps of the following procedure are shown in Figures 1a to 1d.

The main input for our procedure of initial road map computation is the classification result of given image data, which we denote by the binary road-class image  $B$ , cf. Figure 1a. We denote its boundary, usually slightly smoothed by morphological operations, by  $\partial B$ . Starting from  $B$ , we extract the medial axis by means of skeletonization and finally, we apply the vectorization tool of Steger (1998); cf. Figure 1c. The output of this method is a set of open polygonal chains, which we call polylines. An endpoint of a polyline is always either a pixel on  $\partial B$  (usually, a concavity), or a branch point, for which at least three points, belonging to  $\partial B$ , have the same distance. In the first case, we refer to the polyline endpoint as a *dead end* while in the second case, we denote it as a *junction*. Besides these two cases, a particular situation is observed if the polyline is closed, or, equally, if it is homeomorphic to the circular line. In this situation, both dead ends coincide with the same vertex of the polyline.

To recognize whether a polyline endpoint is a dead end or a junction, a range-search procedure is applied. All endpoints are clustered by means of the generalized DBSCAN algorithm (Sander *et al.* 1998), which is still a state-of-the-art tool for down-sampling point clouds. A junction is a cluster with at least three vertices. The structure of junctions contains their 2D coordinates and the corresponding incident polylines. Since every concavity of  $B$  causes one polyline, discarding road segments which exhibit a suspicious geometric appearance (too short, too broad, etc.) and at the same time do not contribute to the topological functionality of the road network has been proposed in the literature (Mena, 2006; Bulatov *et al.*, 2016b). We use an iterative filtering procedure based on polyline attributes, such as width, length, type, etc., which are calculated according to Bulatov *et al.* (2016a). Within one iteration, we delete all polylines of which at least one endpoint is not a junction and whose length or width take on a suspicious value (e. g., the length below 2 m or width out of the range [2 m; 50 m]). After every iteration, the attributes are updated to prevent erosion of road segments. To be more precise, a junction which now connects not more than two road segments must be deleted and both segments are merged while their lengths are summed, so that for the next iteration the new length exceeds 2 m. The result of this pre-processing procedure is shown in Figure 1d and provides the input for our simultaneous chain-forming and generalization procedure, described in the next section.

### Simultaneous Chain-Forming and Generalization

For the most part, the previously discussed polylines serve as connection links between the junctions and do not correspond to the general concept of what a street is. We wish to fuse these polylines to chains which correspond to our understanding of

streets while simultaneously generalizing them by means of sequences of straight line, circular, and ellipse segments.

The proposed method consists of two steps, described in the next two subsections. Given the polylines, we first iteratively segment them into circular segments, which yields an over-segmentation. Second, merging neighboring segments is performed based on model selection. In this step, straight lines, circular arcs, and ellipses are estimated optimally in the least squares sense. In this way, we are more flexible representing curved street shapes than by using straight lines, solely. Finally, the whole road network is subject to a greedy optimization supposed to retrieve the optimal set of chains out of the whole dataset, which is described in detail in Section Chain Forming by Greedy Search.

### Segmenting Point Sequences into Circle Segments

The concept of polyline segmentation into circle segments is based on the `circlePeucker` algorithm (Wenzel and Förstner, 2013), which is an adaption of the Douglas-Peucker algorithm (Douglas and Peucker, 1973). The original algorithm is designed to simplify polylines by recursively splitting a sequence of polyline edges into larger edges until the distance of an eliminated point to the corresponding edge is below a threshold  $t$ .

Instead of straight lines, `circlePeucker` uses circle segments (Wenzel and Förstner, 2013). Given a sequence of points,  $X = \{x_n\}$ ,  $n = 1 \dots N$ , it is recursively partitioned into segments which approximate the according points by

a circular arc up to a pre-specified tolerance  $t$ . If applicable, a segment is split at the point  $x_n$  that has the maximum distance to the circular arc. In order to enforce continuity, the start and endpoints of the segments are fixed and the best fitting circle arc is determined as explained in Section Fitting Straight Lines, Circles, and Ellipses. For each polyline the threshold  $t$  is set to half of the road segments width.

Using this procedure for each initial polyline separately, we obtain a list of indices which represent the endpoints of the sought segments. In order to keep the topology of our road network consistent, we introduce new junctions for each breakpoint of the pre-segmentation and update the list of street segments accordingly. An intermediate result of this step of the procedure is shown in Figure 1e.

### Merging Line Primitives Based on Model Selection

Given the preliminary, over-segmented partition of polylines, we aim at a simplification by merging neighboring segments which share the same geometric model instance. Deciding whether two neighboring segments belong to the same model instance may be based on a statistical hypothesis test. As these tests aim at rejecting the null hypothesis, they can be used as a sieve for keeping false hypotheses. Merging segments solely based on hypothesis testing, however, fails due to the risk of accepting large changes in geometry, in case the parameters of the proposed model are uncertain. On the other hand, deciding which model fits the data best, i.e., whether it should be approximated by a straight line, circle or an ellipse,

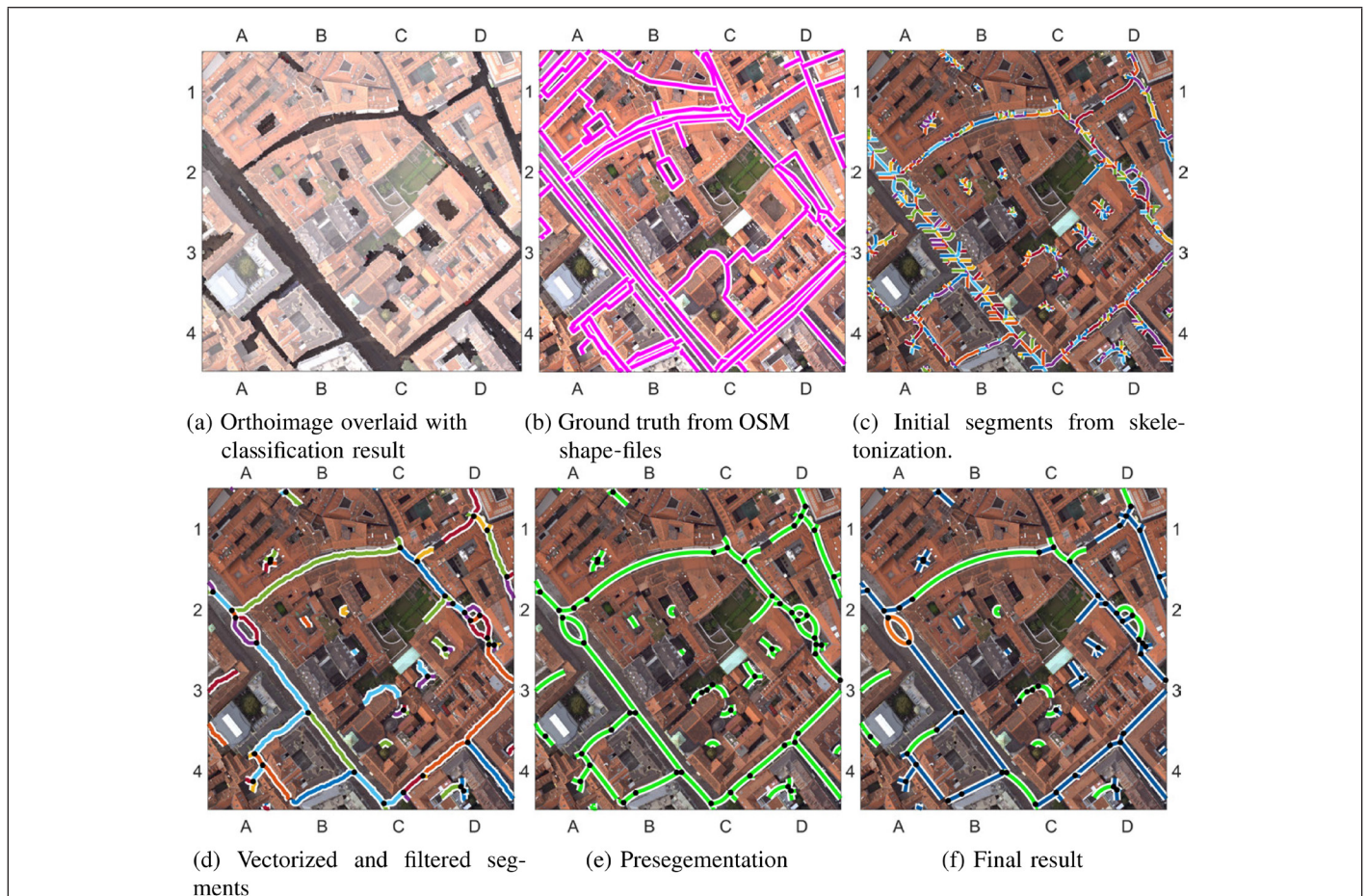


Figure 1. Results for a fragment of the Graz dataset, showing all intermediate steps of the process. For (c) to (d) colors are arbitrary and visualize different segments, i. e., polylines. For (e) and (f) colors represent straight line segments, circular, and elliptic arcs in blue, green, and orange, respectively. In order to denote specific parts of images, we add grid cell names at their outer frame; e.g., (A1) is the area at the upper left corner of an image fragment and (A2) in (f) points at the orange ellipse.

is a typical model selection problem, which addresses the trade-off between goodness-of-fit and simplicity. The former aims at the accuracy of the selected model, with regard to the given data, the latter aims at the number of parameters used to describe the model.

Here, the domain of considered models is {straight line, circle, ellipse}, which differ in the number  $U$  of parameters, {2, 3, 5}, respectively. The term accuracy is related to the residuals,  $\mathbf{v}$ , caused by deviations of the points from the selected model. Let us consider a number of  $N$  i.i.d. observations  $l$  with covariance  $\Sigma_{ll}$ . We are looking for an  $U$ -dimensional parameter vector  $\hat{\theta}$ , whereby observations and parameters are related by the Gauss-Markov functional model  $l + \hat{v} = f(\hat{\theta})$  with residuals denoted by  $\hat{v}$ . Using the usual definition  $\Omega = \mathbf{v}^T \Sigma_{ll}^{-1} \mathbf{v}$ , Schwarz (1978) derived the Bayesian Information Criterion

$$\text{BIC} = \Omega + U \ln N \quad (2)$$

as a criterion for model selection. The lower the complexity of the model, described by  $U$ , the lower BIC. A large number  $N$  of observations increases the relative precision of the parameters and thus the reliability of the model. It can be shown that the BIC is closely related to the *description length* from information theory. Thus, we use these terms synonymously and wish to minimize BIC from Equation (2) to select the best model.

From the pre-segmentation, we only take the information which points belong to the same segment and ignore the parameters of the fitted circle segments. The final representation is achieved by fitting straight line, circle, and ellipse segments through given road segments, using all points belonging to them.

Again, given a set of  $N$  observations  $\mathcal{X} = \{x_n\}$ ,  $n = 1 \dots N$ , where we assume i.i.d. coordinates of each point, sharing the same isotropic covariance  $\Sigma_{x_n x_n} = \sigma_n^2 \mathbf{I}_2$ , we aim at the best fitting line  $\hat{l}$ , circle  $\hat{p}$ , or ellipse  $\hat{c}$  as described in Section Fitting Straight Lines, Circles, and Ellipses. Thereby, for each road segment, we assume  $\sigma_n = t$ , which is half of its width, as introduced in Section Road Net Extraction. For each model, we look for the statistically best fitting parameter vector as well as its covariance by estimating the weighted sum of squared residuals  $\Omega = \sum \hat{v}_n^2 / \sigma_n^2$  as measure of precision.

Let us assume a segmentation of points  $\mathcal{X} = \{x_m\}$  into  $M$  segments. We call the current parameter vector of the  $m^{\text{th}}$  segment  $\theta_m$ . Thus,  $\theta_m$  acts as placeholder for  $\mathbf{l}_m$ ,  $\mathbf{p}_m$  or  $\mathbf{c}_m$  and includes the number  $U_m$  of parameters needed to define the current model. Thus,  $U_m$  acts as our measure of complexity. Initially, we select the best model for each segment by minimizing its description length in terms of the BIC:

$$\hat{\theta}_m = \arg \min_{\theta_m} \text{BIC}(\mathcal{X}_m, \theta_m) = \arg \min_{\theta_m} (\Omega_m + U_m \ln N_m), \quad (3)$$

where  $\Omega_m = (\mathcal{X}_m, \theta_m)$ . We wish to merge neighboring segments by evaluating the gain of description length when fitting a new model to the joined set of points.

Without loss of generality, let us consider two neighboring segments 1 and 2 with the corresponding points  $\mathcal{X}_1$ ,  $\mathcal{X}_2$ , respectively, and the already assigned models  $\hat{\theta}_1$  and  $\hat{\theta}_2$ . We propose the points of both segments to belong to a joined segment, thus,  $\mathcal{X}_{1,2} = \mathcal{X}_1 \cup \mathcal{X}_2$ . Again, we select the best model for this potentially merged segment by minimizing the BIC

$$\hat{\theta}_{1,2} = \arg \min_{\theta_{1,2}} \text{BIC}(\mathcal{X}_{1,2}, \theta_{1,2}). \quad (4)$$

The gain of description length is given by the difference between the joined description length using the model  $\hat{\theta}_{1,2}$  obtained with the merged segments  $\mathcal{X}_{1,2}$  and the sum of descriptions lengths of both previous models  $\hat{\theta}_1$  and  $\hat{\theta}_2$ .

$$\Delta \text{BIC}_{1,2} = \text{BIC}(\mathcal{X}_1, \hat{\theta}_1) + \text{BIC}(\mathcal{X}_2, \hat{\theta}_2) - \text{BIC}(\mathcal{X}_{1,2}, \hat{\theta}_{1,2}) = (\Omega_1 + \Omega_2) - \Omega_{1,2} + (U_1 \ln N_1 + U_2 \ln N_2) - U_{1,2} \ln(N_1 + N_2). \quad (5)$$

If  $\Delta \text{BIC}_{1,2} > 0$ , the description length of the merged segment is shorter than the description length of two separate segments; thus, they should be merged to reduce the overall complexity.

In case of competing but mutually exclusive hypotheses for merging, we apply a greedy strategy described below.

### Chain Forming by Greedy Search

The essential precondition of chain forming is establishing (geometric and topological) similarities between the polylines. That is, to find candidates for fusion, we have to search for similar attributes between pairs of polylines. The necessary condition for similarity is that two polylines are topologically neighboring; in other words, they must share a common junction. This additionally simplifies the implementation since all the remaining steps of the algorithm run over junctions.

Further, we established a width gap: The necessary condition for two road segments to be neighbors is that the width of the narrower one, denoted by  $w_{\min}$ , and that of the broader one,  $w_{\max}$ , are similar, that is:

$$(1 - \varepsilon) w_{\max} < w_{\min}, \quad \text{where } \varepsilon \approx 0.5. \quad (6)$$

This assumption is reasonable because a street usually has a nearly constant width throughout its course. Note that even though this threshold may seem large, it is only a necessary condition.

Finally, to evaluate the whole set of road segments, we proceed in a greedy manner. After initializing all segments by their best models in terms of description length (2), we propose a set of neighboring segments as candidates for merging. Thereby, we take into account all pairs of segments which share a common junction and fulfill the requirement of the width gap given in Equation (6). For each of these pairs, we select the best model, by minimizing the BIC, estimate the gain of description length given in Equation (5) and store the result.

During our greedy search procedure, at each iteration step we select the pair of neighbors with the largest gain of description length. We update the topology of the whole dataset: The recently merged segments are not associated with their common junction(s) anymore. The order of vertices of the merged polylines should be topologically correct. On the one hand, this requires reordering the polyline segments to be fused and, on the other hand, the order of points within one polyline has to be flipped, if necessary. Further we update the geometric models of all affected neighboring road segments and their according gain of description length in case of merging.

The steps mentioned in the last paragraph are repeated until there are no more merging proposals with positive gain of description length. A final result after this step of the procedure is exemplarily shown in Figure 1f.

Note that the resulting partitioning may produce deviations from the original junctions and dead-ends, because during adjustment, the geometric elements are not restricted to any particular points. However, the covariance matrices for junction points (introduced at the beginning of the mathematical section) could be re-weighted in order to prevent the according points changing their positions. This is part of our future work.

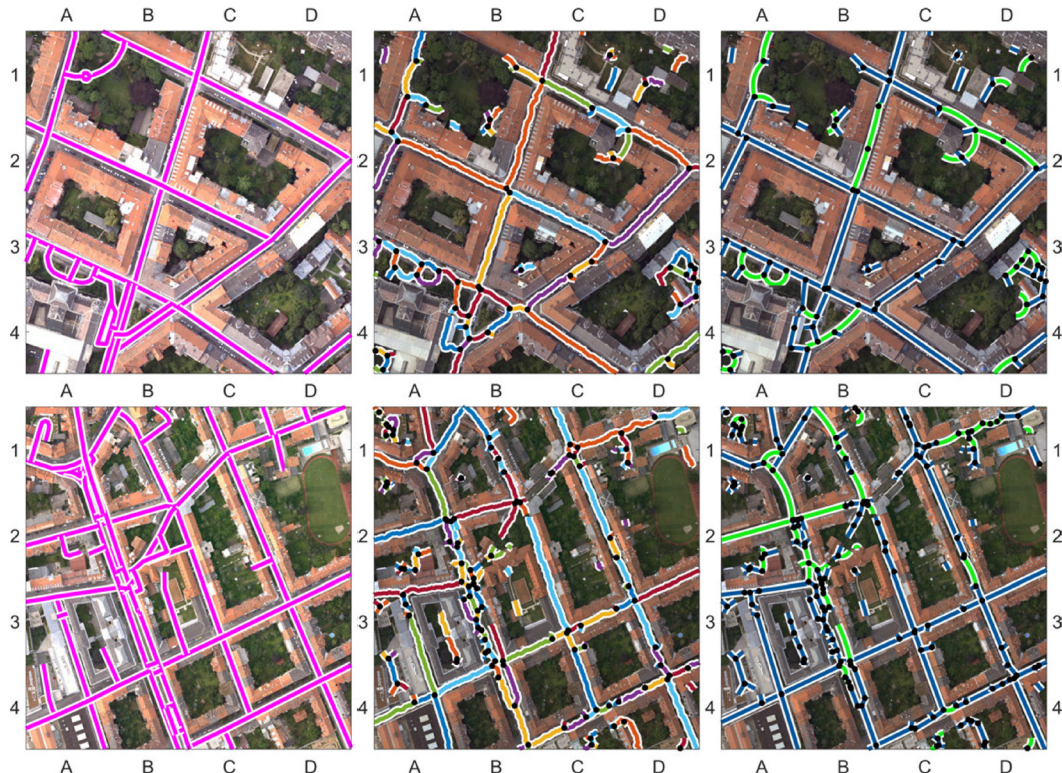


Figure 2. Results for fragments of the Graz dataset. **Left:** OSM shapefiles projected into the image coordinate system. **Middle:** Polylines of road segments after vectorization and filtering. Different colors visualize different segments. **Right:** Results of our procedure, here yielding straight line segments and circular arcs in blue and green, respectively.

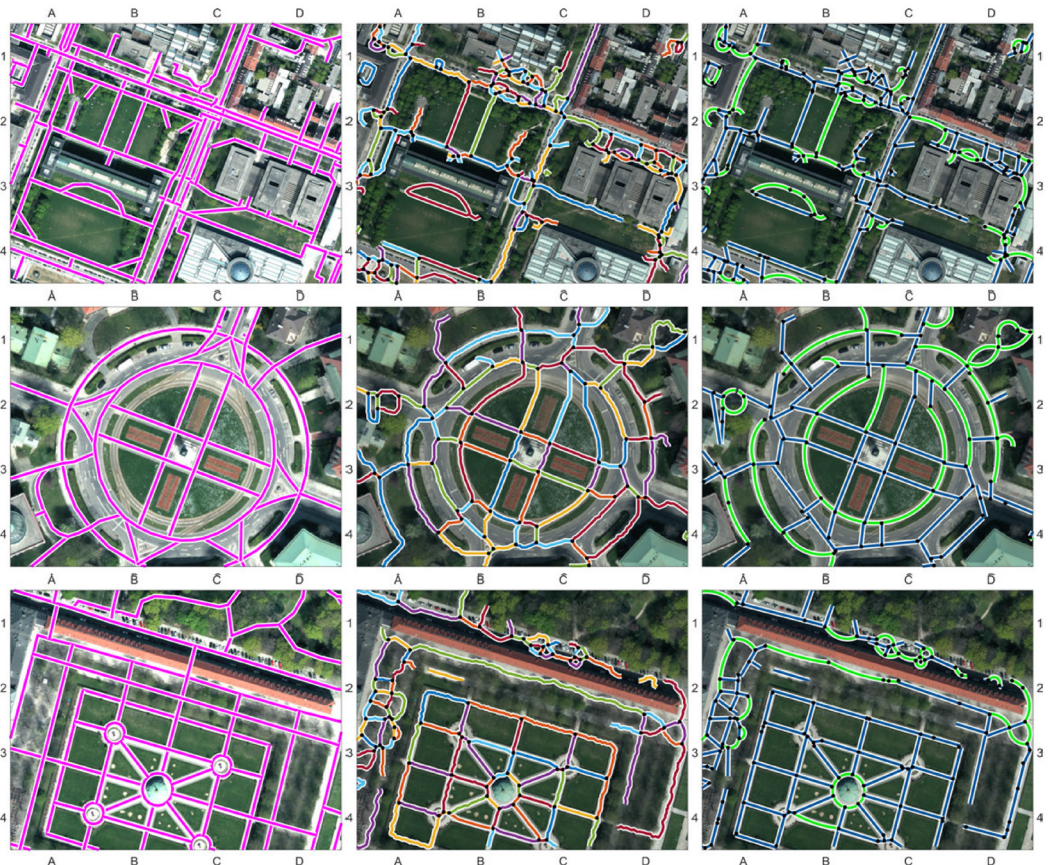


Figure 3. Results for fragments of the Munich dataset. **Left:** OSM shapefiles projected into the image coordinate system. **Middle:** Polylines of road segments after vectorization and filtering. Different colors visualize different segments. **Right:** Results of our procedure, here yielding straight line segments and circular arcs in blue and green, respectively.

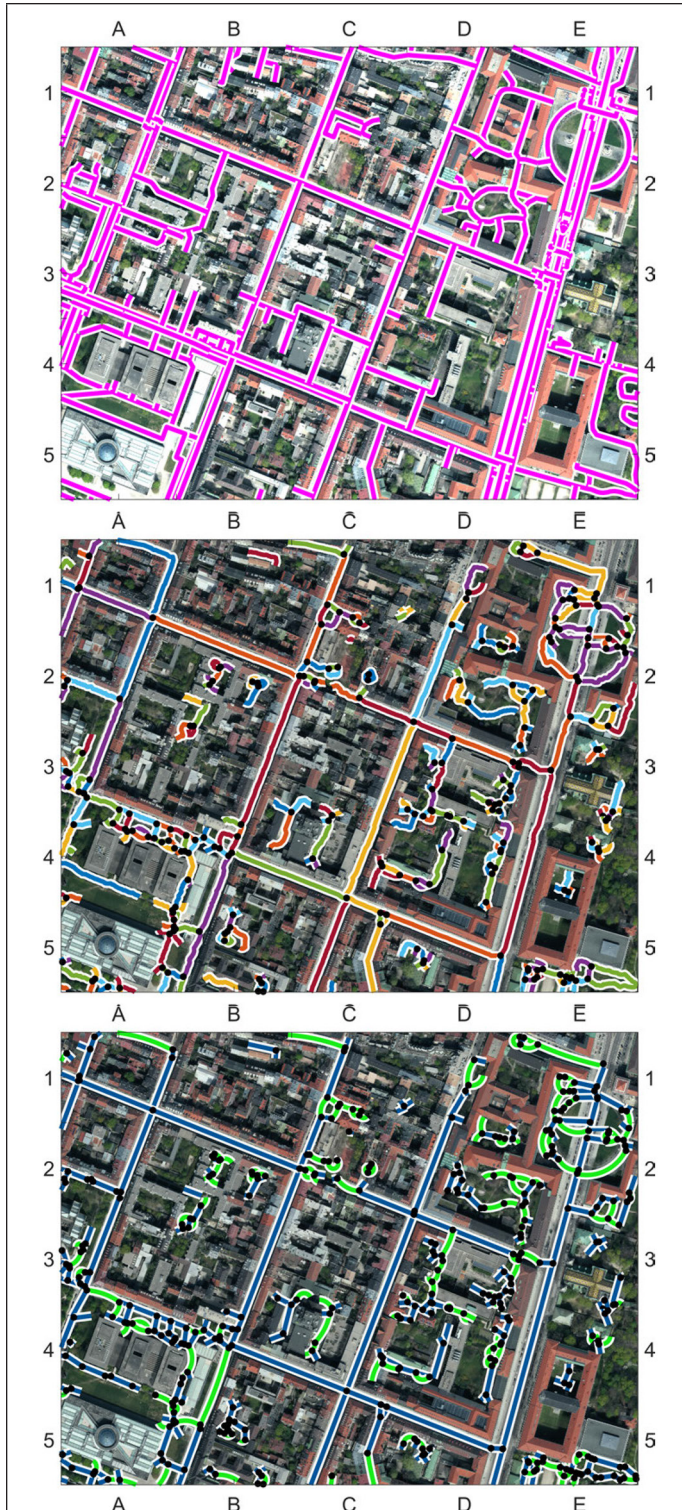


Figure 4. Result for a larger fragment of the Munich dataset containing many straight alleys. **Top:** OSM shapefiles projected into the image coordinate system. **Middle:** Polyines of road segments after vectorization and filtering. Different colors visualize different segments. **Bottom:** Results of our procedure, here yielding straight line segments and circular arcs in blue and green, respectively.

## Experiments

In order to evaluate our proposed procedure, we present two different datasets in the following subsection both showing large fragments of the urban area, however, resulting from different pre-processing procedures. Both datasets are the result of a classification procedure, which yields the information about whether a pixel belongs to the road class. Classification of roads is highly supported by the availability of 3D information. Therefore, description of both pre-processing procedures in the next subsections includes the extraction of 3D information. In the two subsections afterwards, we will refer to the qualitative evaluation, where illustrations of the most interesting and challenging parts of both datasets will be shown, and to the quantitative evaluation, carried out using openly available street data.

### Datasets

The first dataset is a part of the inner city of Graz, Austria. The normalized DSM, computed by a simple method (robust DSM minimum within a window subtracted from DSM), and the orthophoto patches (both of resolution 0.5 m) were provided by the authors of Wegner *et al.*, (2015) together with their classification results. The road class was extracted quite accurately. This dataset is characterized by many long straight streets. There are also squares, or traffic circulation areas, such as parking areas. However, there is only one roundabout-like configuration.

The second dataset represents a rather large fragment of the urban area of the city of Munich, Germany. This dataset is characterized by long straight streets, narrow garden paths, as well as several roundabouts. Extraction of 3D information was accomplished by the pipeline SURE (Rothermel *et al.*, 2012). It contains a DSM and an orthophoto which has a resolution of 0.1 m; however, we decided to reduce it to 0.2 m in order to be able to process a larger portion of the dataset. The digital terrain model was computed by the procedure described by Bulatov *et al.* (2014). Prior to the classification step, we excluded right away the set of *forbidden pixels* with implausible values of relative elevation and NDVI, since these are the most distinctive features for classification. Finally, for classification, we extracted several regions for training and applied a kNN-classifier to the remaining pixels. In a post-processing step, in order to suppress the noise stemming from vehicles, traffic signals, etc., we used our prior knowledge about the typical geometry of roads. Therefore, we computed stripes from pairs of nearly parallel lines in the orthophoto. In stripes which contained a certain minimum relative amount of pixels classified as road, all other non-forbidden pixels were also assigned to this class. However, because of shadows in urban street canyons, there are still many mis-classifications in this difficult dataset. These errors could have seriously degraded the performance of our algorithms. In order to be able to evaluate our method nevertheless, we performed very local interactive corrections of the classification result near the main roundabout. In the future, we could employ a much better classifier, e.g., based on most recent developments on deep learning methods (Marmanis *et al.*, 2016 and 2017)

### Qualitative Evaluation

We present the results of our procedure for the dataset Graz in Figures 1 and 2 while Figures 3 and 4 show different fragments of Munich. In order to denote specific parts of images, we added grid cell names at their outer frame, similar to the labeling of a map.

The following observations can be made from the illustrations. The performance strongly depends on the classification accuracy. The center-lines of well-illuminated alleys have been recovered as straight lines. Under these circumstances, the performance is quite robust despite interruptions by (visually disturbing) side roads, e.g., Figure 2 bottom right (B2-B4),

which as the result of road center-line extraction, cf. Section Road Net Extraction, are the paths towards the concavities of the classification result. Besides, the reasonable description of the squares in Figure 2, top right (A3-B4) and bottom right (A1), and of the roundabouts in Figure 3, middle right and bottom (B3), is encouraging. However, some straight road segments have been spuriously modeled as circle arcs of a quite huge radius, e.g., the park path in Figure 3 bottom right (B4) or the longer, presumably straight road segment in Figure 4 bottom (B4). This may happen because the numbers  $U$  of parameters needed for describing straight lines or circle arcs, respectively, do not differ too much. Hence, because of the unfavorable distribution of the residuals, circle arcs were sometimes spuriously preferred. Penalizing too huge radii may provide improvements in the future. In the shadowy, occluded areas, the results are increasingly affected by classification noise. However, also here, the continuations are plausible.

Further, we observe almost no ellipses or elliptic arcs. Except the full ellipse shown in Figure 1f (A2), we found just a few more elliptic arcs, each resulting from spurious polylines, not referring to real road segments. This observation verifies the character of man-made structures; inside cities, roads are realized as straight lines or circle segments while clothoids are typical for rural regions. Therefore, the almost-absence of ellipses in the result is reasonable and can serve as an indication that the approach performs well.

Nevertheless, we observe a number of mostly very short segments with large deviations from their initial polylines, e.g., short segments in Figure 3 middle right at (D4) and (A3), which can be explained by the fact that, due to the procedure of extracting polylines, the assumption of normally distributed input data is clearly not given here. Therefore, for very short segments, model-based generalization fails because of

outliers among the vertices, contrary to long segments where the estimation procedure mostly yields reasonable results.

### Quantitative Evaluation

The natural way of quantitative evaluation would be to check the overlap of our result with the ground truth data, for example, a geo-referenced OpenStreetMap (OSM) shapefile. The typical geometric measures for the quality of estimated polylines are then *completeness* and *correctness*. This has the disadvantage that not only contributions of this article (that is, model-based generalization) will be subject of the evaluation, but rather the results of classification and initialization. Additionally, OSM data are not error-free, especially, with respect to model assumptions: Some roads pass under trees and so they are not visible at all; others are tunnels. Others again do not correspond to the road center-lines, see the example in Figure 5d right, (B4-C1). Most importantly, we wish to evaluate our approach with respect to what it was designed for: Identification of characteristic road structures, such as long alleys and circular roads. Thus, starting at OSM data, in both datasets we chose about 20 long straight streets (in total 8.15 km and 3.56 km for Graz and Munich, respectively), sampled them into the point set  $\{x_n\}$  with the linear increment of 4 pixels (that is, one point every 2 m for Graz and 0.8 m for Munich), and corrected them interactively so that they coincide with road centerlines. The same procedure took place for all larger roundabouts and arc-like road segments of the Munich dataset (since for Graz, there were too few such structures for a quantitative evaluation, as for elliptic arcs in both datasets). In the following we refer to these corrected OSM data as our *reference*.

We denote our complete road system before and after the generalization  $S_0$  and  $S_1$ , respectively. For a point  $x_n$ , we compute distances once to  $S_0$  and  $S_1$ , obtaining  $d_0$  and  $d_1$ , and once to the subset containing only the corresponding model type

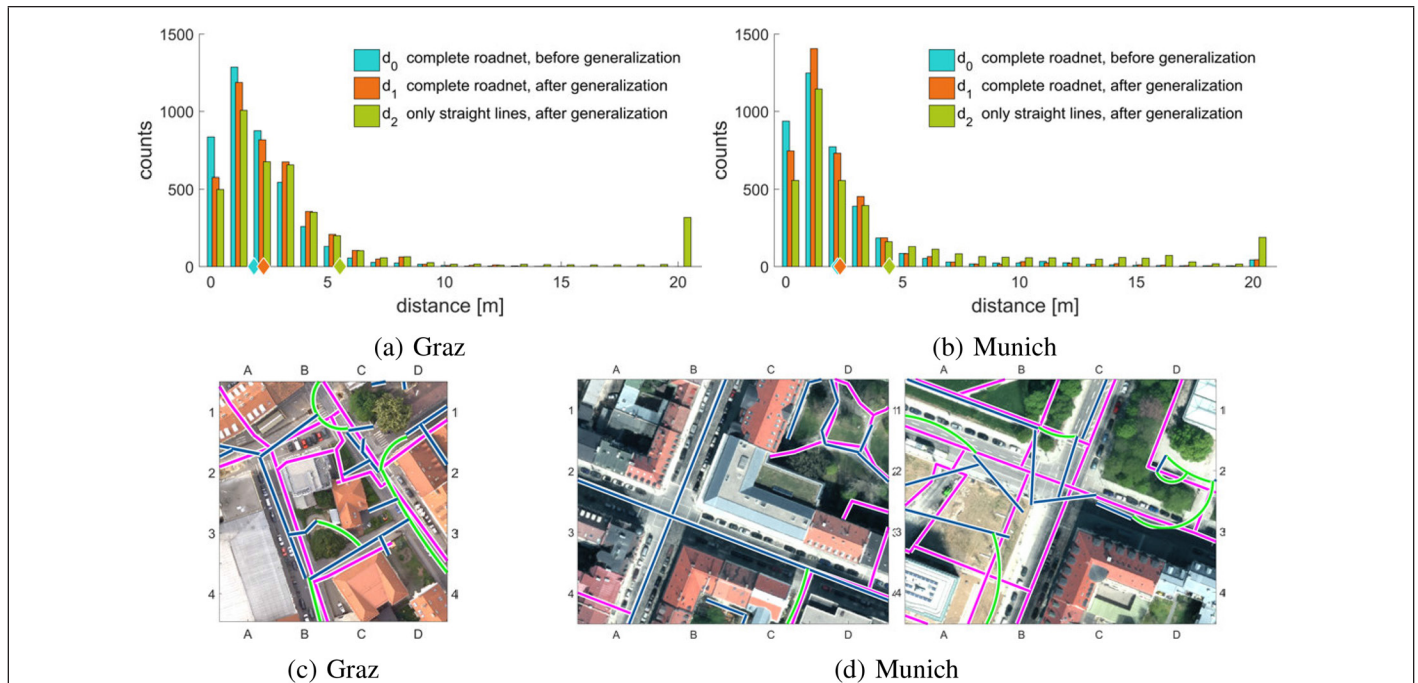


Figure 5. **Top:** Histograms with distances of reference vertices from selected and interactively corrected OSM shapefile streets to our reconstruction results. Blue, orange, and green correspond to entries of  $d_0$ ,  $d_1$  and  $d_2$  as explained in Equation (7). *Diamonds* denote the mean values of deviation. **Bottom:** Image fragments from both datasets visualizing selected reference streets in magenta and our results with colors as given in Figure 1. Please note that for the middle image fragment, the reference segments are hidden by the long straight line segments. The right fragment shows an example where misclassifications due to the construction site yield no reasonable road net extraction results. Therefore, distances of extracted segments to reference segments are large.

$c(\cdot)$ , that is circular to circular and straight line to straight line, thus obtaining  $d_2$ . All distances are defined, analogous to one-sided Hausdorff distance in 2D, as the minimal distance  $\hat{d}(\cdot, \cdot)$  of a reference point  $x_n$  to the set of edges  $\mathcal{X} \in S_{0/1}$ . Formally:

$$d_{0/1}(x_n) = \min_{x \in S_{0/1}} \{\hat{d}(x_n, \mathcal{X})\} \quad \text{and} \quad d_2(x_n) = \min_{x \in S_1} \{\hat{d}(x_n, \mathcal{X}) \mid c(x_n) = c(\mathcal{X})\}. \quad (7)$$

Clearly,  $d_2 \geq d_1$ , since the infimum does not necessarily belong to the road segment of the same type. The results of the evaluation over all  $x_n$  in Equation (7) are recorded in Table 1 and visualized in the histograms in Figure 5. We decided not to plot the histogram for circular segments, because it looks similar to that for straight lines. Furthermore, we used 20 m as a truncation parameter, i.e., if one of the distances mentioned above exceeds this value, the point  $x_n$  is declared to be not retrieved and its distance is set to the maximum value.

The following observations could be made from Figures 5a,b and Table 1. Reasonable error values in the order of 2 m were achieved for both  $d_0$  and  $d_1$ . Even for  $d_2$ , at least two thirds of compared straight lines ( $q_{2/3}$ ) lie below 2.32 m and 3.25 m for the Graz and Munich datasets, respectively. Actually, the deviations in meters are similar, which may seem surprising because Graz data was processed by a much more advanced classification method (Wegner *et al.* 2015). The reasons for this are the lower resolution as well as the fact that the classification results are mostly good for broad straight alleys, which were preferred for comparison. High deviations occur especially at those areas were given initial polylines are strongly affected by mis-classifications. As a result we do not yield reasonable road net extractions. The aforementioned effect that circle arcs are sometimes preferred over straight lines, and therefore, we do not have matches of straight line to straight line for the evaluation, causes even higher values of  $d_2$  than  $d_1$ . This can be observed by peaks in the heavy tails on the right of histograms for  $d_2$ . By assessing differences between values of  $d_2$  and  $d_1$ , one can obtain a rough estimation of how many circles arcs instead of straight lines were obtained and vice versa. In the Graz dataset,  $d_2$  exceeded  $d_1$  for 512 points (12.8%), which means that roughly this percentage of straight alleys was covered by spurious circles arcs. In Munich, these numbers were higher, 23% for straight lines and 32% for circular segments. Finally, the fact that  $d_0 < d_1$  in almost all measures for both datasets is somehow disappointing at the first glance. Nevertheless, it is evident that generalization takes place at cost of accuracy.

Finally, we validate our algorithm in terms of segmentation and merging behavior. Table 2 shows the number of initial polylines in comparison to that of the segments after pre-segmentation, which provides a measure for over-segmentation, and the final number of segments. This was carried out for all polylines, but we also report in parenthesis the numbers considering just the polylines used for evaluation in Table 1, because it was verified that they represent major straight roads and roundabouts and thus are supposed to show a good merging behavior. The lower the final number of segments compared to the initial number of polylines, the better the performance of chain-forming. The number of segments is reduced by 16% and 14%, respectively, for both datasets, which at first glance may seem low. For the main roads, this behavior is more encouraging, achieving 28% and 23%. This means that the total numbers might be affected by numerous side-roads that are not changed much in terms of segmentation and merging. Therefore, in Table 3 we present an evaluation of the merging behavior. Starting from the set of segments from pre-segmentation, for each final segment we count the number of segments which it is merged from. Table 3 states the numbers of final segments which result from at least two

Table 1. Distances  $d_0$ ,  $d_1$ , and  $d_2$  of a subset of straight line segments and circular segments to the ground truth, as given in Equation (7). We provide mean distances ( $m$ ) together with their 33% and 67% quantile values, which are denoted by  $q_{1/3}$  and  $q_{2/3}$ . All distances are given in meters.

Additionally, numbers of tested points and kilometers are provided.

dataset	$d_0$			$d_1$			$d_2$			total pts.	total km
	$m$	$q_{1/3}$	$q_{2/3}$	$m$	$q_{1/3}$	$q_{2/3}$	$m$	$q_{1/3}$	$q_{2/3}$		
Graz	1.80	0.87	2.11	2.25	1.09	2.72	5.53	1.29	2.32	4070	8.15
Munich straight	2.13	0.64	2.08	2.46	1.07	2.53	4.28	1.47	3.25	4106	3.56
Munich circular	1.58	0.58	1.67	1.67	0.54	1.71	4.08	0.72	3.42	1430	1.30

Table 2. Statistics of segmentation, taking into account all poly-lines and segments, respectively. Number of initial polylines compared to the number of segments after pre-segmentation and after merging. Numbers in parenthesis refer to the subset of segments used for the evaluation shown in Table 1.

Data	initial polylines	segments after pre-segmentation	final segments
Graz	2566 (72)	3126	2155 (52)
Munich	2012 (172)	2606	1729 (133)

Table 3. Evaluation of merging behavior taking into account final segments resulting from at least two segments from pre-segmentation. Percentages of sums refer to the number of initial polylines given in Table 2.

Data	Number of merged segments													$\Sigma$
	2	3	4	5	6	7	8	9	10	11	12	13		
Graz	437	146	40	10	8	2	0	1	0	1	0	1	646 (25%)	
Munich	328	132	34	20	8	3	3	0	0	0	0	2	530 (26%)	

and up to 13 initial segments. First, we realize a large difference in the number of final segments given in Table 2 compared to Table 3, which verifies the assumption that a large number of superfluous fragments is not affected by the whole process. Second, even though the majority of final segments results from two to three initial segments, a considerable fraction contains between 4 and 13 merged initial segments. This is a promising indication that chain-forming is successful.

## Conclusions and Outlook

The goal of this work was the identification and estimation of geometric primitives; such as straight line segments, circle, and ellipse arcs; within complicated road networks. The instances of these road networks are chains formed from raw polylines which have been identified as neighbors using geometrical and topological criteria. Using a greedy approach based on Bayesian model selection, we were able to identify most of the important traffic roundabouts and straight street courses, as well as to replace them by circle arcs and long straight lines.

The whole generalization module has only two data-dependent parameters, namely the threshold  $t$  and the width gap  $\epsilon$ . Unfortunately, because of the noisy data and a lack of context information, it was not always possible to trace complete straight lines representing long alleys or whole circle arcs of roundabouts. However, as long as the accuracy of the classification result is high, and consequently the initial raw

polylines represent the streets medial axis, our algorithm performs reasonably well. It is able to identify long chains while accurately estimating geometric entities.

Throughout the process of pre-segmentation and merging, the topology is kept consistent by introducing or deleting junctions if needed and updating the locally affected road network in terms of topology. However, due to the adjustment procedure for fitting geometric entities, their endpoints are not restricted to the positions of junctions anymore. In order to avoid this effect, we may change the covariance matrix of observations, such that junction points get high precision. Further, we may use common points of transition between individual segments as hard constraints which grant more stability to the normal equation system. Both approaches assume a sufficiently large number of observations to prevent the normal equation system from rank deficiency and will be an important topic of our future work.

## Acknowledgments

We wish to thank Gisela Häufel (Fraunhofer IOSB) for downloading and preparing the shapefiles for the Graz dataset, as well as Jan-Dirk Wegner and Mathias Rothermel (ETH Zürich) for providing the necessary input for our approach. This work has partly been supported by the DFG-Project FOR 1505 Mapping on Demand.

## References

- A. Albano, 1974. Representation of digitized contours in terms of conic arcs and straight-line segments. *Computer Graphics and Image Processing*, 3(1):23–33.
- D. Bulatov, G. Häufel, J. Meidow, M. Pohl, P. Solbrig, and P. Wernerus. 2014. Context-based automatic reconstruction and texturing of 3D urban terrain for quick-response tasks, *ISPRS Journal of Photogrammetry and Remote Sensing*, 93:157–170.
- D. Bulatov, G. Häufel, and M. Pohl, 2016a. Identification and correction of road courses by merging successive segments and using improved attributes. *SPIE Remote Sensing*, International Society for Optics and Photonics, Volume 100080V.
- D. Bulatov, G. Häufel, and M. Pohl, 2016b. Vectorization of road data extracted from aerial and UAV imagery, *ISPRS-International Archives of the Photogrammetry, Remote Sensing and Spatial Information Sciences*, 41-B3:567–574.
- D. Bulatov, S. Wenzel, G. Häufel, and J. Meidow, 2017. Chain-wise generalization of road networks using model selection. *ISPRS Annals of Photogrammetry, Remote Sensing and Spatial Information Sciences*, Volume IV-1/W1, pages 59–66.
- S. Clode, F. Rottensteiner, P. Kootsookos, and E. Zelniker, 2007. Detection and vectorization of roads from lidar data. *Photogrammetric Engineering & Remote Sensing*, 73(5):517–535.
- D. H. Douglas and T. K. Peucker, 1973. Algorithms for the reduction of the number of points required to represent a digitized line or its caricature, *Cartographica: The International Journal for Geographic Information and Geovisualization*, 10(2):112–122.
- A. Fitzgibbon, M. Pilu, and R.B. Fisher, 1999. Direct least square fitting of ellipses. *IEEE Transactions on Pattern Analysis and Machine Intelligence*, 21(5):476–480.
- W. Förstner and B. Wrobel, 2016. *Photogrammetric Computer Vision - Statistics, Geometry, Orientation and Reconstruction*. Springer International Publishing, First edition.
- O. Günther and E. Wong, 1990. The arc tree: An approximation scheme to represent arbitrary curved shapes, *Computer Vision, Graphics, and Image Processing*, 51(3):313–337.
- F. Heinzele, K.-H. Anders, and M. Sester, 2006. Pattern recognition in road networks on the example of circular road detection. *Proceedings of the International Conference on Geographic Information Science*, pages 153–167. Springer.
- Q. Ji, and R. M. Haralick, 1999. A statistically efficient method for ellipse detection, *Proceedings of the International Conference on Image Processing (ICIP)*, pp. 730–734.
- B. Jiang, and C. Claramunt, 2004. A structural approach to the model generalization of an urban street network. *GeoInformatica*, 8(2):157–171.
- W.A. Mackaness, and G.A. Mackechnie, 1999. Automating the detection and simplification of junctions in road networks, *GeoInformatica*, 3(2):185–200.
- D. Marmanis, J.D. Wegner, S. Galliani, K. Schindler, M. Datcu, and U. Stilla, 2016. Semantic segmentation of aerial images with an ensemble of CNNs. *ISPRS Annals of the Photogrammetry, Remote Sensing and Spatial Information Sciences*, 3-3:473–480.
- D. Marmanis, K. Schindler, J.D. Wegner, M. Datcu, and U. Stilla, 2017. Semantic segmentation of aerial images with explicit class-boundary modeling, *Proceedings of the IEEE International Geoscience and Remote Sensing Symposium (IGARSS)*, pp. 5165–5168.
- J. Meidow, C. Beder, and W. Förstner, 2009. Reasoning with uncertain points, straight lines, and straight line segments in 2D, *ISPRS Journal of Photogrammetry and Remote Sensing*, 64(2):125–139.
- J.B. Mena, 2006. Automatic vectorization of segmented road networks by geometrical and topological analysis of high resolution binary images, *Knowledge-Based Systems*, 19(8):704–718.
- A. Moore, C. Mason, P.A. Whigham, and M. Thompson-Fawcett, 2003. The use of the circle tree for the efficient storage of polygons, *Proceedings of GeoComputation*, pages 1–20.
- V. Patraucean, P. Gurdjos, and R.G. von Gioi, 2012. A parameterless line segment and elliptical arc detector with enhanced ellipse fitting, *Proceedings of the 12<sup>th</sup> European Conference on Computer Vision ECCV 2012*, Volume 7573 of Lecture Notes in Computer Science, pages 572–585. Springer.
- J. Porrill, 1990. Fitting ellipses and predicting confidence envelopes using a bias corrected kalman filter, *Image and Vision Computing*, 8(1):37–41.
- P. L. Rosin, and G.A.W. West, 1995. Nonparametric segmentation of curves into various representations, *IEEE Transactions on Pattern Analysis and Machine Intelligence*, 17(12):1140–1153.
- M. Rothermel, K. Wenzel, D. Fritsch, and N. Haala, 2012. SURE: Photogrammetric surface reconstruction from imagery, *Proceedings of the LC3D Workshop*, pp. 1–9.
- A. Saalfeld, 1999. Topologically consistent line simplification with the douglas-peucker algorithm, *Cartography and Geographic Information Science*, 26(1):7–18.
- J. Sander, M. Ester, H.-P. Kriegel, and X. Xu., 1998. Density-based clustering in spatial databases: The algorithm gbscan and its applications, *Data Mining and Knowledge Discovery*, 2(2):169–194.
- G. Schwarz, 1978. Estimating the dimension of a model, *The Annals of Statistics*, 6(2):461–464, 1978.
- D. Sheeren, S. Mustière, and J.-D. Zucker, 2004. How to integrate heterogeneous spatial databases in a consistent way?, *Proceedings of the East European Conference on Advances in Databases and Information Systems*, pages 364–378. Springer.
- C. Steger. An unbiased detector of curvilinear structures, 1998. *IEEE Transactions on Pattern Analysis and Machine Intelligence*, 20(2):113–125.
- J. Tian, Z. Song, F. Gao, and F. Zhao, 2016. Grid pattern recognition in road networks using the c4.5 algorithm. *Cartography and Geographic Information Science*, 43(3):266–282.
- G. Touya, 2010. A road network selection process based on data enrichment and structure detection. *Transactions in GIS*, 14(5):595–614.
- J.D. Wegner, J.A. Montoya-Zegarra, and K. Schindler, 2015. Road networks as collections of minimum cost paths, *ISPRS Journal of Photogrammetry and Remote Sensing*, 108:128–137.
- S. Wenzel, 2016. *High-Level Facade Image Interpretation Using Marked Point Processes*, PhD thesis, Department of Photogrammetry, University of Bonn.
- S. Wenzel and W. Förstner, 2013. Finding poly-curves of straight line and ellipse segments in images, *Photogrammetrie, Fernerkundung, Geoinformation (PFG)*, 4:297–308.
- B. Yang, X. Luan, and Q. Li, 2010. An adaptive method for identifying the spatial patterns in road networks, *Computers, Environment and Urban Systems*, 34(1):40–48.

# Integration of Lidar Data and GIS Data for Point Cloud Semantic Enrichment at the Point Level

Harith Aljumaily, Debra F. Laefer, and Dolores Cuadra

## Abstract

Commercial aerial laser scanning is generally delivered with point-by-point metadata for object identification, but current vendor-generated classification approaches (which rely exclusively on that data) generate high misclassification rates in urban areas. To overcome this problem and provide a fully scalable solution that harnesses distributed computing capabilities, this paper introduces a novel system, employing a MapReduce framework and existing GIS-based data, to provide more detailed and accurate classification. The approach goes beyond traditional gross-level classification (roads, buildings, trees, noise) by enriching the point cloud metadata with detailed semantic information about the object type. The approach was evaluated using two datasets of differing point density, separated by eight years for the same study area in Dublin, Ireland. As evaluated against manually classified data, classification quality ranged from 76% to 91% depending upon category and only 8% remained unclassified, as opposed to the commercial vendor's classification quality which ranged from 43% to 78% with 82% left unclassified.

## Introduction

Light Detection and Ranging (lidar) is a common form of remote sensing that can acquire data from aerial, mobile, and stationary platforms. Lidar data are typically stored according to the LAS specification (ASPRS, 2013), a binary format approved by the American Society for Photogrammetry and Remote Sensing (ASPRS) to provide a common, open format to exchange lidar data between hardware components and software tools. As with any data standard, the LAS specification is a compromise between storage efficiency and data richness (Graham, 2009). In a LAS file, the data and metadata are included in a header section, with general information about the file and data followed by more specific information such as point data format and a reference system. The core information in a LAS file is the Point Data Record, where the lidar data are described such that each point is represented by a single record.

Although later versions of the LAS specification (currently version 1.4) support various point record formats (0 to 10) with a wide range of information such as X, Y, Z, Intensity, Return Number, Number of Returns, Scan Direction Flag, Edge of Flight Line, Classification. For this paper, the focus was on the X, Y, Z coordinates and the classification fields (ASPRS, 2013). The X, Y, and Z values are stored as long integers of 4 bytes for each value. The X, Y, and Z values are used in conjunction with the scale values and the offset values to determine the geographic coordinates for each point. The

“classification” field describes the classification category of the object from which the laser pulse was reflected. All supported point record formats have a predefined classification field, in which a 1 byte field is set to zero, if a point is without classification. In LAS 1.4, a point is classified using predefined categories (i.e., categories 0 to 63 shown in Table 1), where each is pre-associated with a specific value (e.g., 6 = building object). Categories 64 to 255 are user-defined. Assignment is currently proprietary, based on each lidar equipment vendor's own internal algorithm (OpenTopography, 2017).

Table 1. LAS Classification Value Table

Classification Value	Meaning	Classification Value	Meaning
0	Created, never classified	11	Road Surface
1	Unclassified	12	Reserved
2	Ground	13	Wire – Guard (Shield)
3	Low Vegetation	14	Wire – Conductor (Phase)
4	Medium Vegetation	15	Transmission Tower
5	High Vegetation	16	Wire-structure Connector (e.g. Insulator)
6	Building	17	Bridge Deck
7	Low Point (noise)	18	High Noise
8	Reserved	19-63	Reserved
9	Water	64-255	User definable

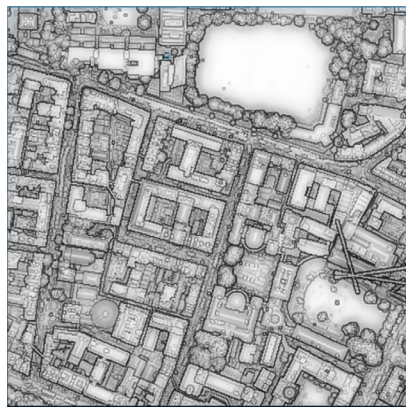
Provider-delivered LAS data are commonly misclassified or not classified at all, which results in low accuracy and difficult-to-use data. For example, of the approximately 290 million lidar points in Figure 1, a minimum of 82% of the data were not correctly classified as shown by the sheer absence of a classification; 82% were delivered assigned to Category 1 - “Unclassified” (Figure 1a), a further 9% were delivered assigned as Category 2 - Ground level (Figure 1b), 9% as Category 4 - Medium Vegetation (Figure 1c), and the remainder (less than 0.01%) as Category 7 – Low point (noise) (Figure 1d). Notably, while a road specific category exists (Category 11 - “Road Surface”) in the LAS specification (Table 1), the Provider-delivered LAS data aggregated the roads with all other ground level points (Figure 1b). This example demonstrates the existing problem of automated LAS classification in urban areas. Overcoming this classification assignment issue is the

Harith Aljumaily and Dolores Cuadra are with the Department Computer Science and Engineering, Carlos III University of Madrid, Av., Universidad 30 – 28911 - Madrid, Spain.

Debra F. Laefer is with the Center for Urban Science and Progress and the Department of Civil and Urban Engineering, Tandon School of Engineering, New York University, 370 Jay Street, Brooklyn, NY 11201 (debra.laefer@nyu.edu).

Photogrammetric Engineering & Remote Sensing  
Vol. 85, No. 1, January 2019, pp. 29–42.  
0099-1112/18/29–42

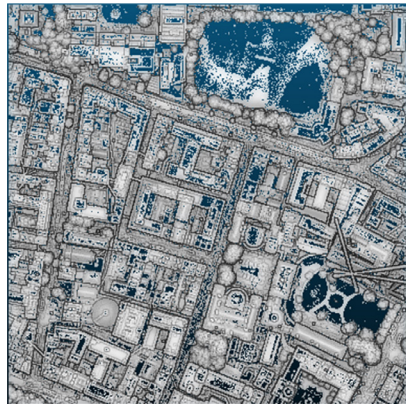
© 2019 American Society for Photogrammetry  
and Remote Sensing  
doi: 10.14358/PERS.85.1.29



(a) Unclassified (82%)



(b) Ground (9%)



(c) Medium vegetation (9%)



(d) Low point (noise) [0.01%]

Figure 1. Example of LAS classification in an urban area showing 82% of all points delivered unclassified by the commercial vendor: (a) Unclassified (82%); (b) Ground (9%); (c) Medium vegetation (9%); and (d) Low point (noise) [0.01%].

focus of this paper, which is organized as follows: The next Section summarizes the peer-reviewed literature followed by a detailed description of the proposed approach. Subsequently the experimental results and accompanying validation are provided followed by conclusions about the work

## Related Work

Significant research has been done in the area of lidar processing. The majority of that scholarship has involved some form of segmentation for object detection or classification. For example, after dividing a lidar point cloud into ground and non-ground points (as provided by the data supplier), Xu *et al.* (2014) segmented points into planar segments using a surface-growing method, then classified the planar segments as roof, ground surface, vegetation, water surface, or undefined. In contrast, Choi *et al.* (2008) employed lidar elevation and reflectance values for road detection through a more simplified clustering strategy. Subsequently, Aljumaily *et al.* (2017) applied a combined partitioning and clustering method to automatically classify, localize, and extract urban buildings from the ground. In contrast, Yang *et al.* (2016) generated grid points from lidar and then classified them into segments and individual points. Segment-based and multi-scale morphological filtering were then applied to extract ground points and break lines of roads for road identification. A recent and highly novel approach was introduced by Azadbakht *et al.* (2016) using the entire signal of full-waveform lidar to perform an urban classification using 11 classes. The classification approach employed random forests and RUSBoost. The

dataset was divided into majority and minority entities and demonstrated the superiority of Random Forest over RUSBoots for majority entities.

Similarly, but working with much higher density terrestrial lidar, Dohan *et al.* (2015) used a neural network to detect small objects. They associated each point with a semantic class label such as car, van, street light, traffic light, etc. This was possible as the terrestrial lidar was extremely dense compared to aerial scans, which are currently limited to only a few hundred points per square meter (e.g., Hinks *et al.* 2009). Using high density lidar from car-mounted units, Yu *et al.* (2015) applied semantic labeling to building facades and roads by fitting large planes and to cars by using visual Structure from Motion (vSM) to address image alignment problems as per Pollefeys and Gool (2002). Yu *et al.* (2015) then aligned their features with the detected point cluster for each object using a coarse-to-fine iterative closest point (ICP) algorithm as per Rusinkiewicz and Levoy (2001).

The other major approach to this type of lidar point data classification has involved the incorporation of supplementary data. For instance, Carneiro *et al.* (2009) combined GIS and lidar data to extract morphological indicators of buildings such as 3D volume, 3D complexity, roof type, and mean roof slope. Each was achieved through a different method (e.g., roof type and mean roof slope were derived through a Hough transform based approach) resulting in a successful but non-robust approach. A more general method was proposed by Kim and Medioni (2011) using a combination of aerial and terrestrial lidar data, as well as segmentation. Their work included three tasks: (1) ground and roof surface identifica-

tion by fitting planar patches and subsequent grouping of smooth planar surfaces; (2) wall identification by finding vertical planar structures, and (3) small object segmentation based on context constraints. Contemporaneously, Boyko and Funkhouser (2011) segmented only road surfaces using a combination of aerial and terrestrial lidar with a GIS road map. After co-registration, both datasets were subdivided. For each lidar subcloud, a 2D attractor map was built to localize elevational discontinuities, after which fitting was used to approximate the boundaries. Finally, the points in each subcloud that fell inside an active contour were labeled as road points. While effective for the road network, the work is not easily extendable to a more general classification system.

Another highly successful but circumscribed approach considered only rooftops. This was done by Awrangjeb *et al.* (2013) who proposed an integration method for lidar data and multispectral orthoimagery, where the dataset was divided into ground points (as a ground mask) and non-ground points according to ground height derived from a digital elevation model. Image lines were then extracted from the grey-scale version of the ortho-image and used with the ground mask with color and texture information to extract several classes such as 'ground', 'tree', 'roof edge', and 'roof ridge'.

An alternative approach to this problem was presented by Jochem *et al.* (2012) who combined lidar and raster data to detect roof planes. First, the whole area was subdivided into smaller tiles, in which they detected areas potentially containing buildings. All detected areas were then merged to construct a single building area, and 3D roof planes were

extracted from the candidate regions. A similar strategy of combining the lidar data with existing municipal GIS data was undertaken by Chen and Zhu (2013) to identify tree species by extracting tree objects from the lidar data and then matching canopy height models to identify individual species. More recently Lee *et al.* (2016) proposed a feature based method to register individual trees using lidar data and aerial images.

In summary, generic labeling approaches that can be applied to many object types have to date focused on object-level classification after some form of segmentation. Arguably, this unnecessarily complicates exchanging data and metadata across different hardware and software tools. Furthermore, the increasing density and temporal recurrence of such data already challenges the capabilities of traditional Geographic Information Systems and other spatial databases. For example, a 1 km<sup>2</sup> tile can contain more than 60,000,000 3D lidar points (Mosa *et al.* 2012). Therefore, developing appropriate querying tools to significantly improve the outcomes of relevant data retrieval exercises is quite critical. In addition, making these points compatible with a Spatial Data Model (i.e., generating a Geo Identification Key and a Spatial Object for each point) requires more than 10 GB in relational database storage (Mosa *et al.* 2012). For this reason, writing queries against this huge data storage arrangement is complicated and time consuming. Since point clouds are weakly relational and do not strictly require transactional consistency, distributed computing platforms are suitable to handle these data (Vo *et al.* 2018). A distributed platform enables parallel programming and scalability across multiple nodes to efficiently process the massive lidar datasets that are becoming increasingly prevalent through national repositories and elsewhere. For this reason, this paper introduces a novel means for automatic classification of aerial lidar data in a distributed computing environment using an a priori dataset, as described in the next Section.

## The Proposed Approach

To improve on the 82% non-classification delivered by the commercial vendor, this paper proposes a data integration approach between GIS data and lidar point cloud data to create an automatic pipeline using *a priori* data. This will enable the addition of semantic content to the lidar. The proposed distributed solution enables this within the context of the existing LAS file format. The further goals of the presented work include the use of a data integration approach to classify data in a more highly detailed manner than previously achieved, where building type classification (e.g., commercial, university, residential, bank, etc.) and road type classification (e.g., principal, secondary, service, residential, pedestrian, footway, etc.) could be generated, as well as categories classifying bare earth, vegetation, and noise. With the help of a big data platform, this approach used two input data sources: a lidar cloud point for the scene geometry and GIS vector data (i.e., vectors of points obtained from GIS), in the form of OpenStreetMap (OSM) data, to inform the point classification (OpenStreetMap 2016).

While arguably not fully verified, and therefore, not fully reliable, OSM data have the advantage of being freely available for much of the world and traditionally stored in a GIS. Thus, this data stream was selected to show the potential of the new method. The OSM data considered in this work was in a text file (\*.xml) and provided geometric data (coordinates) and non-geometric data (e.g., class, type, name) for objects in the built environment. In addition to the OSM data class 'building', OSM provides general function classifications (e.g., commercial, university, residence, etc.).

On the big data side, a MapReduce framework (Dean and Ghemawat, 2008) was implemented. MapReduce is a software model used to support parallel computing of huge sets of data. The approach operates using key/value data types and consists of two functions: Map and Reduce. The Map function processes the original data into key/value pairs, and the Reduce function takes these pairs and merges them so that all values corresponding to a specific key are combined into a single set, as was previously achieved with lidar data by Aljumaily *et al.* (2015).

Previously, Wu *et al.* (2007) used MapReduce to automatically align a combination of satellite images and vector data for roads. Given the ever-increasing size of lidar datasets, which have rapidly gone from only a few points per square meter to over 300 points per square meter requiring more than a terabyte of data per square kilometer when paired with imagery and other concurrently collected datasets (e.g., Aljumaily *et al.*, 2017), big data capabilities are increasingly vital when working with these datasets, especially for new application requirements (e.g., map updating, disaster mitigation, illegal activity detection, and high-level modeling), as previously noted by Xu *et al.* (2014).

Figure 2 shows the two streams for the data flow: (A) GIS-based data, and (B) point cloud data. In the following section, the processing details for each data stream are described in detail.

### GIS-Based Data

For the GIS-based data, a series of processes are applied where the output of one process is the input of the next one. These processes are as described below.

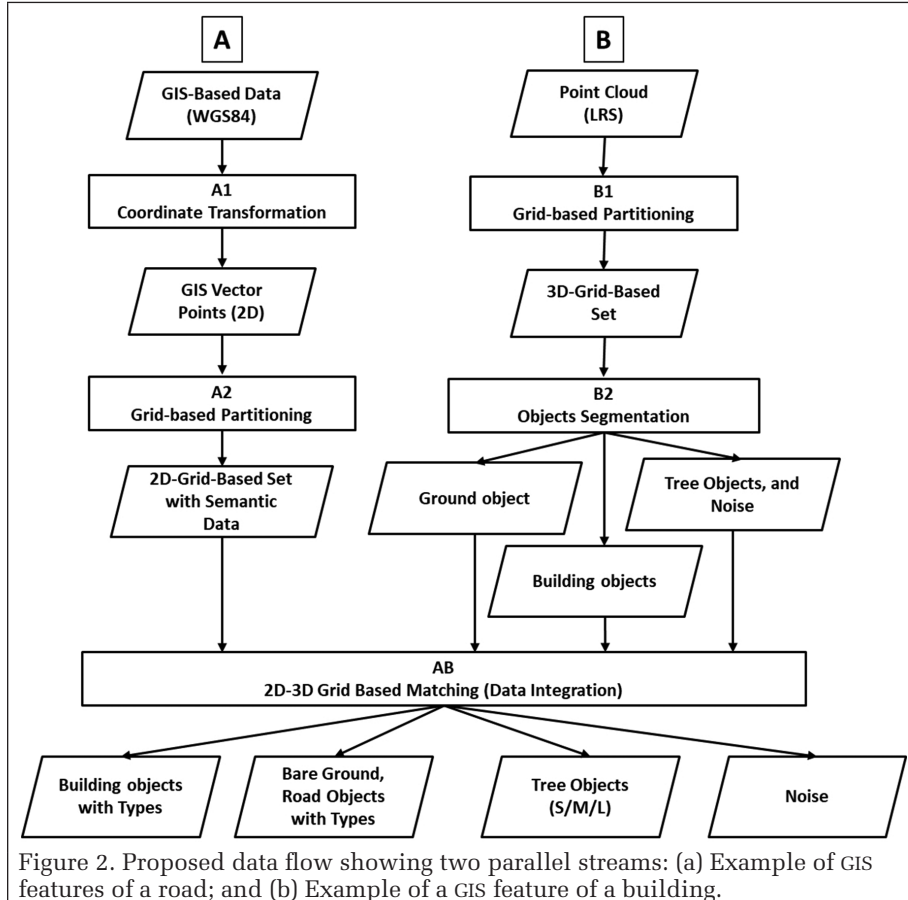


Figure 2. Proposed data flow showing two parallel streams: (a) Example of GIS features of a road; and (b) Example of a GIS feature of a building.

### Coordinate Transformation

Coordinate transformation was needed, because the aerial lidar test data employed the dominant local geo-referencing system [TM75 Irish Grid Reference System for Ireland (Ordnance Survey of Ireland, 1996)], while the OSM uses the World Geodetic System (WGS84). This process performs the needed transformation to rectify the two coordinate systems (lidar and GIS).

This process' output is the GIS *vector points (2D)*, which is an OSM file that contains features represented by the coordinates of the outermost points of an object's boundary geometry. However, more than one feature can form the outermost points of an object (e.g., the three independent features in Figure 3a that together constitute a single object represented by only one identification name, in this case, the street name of Stephen Street Upper).

Although OSM provides many features, only features corresponding to road and building objects were considered (Figure 3). These are identifiable as three geometric types (points, polylines, and polygons), and each can be described semantically by a limitless number of attributes, where each attribute has one or more values. For example, a road feature may consist of one or more sets of geometric points in the form of a LineString (open ways), while building features consist of one or more sets of geometric points in the form of a Polygon (closed ways). Table 2 and Table 3 highlight the manually-entered GIS attributes of greatest interest for roads and buildings, respectively (ASPRS 2013).

### Grid-Based partitioning (GIS Data)

This step enables the use of the MapReduce framework to facilitate data processing and integration in a distributed computing environment. In the proposed approach, MapReduce

Table 2. Road classification attributes of greatest interest.

Attributes	Description
Geom	An array of the geometric coordinates of the corresponding points.
Fclass	The class type of the road such as principal, secondary, service, residential, pedestrian, footway, etc.
Name	The road name, which is an official name of the road (e.g. Stephen Street Upper)

Table 3. Building classification attributes of greatest interest.

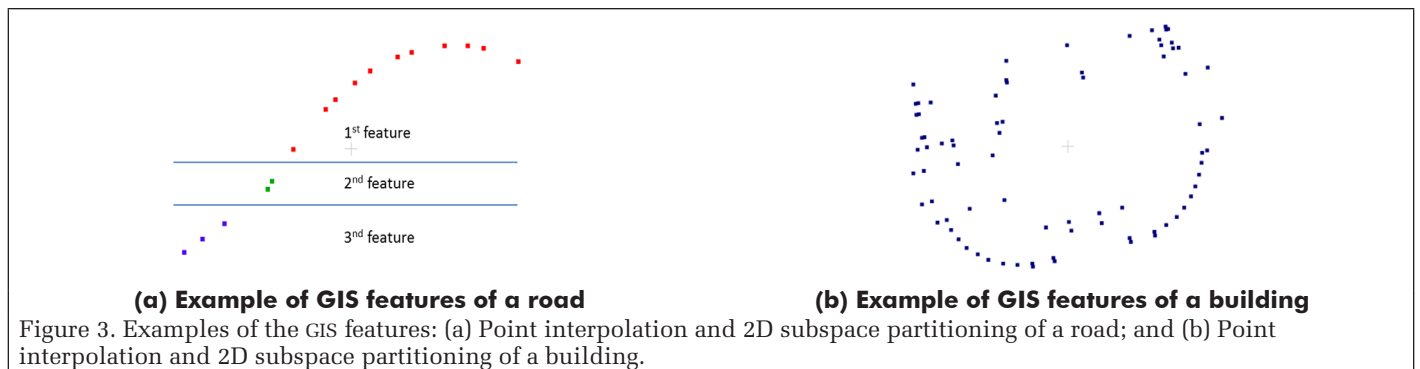
Attributes	Description
Geom	An array of the geometric coordinates of the corresponding points. As justified in Table 2, the coordinates are specified by TM75 Irish Grid coordinates.
Fclass	There is only one feature which is a building.
Name	The building name.
Type	Types such as commercial, university, residential, hospital, bank, etc.

is used primarily to co-register the lidar data to the GIS data. The co-registration is conducted by grid based-partitioning; segmenting an area into smaller subspaces of dimension  $D$ , to which the data from both resources were mapped according to their respective locations. A value of  $D = 1\text{m}$  is used as the grid resolution, because the resulting volume is smaller than most urban objects and relatively insignificant compared to the volume of the entire point cloud [as previously demonstrated in Aljumaily *et al.* (2017)].

Working with the GIS vector points poses two problems. First, a real object (e.g., building or road) may be defined in the OSM file by multiple features. Second, a GIS feature consists of individual points (a vector of points) separated by potentially unequal spacing that may exceed the previously recommended threshold of  $D = 1\text{m}$ . To solve the aforementioned problems and to map the GIS feature points to 2D subspaces (squares), the MapReduce framework is applied. The Map function performs two tasks. First, the Map function receives a GIS vector of points related to a specific feature and normalizes the distance between each pair of consecutive points, using a *Linear Interpolation* algorithm. This algorithm calculates the distance ( $D_{AB}$ ) between each pair of consecutive points (A and B in Figure 4a) and, if  $D_{AB} > D$  (the grid threshold), then new points are temporarily seeded between A and B in the GIS-based data as an interim measure (Figure 4a - green points). The seeding is done in such a way that the distances ( $d \leq D$ ) between the original points are equalized. The main objective of seeding points is to divide the space between each pair of consecutive points into equal subspaces. By having at least one point per square, the process ensures that consecutive points are mapped to adjacent squares. For buildings, in addition to the linear interpolation (Figure 4b - green points), the Map function seeds new temporary GIS-based points across the building's spatial extent to achieve a minimum of 1 point per square (Figure 4b - red points).

In the next subtask, the Map function emits key/value (feature id, square coordinates) pairs, where the key represents the identification name of a feature, and the value represents the southwest corner coordinates (eastings, northings) of the grid square where the point in question belongs. For example, if a point's coordinates are 309958.2645, 236141.9291 and  $d = D = 1\text{m}$ , then the Map function emits the square coordinates 309958, 236141. The Reduce function then receives the pairs from the Map function and groups them to form a *2D-Grid-Based Set* with semantic data, where the grid represents all the geometric data (southwest corner coordinates) of the squares to which the points belong. The semantic data represents all the non-geometric data of the corresponding feature such as id, name, type, etc.

In general, grid-based partitioning provides two advantages. First, instead of accessing individual points, point grouping into subspaces enables the accessing of each subspace only once, as opposed to once for every subspace point.



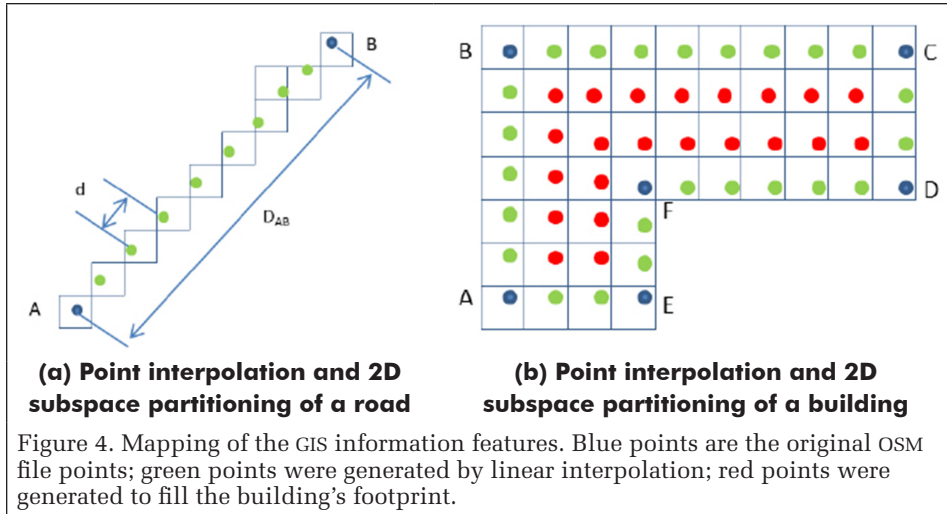


Figure 4. Mapping of the GIS information features. Blue points are the original OSM file points; green points were generated by linear interpolation; red points were generated to fill the building's footprint.

This assumes that neighboring points belonging to a single subspace belong to the same object. This improves nearest neighbor searching (e.g., Lee *et al.* 2008; Wang and Shan, 2009), which is computationally expensive when applied indiscriminately (Athitsos *et al.*, 2008), hence the advantage of a distributed computing approach. Second, two subspaces with the same coordinates are considered to belong to the same object, even when they come from different datasets. Thus, using a 2D subspace from the GIS data and a 3D subspace from the lidar data (as described in the next Section) with the same coordinates facilitates the subspace matching of the two datasets. This can overcome problems with one-to-one assignments in the presence of disparate dataset granularities or distinctive data distributions.

### Point Cloud

For the Point Cloud data, there is no need to do any type of transformation, because this type of data is already expressed in a local reference system. Here, a series of sequential processes are applied, as described below.

#### Grid-based Partitioning (Lidar Data)

While point clouds can include 3D coordinates, timestamps, intensity, and Red-Green-Blue (RGB) measurements (when imagery is co-registered), the proposed approach uses only the 3D coordinates and the classification field. With these data, as with the OSM data, the same MapReduce strategy is adopted, except this time in three dimensions instead of two. Again, the Map function is used to partition the lidar point cloud into smaller 3D subspaces or cubes. For example, for point coordinates  $X = 2.8$ ,  $Y = 0.25$ ,  $Z = 1.8$ , and  $D = 1$ , the point is mapped to the cube coordinates of  $X = 2$ ,  $Y = 0$ ,  $Z = 1$  (see Figure 5). Each cube is considered to correspond to only a single object. Consequently, if two neighboring points belong to the same cube, then they belong to the same object. As with the GIS data, the Map function emits Key/Value (cube id, point coordinates) pairs, where the key represents the cube identification (grid cube coordinates), and the value represents the point being processed.

In this case, the Reduce function is used to perform two tasks. The first receives the previous pairs and sets them in groups where each group consists of the cube identification as a unique key and a list of values of all points that belong to that cube. Once a group is formed, the Reduce function applies a clustering classification algorithm. The main objective of this classification is to distinguish between dense and sparse cubes. Dense cubes are assumed to be part of an object, while sparse cubes are assumed to represent either vegetation, vertical walls, or noise. To achieve this classification,

the Density-Based Spatial Clustering of Applications with Noise (DBSCAN) algorithm is used.

The DBSCAN algorithm was introduced by Ester *et al.* (1996) to find arbitrarily shaped clusters, handle noise, and address data of any type in clustering. DBSCAN distinguishes densely populated from sparsely populated cubes within a point cloud. Each dense cube contains a set of successfully clustered points (Figure 6a) that are grouped together in the cube to form a point dense (i.e., highly populated) sector within the cube. Importantly, the approach detects arbitrarily shaped clusters, which means that cluster formation is independent of the cube's orientation and the specific details of the actual object. Normally, a dense cube forms part of the ground

or a building object (mostly in the form of roofs).

The second cube type is sparse, where the points within the cube are dispersed and occupy more space (Figure 6b). Typically, a sparse cube represents vegetation, because the discontinuous nature of the foliage combined with the laser scanner's ability to penetrate gaps in the canopies, results in the laser pulses hitting leaves, branches, and portions of the ground (Slatton *et al.* 2008). For this reason, such results will generate more dispersed and less compact cubes than the first type. In addition, most vertical wall cubes are classified as sparse, because, as previously noted by Hinks *et al.* (2009), the relative position of the aircraft to the building wall and the large angles of incidence often limit point acquisition on these vertical surface, thereby leading to relatively low point densities in vertical wall cubes.

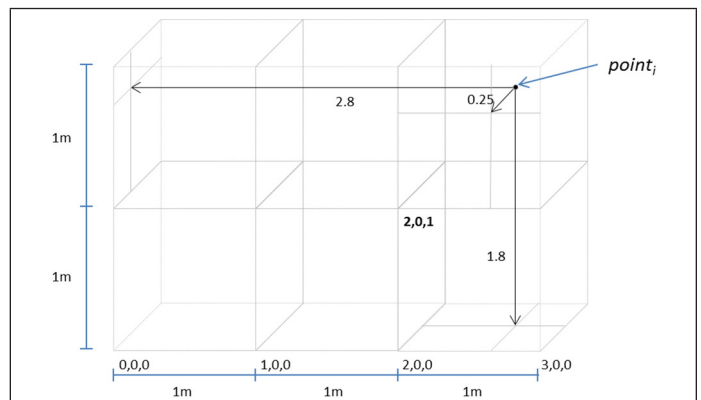


Figure 5. Lidar point cloud mapping: (a) Dense cube; and (b) Sparse cube.

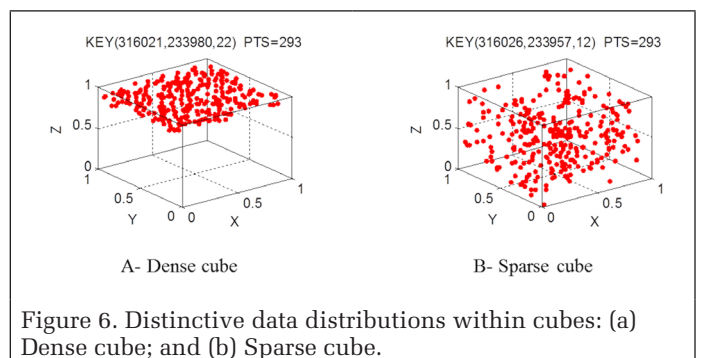


Figure 6. Distinctive data distributions within cubes: (a) Dense cube; and (b) Sparse cube.

Finally, noise and obstructions such as pedestrians, vehicles, and lighting poles may also be classified as sparse cubes, as they represent transitory and/or less substantial things in the built environment. The final result of the Reduce function is a *3D-Grid-Based set* (i.e., all the dense cubes and sparse cubes). This set represents the entire point cloud mapped onto cubes where each cube is classified as either dense or sparse. Based on the empirical work by Aljumaily *et al.* (2017), a threshold of 30% was adopted as the percentage of outlier points used to categorize cubes: a cube with less than 30% outlier points is considered dense, while a cube with greater than 30% outlier points is considered as sparse.

#### Objects Segmentation

Many GIS datasets are incomplete in their labeling and GIS feature dimensions do not necessarily match the corresponding real objects. For this reason, the relevant geometric data must be segmented from the more accurate point cloud (He *et al.*, 2015). This segmentation is shown in Figure 7, where the process begins by splitting the *3D-Grid-Based Set* provided from the previous process. The output is two datasets: dense cubes and sparse cubes.

As previously noted, because the selected cube volume (i.e., 1 m<sup>3</sup>) is small in comparison to the point cloud's total volume, when two neighboring dense cubes exist, they are assumed to belong to the same cluster. In order to identify and extract objects, the Neighbor Adjacent Cube Algorithm (NACA) (Aljumaily *et al.*, 2017) is applied to the set of dense cubes. This step's output is a ground object and the building clusters. The ground object is the set of all dense cubes that belong to the bare ground and the roads, while a building cluster is the set of the dense cubes that belong to the roof of a specific building. Assuming that two adjacent dense cubes belong to the same object, this algorithm starts from the highest cube in the dataset and moves downwards towards the lowest one. This continues, until all clusters are segregated from the set of the dense cubes. Notably, although the algorithm always starts with the highest cluster, this did not require a height calculation of the corresponding object, only a determination as to which cube has the highest Z coordinate.

As previously mentioned, because most vertical wall cubes are not classified as dense cubes, empty spaces form between the roof building cubes and the ground cubes. This enables easy segregation of the building clusters and the ground object. The building clusters obtained in this step (Figure 8a and

8c) are then used as patterns for building object extraction from all the cubes in the *3D-Grid-Based set* (i.e., the full, original point cloud mapped into dense cubes and sparse cubes). The patterns help prevent extraction beyond a building's boundaries in the horizontal direction; vertically oriented extraction remained unconstrained. For example, if a building cluster contains a cube with the following coordinates (309958, 236141, 22) then the algorithm would segregate all the cubes (309958, 236141, Z) within the *3D-Grid-Based Set*, where Z is the range of Z coordinates with values starting at 22 and ending with the minimum value of Z. This step result in two point sets: *Ground Object* and *Building Objects*.

The extraction process is done directly on all the cubes in the *3D-Grid-Based Set* to maximize vertical wall extraction with the corresponding roof components (see Figure 8b and 8d). However, low point density on these walls, the lack of a roof (representing a barrier wall and not a building), or low roof point densities (e.g., those with glass or other highly reflective surfaces) are not uncommon problems in vertical wall recovery. Thus, the next process localizes and recovers the remainder of these walls from the sparse cubes.

Vegetation and previously unclassified walls are distinguished and extracted from within the set of sparse cubes by applying the NACA, despite the absence of a clear point distribution within each cube. To aid in this, the RANdom SAMple Consensus (RANSAC) algorithm proposed by Fischler and Bolles (1981) is first applied within each object.

As previously mentioned, the main objective of using RANSAC is to localize and recover the unclassified walls. Once a wall is localized, it is aggregated into the set of building objects previously obtained.

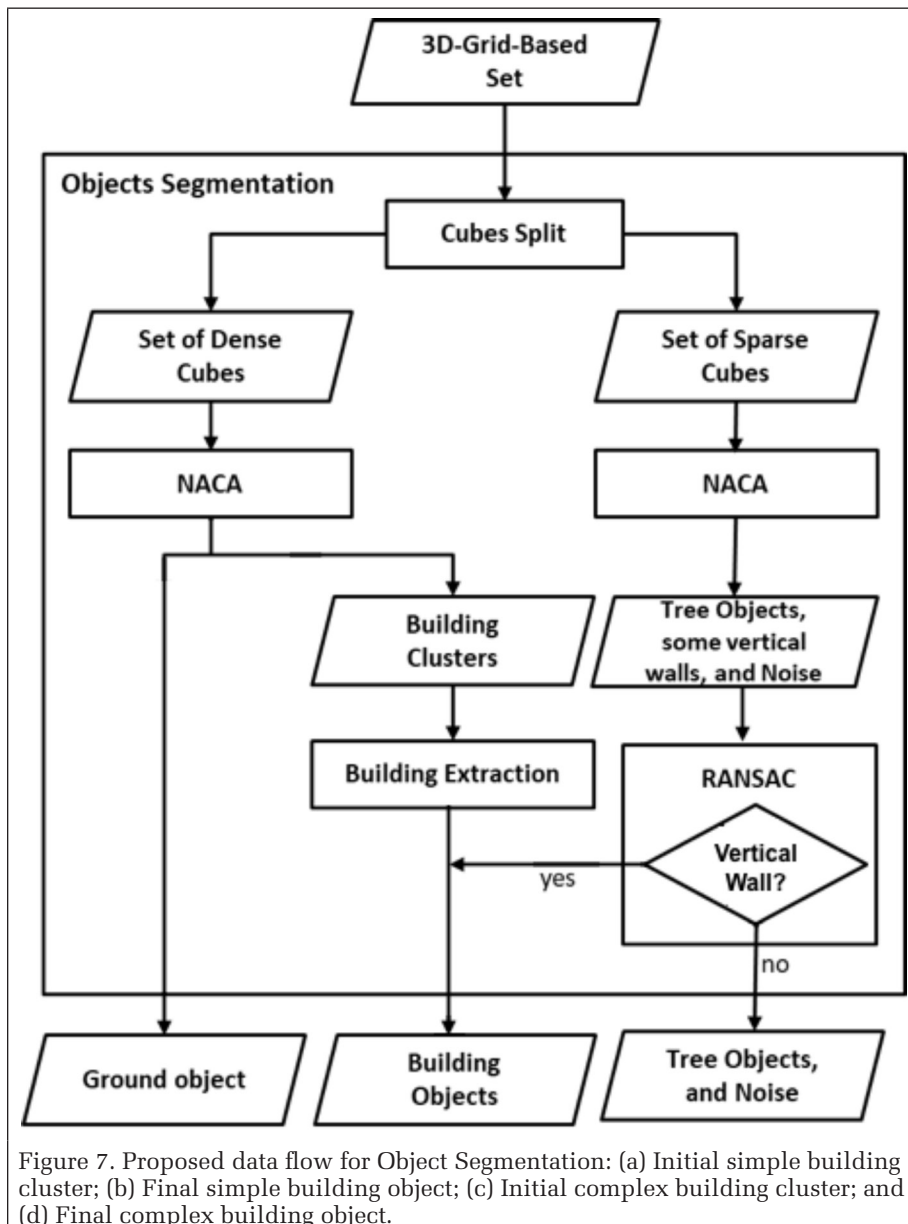


Figure 7. Proposed data flow for Object Segmentation: (a) Initial simple building cluster; (b) Final simple building object; (c) Initial complex building cluster; and (d) Final complex building object.

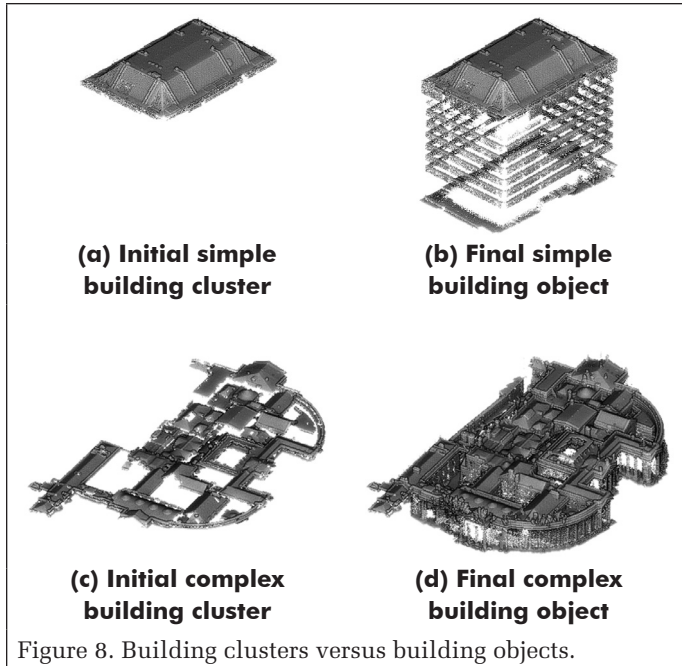


Figure 8. Building clusters versus building objects.

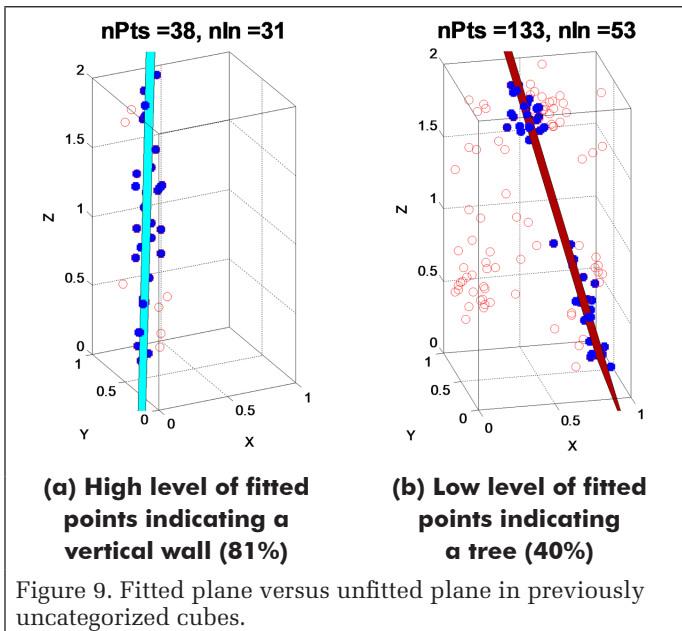


Figure 9. Fitted plane versus unfitted plane in previously uncategorized cubes.

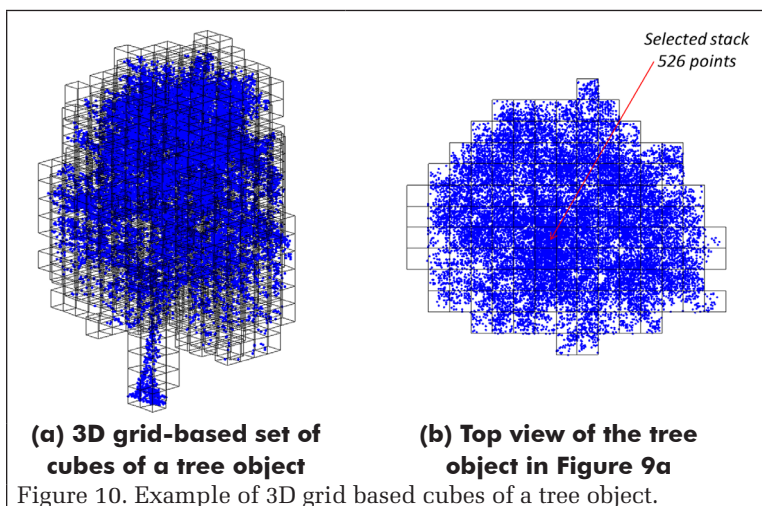


Figure 10. Example of 3D grid based cubes of a tree object.

RANSAC is used to find the best plane that can be fitted through a set of 3D points within a cube. According to this algorithm, a plane is calculated using three points randomly selected from the set. Inlier and outlier points are designated with respect to the threshold distance. In this work, a threshold distance value of 0.1m is selected and a threshold of 70% is adopted as a vertical wall indicator for the inlier points based on the empirical work by Aljumaily *et al.* (2017). The number of iterations  $k$  of the algorithm is calculated, according to the following formula:  $k = \log(1-p) / \log(1-(1-e)^s)$ , where parameters are defined as follows ( $p = 0.99$ ,  $s = 3$ , and  $e = 30\%$ );  $p$  is the probability of finding at least one good set of inlier points in  $k$  iterations;  $s$  is the minimum number of points to fit into a model; and  $e$  is the percentage of outliers.

Figure 9 shows an example of the application of the RANSAC algorithm in this incarnation. This fitting facilitates clear distinctions between adjacent cubes. The object shown in Plate 6a is labelled as vertical wall, because the percentage of the inlier points was (81%), while the object shown in Figure 9b is labeled as vegetation since the percentage of inliers (40%) is less than the defined inlier points percentage. Single isolated cubes with less than 70% inliers are labeled as noise. In the proposed approach most objects with dimensions less than  $1\text{m}^2$  (e.g., small bushes, signage, fire hydrants, etc.) fall into this classification.

Figure 10a shows 3D grid based cubes for a tree. Once all the cubes of an object are extracted, the RANSAC algorithm is applied to the stack of cubes within the object that contains the greatest number of points of all the stacks in the object. Figure 10b shows the top view. The selected stack contained 526 points. RANSAC is applied with the 70% inlier ratio criterion.

### 2D-3D Grid Based Matching (Data Integration)

Next, the extracted datasets from the two datasets (A-GIS Data and B-Point Cloud) are integrated together for semantic enrichment, classifying the points in reference to the objects to which they belong. Integration is done by co-registering the 2D and 3D gridding by matching the X-, Y-coordinates of the object cubes with the corresponding X-, Y-coordinates of the GIS squares. For roads, matching involves pairing the GIS road squares with the corresponding ground object cubes. However, a GIS road consists of a set of adjacent squares, where adjacent squares have a common side or a common vertex (Figure 4a). Thus, the GIS road width at each square is only 1m, while the real road (as represented by the point cloud) could span several meters. To resolve this discrepancy, Choi *et al.* (2008) recommended employing local road standards.

To achieve enriched semantic labeling, the algorithm starts by matching the first square (point A in Figure 4a and 4b) of a GIS-labeled road with its ground object cubes. The initial point was the array's first value. The first square represents the road's beginning point within the GIS vector data. Once the corresponding cube is found within the ground object, the algorithm marks all nearest neighbor cubes in the ground object as part of that road. If the algorithm encounters an empty cube, aggregation does not occur. Furthermore, if the road width exceeds the standard average width for that road type [in this case 6 m wide for service roads (Cavan Local Authority Road Design Office, 2017)], then classification processing terminates at that location. This prevents the inclusion of driveways and parking lots. Although these values do not give an exact width, they provide useful approximations. For buildings, the process is easier, as correspondence between GIS data squares and lidar grid-based cubes is more straightforward. A square and a cube of the same X, Y coordinates belong to the same object.

When the algorithm matches X-, Y-coordinates of a square and a cube, all cube points are classified

according to the GIS designator employing the user-defined LAS fields 64 to 255 (Table 1), as per the user's own classification tags. While OpenStreetMap has a set of road designators (OpenStreetMap, 2016), tags compatible with local national practice are used. For Ireland, where the testing data in the Experiments And Evaluation Section was collected, the principal tags are motorway, trunk, primary, secondary, tertiary, residential, service, track, footway, cycleway, and unclassified. A similar set of tags are available for buildings (e.g., residential, commercial, government, college, bank, church, hospital, hotel, university, museum, etc.). Since these values are difficult to unify, specific descriptions and designators of the classification categories should be attached as a metadata file. Since point cloud visualization tools such as CloudCompare (2017) do not support a legend for this type of information, colors were used to represent classifications in the demonstrated outputs. Additionally, while the authors' approach can specify the road name to which a point belongs, this facility was ignored as it could not be supported in the current LAS specification.

Finally, the last major classification is vegetation. In this study, vegetation classifications as proposed by Khosravipour *et al.* (2014) were assigned based on height: Low vegetation ( $0.5\text{m} < \text{height} \leq 2.0\text{m}$ ), Medium vegetation ( $2.0\text{m} < \text{height} \leq 5.0\text{m}$ ), and High vegetation ( $5.0\text{m} < \text{height}$ ); 3, 4, and 5, respectively in Table 1. Height was measured as the difference of the tree's top and bottom (distance between top of the uppermost cube to bottom of the lowermost cube using the known cube coordinates, Figure 10a). Finally, the points of any remaining unclassified cubes were assigned the value 7 of noise (Table 1).

## Experiments and Evaluation

The approach presented in the previous section was evaluated using a  $1.5 \text{ km}^2$  study area in the centre of Dublin, Ireland (Figure 12a). A total of  $\sim 225$  million points from aerial laser scanning were acquired in the winter of 2007 for a dense, urban area of Dublin, Ireland. The data were acquired using a FLI-MAP 2 system. The system operated at a scan angle of 60 degrees, with an angular spacing of 60/1000 degrees between pulses. While the FLI-MAP 2 system can provide spectral data in the form of intensity and color, the color data were not collected due to equipment malfunction. The flying altitude varied between  $\sim 380$  to  $480\text{m}$ , with an average value of  $\sim 400\text{m}$ . A total of 44 flight strips were acquired and 2,823 flight path points were recorded, providing instantaneous aircraft position over time (Laefer *et al.*, 2013). Figure 11b shows the corresponding road and building OpenStreetMap data.

The original 225,791,517 lidar points were mapped to 3,248,506 cubes resulting in an average of 70 points per cube.

Their distribution is shown in Figure 12a, where the x-axis shows the density in 10 point bins (e.g., the first bin represents cubes containing 1 to 10 points). The histogram peak of 3.95% is for cubes containing 241 to 250 points. Figure 12b represents the generated ground object of the study area, which consists of 83,194,139 points (i.e. 37% of the original point cloud data) with approximately 200 points per cube. Figure 12c represents the derived building objects, containing a total of 125,224,191 points (55.5% of the original point cloud data) with an average of 66 points per cube. The first of the two peaks represents the low density vertical wall cubes. The second is composed of the high density cubes representing building roof cubes. Figure 12d shows the vegetation objects with 6,192,861 points (3% of the total points) with an average of 13 points per cube. Finally, approximately 4.5% of the points were classified as noise.

Evaluation considered three object classes (buildings, roads, and vegetation) according to [1] correctness (or precision), [2] completeness (or recall) and [3] quality measure (F-measure). These measures were calculated by comparing automatically classified objects with manually classified reference objects (Maurya *et al.* 2012) as identified using CloudCompare (2017). Correctness is the ratio of relevant points to the total number of points assigned by the algorithm (Equation 1). Completeness is the ability to extract all relevant points for an object (i.e., coverage) (Equation 2). The quality is the correctness and completeness in a single metric (Equation 3).

$$\text{correctness} = \frac{TP}{TP + FP} \quad (1)$$

$$\text{completeness} = \frac{TP}{TP + FN} \quad (2)$$

$$\text{quality} = \frac{(2 * \text{correctness} * \text{completeness})}{(\text{correctness} + \text{completeness})} \quad (3)$$

where True Positives (TP) are the points correctly included in the object, False Positives (FP) are the points incorrectly included in the object, and False Negatives (FN) are the points mistakenly excluded from the object. FPs and FNs are sometimes called errors of commission and errors of omission, respectively (Yenigün *et al.*, 2017). Evaluation results are shown in Figure 13.

After applying the proposed approach to this 2007 dataset, 3,248,506 cubes were generated. As shown in Figure 13, the results showed correct classification (TP) of cubes related to buildings as 42%, roads as 21%, and vegetation as 9.5% of

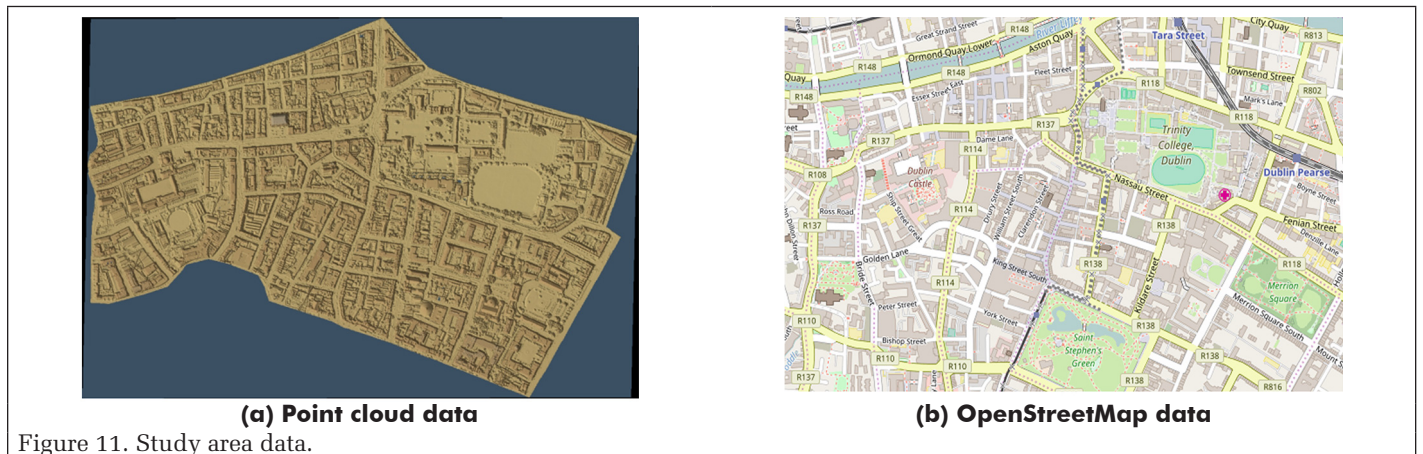


Figure 11. Study area data.

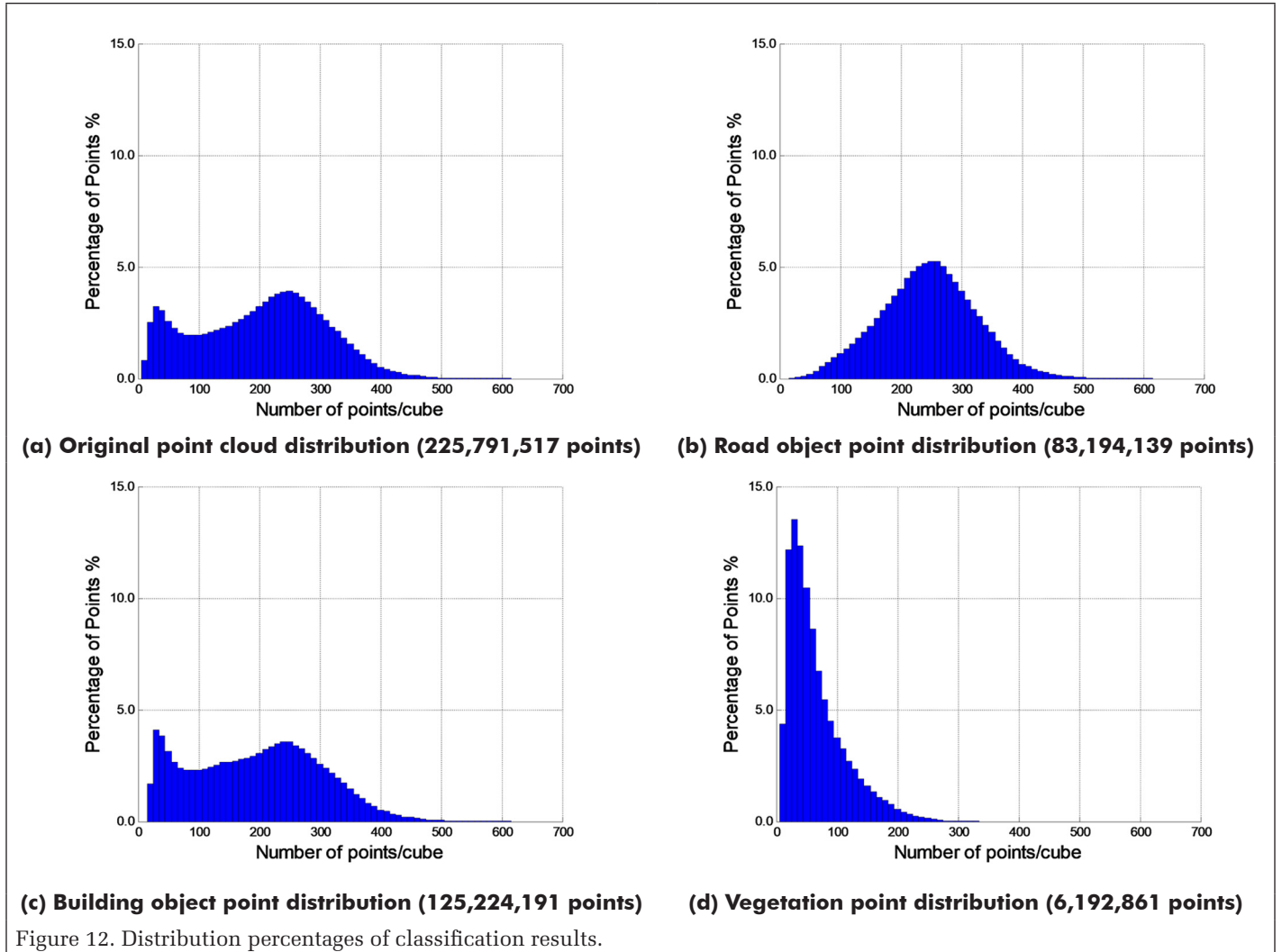


Figure 12. Distribution percentages of classification results.

the total cubes. Incorrect inclusion (FP) for these 3 categories was 6.3%, 5.5%, and 3.7%. Incorrect exclusion (FN) was respectively 10.6%, 1%, and 2.3%. Finally, almost 12.3% of the total cubes were not classified due to low data density in these cubes (down from 82% without this procedure).

As shown in Table 4, the approach was able to extract 95.8% of the relevant points for the roads and 82.88% for vegetation objects but with lower correctness levels, 78.69% and 71.76% respectively. However, this still resulted in a relatively high-quality output: 86.4% for roads; 76.9% for vegetation. The building objects were much more consistent with 84.7% for quality and with 86.97% of the relevant points correctly classified (the highest performance of the three classes but only an 82.5% completeness of relevant points, which may be in part an outgrowth of the difficulty of manual extracting the referenced objects to generate the benchmarking dataset).

The vegetation correctness classification was less impressive (71.76%). The missing points are likely to have been lost because of the complexity of the manual extraction and because vegetation cubes do not have clear distribution patterns. The approach was, however, very successful for buildings with complicated roof geometries and with multiple sections of varying heights, where some objects had more than ten adjacent components of differing heights. Figure 14 shows the classification results represented on the point cloud of the study area, where each color represents a specific object type (e.g., secondary roads in red and bare ground in brown in Figure 14a); notably, colors are not inherent to the LAS

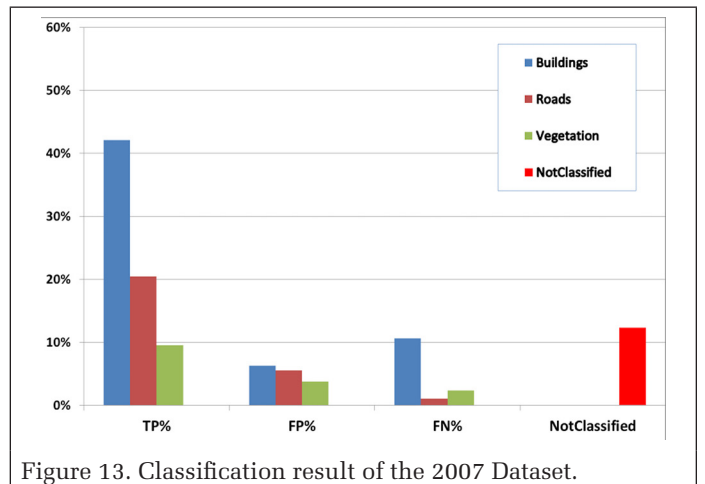


Figure 13. Classification result of the 2007 Dataset.

Table 4. Classification quality of the 2007 Dataset.

	Correctness (%)	Completeness (%)	Quality (%)
Buildings	86.97	82.52	84.69
Roads	78.69	95.83	86.42
Vegetation	71.76	82.88	76.92
		Average	82.67

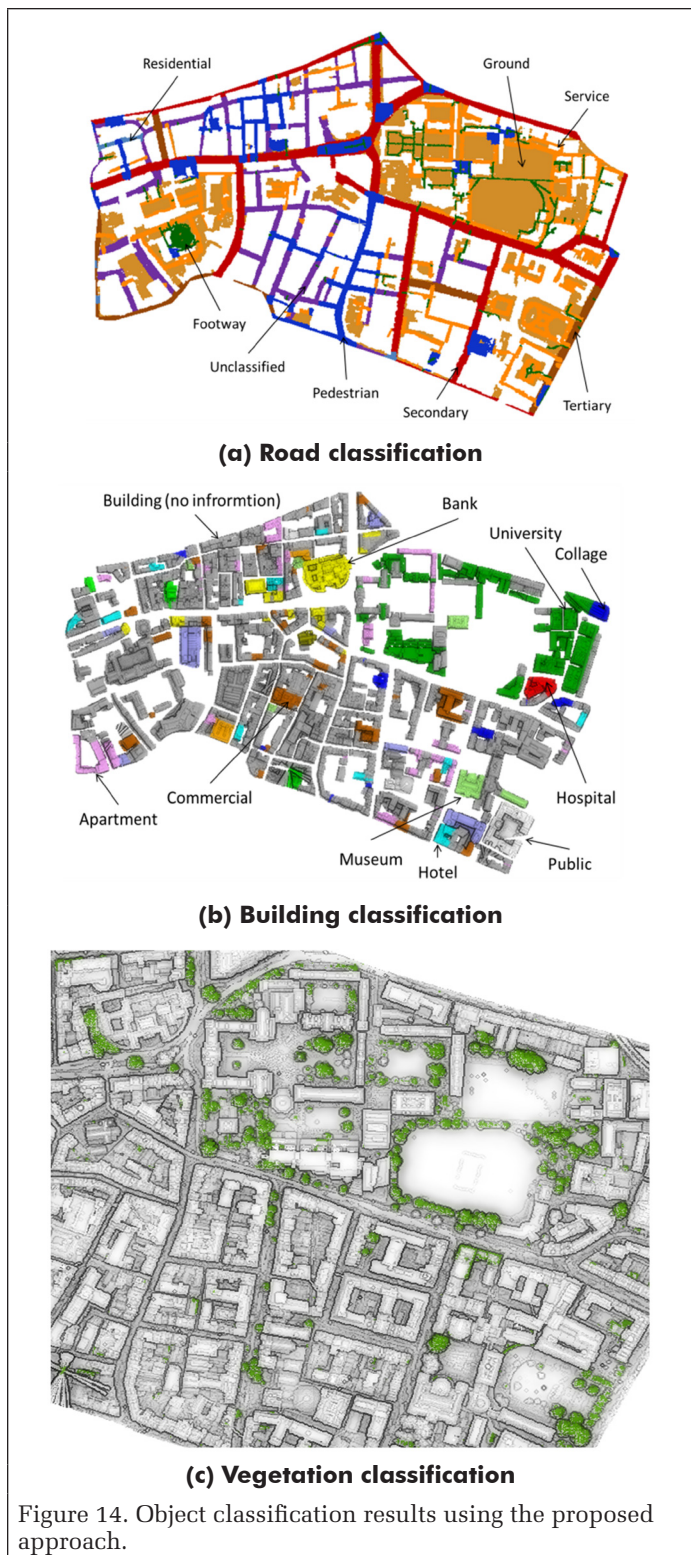
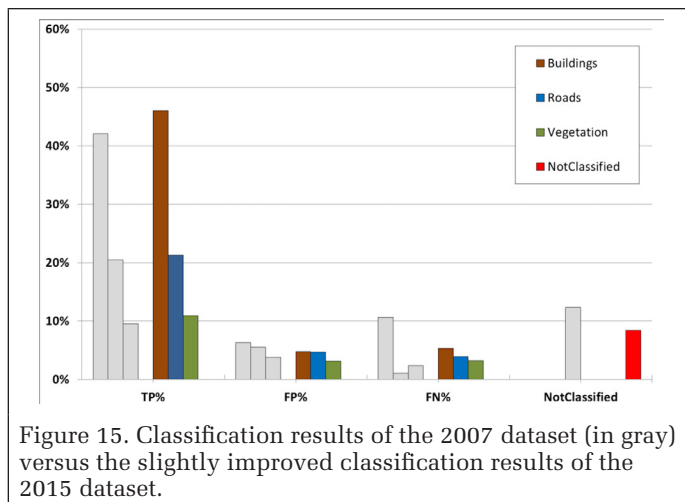


Figure 14. Object classification results using the proposed approach.

assignments. Building objects are similarly denoted (Figure 14b). Problems arose when two buildings were joined (e.g., terraced housing), as the proposed approach recognized them as a single object. This is a well-known problem for many techniques, as reported by Truong-Hong and Laefer (2015), for which a simple solution has yet to be devised. Finally, Figure 14c shows the vegetation objects.

To further validate the quality of the classification, the approach was applied to a second publicly-accessible lidar



dataset for the same the area (Laefer *et al.* 2017). The new dataset is approximately 50% denser and was collected in March 2015 by a TopEye System S/N 443. The dataset consists of 315,439,276 points that were mapped to 3,221,440 cubes resulting in an average of 98 points per cube. The results of the classification of the second dataset are shown in Figure 15.

As shown in Figure 15, with the 2015 dataset (which typically had a 50% increase in data density) the approach was able to further improve the results including reducing unclassified cubes from 12.3% to 8.4% possibly implying a dependency on data density. Overall, the results of the extraction quality of the 2015 dataset were slightly better (correctness =90.91%, completeness=86.18%, and overall quality=79.00%) as seen in Table 5. The difference between the quality is in part an outgrowth of the difficulty of manual extraction in sparser data sets.

Table 5. Classification Evaluation of the 2015 Dataset.

	Correctness (%)	Completeness (%)	Quality* (%)
Buildings	90.66	91.16	90.91 (+6.22)
Roads	81.85	86.64	84.18 (-2.24)
Vegetation	77.81	80.23	79.00 (+2.08)
		Average	84.69 (+2.0)

\*Improvement over 2007 dataset shown in parentheses

The 50% data density increase of the 2015 data over that of the 2007 demonstrated a mild dependency on the dataset for the roads and vegetation, but nearly no change in building detection, which is probably related to the fact that for these datasets every ten points on the ground generate only one additional point on the facade. So, typically the building facades in the 2007 dataset had less than 23 pt/m<sup>2</sup>, while those in the 2015 dataset had only slightly more than 34 pt/m<sup>2</sup>. This implies that the proposed approach may work significantly better with a data density that is higher than the 34 pt/m<sup>2</sup> available in the 2015 data. Alternatively, the dense pattern of buildings and their complex architecture might require a smaller voxel size for significantly improved results (e.g., 0.5m<sup>3</sup> versus the currently selected 1.0 m<sup>3</sup>, at least for those currently characterized as noise), or as previously mentioned, the benchmark data may in and of itself have to be improved. Furthermore, buildings that have overhangs and colonnades should actually have two designations along the vertical direction, but this is not currently a supported feature, because

of the two-dimensional nature of the GIS tagging information. Despite the remaining inaccuracies, the proposed approach represents a major advancement in automatic metadata enrichment.

To calculate the degree of uncertainty of the proposed approach, a standard error (SE) can be calculated (Altman and Bland, 2005), which can be considered as a measure of the precision of the sample mean and depends upon the standard deviation and the sample size; i.e.,  $SE = SD/\sqrt{\text{sample size}}$ . To calculate the SE of the proposed approach, both datasets (2007 and 2015) were divided into 15 tiles of equal dimensions to get a set of samples for classification. After application to the tiles, the precision was calculated for each category (Building, Road, and Tree) within each tile (Figure 16). For example, each column in each category represents the correctness percentage of the classification of one of the 15 evaluation tiles. The black points represent the mean for each category.

The SE results are compiled in Table 6, with the best being  $90.66 \pm 0.76$  (the building classification using the 2015 data) and the worst being  $71.76 \pm 3.75$  (the vegetation classification using the 2007 dataset). Notably these two datasets were collected with an eight-year gap between them and were collected by two different companies employing different sensors, which begins to lend credence to the robustness of the approach.

A comparison was then done looking at only those points that were classified by the vendor (Table 7). Of those, only two labels were used: ground and vegetation. As nearly all of the study area was paved, the ground labeled points were compared to the manually extracted roads areas (Figure 1b), which resulted in 66.98 % correctness (which was nearly 15% less than with the proposed approach) and a 93.19 completeness (6.55% better than the proposed approach), which means that almost all the manually-extracted roads were included in the provider's classification. Overall, however, the road quality measure was more than 6% less than that from the proposed method. Vegetation classification was even less successful with a difference of more than 36% between the two methods. Of the vendor labeled points, the total quality score was only 50%. When this is considered in the context of those that had no label, this further reduces the quality of the entirety of the vendor provided labeling to 11.08%.

## Discussion

The proposed approach offers three notable advancements in the field of automatic aerial lidar point classification. The first is to facilitate a means for a richer set of classifications through a generic means to integrate GIS data for labeling, while benefitting from the more accurate geometric positioning of the lidar data. This is especially valuable where official, municipal GIS data are not available. Even though the OSM data are not fully verified and, therefore, not fully reliable in their geometry and may also be incomplete, this does not jeopardize the final output. This is shown in Figure 17a, where some of the GIS-based roads do not exactly match the corresponding lidar-based roads, such as, along the bottom border of the study area or the diagonal line towards the area's top-most border. A similar issue arises with respect to the building objects where some buildings exist in the lidar point cloud but do not exist in the GIS data, as they were never recorded in the GIS dataset; these appear as grey areas in Figure 17b.

The second contribution is the point level (as opposed to the object-level) labeling. As the remote sensing community moves forward with more sophisticated means for automated material detection (e.g., hyperspectral imagery), this point-level labeling approach (as opposed to an object-level one) may open significantly more sophisticated and accurate means for small feature detection and extraction. Despite the

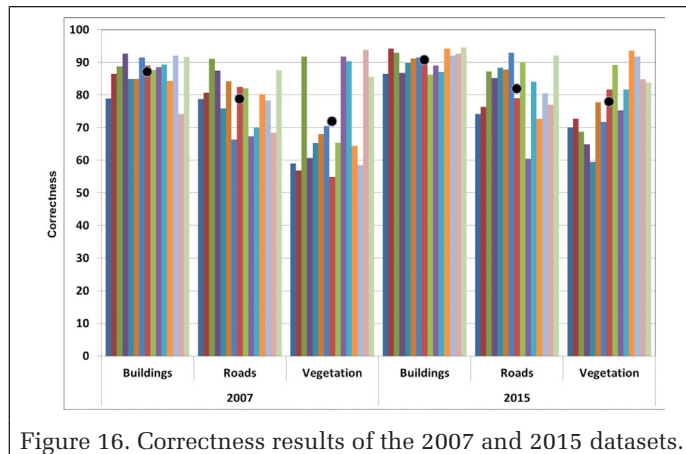


Figure 16. Correctness results of the 2007 and 2015 datasets.

Table 6. Standard Error of the proposed approach.

	2007			2015		
	Buildings	Roads	Vegetation	Buildings	Roads	Vegetation
Mean	86.97	78.69	71.76	90.66	81.85	77.81
STD	5.09	7.74	14.52	2.95	8.80	10.02
Standard Error	1.32	2.00	3.75	0.76	2.27	2.59

Table 7. Classification Evaluation of the provider's classification of 2015.

Category	Correctness (%)	Completeness (%)	Quality (%)	
	As provided	As provided	As provided	Proposed method
Buildings 0 pts = 0%	NA	NA	NA	90.91
Roads 26,305,254 pts = 9.07%	66.98	93.19	77.94	84.18
Vegetation 27,203,017 pts = 9.38%	33.84	57.89	42.71	79.0
Unclassified 236,408,815 = 81.54%	-	-	-	-

high level of classification accuracy for larger objects, the assignment of only one value in the vertical direction precludes full assignment accuracy. New technologies and citizen science approaches may change this in future years and can be easily incorporated into this framework, which notably is fully within the existing LAS data storage format. The final important contribution is that the approach employs distributed computing, which will well position it for addressing the ever increasing point density of aerial and mobile lidar datasets.

The computational efficiency and scalability of the approach needs to be demonstrated with respect to the execution time required for each step of the proposed approach. Most of execution time was consumed by Step 1 (Grid-Based Partitioning). In Figure 18, the Step 1 experiments were done by selecting three different cube dimensions (0.5 m, 1.0 m, and 2.0 m) of the same study area. Notably, the execution time using cubes with dimensions of 0.5 m were very similar to those using dimensions of 1.0 m. A value of  $d$  of 1.0 is recommended, however, because when the cube dimension is small and there are many cubes of low density with complex



(a) Matching GIS road (red lines) with bare ground



(b) Matching GIS building patterns (red plans) with building objects

Figure 17. Matching GIS data with lidar objects.

architecture, the original object will unnecessarily be divided into smaller objects, and this will reduce the quality of the clustering. If a larger cube dimension such as 2.0 m is selected, a cube may contain parts of different objects including vegetation, which will result in more misclassification. Although the experiment was performed in a single Hadoop installation, the execution time of the Grid-Based Partitioning step can easily be improved by adding more nodes as is common for a big data platform cluster (Xu *et al.*, 2015).

The complexity of the DBSCAN algorithm is  $O(n^2 \log n)$  (Xu and Tian, 2015). However, to ensure the validity of the performance of the DBSCAN algorithm, a comparison between DBSCAN and K-Means has been done. The results are shown in Figure 19, where the DBSCAN algorithm outperformed the K-Means algorithm. For example, in order to cluster 200,000,000 points the DBSCAN needed less than 9 minutes, while the K-Means required approximately 25 minutes.

## Conclusions

To address the shortcomings of existing LAS-based classification techniques in an urban context, a new and fully automatic approach is proposed. The approach is entirely compatible with the current LAS specification format and directly deployable in a distributed computing environment through a MapReduce framework: something not previously achieved for data integration of point clouds with GIS data. Using this approach, semantic categories such as the types of roads, buildings, and vegetation categories can be included

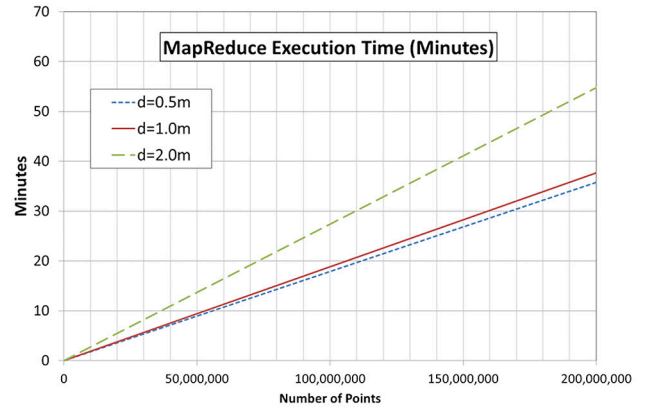


Figure 18. Execution time of the Grid-Based Partitioning step with three different dimensions of cubes.

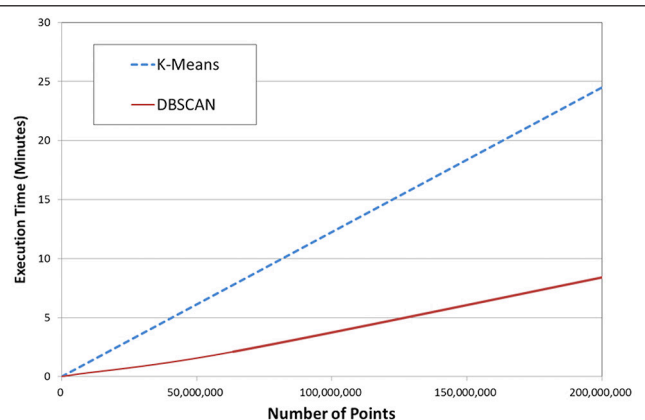


Figure 19. Comparison between the execution time for DBSCAN versus K-Means.

in the LAS specification of a point cloud as a means of point-level enrichment. This is done by integrating a lidar point cloud with GIS data obtained from OpenStreetMap. The result is a broad-based, point by point classification system. The approach was tested with two datasets for the same study area of approximately 1 km<sup>2</sup> reaching a typical classification quality level in excess of 83% for a point cloud with 225pt/m<sup>2</sup> data density and 85% for one with 355pt/m<sup>2</sup> data density. Two prominent limitations of the approach remain: (1) objects smaller than 1 m<sup>3</sup> or less are classified as noise, and (2) only two-dimensional tagging information is applied in a three-dimensional context.

## Acknowledgments

Funding for collection of the data used in this project was provided by the European Commission through an FP7 ERC Consolidator grant [ERC StG 2012-307836-RETURN].

## References

- Aljumaily, H., D.F. Laefer, and D. Cuadra, 2015. Big-data approach for three-dimensional building extraction from aerial laser scanning, *Journal of Computing in Civil Engineering*, 30(3):04015049.
- Aljumaily, H., D.F. Laefer, and D. Cuadra, 2017. Urban point cloud mining based on density clustering and MapReduce, *Journal of Computing in Civil Engineering* 31(5):04017021.
- Altman, D.G., and J.M. Bland, 2005. Standard deviations and standard errors, *British Medical Journal*, 331:903.

- American Society for Photogrammetry and Remote Sensing (ASPRS) 2013. LAS Specification Version 1.4 – R13, URL: [http://www.asprs.org/a/society/committees/standards/LAS\\_1\\_4\\_r13.pdf](http://www.asprs.org/a/society/committees/standards/LAS_1_4_r13.pdf), ASPRS, Bethesda, M.D. (last date accessed: 19 October 2018).
- Athitsos, V.J. S. Alon S. Sclaroff, and G. Kollios, 2008. Boostmap: An embedding method for efficient nearest neighbor retrieval, *IEEE Transactions on Pattern Analysis and Machine Intelligence*, 30(1):89-104.
- Awrangjeb, M., C. Zhang, and C.S. Fraser, 2013. Automatic extraction of building roofs using LiDAR data and multispectral imagery, *ISPRS Journal of Photogrammetry and Remote Sensing*, 83:1–18.
- Azadbakht M., C.S. Fraser, and K. Khoshelham, 2016. Improved urban scene classification using full-waveform lidar, *Photogrammetric Engineering & Remote Sensing*, 82(12):973-980.
- Boyko, A., and T. Funkhouser, 2011. Extracting roads from dense point clouds in large scale urban environment, *ISPRS Journal of Photogrammetry and Remote Sensing*, 66(6):S2-S12.
- Carneiro, C., F. Golay, V. Silva, C. Plazanet, and J.J. Park, 2009. GIS and LiDAR data analysis for the integration of multidimensional indicators on urban morphogenesis multi-agent vector based geosimulation, *Geocomputation and Urban Planning* (G. Borruso, editor), Springer, Berlin Heidelberg, Germany, pp. 187-207.
- Cavan Local Authority Road Design Office, 2017. Guide to road design & road safety issues, URL: <http://www.cavancoco.ie/file/development-plans/county-cavan/old-documents/Appendices/Appendix%2025%20Road%20Desgin%20Guidelines.pdf>, Cavan Local Authority, Cavan, Ireland (last date accessed: 19 October 2018).
- Chen Y., and X. Zhu, 2013. An integrated GIS tool for automatic forest inventory estimates of Pinus radiata from LiDAR data, *GIScience & Remote Sensing*, 50(6):667-689.
- Choi, Y.W., Y.W. Jang, H.J. Lee, and G.S. Cho, 2008. Three-dimensional LiDAR data classifying to extract road point in urban area, *IEEE Geoscience and Remote Sensing Letters*, 5(4):725-729.
- CloudCompare, 2017. 3D point cloud and mesh processing software Open Source Project, Version 2.6, URL: <http://www.danielgm.net/cc> (last date accessed: 19 October 2018).
- Dean, J., and S. Ghemawat, 2008. MapReduce: Simplified data processing on large clusters, *Communications of the ACM*, 51(1):107-113.
- Dohan, D., B. Matejek, and T. Funkhouser, 2015. Learning hierarchical semantic segmentations of LiDAR data, *2015 International Conference on 3D Vision (3DV)*, 19-22 October 2015, Lyon, France (IEEE, New York, United States) pp. 273-281.
- Ester, M., H. P. Kriegel, J. Sander, and X. Xu, 1996. A density-based algorithm for discovering clusters in large spatial databases with noise, *KDD'96 Proceedings of the Second International Conference on Knowledge Discovery and Data Mining*, 02-04 August, Portland, Oregon, (AAAI Press, Palo Alto, California), pp. 226-231.
- Fischler, M.A., and R.C. Bolles, 1981. Random sample consensus: A paradigm for model fitting with applications to image analysis and automated cartography, *Communications of the ACM*, 24(6):381-395.
- Graham, L., 2009. Data management of LiDAR, *Topographic Laser Ranging and Scanning: Principles and Processing* (J. Shan and C.K. Toth, editors), CRC Press, Boca Raton, Florida, pp. 295-306.
- He, F., A. Habib, and A. Al-Rawabdeh, 2015. Planar constraints for an improved UAV-image-based dense point cloud generation, *The International Archives of Photogrammetry, Remote Sensing and Spatial Information Sciences*, 40(1):269.
- Hinks, T., H. Carr, and D.F. Laefer, 2009. Flight optimization algorithms for aerial LiDAR capture for urban infrastructure model generation, *Journal of Computing in Civil Engineering*, 23(6):330-339.
- Jochem, A., B. Höfle, V. Wichmann, M. Rutzinger, and A. Zipf, 2012. Area-wide roof plane segmentation in airborne LiDAR point clouds, *Computers Environment and Urban Systems*, 36:54-64.
- Khosravipour, A., A.K. Skidmore, M. Isenburg, T. Wang, and Y.A. Hussin, 2014. Generating pit-free canopy height models from airborne lidar, *Photogrammetric Engineering & Remote Sensing*, 80(9):863-872.
- Kim, E., and G. Medioni, 2011. Urban scene understanding from aerial and ground LiDAR data, *Machine Vision and Applications*, 22(4):691-703.
- Laefer D.F., C. O'Sullivan, H. Carr, L. Truong-Hong, 2013. Aerial laser scanning (ALS) data collected over an area of around 1 square km in Dublin city in 2007, URL: [https://doi.org/10.7925/drs1.ucdlib\\_30462](https://doi.org/10.7925/drs1.ucdlib_30462), UCD Digital Library, Dublin, Ireland (last date accessed: 19 October 2018).
- [dataset] Laefer, D.F., S. Abuwarda, A.-V. Vo, L. Truong-Hong, and H. Gharibi, 2017. 2015 Aerial Laser and Photogrammetry Survey of Dublin City Collection Record, URL: [https://geo.nyu.edu/catalog/nyu\\_2451\\_38684](https://geo.nyu.edu/catalog/nyu_2451_38684), NYU Spatial Data Repository, New York. (last date accessed: 19 October 2018), doi:10.17609/N8MQ0N
- Lee, J.H., G.S. Biging, and J.B. Fisher, 2016. An Individual tree-based automated registration of aerial images to lidar data in a forested area, *Photogrammetric Engineering & Remote Sensing*, 82(9):699-710.
- Lee, D.H., K.M. Lee, and S.U. Lee, 2008. Fusion of lidar and imagery for reliable building extraction, *Photogrammetric Engineering & Remote Sensing*, 74(2):215-225.
- Maurya, R., P.R. Gupta, A.S. Shukla, and M.K. Sharma, 2012. Building extraction from very high resolution multispectral images using NDVI based segmentation and morphological operators, *Proceedings of the International Conference on Advances in Engineering, Science and Management (ICAESM)*, 30-31 March, Nagapattinam, India (IEEE, New York), pp. 577-581.
- Mosa, A.S.M., B. Schön, M. Bertolotto, and D.F. Laefer, 2012. Evaluating the benefits of octree-based indexing for lidar data, *Photogrammetric Engineering & Remote Sensing*, 78(9):927-934.
- OpenStreetMap, 2016. OpenStreetMap Wiki, URL: [http://wiki.openstreetmap.org/wiki/Main\\_Page](http://wiki.openstreetmap.org/wiki/Main_Page), Openstreetmap Foundation, Sutton Coldfield, U.K. (last date accessed: 19 October, 2018).
- OpenTopography, 2017. High-Resolution Topography Data and Tools, URL: <http://www.opentopography.org/blog/tools-lidar-point-cloud-filtering-classification>, OpenTopography, San Diego, C.A. (last date accessed: 19 October 2018).
- Ordnance Survey of Ireland, 1996. *The Irish Grid: A Description of the Co-ordinate Reference System used in Ireland*, URL: <https://www.osi.ie/wp-content/uploads/2015/04/The-Irish-Grid-A-Description-of-the-Coordinate-Reference-System-Used-in-Ireland.pdf>, Ordnance Survey Ireland, Dublin, Ireland (last date accessed: 19 October 2018).
- Pollefeys, M., and L.V. Gool, 2002. From images to 3D models, *Communications of the ACM*, 45(7):50-55.
- Rusinkiewicz, S., and M. Levoy 2001. Efficient variants of the ICP algorithm, *Proceedings, Third International Conference on 3-D Digital Imaging and Modeling*, 28 May-01 June 2001, Quebec City, Canada (IEEE, New York), pp. 145-152.
- Slatton K.C., and W.E. Carter, 2008. A Primer for airborne lidar, URL: <http://ncalm.cive.uh.edu/sites/ncalm.cive.uh.edu/files/files/publications/reports/LidarPrimer-Final02.pdf>, The National Center for Airborne Laser Mapping (NCALM), University of Florida, Gainesville, Florida (last date accessed: 19 October 2018).
- Truong-Hong, L., and D.F. Laefer 2015. Quantitative evaluation strategies for urban 3D model generation from remote sensing data, *Computers and Graphics*, 49:82-91. doi:10.1016/j.cag.2015.03.001
- Vo, A.-V., N. Konda, N. Chauhan, H. Aljumaily, and D.F. Laefer 2018. Lessons learned with laser scanning point cloud management in Hadoop HBase, *Proceedings of the 25<sup>th</sup> International Workshop on Intelligent Computing in Engineering* (pp. 231-253), Springer, Cham.
- Wang, J., and J. Shan, 2009. Segmentation of lidar point clouds for building extraction, *Proceedings of the American Society for Photogrammetry and Remote Sensing Annual Conference*, 09-13 March, 2009, Baltimore, Maryland (American Society for Photogrammetry and Remote Sensing, Bethesda, Maryland), pp. 9-13.

- Wu, X.R., H. Carceroni, H. Fang, S. Zelinka, and A. Kirmse, 2007. Automatic alignment of large-scale aerial rasters to road-maps, *Proceedings of the 15<sup>th</sup> Annual ACM international Symposium on Advances in Geographic Information Systems*, 07-09 November, Seattle, Washington (ACM, New York), Article No. 17, doi:10.1145/1341012.1341035
- Xu, D., and Y. Tian, 2015. A comprehensive survey of clustering algorithms, *Annals of Data Science*, 2(2):165-193.
- Xu, S., G. Vosselman, and S.O. Elberink, 2014. Multiple-entity based classification of airborne laser scanning data in urban areas, *ISPRS Journal of Photogrammetry and Remote Sensing*, 88:1-15.
- Xu, G., W. Yu, Z. Chen, H. Zhang, P. Moulema, X. Fu, and C. Lu, 2015. A cloud computing based system for cyber security management, *International Journal of Parallel, Emergent and Distributed Systems*, 30(1):29-45.
- Yang, B., R. Huang, Z. Dong, Y. Zang, and J. Li, 2016. Two-step adaptive extraction method for ground points and breaklines from lidar point clouds, *ISPRS Journal of Photogrammetry and Remote Sensing*, 119:373-389.
- Yenigün, D., G. Ertan, and M. Siciliano, 2017. Omission and commission errors in network cognition and network estimation using ROC curve, *Social Networks*, 50:26-34.
- Yu, F., J. Xiao, and T. Funkhouser, 2015. Semantic alignment of LiDAR data at city scale, *Proceedings of the IEEE Conference on Computer Vision and Pattern Recognition*, 08-12 June 2015, Boston, Massachusetts (IEEE, New York), pp. 1722-1731.

# Assessment of Different Vegetation Parameters for Parameterizing the Coupled Water Cloud Model and Advanced Integral Equation Model for Soil Moisture Retrieval Using Time Series Sentinel-1A Data

Long Wang, Binbin He, Xiaojing Bai, and Minfeng Xing

## Abstract

Soil moisture is an important state variable of the land surface ecosystem. In this paper, the water cloud model (WCM) and advanced integral equation model (AIEM) are coupled to retrieve soil moisture using time series Sentinel-1A data and moderate resolution imaging spectroradiometer (MODIS) data. Normalized difference vegetation index (NDVI), enhanced vegetation index (EVI), leaf area index (LAI) and fraction of photosynthetically active radiation (FPAR), are cross-combined to initialize the calibrated model. The calibration results show the following: (1) Vegetation parameters have a great influence on model calibration; and (2) The combination of (NDVI, LAI) is recommended to calibrate the coupled model, the RMSE,  $R^2$  is 0.739 dB, and 0.716 for the observed and estimated backscattering coefficients. The soil moisture inversion results show that: (1) the accuracy of model calibration and soil moisture inversion are inconsistent; and (2) The normalized vegetation parameters, such as NDVI, EVI and FPAR, are suitable for WCM to describe vegetation characteristics, and NDVI is the optimum. When V2 is the NDVI, the average bias, MAE, RMSE, ubRMSE and  $R^2$  are  $-0.007 \text{ m}^3/\text{m}^3$ ,  $0.074 \text{ m}^3/\text{m}^3$ ,  $0.087 \text{ m}^3/\text{m}^3$ ,  $0.087 \text{ m}^3/\text{m}^3$  and 0.750, respectively.

## Introduction

Soil moisture is an important component of the water cycle and energy exchange in the global terrestrial ecosystem and is considered one of the core climate variables by the global climate observing system (Kornelsen *et al.*, 2013). The spatio-temporal distribution of soil moisture over the regional and global scales helps us to understand the process of the global water cycle and energy balance. Remote sensing provides an effective method for monitoring soil moisture at different spatial and temporal scales. Visible remote sensing uses the surface emission characteristics to estimate soil moisture, while thermal infrared remote sensing utilizes the soil surface temperature. They both have high spatial resolution and multiple available satellite data. However, the optical signal is weakly related to soil moisture and can only obtain the soil information at approximately 1 mm. In densely vegetated

areas, optical remote sensing can hardly detect soil information. In contrast, microwave remote sensing, considering its all-time and all-weather work capability and high sensitivity to soil moisture, has been widely used for soil moisture monitoring. In particular, the active microwave remote sensing represented by synthetic aperture radar (SAR) with its high spatial resolution provides an unparalleled advantage for monitoring soil moisture at finer scales (Aubert *et al.*, 2013; Baghdadi *et al.*, 2012; Bai *et al.*, 2015, 2016, and 2017; Dong *et al.*, 2013; El Hajj *et al.*, 2017;).

In recent years, spaceborne SAR has continuously shifted from low-resolution, single-band, single polarization, fixed incidence angle, and single operation mode to high-resolution, multiband, multi-polarization, multi-angle, and multi-operation modes. In addition, the spatial and temporal resolution and scanning width of the satellite systems have been greatly improved, which provides a possibility for obtaining fine-scale soil moisture over large regions. Currently, satellites equipped with SAR include L-band ALOS-2, C-band Radar-sat-2 and Sentinel-1A/B, and X-band TerraSAR-X, TanDEM-X, TecSAR, RISAT-1/2, and SeoSAR. From the perspective of science, these SARs provide detailed observations of the surface parameters such as vegetation cover and soil moisture. With the research and practical application of satellite constellations, the spaceborne SAR is gradually being transformed into an SAR satellite constellation with higher temporal resolution and continuous coverage over large areas, which will provide high-quality radar data for soil moisture monitoring (Breit *et al.*, 2010; Das *et al.*, 2015; Gherboudj *et al.*, 2011; Krieger *et al.*, 2007; Malenovský *et al.*, 2012; Rosenqvist *et al.*, 2014;). The Sentinel-1, consisting of the Sentinel-1A and Sentinel-1B satellites, has a short revisit cycle, which can obtain repeated observations of the target surface over six days. This is very important in seasons of vegetation growth and dynamically changing soil moisture. Since October 2014, the Sentinel-1 data has been accessible and freely downloadable by global users. Compared with other satellite data, the high spatial and temporal resolution, radiation stability, and coverage of the Sentinel-1 data provide favorable opportunities for the long-term monitoring of high spatial resolution soil moisture (Baghdadi *et al.*, 2018; Bai *et al.*, 2017; Gao *et al.*, 2017; El Hajj *et al.*, 2017; Pulvirenti *et al.*, 2018).

Long Wang, Binbin He, and Minfeng Xing are with the School of Resources and Environment, University of Electronic Science and Technology of China, Sichuan 611731, China (binbinhe@uestc.edu.cn).

Xiaojing Bai is with the School of Hydrology and Water Resources, Nanjing University of Information Science & Technology, Jiangsu 210044, China.

Photogrammetric Engineering & Remote Sensing  
Vol. 85, No. 1, January 2019, pp. 43–54.  
0099-1112/18/43–54

© 2019 American Society for Photogrammetry  
and Remote Sensing  
doi: 10.14358/PERS.85.1.43

Over the past few decades, soil moisture retrieval using SAR data has achieved great success in bare and sparsely vegetated areas. Researchers have proposed several models to describe the scattering process of bare soil surfaces, such as the Oh (Oh *et al.*, 1992, 1994, 2002, and 2004) model, the Dubois (Dubois *et al.*, 1995) model, the Shi (Shi *et al.*, 1995) model, the Baghdadi model (Baghdadi *et al.*, 2016), the integral equation model (IEM), and the advanced IEM (AIEM) (Chen *et al.*, 2003; Fung, 1994; Fung *et al.*, 1992; Wu *et al.*, 2001). Within these models, the challenge of soil moisture retrieval is how to parameterize the surface roughness parameter. Several methods have been proposed to weaken the effect of surface roughness, such as the combined roughness parameter (a new surface roughness parameter combined  $s$  and  $l$ , Kong *et al.*, 2016; Oh *et al.*, 2002), the calibrated roughness parameters and effective roughness parameters (surface roughness parameters are calibrated by repeated observation of different phase SAR data, assuming that the surface roughness parameters remain constant for a short period or their change is smaller than the soil moisture. Baghdadi *et al.*, 2002, and 2004; Bai *et al.*, 2016; Su *et al.*, 1997), and the eliminated roughness parameters (the surface roughness parameter retrieved by a physical algorithm and SAR data, Dubois *et al.*, 1995; Kseneman *et al.*, 2013; Zhou *et al.*, 2007) using multi-configuration SAR data. The feasibility of these methods has been proven in previous studies (Bai *et al.*, 2015, 2016, and 2017; Beckann *et al.*, 1987; Fung *et al.*, 2010; Rahman *et al.*, 2008; Sancer *et al.*, 1969; Yu *et al.*, 2010), and the effective roughness method is considered a good method for solving the roughness parameters (Bai *et al.*, 2016). In the vegetated area, the scattering contribution from vegetation may exceed the soil surface (Baghdadi *et al.*, 2017). Parameterizing the scattering contribution of the vegetation has become a major problem in soil moisture retrieval (Bai *et al.*, 2017; Prevot *et al.*, 1993). Because of concerns about vegetation characteristics, some vegetation backscattering models have been established to describe the contribution of vegetation. The most widely used vegetation scattering models mainly include the ratio method, the water cloud model (WCM) (Attema *et al.*, 1978), the Michigan microwave canopy scattering model (MIMICS) (Ulaby *et al.*, 1990), and the Tor Vergata model (Bracaglia *et al.*, 1995; Ferrazzoli *et al.*, 1996; Joseph *et al.*, 2010; Saatchi *et al.*, 2000). These vegetation backscattering models are often coupled with a bare soil backscattering model to estimate the soil moisture in the vegetation area (Baghdadi *et al.*, 2016, 2017; Bao, 2007; El Hajj *et al.*, 2016 and 2017). For example, the WCM and AIEM are generally coupled to estimate soil moisture because of their effectiveness and conciseness compared with other models (Joseph *et al.*, 2010; He *et al.*, 2014; Lievens *et al.*, 2013; Wang *et al.*, 2011).

However, the contentious issue in the coupled WCM and AIEM is quantifying the vegetation characteristics and determining which vegetation parameter is more suitable for describing the scattering and attenuation of vegetation (Quan *et al.*, 2015 and 2017). Currently, different vegetation indexes, such as the vegetation water content (VWC), leaf area index (LAI), normalized difference vegetation index (NDVI), enhanced vegetation index (EVI), leaf water area index (LWAI), and fraction of photosynthetically active radiation (FPAR), have been used to parameterize the vegetation variable in the WCM (Bai *et al.*, 2015 and 2017; Bajhdadi, 2016, 2017; El Hajj *et al.*, 2016). Generally, the scattering and attenuation indicators are assumed to be uniform. These vegetation parameters can be estimated from optical remote sensing data. In fact, there is no general agreement on the precise setup of the vegetation descriptor in the process of soil retrieval (Lievens, 2013). Selecting the vegetation parameters used as scattering and attenuation indicators is still a problem for modeling the

backscatter and retrieving soil moisture. It is necessary to evaluate the capability of the above vegetation parameters for soil moisture retrieval.

In this paper, we aim to explore the performance of four vegetation parameter combinations, including NDVI, EVI, LAI, and FPAR, for parameterizing the scattering contribution of vegetation in the coupled model of WCM and AIEM. The implementation of this approach can be divided into five steps: (1) The surface roughness parameters required in the AIEM are parameterized using the effective roughness parameter; (2) The vegetation parameter required in the WCM is parameterized by the different combinations of NDVI, EVI, LAI and FPAR; (3) The coupled model is calibrated by minimizing the root-mean-square error (RMSE) between the observed and the simulated backscattering coefficients; (4) The soil moisture is retrieved using a look-up table (LUT) method calculated by the calibrated model; and (5) The retrieval accuracy is computed by comparing the retrieved and *in situ* soil moisture. The structure of this paper is organized as follows. The next Section introduces the study area, *in situ* soil moisture measurements, the Sentinel-1A data, and the moderate resolution imaging spectroradiometer (MODIS) data. Next the introduction of the WCM, the AIEM, and the method used for model calibration and soil moisture retrieval; followed by the calibrated results of the coupled model and the inversion results of soil moisture. The discussion is addressed, which consists of an impact analysis on the surface roughness parameters and on the vegetation parameter combinations for soil moisture retrieval accuracy, with conclusions are summarized in the final Section.

## Materials

### Study Area and *In Situ* Measurements

The study area is located in northern Iowa, in the Central Plains of the United States (Figure 1). The climate belongs to the temperate continental climate with cold winters and hot summers, and the daily and annual temperature difference is relatively large. The average annual rainfall and snowfall are 711 mm and 760 mm and are mainly concentrated in summer and winter, respectively. The dominant vegetation cover type is grassland, whose growth period is consistent with the rainy season.

The Shagbark Hills ground monitoring station (Schaefer *et al.*, 2010) is sited within the study area (42.50° N, 95.75° W) and is one of the monitoring stations of the Soil Climate Analysis Network (SCAN). The SCAN supports natural resource assessment and conservation activities through its network of automated climate monitoring and data collection sites. The elevation is approximately 427 m, and the topography is relatively flat. This monitoring station contains five components to monitor the local ecological and environmental indicators, including the wind speed and direction sensor, liquid precipitation gauge, solar radiation sensor, relative humidity and air temperature sensor and soil moisture and temperature sensors. The soil moisture is measured by a dielectric constant measuring device, and the soil temperature is measured by an encapsulated thermistor. The precipitation is measured by a tipping bucket gauge, and the air temperature is measured by a shielded thermistor. The precipitation, air temperature, soil moisture with five different soil depths (5 cm, 10 cm, 20 cm, 50 cm and 100 cm), and soil temperature were downloaded from the International Soil Moisture Network (ISMN) (<http://ismn.geo.tuwien.ac.at>), and the data were calibrated. Considering the penetrability of microwave signals, the soil moisture data at 5 cm depth were used to validate the soil moisture inversion method. Figure 2 displays the soil moisture data at 5 cm and the precipitation in 2015 and 2016.

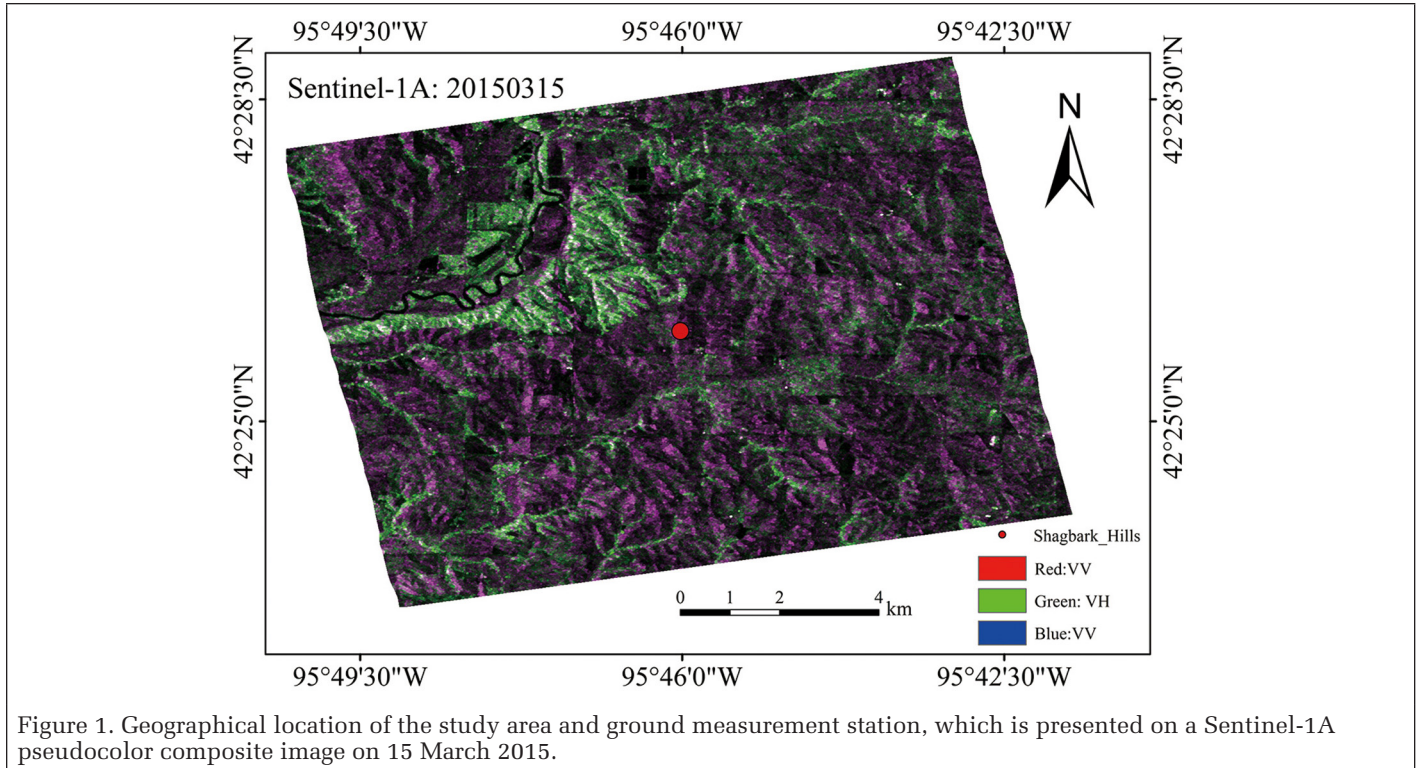


Figure 1. Geographical location of the study area and ground measurement station, which is presented on a Sentinel-1A pseudocolor composite image on 15 March 2015.

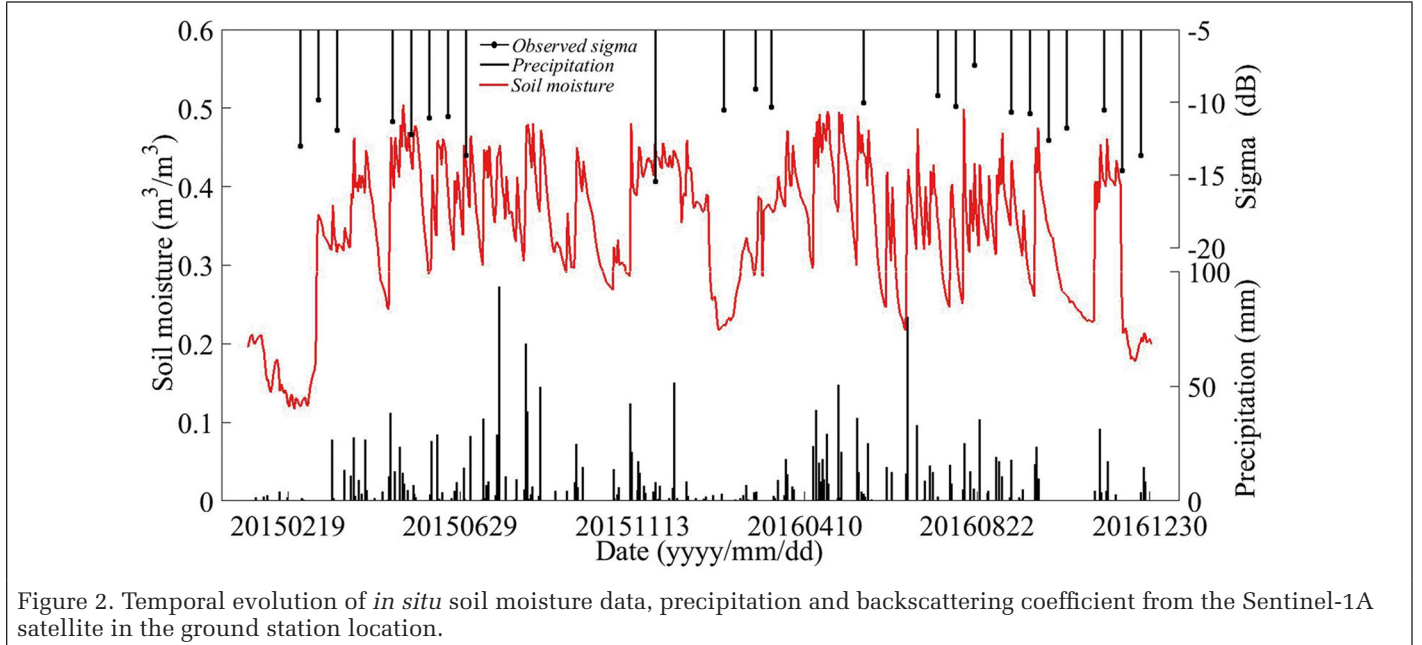


Figure 2. Temporal evolution of *in situ* soil moisture data, precipitation and backscattering coefficient from the Sentinel-1A satellite in the ground station location.

### Sentinel-1A Data

The Sentinel-1A satellite is the first satellite of the ESA's Copernicus plan, which was launched on 03 April 2014 (Schubert., 2015). It is equipped with a C-band (5.405 GHz) SAR sensor, which can be operated in four imaging modes including stripmap, interferometric wide swath (IW), extra wide swath, and wave mode with different polarization combination modes including single polarization VV or HH, and dual polarization VH or HV. The revisit period is 12 days when ascending, and descending data are included (Sentinel-1A Handbook;

<https://sentinel.esa.int/web/sentinel/user-guides/sentinel-1-sar>).

In this paper, considering the uniformity of data and the insufficient number of ascending data, the Level-1 ground range detected (GRD) Sentinel -1A data with the IW and VV polarization from 01 January 2015, to 01 January 2017, were used, and only the descending data from 31 May 2015, to 27 December 2016, were selected. The number of selected data was 23 scenes, which consisted of 8 scenes in 2015 and 15 scenes in 2016. The dataset from 2015 was used for model calibration, and the remaining data were used to retrieve the soil moisture. The details of the acquired Sentinel-1A data are shown in Table 1.

The preprocessing of the Sentinel-1A data was conducted by SNAP software (<http://step.esa.int/main/toolboxes/snap/>), which includes radiometric correction, speckle noise filtering

Table 1. The details of the Sentinel-1A data

No.	Date	UTC time	Incidence angle (°)
1	2015/05/31	00:21:41-00:22:06	30.519-45.893
2	2015/06/12	00:21:42-00:22:07	30.520-46.087
3	2015/06/24	00:21:43-00:22:08	30.518-46.086
4	2016/07/30	00:21:44-00:22:09	30.521-45.895
5	2015/08/11	00:21:45-00:22:10	30.519-46.086
6	2015/08/23	00:21:45-00:22:10	30.521-45.864
7	2015/09/04	00:21:43-00:22:08	30.507-46.102
8	2015/09/16	00:21:46-00:22:11	30.520-45.999
9	2016/01/26	00:21:38-00:22:03	30.522-45.968
10	2016/03/26	00:21:36-00:22:01	30.516-46.104
11	2016/04/19	00:21:29-00:21:53	30.505-45.899
12	2016/05/01	00:21:43-00:22:10	30.506-45.884
13	2016/06/30	00:21:49-00:22:14	30.501-46.076
14	2016/08/17	00:21:52-00:22:17	30.502-46.288
15	2016/08/29	00:21:52-00:22:17	30.501-46.076
16	2016/09/10	00:21:53-00:22:18	30.499-46.075
17	2016/10/04	00:21:40-00:22:04	30.496-45.893
18	2016/10/16	00:21:40-00:22:04	30.494-45.892
19	2016/10/28	00:21:40-00:22:04	30.492-45.891
20	2016/11/09	00:21:40-00:22:04	30.491-45.890
21	2016/12/03	00:21:39-00:22:04	30.489-45.889
22	2016/12/15	00:21:39-00:22:03	30.490-45.889
23	2016/12/27	00:21:38-00:22:03	30.489-45.889

(refined Lee filter (Lee, *et al.*, 1999)), geometric correction with Range-Doppler terrain correction, projection transformation, and resampling (from 10 m to 1 km to match the spatial resolution of MODIS data). Figure 2 presents the extracted backscattering coefficients.

### MODIS Data

In this study, we aim to compare the effects of NDVI, EVI, LAI, and FPAR these four vegetation parameters on soil moisture inversion. Only MODIS provides these four data product directly and its quality was approved by most researchers, so we choose MODIS data to describe the vegetation character.

MODIS is an important sensor for the observation of global biological and physical processes in the US earth observing system program and is conducted on the satellites of Terra and Aqua (Huete *et al.*, 2002). In this paper, the 16-day synthetic NDVI and EVI products with a spatial resolution of 1000 m and 8-day synthetic LAI and FPAR products with a spatial resolution of 500 m were used to describe the vegetation characteristics of the grassland. The LAI and FPAR products were first resampled to 1 km to match the Sentinel-1A data, which corresponds to the spatial resolution of NDVI and EVI. To eliminate the influence of clouds, the Savitzky-Golay smooth filter (Savitzky *et al.*, 1964) was applied to smooth the original MODIS data. To resolve the values on the Sentinel-1A date, a cubic spline interpolation method was used to interpolate the smoothed MODIS data. The original and interpolated MODIS data are shown in Figure 3.

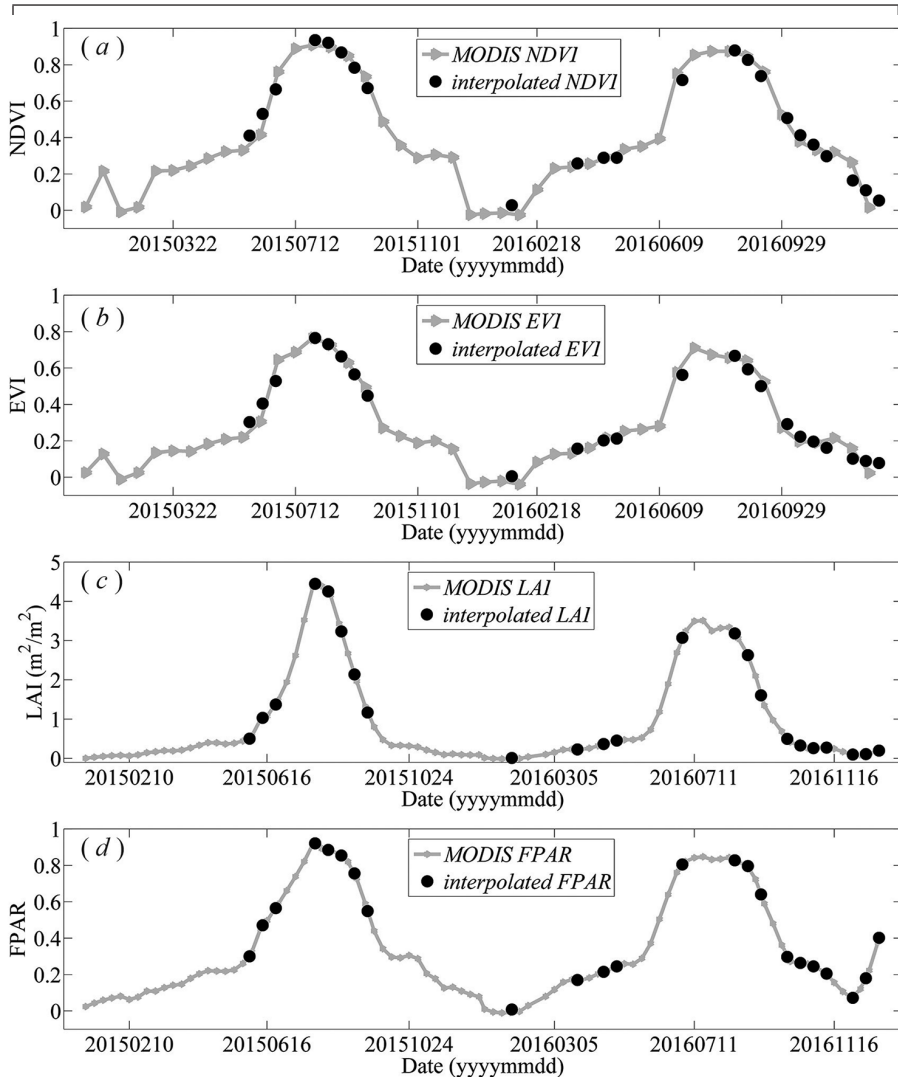


Figure 3. The original and the interpolated MODIS data: (a) NDVI, (b) LAI, (c) EVI, and (d) FPAR

a cubic spline interpolation method was used to interpolate the smoothed MODIS data. The original and interpolated MODIS data are shown in Figure 3.

### Methodology

In this paper, the AIEM and WCM are coupled to model the backscatter and then used for soil moisture retrieval. The roughness parameters required by the AIEM are parameterized by the effective roughness parameters, which have been widely used for soil moisture retrieval. In WCM, the scattering and attenuation indicators are characterized by different combinations of four vegetation parameters, including NDVI, EVI, LAI, and FPAR. The flowchart for the model calibration and soil moisture retrieval is shown in Figure 4. The detailed descriptions are introduced in the following sections.

### Bare Soil Backscattering Modeling

The backscatter of the bare surface is modeled by the AIEM, which is established based on the electromagnetic radiative transfer equation (Fung *et al.*, 1994; Shi *et al.*, 1995). This model can simulate the backscattering coefficient over a wide range of soil moisture and surface roughness, which has been widely used in the simulation of microwave surface scattering (Bai *et al.*, 2016; Fung *et al.*, 1994; Shi *et al.*, 1995). The formulation of AIEM can be conceptually expressed as

$$\sigma_{soil}^o = AIEM(\epsilon, s, l, ACF, f, \theta, pp) \quad (1)$$

where  $\epsilon$  is the soil dielectric constant,  $s$  is the root mean square (RMS) height,  $l$  is the correlation length, ACF is the autocorrelation function,  $f$  is the frequency of the Sentinel-1A satellite (5.405 GHz),  $\theta$  is the incidence angle of the Sentinel-1A data, and  $pp$  is the polarization mode (vv).

The Dobson dielectric mixing model was used to convert soil moisture to a soil dielectric constant (Dobson et al., 1985). The topsoil texture parameters required by this model were obtained from the Harmonized World Soil Database (HWSD), which was built by the Food Agriculture Organization (FAO) and International Institute for Applied Systems Analysis (IIASA); <http://web.archive.iiasa.ac.at/>). The topsoil texture parameters in the Shagbark Hills ground monitoring station are 23% clay, 39% sand, 38% silt, and 1.33 g/cm<sup>3</sup> soil density. Because the topography around the ground station is relatively flat, the exponential ACF, which is most widely used for smooth surfaces, was adopted in AIEM. (Su et al., 1997). The  $s$  and  $l$  were parameterized based on the effective roughness parameters, which means assuming that the surface roughness parameters remain constant for a short period or that their change is smaller than the soil moisture. Additionally, we used the effective parameters selected from the process of model calibration with the dataset from 2015 using a cost function as a calibrated parameter to retrieve the soil moisture with the dataset from 2016 (Baghdadi et al., 2002 and 2004; Bai et al., 2016; Su et al., 1997). In this study, only the single scattering was considered in the AIEM. Therefore, for the C-band Sentinel-1A satellite, the effective range of  $s$  for AIEM required  $ks < 3.0$ , with  $k$  being the wavenumber of radar signal  $k = 1.11 \text{ cm}^{-1}$ . This means that  $s$  should be less than 30 mm (Baghdadi et al., 2006; Bai et al., 2016 and 2017; Lievens et al., 2010;). There is no theoretical constraint for the values of  $l$ , and we chose a relatively large range, which has been used in previous work (Bai et al., 2016; Lievens et al., 2010). Therefore, the LUT is constrained within [0.1, 3.0] cm and [1.0, 70.0] cm, respectively, for the effective roughness parameters ( $s$  and  $l$ ) that will be selected within the constrained ranges.

### Vegetation Backscattering Modeling

The WCM is a semiempirical vegetation scattering model. Its relative simplicity makes it a good candidate for soil moisture retrieval. This model divides the total radar backscattering coefficient  $\sigma_{can}^o$  into three parts: the direct scattering contributions of vegetation  $\sigma_{veg}^o$ , the double-bounce scattering components between the vegetation and soil surface  $\sigma_{veg+soil}^o$ , and the direct soil backscattering  $\sigma_{soil}^o$  attenuated by the vegetation layer (Bai et al., 2016). The formulations are written as:

$$\sigma_{can}^o = \sigma_{veg}^o + \sigma_{veg+soil}^o + \tau^2 \sigma_{soil}^o \quad (2)$$

$$\sigma_{veg}^o = AV_1 \cos\theta(1 - \tau^2) \quad (3)$$

$$\tau^2 = \exp(-2BV_2 / \cos\theta) \quad (4)$$

where  $\tau^2$  represents the two-way attenuation of the vegetation layer,  $V_1$  stands for the scattering of the vegetation,  $V_2$  stands for the attenuation of the vegetation,  $\theta$  is the radar incidence angle, and  $A$  and  $B$  are empirical coefficients.

In general, the double-bounce scattering components between the vegetation and soil surface  $\sigma_{veg+soil}^o$  is neglected because of its influence on the total radar backscattering

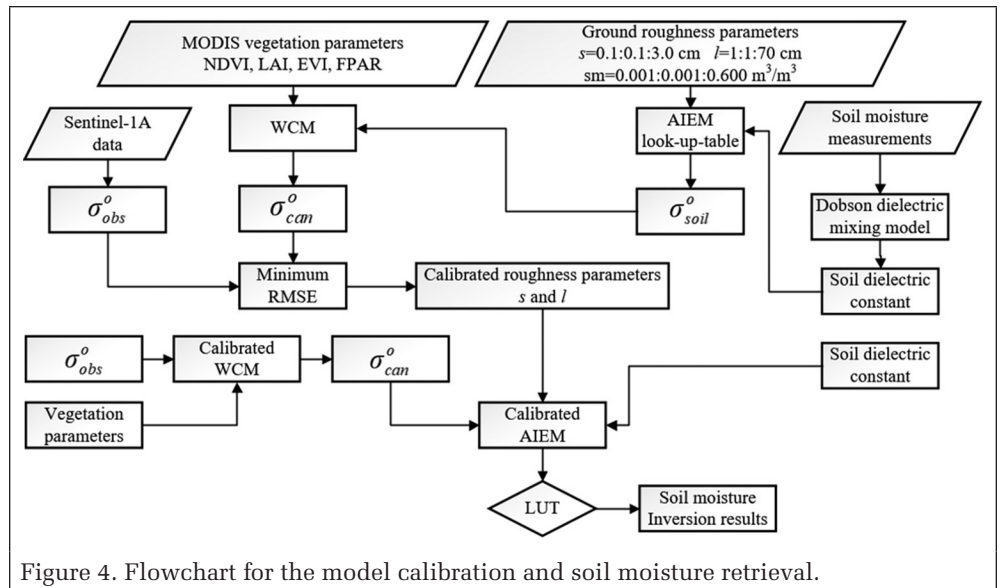


Figure 4. Flowchart for the model calibration and soil moisture retrieval.

coefficient is relatively small compared with the other two parts (Bai et al., 2015 and 2016). Thus, the WCM can be written as follows:

$$\sigma_{\theta_{ref}}^o = \sigma_{\theta}^o \frac{\cos^2 \theta_{ref}}{\cos^2 \theta} \quad (5)$$

The empirical coefficients  $A$  and  $B$  can be optimized by the least squares method.  $V_1$  and  $V_2$  are parameterized by NDVI, EVI, LAI, and FPAR. The backscatter of the soil surface  $\sigma_{soil}^o$  is simulated from the AIEM.

### Model Calibration and Soil Moisture Retrieval

Model calibration is very important for high-precision inversion of soil moisture, which determines  $A$  and  $B$  in WCM and the effective roughness parameters  $s$  and  $l$  in AIEM. The model calibration and soil moisture estimation procedures are given as follows:

**Step 1:** Normalization of the radar backscattering coefficient. To eliminate the influence of the local incidence angle on soil moisture retrieval accuracy, the theoretical method proposed by Ulaby et al. (1986) was used to normalize the vv-polarized backscattering coefficients.

$$\sigma_{\theta_{ref}}^o = \sigma_{\theta}^o \frac{\cos^2 \theta_{ref}}{\cos^2 \theta} \quad (6)$$

where  $\theta_{ref}$  is the reference angle,  $\theta$  is the incidence angle of the Sentinel-1A data, and  $\sigma_{\theta_{ref}}^o$  and  $\sigma_{\theta}^o$  are the backscattering coefficients at corresponding angles. The reference angle is chosen as the center angle of the acquired Sentinel-1A data (41°).

**Step 2:** Simulation of bare soil backscattering coefficient. The AIEM was used to simulate the bare soil backscatter, while the Dobson dielectric mixing model was adopted to compute the soil dielectric constant using *in situ* soil moisture measurements and soil texture parameters. The  $s$  ranges from 0.1 to 3.0 cm with an interval of 0.1 cm, the  $l$  ranges from 1 to 70 cm with an interval of 1 cm, and the soil moisture range from 0.001 to 0.600 m<sup>3</sup>/m<sup>3</sup> with an interval of 0.001 m<sup>3</sup>/m<sup>3</sup> to match the *in situ* soil moisture data.

**Step 3:** Estimation of vegetation backscatter. The WCM was used to compute the total radar backscattering coefficients,  $\sigma_{can}^o$  and  $\sigma_{soil}^o$  were obtained from Step 2, and  $V_1$  and  $V_2$  are parameterized by different combinations of NDVI, EVI, LAI, and FPAR.

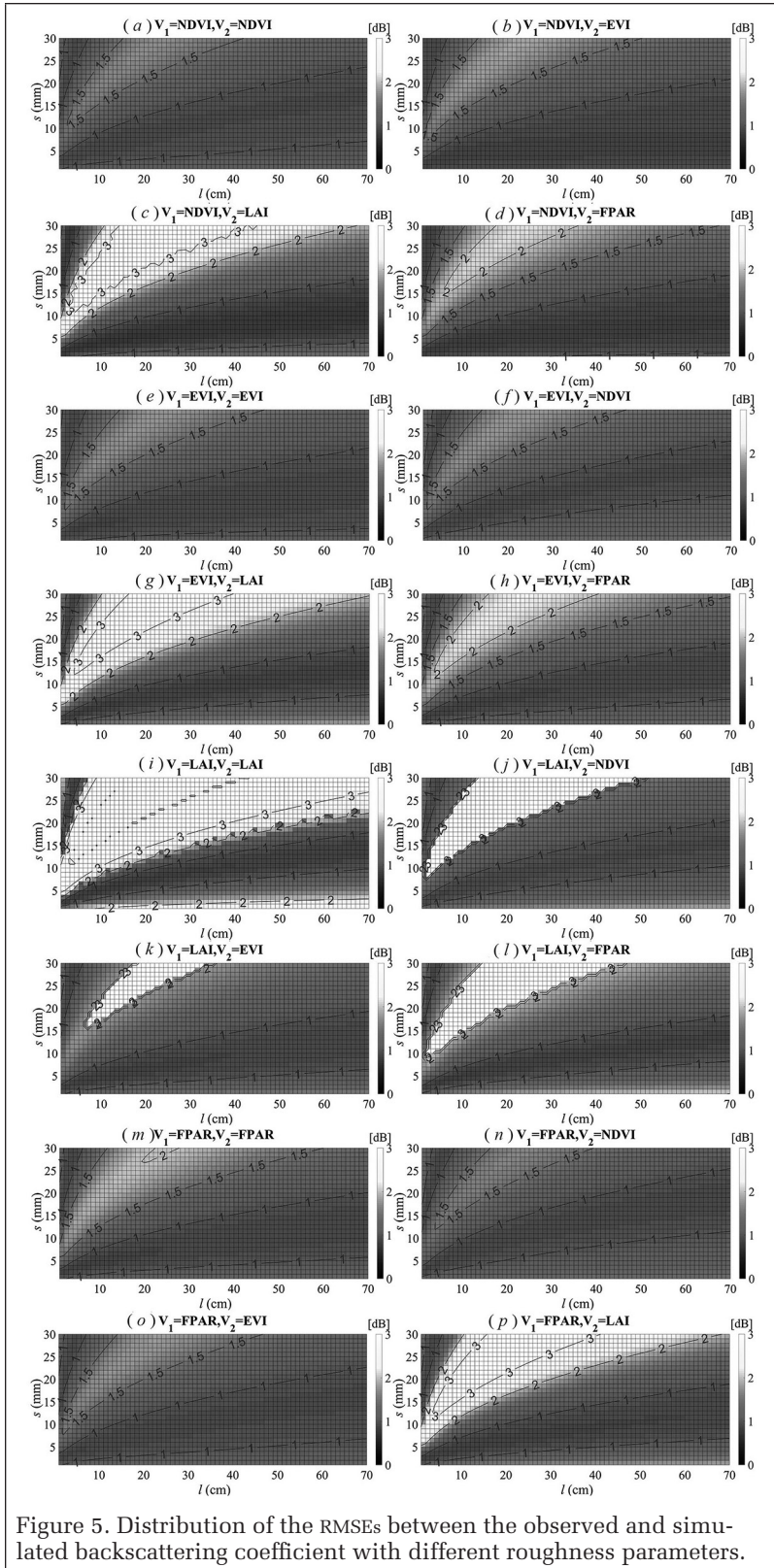


Figure 5. Distribution of the RMSEs between the observed and simulated backscattering coefficient with different roughness parameters.

**Step 4:** Selection of the effective roughness parameters ( $s$  and  $l$ ) and optimization of  $A$  and  $B$ . The effective roughness parameters were selected by the principle of least-cost function, which is constructed using the root-mean-square error (RMSE), as shown in Equation 7. The RMSE is calculated by the estimated and the observed backscattering coefficients ( $\sigma_{est}^o$  and  $\sigma_{obs}^o$ ). With the effective roughness parameters, the

Table 2. Model coefficients and selected effective roughness parameters with different vegetation parameter combinations using the data from 2015.

Vegetation Parameter		Model Coefficients		Effective Roughness Parameters		RMSE	$R^2$
$V_1$	$V_2$	A	B	$s$ (cm)	$l$ (cm)		
NDVI	NDVI	-5.689	0.024	0.4	5	0.893	0.473
NDVI	EVI	-11.999	0.418	0.4	12	0.861	0.668
NDVI	LAI	-16.275	0.229	0.4	12	0.739	0.717
NDVI	FPAR	-13.237	0.425	0.4	13	0.810	0.708
EVI	EVI	-12.573	0.171	0.4	7	0.879	0.567
EVI	NDVI	-1.250	0.018	0.4	5	0.893	0.458
EVI	LAI	-19.464	0.121	0.4	8	0.830	0.574
EVI	FPAR	-13.802	0.157	0.4	7	0.857	0.586
LAI	LAI	-3.114	0.058	0.4	7	0.798	0.602
LAI	NDVI	-1.628	0.063	0.4	6	0.887	0.570
LAI	EVI	-1.931	0.174	0.4	8	0.850	0.684
LAI	FPAR	-2.105	0.152	0.4	8	0.830	0.618
FPAR	FPAR	-10.615	0.178	0.4	7	0.866	0.582
FPAR	NDVI	-12.682	-0.049	0.4	4	0.886	0.425
FPAR	EVI	-2.542	0.026	0.4	5	0.888	0.462
FPAR	LAI	-15.717	0.117	0.4	8	0.848	0.640

empirical coefficients also can be calculated by the least squares method:

$$RMSE = \sqrt{\frac{1}{n} \sum (\sigma_{est}^o - \sigma_{obs}^o)^2}. \quad (7)$$

**Step 5:** Soil moisture inversion. Based on the calibrated model and the Sentinel-1A observations, the estimated soil moisture was estimated using a look-up table (LUT) method. The statistical metrics including bias, mean absolute error (MAE), RMSE, unbiased RMSE (ubRMSE) (Entekhabi *et al.*, 2010), and correction coefficient square ( $R^2$ ) were chosen to evaluate the accuracy of soil moisture retrieval.

$$bias = \frac{1}{n} (\sum \mu_{obs} - \sum \mu_{est}) \quad (8)$$

$$MAE = \frac{1}{n} \sum |\mu_{obs} - \mu_{est}| \quad (9)$$

$$RMSE = \sqrt{\frac{1}{n} \sum (\mu_{est} - \mu_{obs})^2} \quad (10)$$

$$ubRMSE = \sqrt{RMSE^2 - bias^2} \quad (11)$$

$$R^2 = \left( \frac{\sum (\mu_{est} - \bar{\mu}_{est})(\mu_{obs} - \bar{\mu}_{obs})}{\sqrt{(\sum (\mu_{est} - \bar{\mu}_{est})^2) (\sum (\mu_{obs} - \bar{\mu}_{obs})^2)}} \right)^2 \quad (12)$$

where  $\mu_{obs}$  and  $\mu_{est}$  are the observed and estimated backscattering coefficient or soil moisture, respectively.

The observed data from 2015 was used to calibrate the coupled model, and the data from 2016 were adopted for the soil moisture estimation. The coupled model calibration and soil moisture inversion results are analyzed in the next section. The impact of different roughness parameters and

vegetation parameter combinations on the accuracy of soil moisture inversion are discussed in a following Section.

## Results

### Model Calibration Results

The calibration of the coupled model was conducted by minimizing the RMSE between the observed and simulated backscattering coefficients to optimize the effective roughness parameters and model unknown coefficients. Figure 5 displays the distributions of RMSE. Table 2 lists the model coefficients, selected effective roughness parameters and corresponding statistical metrics. Figure 6 presents the temporal evolution of the observed and simulated backscattering coefficients from the calibrated model.

Figure 5 shows that the trends of RMSE are similar when different vegetation parameters are used. With the increase of  $s$  or  $l$ , the performance of RMSE decreases first and then increases. This means that the effective roughness parameters

corresponding to the minimum RMSE are almost completely chosen within the given range of  $s$  and  $l$ , and  $s$  is more effective to model the calibration than  $l$ . From the contours, it is observed that the impact of an increase in  $s$  can be balanced by an increase in  $l$ . Therefore, it is possible that a set of roughness parameters corresponds to the minimum RMSE, and there may exist multiple solutions for the effective roughness parameters. This phenomenon was caused by an ill-posed AIEM, which can also be found in previous studies (Bai *et al.*, 2016). Although the RMSE-trend is similar, when LAI is used to describe the growth of the vegetation, the RMSE value is larger than the others and varies dramatically with the increase of  $s$  and  $l$ . This indicates that the selection of vegetation parameters can affect the calibration result of the coupled model. When LAI is adopted, the impact of  $s$  and  $l$  on the model calibration results is enhanced.

Table 2 shows that the results are similar between different vegetation parameter combinations and their RMSE range from 0.798 dB to 0.893 dB, and their  $R^2$  range from 0.425 to 0.716. From the perspective of statistical metrics, it can be said that

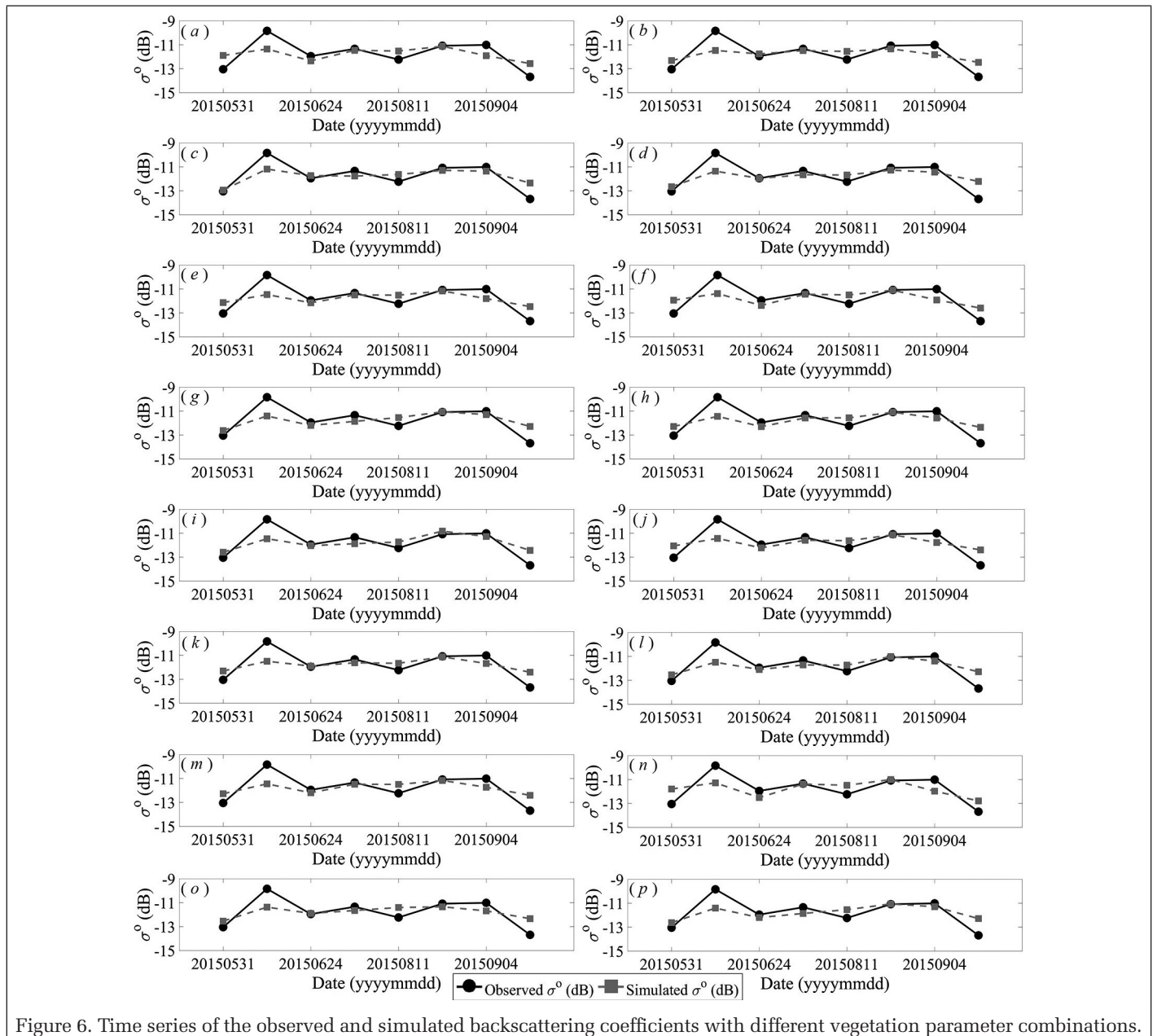


Figure 6. Time series of the observed and simulated backscattering coefficients with different vegetation parameter combinations.

Table 3. The statistical metrics between the *in situ* and retrieved soil moisture using the data from 2016.

Vegetation Parameter		bias	MAE	RMSE	ubRMSE	$R^2$
$V_1$	$V_2$					
NDVI	NDVI	-0.002	0.075	0.088	0.087	0.750
NDVI	EVI	-0.008	0.130	0.152	0.152	0.315
NDVI	LAI	-0.037	0.169	0.197	0.194	0.169
NDVI	FPAR	-0.058	0.196	0.217	0.209	0.249
EVI	EVI	-0.011	0.091	0.107	0.107	0.610
EVI	NDVI	-0.009	0.073	0.086	0.086	0.753
EVI	LAI	0.007	0.134	0.171	0.171	0.279
EVI	FPAR	-0.039	0.129	0.140	0.135	0.575
LAI	LAI	-0.001	0.113	0.152	0.152	0.338
LAI	NDVI	-0.015	0.078	0.093	0.093	0.728
LAI	EVI	-0.020	0.086	0.106	0.104	0.616
LAI	FPAR	-0.037	0.124	0.134	0.129	0.615
FPAR	FPAR	-0.028	0.113	0.123	0.120	0.663
FPAR	NDVI	-0.001	0.071	0.082	0.082	0.753
FPAR	EVI	-0.007	0.077	0.087	0.087	0.726
FPAR	LAI	-0.014	0.137	0.177	0.177	0.244

the calibration results of the coupled model are acceptable. However, the calibration result of the coupled model depends on the selection of the vegetation parameters. When NDVI is chosen as  $V_2$ , the statistical results show that the calibration of the coupled model is the worst. When NDVI is chosen as  $V_1$ , the statistical results show that the calibration of the coupled model is the best. This means that the contributions of  $V_1$  and  $V_2$  are different. Therefore, the proper combination of vegetation parameters should be selected in the calibration process of the coupled model.

Figure 6 shows that the simulated backscattering coefficients from the calibrated coupled model can capture the change in the observed value well. Although the estimated value may be higher or lower than the observed value, the overall trend of the estimated value can reflect the changing trend of the observed value in the time dimension.

### Soil Moisture Retrieval Results

Based on the calibrated model, the soil moisture retrieval is retrieved from the remaining data. The statistical metrics, i.e., bias, MAE, RMSE, ubRMSE, and  $R^2$ , are listed in Table 3. Figure

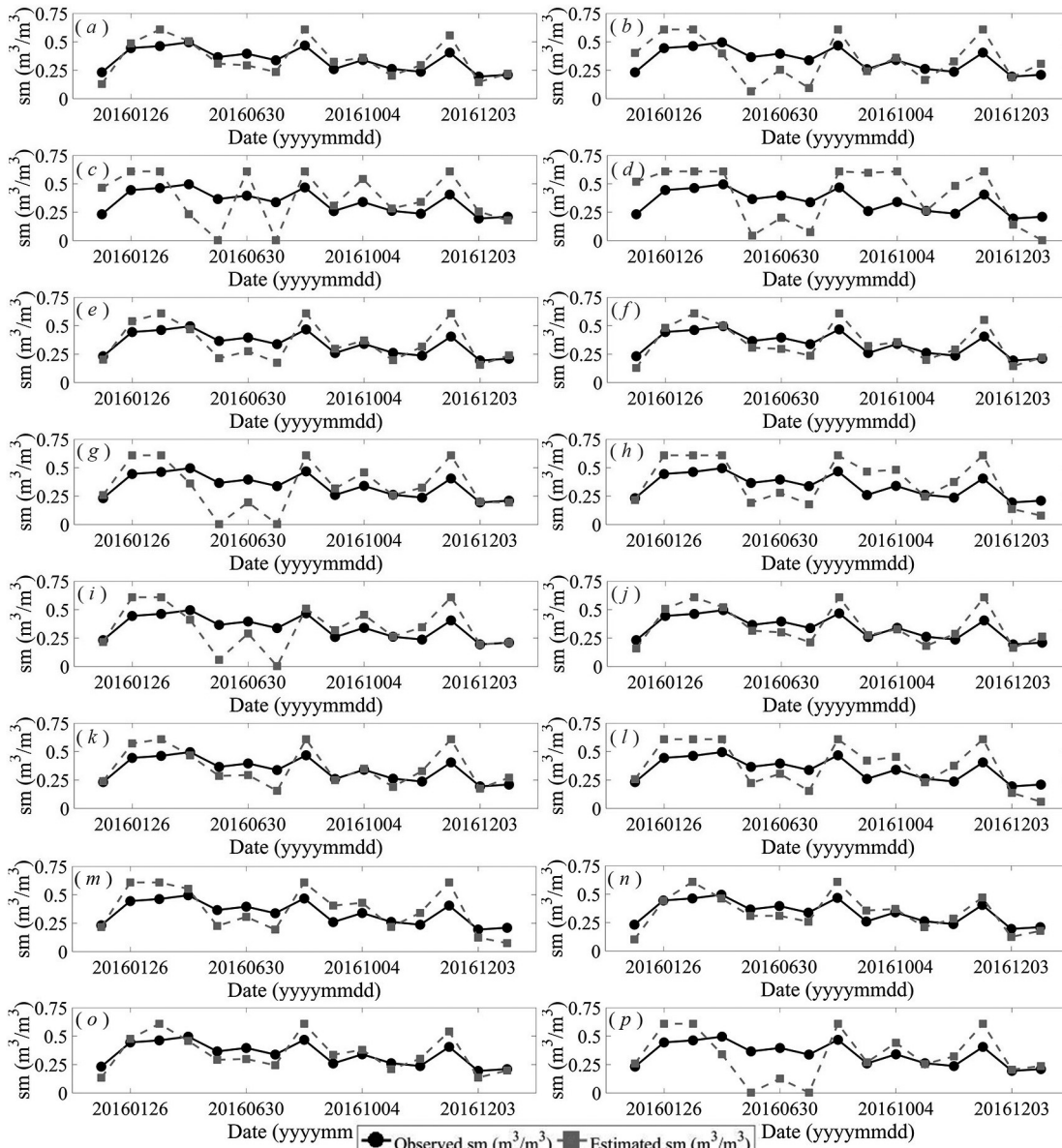


Figure 7. Time series of the *in situ* and retrieved soil moistures with different vegetation parameter combinations.

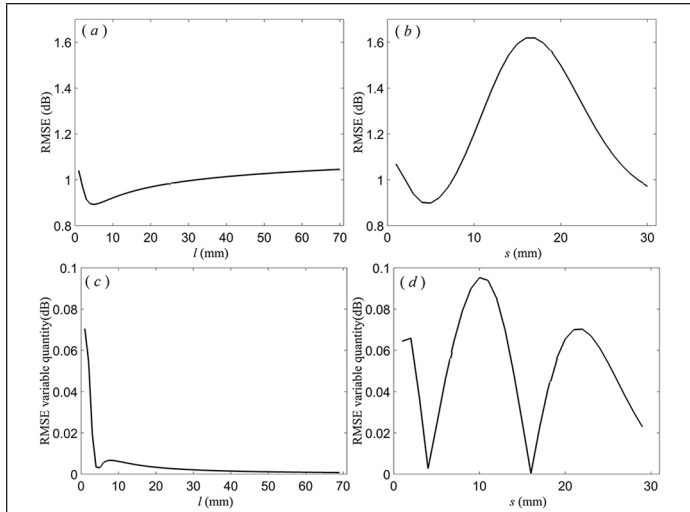


Figure 8. Analysis results of roughness parameters with control variables method. (left:  $s$  is 0.4 cm; right:  $l$  is 5 cm.  $V_1$  and  $V_2$  are NDVI).

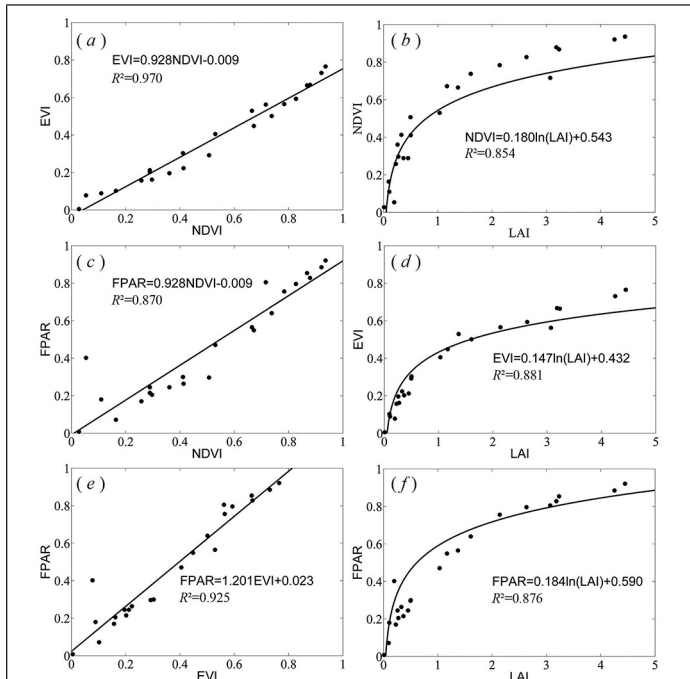


Figure 9. The correlation of different vegetation parameters.

7 shows the time series of the *in situ* measurements and retrieved soil moistures.

Table 3 and Figure 5 show that the accuracy of the soil moisture retrieval has an obvious difference when different vegetation parameter combinations are used. When  $V_2$  is NDVI, the inversion results are the best, and when  $V_2$  is LAI, the inversion results are the worst. These inversion results of the other vegetation parameters are atypical. This means that NDVI and LAI play a very important role in the soil moisture inversion process. They can suppress the effect of other vegetation parameters in soil moisture inversion. This illustrates that different vegetation parameters have an influence on soil moisture inversion, and it is necessary to select optical vegetation parameters for high accuracy soil moisture inversion. Compared with RMSE and  $R^2$  of the model calibration and soil moisture retrieval, it can be found that the model calibration

is negatively correlated with soil moisture retrieval. This phenomenon indicates that it is unwise to pursue high precision in the process of model calibration.

## Discussion

In this paper, the WCM and AIEM are coupled to retrieve soil moisture. The retrieval results show that the accuracy evaluation index has an obvious difference when different vegetation parameter combinations were adopted. Thus, it can be said that the input parameters have a very important impact on the soil moisture retrieval. In this section, the influence of different roughness parameters and vegetation parameter combinations on the retrieval results is discussed.

### Analysis of the Effective Roughness Parameters

Figure 5 shows that the different combinations of roughness parameters have a great influence on the calibration accuracy of the coupled model. When the coupled model is initialized with different roughness parameters, the RMSE between the estimated and observed backscattering coefficients will reach 3 dB or higher. Therefore, it is very meaningful to select effective roughness parameters according to the cost function to minimize the influence of ground surface undulation on the accuracy of soil moisture inversion and to analyze the individual effect of the two surface roughness parameters on the calibration accuracy. In this paper, the control variables method was chosen to analyze the effects of  $s$  and  $l$  on the model calibration separately. Table 2 shows the effective  $s$  is 0.4 cm and the effective  $l$  is 5 cm when NDVI is selected as the vegetation parameter in WCM. Thus, the effect of different  $l$  on the model's calibrated accuracy is analyzed with the effective  $s$ , and then the effect of a different  $s$  to the model calibration accuracy is analyzed with the effective  $l$ .

Figure 8 shows the analysis results of the roughness parameters with the control variables method. The two images above are RMSEs with different  $l$  and  $s$  when another parameter is fixed, and the two images below show the variation quality with the successive growth of  $l$  and  $s$ .

Figure 8 shows that with the independent increase of  $s$  or  $l$ , the trends of RMSE decrease first and then increase. This phenomenon indicates that the effective roughness parameters are within the parameter range chosen by this paper. This result can also be concluded based on Figure 8. When  $l$  is greater than 10 cm, the change rate of RMSE gradually slows down, and its change volume is attributed to 0 with the increase of  $l$ , but RMSE is very active with the change of  $s$ . This means that the impact of  $s$  on model calibration is more serious than  $l$ . This phenomenon can also be found in Bai's article (Bai *et al.*, 2016). Therefore, in the process of soil moisture inversion, the selection of  $s$  is very critical to the high accuracy of soil moisture inversion.

It is worth noting that the selected effective roughness parameters are used as a tuning parameter to improve the accuracy of soil moisture inversion; there is no physical meaning for them, and they do not represent the real surface parameters of the study area.

### Analysis of the Vegetation Parameters

In this study, a total of sixteen combinations of four vegetation parameters were used to calibrate the coupled model and retrieve soil moisture. The correlation of different vegetation parameters was very high, which is shown in Figure 9. The correlation of LAI and the other three parameters were exponential, the correlation of the other three parameters had a linear correlation, and their  $R^2$  were above 0.85; this result can also be found in Baghdadi's article (Baghdadi *et al.*, 2016). It demonstrates that the vegetation data used in this paper were correct, but the accuracy of soil moisture inversion was

very different when different vegetation parameters were used; thus, the applicability of these vegetation parameter combinations need to be discussed.

Among the four vegetation parameters, LAI has a specific physical meaning. It represents the total area of the plant leaves in the unit land area. Its value varies with changes in surface vegetation coverage, which may be more than 1. NDVI, EVI, and FPAR are normalized mathematical quantities. Table 3 shows that the accuracy of soil moisture inversion when  $V_2$  is LAI is lower than when  $V_2$  is another vegetation parameter; specifically, when  $V_2$  is NDVI, the accuracy of the soil moisture inversion was the highest. This result also concluded in a previous study that the use of NDVI as the vegetation descriptor allows for computation of the vegetation effects on the total backscattering coefficients with good accuracy (El Hajj *et al.*, 2017). This means that LAI is not suitable as  $V_2$  in WCM to estimate the contribution of vegetation in grasslands, and a normalized vegetation parameter can often achieve better results. When the same analysis method is adopted for  $V_1$ , it can be concluded that NDVI is not suitable as  $V_1$  in WCM to estimate the contribution of vegetation.

When  $V_1$  and  $V_2$  are NDVI, the bias, MAE, RMSE, ubRMSE and  $R^2$  of soil moisture inversion are  $-0.002 \text{ m}^3/\text{m}^3$ ,  $0.075 \text{ m}^3/\text{m}^3$ ,  $0.088 \text{ m}^3/\text{m}^3$ ,  $0.087 \text{ m}^3/\text{m}^3$  and  $0.750$ , respectively. Combining the previous conclusions indicates that the impact of  $V_1$  is suppressed by  $V_2$  in the computing process of vegetation contribution; thus,  $V_2$  in the WCM is the decisive vegetation factor affecting the accuracy of soil moisture inversion. From Table 3 and the analysis of the vegetation parameter, it can be found that soil moisture retrieval may vary greatly when different vegetation parameters are used to calculate the contribution of vegetation in WCM, so the selection of an optimal combination of vegetation is very important to improve the accuracy of soil moisture retrieval.

## Conclusions

In this paper, the WCM and AIEM are coupled to retrieve soil moisture in the Central Plains of the United States using time series Sentinel-1A data, Terra MODIS vegetation data and *in situ* soil moisture measurements. To characterize the scattering contribution of vegetation, different vegetation parameters, including NDVI, EVI, LAI, and FPAR, are cross-combined to parameterize the coupled model. The model calibration is conducted by minimizing the RMSE between the observed and simulated backscattering coefficient. The soil moisture is retrieved based on the calibrated model using the LUT method. The results of model calibration and soil moisture retrieval show that the roughness parameter and vegetation parameter have an important influence on soil moisture retrieval, and model calibration is a necessary step in the process of soil moisture retrieval, but it is unwise to pursue high precision in the process of model calibration. The coupled model is performed with different combinations of NDVI, EVI, LAI and FPAR as vegetation descriptors. The use of NDVI is recommended, as this resulted in the highest soil moisture retrieval bias, MAE, RMSE, ubRMSE and  $R^2$  of  $-0.002 \text{ m}^3/\text{m}^3$ ,  $0.075 \text{ m}^3/\text{m}^3$ ,  $0.088 \text{ m}^3/\text{m}^3$ ,  $0.087 \text{ m}^3/\text{m}^3$  and  $0.753$ , respectively. When the best vegetation parameter combination is adopted, the retrieved soil moisture is in good agreement with the *in situ* measurement, and the trend of ground observations is reproduced well using the estimated soil moisture. The impact of the roughness parameters and the vegetation parameter on the soil moisture retrieval has been discussed. These discussions further validate the importance of the accurate parameterization of the surface roughness and vegetation. The results of this study provide a preliminary assessment for estimating the soil moisture from Sentinel-1A data. It is expected that this

work will be beneficial for developing soil moisture retrieval methodologies for the Sentinel-1A satellites.

## Acknowledgements

The present work was funded by the National Natural Science Foundation of China (Contract #41671361, #41471293, and #41601373)

## References

- Attema, E., and F.T. Ulaby, 1978. Vegetation modeled as a water cloud, *Radio Science*, 13(2):357-364.
- Aubert, M., N. Baghdadi and M. Zribi, 2013. Toward an operational bare soil moisture mapping using TerraSAR-X data acquired over agricultural areas, *IEEE Journal of Selected Topics in Applied Earth Observations and Remote Sensing*, Vol. 6, Issue 2, pp. 900-916.
- Baghdadi, N.I. Gherboudj, and M. Zribi, 2004. Semi-empirical calibration of the IEM backscattering model using radar images and moisture and roughness field measurements. *International Journal of Remote Sensing*, 25(18):3593-3623.
- Baghdadi, N., C. King, and A. Chanzy, 2002. An empirical calibration of the integral equation model based on SAR data, soil moisture and surface roughness measurement over bare soils, *International Journal of Remote Sensing*, 23(20):4325-4340.
- Baghdadi, N., M. El Hajj, and M. Choker M, 2018. Potential of Sentinel-1 images for estimating the soil roughness over bare agricultural soils, *Water*, 10(2):131.
- Baghdadi, N., 2017. Calibration of the water cloud model at C-Band for winter crop fields and grasslands, *Remote Sensing*, 9(969):13.
- Baghdadi, N., R. Cresson, and M. El Hajj, 2012. Estimation of soil parameters over bare agriculture areas from C-band polarimetric SAR data using neural networks, *Hydrology and Earth System Sciences*, Vol. 16, pp. 1607-1621.
- Baghdadi, N., and M. Zribi, 2006. Evaluation of radar backscatter models IEM, Oh and Dubois using experimental observations, *International Journal of Remote Sensing*, 27(18):3831-3852.
- Baghdadi, N., M. Aubert, and M. Zribi, 2012. Use of TerraSAR-X data to retrieve soil moisture over bare soil agricultural fields, *IEEE Geoscience and Remote Sensing Letters*, Vol. 9, No. 3, pp. 512-516.
- Baghdadi, N., M. Choker, and M. Zribi, 2016. A new empirical model for radar scattering from bare soil surfaces, *Remote Sensing*, Vol. 8, Issue 11, pp. 1-14.
- Baghdadi, M. El Hajj, and M. Zribi, 2017. Calibration of the water cloud model at C-band for winter crop fields and grasslands, *Remote Sensing*, 9:969.
- Baghdadi, N., M. El Hajj, and M. Zribi, 2016. Coupling SAR C-band and optical data for soil moisture and leaf area index retrieval over irrigated grasslands, *Proceedings of the Geoscience and Remote Sensing Symposium*, IEEE, pp. 1229-1243.
- Bai, X, B. He, and X. Li., 2017. First assessment of Sentinel-1A data for surface soil moisture estimations using a coupled water cloud model and advanced integral equation model over the Tibetan plateau, *Remote Sensing*, 9(7):714.
- Bai, X., B. He, and X. Li, 2016. Optimum surface roughness to parameterize advanced integral equation model for soil moisture retrieval in prairie area using Radarsat-2 data, *IEEE Transactions on Geoscience and Remote Sensing*, 54(4):2437-2449.
- Bai, X., and B. He, 2015. Potential of Dubois model for soil moisture retrieval in prairie areas using SAR and optical data, *International Journal of Remote Sensing*, 36(22):5737-5753.
- Bao, Y., 2007. Soil moisture estimation based on optical and microwave remote sensing data, *Journal of Beijing Normal University*.
- Beckmann, P., and A. Spizzichino, 1987. The scattering of electromagnetic waves from rough surfaces, Norwood, Massachusetts, Artech House.

- Bracaglia, M., P. Ferrazzoli, and L. Guerriero, 1995. A fully polarimetric multiple scattering model for crops, *Proceedings of the Geoscience and Remote Sensing Symposium, IGARSS 95*, Quantitative Remote Sensing for Science and Applications, 1995:1339.
- Breit, H., T. Fritz, and U. Balsas U, 2010. TerraSAR-X SAR Processing and Products, *IEEE Transactions on Geoscience & Remote Sensing*, 48(2):727-740.
- Chen, K.S., T.D. Wu, and L. Tsang, 2003. Emission of rough surfaces calculated by the integral equation method with comparison to three-dimensional moment method simulations, *IEEE Transactions on Geoscience & Remote Sensing*, 41(1):90-101.
- Das, K., and P.K. Paul, 2015. Soil moisture retrieval model by using RISAT-1, C-band data in tropical dry and sub-humid zone of Bankura district of India, *Egyptian Journal of Remote Sensing & Space Sciences*, 18(2):297-310.
- Dobson, M.C., F.T. Ulaby, and M.T. Hallikainen, 1985. Microwave dielectric behavior of wet soil-part II: Dielectric mixing models, *IEEE Transactions on Geoscience and Remote Sensing*, 23(1):35-46.
- Dong, L., N. Baghdadi and R. Ludwig, 2013. Retrieving surface soil moisture using radar imagery in a semi-arid environment, *IEEE Geoscience and Remote Sensing Letters*, Vol. 10, No. 3, pp. 461-465.
- Dorigo, W.A., K. Scipal, and R.M. Parinussa, 2010. Error characterization of global active and passive microwave soil moisture datasets, *Hydrologic Earth Systems Science*, 14:2605-2616.
- Dubois, P.C., J.J. Zyl, and T. Engman, 1995. Measuring soil moisture with imaging radars, *IEEE Transactions on Geoscience and Remote Sensing*, 33(4):915-926.
- El Hajj, M., 2016. Soil moisture retrieval over irrigated grassland using X-band SAR data, *Remote Sensing of Environment*, 176:202-218.
- El Hajj, M., and N. Baghdadi, 2016. Analysis of Sentinel-1 radiometric stability and quality for land surface applications, *Remote Sensing*, 8(5):406.
- El Hajj, M., 2017. Synergic use of Sentinel-1 and Sentinel-2 images for operational soil moisture mapping at high spatial resolution over agricultural areas, *Remote Sensing*, 9, 1292.
- Entekhabi, D., R.H. Reichle, and R.D., Koster, 2010. Performance metrics for soil moisture retrievals and application requirements, *Journal of Hydrometeorology*, 11(3):832-840.
- European Space Agency (ESA). Sentinel-1 User Handbook, URL: [https://earth.esa.int/documents/247904/685163/Sentinel-1\\_User\\_Handbook](https://earth.esa.int/documents/247904/685163/Sentinel-1_User_Handbook) (last date accessed: 31 October 2018).
- Ferrazzoli, P., Guerriero, L., 1996. Emissivity of vegetation: theory and computational aspects, *Journal of Electromagnetic Waves & Applications*, 10(5):609-628.
- Fung, A.K., 1994. *Microwave Scattering and Emission Models and Their Applications*, Boston, Massachusetts, Artech House, 62-362.
- Fung, A.K., Z. Li, and K. Chen, 1992. Backscattering from a randomly rough dielectric surface, *IEEE Transactions on Geoscience and Remote Sensing*, 30(2):356-369.
- Fung, A.K., and K.S. Chen, 2010. *Microwave Scattering and Emission Models for Users*, Artech house.
- Gao, Q, M. Zribi and M.J. Escorihuela M. J., 2017. Synergic use of Sentinel-1 and Sentinel-2 data for soil moisture mapping at 100 m resolution, *Sensors*, 17(9):1966.
- Gherboudj, I., R. Magagi, and A. Berg, 2011. Soil moisture retrieval over agricultural fields from multi-polarized and multi-angular RADARSAT-2 SAR data, *Remote Sensing of Environment*, 115(1):33-43.
- He, B., 2015, Method for soil moisture retrieval in arid prairie using TerraSAR-X data, *Journal of Applied Remote Sensing*, 9(1):096062.
- He, B., and M. Xing, 2014. A synergistic methodology for soil moisture estimation in an alpine prairie using radar and optical satellite data, *Remote Sensing*, 6(11):10966-10985.
- Huete, A., and K. Didan, 2002. Overview of the radiometric and biophysical performance of the MODIS vegetation indices, *Remote Sensing of Environment*, 83(1-2):195-213.
- Joseph, A.T., and V.R. Vand, 2010. *Application of the Tor Vergata Scattering Model to L Band Backscatter During the Corn Growth Cycle*, American Geophysical Union.
- Joseph, A.T., R.V.D.Velde, and P.E. O'Neill, 2010. Effects of corn on C- and L-band radar backscatter: A correction method for soil moisture retrieval, *Remote Sensing of Environment*, 114(11):2417-2430.
- Kornelsen, K.C., and P. Coulibaly, 2013. Advances in soil moisture retrieval from synthetic aperture radar and hydrological applications, *Hydrology*, 476:460-489.
- Kong, J.L., 2016, Retrieval for soil moisture using microwave remote sensing data based on a new combined roughness parameter, *Geography and Geo-Information Science*.
- Krieger, G, H. Fiedler, and M. Zink, 2007. The TanDEM-X mission: A satellite formation for high-resolution SAR interferometry, URL: <https://ieeexplore.ieee.org/document/4373373> (last date accessed: 31 October 2018).
- Kseneman, M, and D. Gleich, 2013. Soil-moisture estimation from X-band data using Tikhonov regularization and neural net, *IEEE Transactions on Geoscience & Remote Sensing*, 51(7):3885-3898.
- Lee, J.S., and M.R. Grunes, 1999. Polarimetric SAR speckle filtering and its implication for classification, *IEEE Transactions on Geoscience and Remote Sensing*, 37:2363-2373.
- Lievens, H., N.E.C. Verhoest, and E. De Keyser, E., 2011. Effective roughness modelling as a toll for soil moisture retrieval from C-band and L-band SAR, *Hydrology and Earth Systems*, 15:151-162.
- Lievens, H., and N.C. Verhoest, 2013, On the retrieval of soil moisture in wheat fields from L-band SAR based on water cloud modeling, the IEM, and effective roughness parameters, *IEEE Geoscience and Remote Sensing*, 10(4):890-894.
- Malenovsky, Z, H. Rott, and J. Cihlar, 2012. Sentinels for science: Potential of Sentinel-1, -2, and -3 missions for scientific observations of ocean, cryosphere, and land, *Remote Sensing of Environment*, 120(10):91-101.
- Oh, Y., K. Sarabandi, and F.T. Ulaby, 1992. An empirical model and an inversion technique for radar scattering from bare soil surfaces, *IEEE Transactions on Geoscience and Remote Sensing*, 30(2): 370-381.
- Oh, Y., K. Sarabandi K., and F.T. Ulaby, 1994. An inversion algorithm for retrieving soil moisture and surface roughness from polarimetric radar observation, *Proceedings of the Geoscience and Remote Sensing Symposium*, 1994:1582-1584 Vol. 3.
- Oh, Y., K. Sarabandi K., and F.T. Ulaby., 2002. Semi-empirical model of the ensemble- averaged differential Mueller matrix for microwave backscattering from bare soil surfaces *IEEE Transactions on Geoscience & Remote Sensing*, 40(6):1348- 1355.
- Oh Y., 2004. Quantitative retrieval of soil moisture content and surface roughness from multipolarized radar observations of bare soil surfaces, *IEEE Transactions on Geoscience & Remote Sensing*, 42(3):596-601.
- Prevot, L., I. Champion, and G. Guyot, 1993. Estimating surface soil moisture and leaf area index of a wheat canopy using a dual-frequency (C and X bands) scatter meter, *Remote Sensing of Environment*, 46(3):331-339.
- Pulvirenti, L, G. Squicciarino, and L. Cenci L, (2018). A surface soil moisture mapping service at national (Italian) scale based on Sentinel-1 data, *Environmental Modelling & Software*, 102:13-28.
- Quan, X., B. He, and X. Li, 2015. A Bayesian Network-based method to alleviate the ill-posed inverse problem: A case study on leaf area index and canopy water content retrieval, *IEEE Transactions on Geoscience & Remote Sensing*, 53(12):6507-6517.
- Quan, X., B. He, and M. Yebra, 2017. Retrieval of forest fuel moisture content using a coupled radiative transfer model, *Environmental Modelling & Software*, Vol. 95, pp. 290-302.
- Quan, X., B. He, and M. Yebra, 2017. A radiative transfer model-based method for the estimation of grassland aboveground biomass, *International Journal of Applied Earth Observation and Geoinformation*, Vol. 54, pp. 159-168.
- Rahman, M., M. Moran, and D. Thoma, 2008. Mapping surface roughness and soil moisture using multi-angle radar imagery without ancillary data, *Remote Sensing of Environment*, 112(2):391-402.

- Rosenqvist, A, M. Shimada, and S. Suzuki S, 2014. Operational performance of the ALOS global systematic acquisition strategy and observation plans for ALOS-2 PALSAR-2, *Remote Sensing of Environment*, 155(4):3-12.
- Saatchi, S.S., and M. Moghaddam, 2000. Estimation of crown and stem water content and biomass of boreal forest using polarimetric SAR imagery, *IEEE Transactions on Geoscience and Remote Sensing*, 38(2):697-709.
- Sancer, M.I., 1969. Shadow-corrected electromagnetic scattering from a randomly rough surface, *IEEE Transactions on Antennas and Propagation*, 17(5):577-585.
- Savitzky, A., and M.J.E. Golay, 1964. Smoothing and differentiation of data by simplified least square procedure, *Analytical Chemistry*, 36:1627-1639.
- Schaefer, G.L., and R.F. Paetzold, 2010. SNOTEL (SNOWpack TELemetry) and SCAN (Soil Climate Analysis Network), *Directory of Asia Scholars in Canada, Canadian Asian Studies Association*.
- Schubert, A., D. Small, and N. Miranda, 2015. Sentinel-1A product geolocation accuracy: Commissioning phase results, *Remote Sensing*, 7(7):9431-9449.
- Shi, J., J. Wang, and A. Hsu, A., 1995. Estimation of soil moisture and surface roughness parameters using L-band SAR measurements, *Proceedings of SPIE*, 1:507 - 509.
- Su, Z., P.A. Troch, and F.P.D. Troch, 1997. Remote sensing of bare surface soil moisture using EMAC/ESAR data, *International Journal of Remote Sensing*, 18(10):2105-2124.
- Ulaby, F.T., K. Sarabandi, and K. McDonald, 1990. Michigan microwave canopy scattering model, *International Journal of Remote Sensing*, 11(7):1223-1253.
- Ulaby, F.T., R.K. Moore, and A.K. Fung, 1986. *Microwave Remote Sensing: Active and Passive, Volume II: Radar Remote Sensing and Surface Scattering and Emission Theory*, Artech House Publishers.
- Wang, S.G., X. Li, and X.J. Han, X. J., 2011. Estimation of surface soil moisture and roughness from multi-angular ASAR imagery in the Watershed Allied Telemetry Experimental Research (WATER), *Hydrology & Earth System Sciences*, 15(5):1415-1426.
- Wang, L., 2006. New calibration method for soil roughness parameters with AMSR-E observations, *Journal of Remote Sensing*, 10(5):656-660.
- Wu, T.D., K.S. Chen, and J. Shi, J., 2001. A transition model for the reflection coefficient in surface scattering, *IEEE Transactions on Geoscience & Remote Sensing*, 39(9):2040-2050.
- Yu, F., and Y. Zhao, 2010. A new method for soil moisture inversion by synthetic aperture radar, *Geomatics & Information Science of Wuhan University*, 35(3):317-321.
- Zhou, Y.L., X.M. Sun X. M., and Z.L. Zhu, 2007. Comparative research on four typical surface roughness length calculation methods, *Geographical Research*, 26(5):887-896.

# Individual Tree Detection and Crown Delineation with 3D Information from Multi-view Satellite Images

Changlin Xiao, Rongjun Qin, Xiao Xie, and Xu Huang

## Abstract

*Individual tree detection and crown delineation (ITDD) are critical in forest inventory management and remote sensing based forest surveys are largely carried out through satellite images. However, most of these surveys only use 2D spectral information which normally has not enough clues for ITDD. To fully explore the satellite images, we propose a ITDD method using the orthophoto and digital surface model (DSM) derived from the multi-view satellite data. Our algorithm utilizes the top-hat morphological operation to efficiently extract the local maxima from DSM as treetops, and then feed them to a modified superpixel segmentation that combines both 2D and 3D information for tree crown delineation. In subsequent steps, our method incorporates the biological characteristics of the crowns through plant allometric equation to falsify potential outliers. Experiments against manually marked tree plots on three representative regions have demonstrated promising results – the best overall detection accuracy can be 89%.*

## Introduction

Forest is one of the most important land surfaces and plays an important role in the global ecosystem. Timely and accurate measurements of the forest parameters at the individual tree level such as tree count, tree height, and crown size are essential for quantitative analysis of forest structure, ecological modeling, biomass estimation, and evaluation of deforestations (Mohan *et al.*, 2017; Weng *et al.*, 2015). Over the past several decades, remote sensing techniques have greatly improved the capability of extracting forest metrics with high spatial resolution imagery (Gonçalves *et al.*, 2017; Sousa *et*

*al.*, 2015). However, the majority of these methods use spectral or texture information and are limited to the radiometric quality which makes them vulnerable to erroneous detections, either over-/under- segmenting tree crowns at the individual plot level.

The addition of 3D information to these forest metric estimations can greatly enhance the measurement accuracy. Recently, much attention has been given to lidar data, which provides an accurate 3D representation of the surface objects. A number of algorithms have been proposed to analyze the forest structure at individual tree level with this data (Ferraz *et al.*, 2016; Kathuria *et al.*, 2016; Liu *et al.*, 2015). Many of the methods that are based on either lidar or photogrammetric 3D points use the normalized digital surface model (nDSM) or the canopy height model (CHM, for the forest applications), which can naturally highlight the treetops and directly offer the tree heights (Liu *et al.*, 2015; Lu *et al.*, 2014). The CHM can be generated by subtracting the digital terrain model (DTM) from the digital surface model (DSM). Similar to the 2D image-based methods, the CHM-based methods use procedures such as image smoothing, local maximum localization, and template matching to detect the individual trees and their boundaries (Koch *et al.*, 2006; Popescu *et al.*, 2002). In Strîmbu and Strîmbu (2015), they used graph theory to model the forest topological structure and correct two potentially over-identified treetops. Also, multi-scale segmentations have been proposed to dynamically select the best set of apices and generate the final segmentation (Véga *et al.*, 2014). For tree crown delineation, image segmentation methods such as valley following, region growing, and watershed segmentation can be directly used on CHM (Ferraz *et al.*, 2016; Kathuria *et al.*, 2016; Strîmbu and Strîmbu, 2015). Among these methods, the watershed segmentation is the most popular as it can naturally and efficiently model the treetops and crowns, for example, Liu *et al.* (2015) proposed the Fishing Net Dragging (FND) method which uses the watershed segmentation with the Gaussian filtering to find the boundaries of trees. Even though these methods have demonstrated great successes in their applications, they are limited by the cost of lidar surveying making them impractical for repetitive acquisition of at large scales (Wulder *et al.*, 2013). Also, lidar systems offering compensatory spectrometers are not widely available to provide additional spectrum data for more advanced analysis, such as LAI (leaf area index), NDVI (normalized difference vegetation index) for vegetation classification. A demand for such data normally requires an additional light for multi-/hyper-spectral data acquisition while which subsequently brings in registration issues.

---

Changlin Xiao is with the Future Cities Laboratory, Singapore-ETH Centre, ETH Zurich, 1 Create Way, CREATE Tower, #06-01, 138602, Singapore; and the Department of Civil, Environmental and Geodetic Engineering, The Ohio State University, 218B Bolz Hall, 2036 Neil Avenue, Columbus, OH 43210.

Rongjun Qin is with the Department of Civil, Environmental and Geodetic Engineering, The Ohio State University, 218B Bolz Hall, 2036 Neil Avenue, Columbus, OH 43210; and the Department of Electrical and Computer Engineering, The Ohio State University, 205 Drees Labs, 2015 Neil Avenue, Columbus, OH, 43210 (qin.324@osu.edu).

Xiao Xie is with the Research Center for Industrial Ecology & Sustainability, Institute of Applied Ecology, Chinese Academy of Sciences, No.72, Wenhua Road, Shenhe District, Shenyang City 110016, China; and the Key Laboratory for Environment Computation & Sustainability of Liaoning Province, No.72, Wenhua Road, Shenhe District, Shenyang City 110016, China.

Xu Huang is with the Department of Civil, Environmental and Geodetic Engineering, The Ohio State University, 218B Bolz Hall, 2036 Neil Avenue, Columbus, OH 43210.

---

Photogrammetric Engineering & Remote Sensing  
Vol. 85, No. 1, January 2019, pp. 55–63.  
0099-1112/18/55–63

© 2019 American Society for Photogrammetry  
and Remote Sensing  
doi: 10.14358/PERS.85.1.55

Considering the merits of both 2D spectral and 3D structure data, for the first time, we propose to use multi-view high-resolution satellite imagery to perform forest parameters retrieval at the individual tree level. With the growing number of high-resolution satellite sensors, the chances of a spot being viewed multiple times with multiple angles are greatly increased. These multi-view images can facilitate many remote sensing tasks, for example, Liu and Abd-Elrahman (2018) used multi-view images in a deep convolutional neural network for the wetlands classification. Also, the development of the advanced image matching algorithms makes it possible to produce comparably dense 3D measurements as lidar, while with much lower cost, higher flexibility in acquiring information in a large geographical region. With the highly accurate 3D digital surface models (DSM) and true orthophotos generated from these multi-view satellite images, we expect it will significantly enhance the performance of individual tree detection and crown delineation (ITDD).

The terrain data is critical for many 3D points based ITDD methods. However, for DSM generated from satellite images, terrain data under the forest canopy might not be captured. Moreover, considering that the accuracy of image-based DSM is normally lower than those from lidar, it can be particularly challenging to directly use the point cloud based methods on this DSM. Hence, to fully explore the multi-view satellite imagery based data, we propose a novel algorithm that utilizes both 2D spectral and 3D structural information with the orthophoto and DSM. Based on the assumption that tree crowns are normally well rounded in shape with a single maximum as the treetops, we propose to use morphological top-hat by reconstruction (THR) to detect treetops. Compared to other local maximum detectors, for example, window-based local maximum filters (Pouliot and King, 2005; Wulder *et al.*, 2000), the THR detector is less sensitive to the window or filter size. For the crown delineation, we adopt a modified superpixel segmentation framework to generate compact segments that leverage the boundary of crowns based on the DSM and multispectral information, thus are able to account for crown delineation in both sparsely and densely forested area. Compared to the previous methods, for instance, valley following, region growing, and watershed segmentation (Gougeon and Leckie, 2006; Ke and Quackenbush, 2011), the modified superpixel segmentation is similar to region growing, but with an extra spatial constraint which ensures more compact shapes for trees. The tree crowns are complex in their 3D structure, including overlapping canopies, adjacent crowns reflecting similar spectrums but different in height, and smooth crowns. Hence, the combination of both 2D spectral and 3D structural information would greatly help to identify the individual trees.

To the authors' best knowledge, this work contributes to the community as the first to demonstrate and offer the use of multi-view high-resolution satellite imagery as an alternative data source for the forest parameter retrieval at the individual tree level. In addition, the contributions include the development of a novel top-hat and superpixel based detection framework that is able to (1) accommodate multi-modal data for segmenting objects under complex scenarios; (2) utilize biometric characteristics of trees through the allometric equation to constrain size and shape of tree segments; and (3) achieve high accuracy in areas with different canopy densities. In particular, the proposed method is able to account for densely forested regions, even without a high precision DTM.

## Study Area and the Data Processing

The study area is located in Don Torcuato, a small city on the west side of Buenos Aires, Argentina. In this area, we choose three experimental sites with tree plots at different levels of density as illuminated in Figure 1 and Figure 2. Site A, covering an area of  $0.30 \times 0.30 \text{ km}^2$ , which we treat as the sparsely forested area mainly consists of sparsely distributed trees, wild shrubs, and grasslands. In the densely forested site B, covering  $0.25 \times 0.34 \text{ km}^2$ , different types of trees at different heights intersect with each other and only a small part of it being ground surface. Site C is part of a small town, covering an area of  $0.30 \times 0.30 \text{ km}^2$ , the surface objects of which are complicated: trees at the courtyard or around buildings with

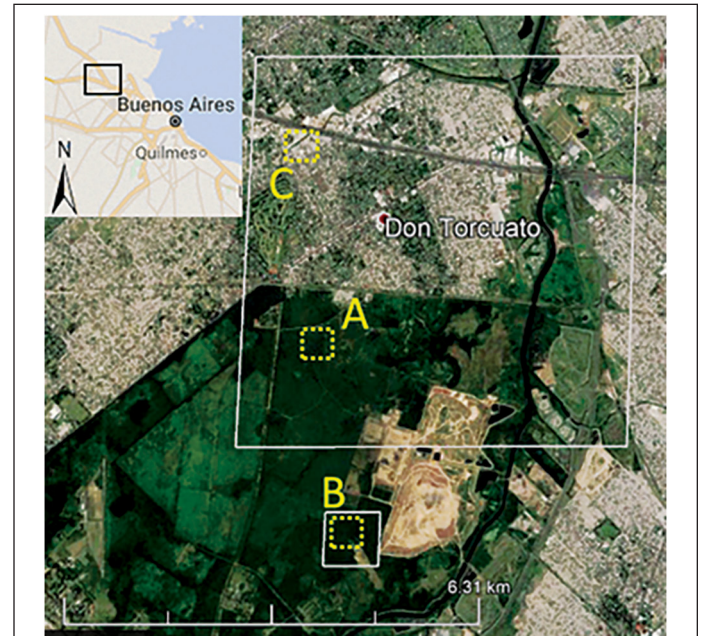


Figure 1. The study area near Buenos Aires, Argentina. The two large solid rectangles mark the areas where we have generated the DSM and orthophoto and A, B, C mark the experimental sites.

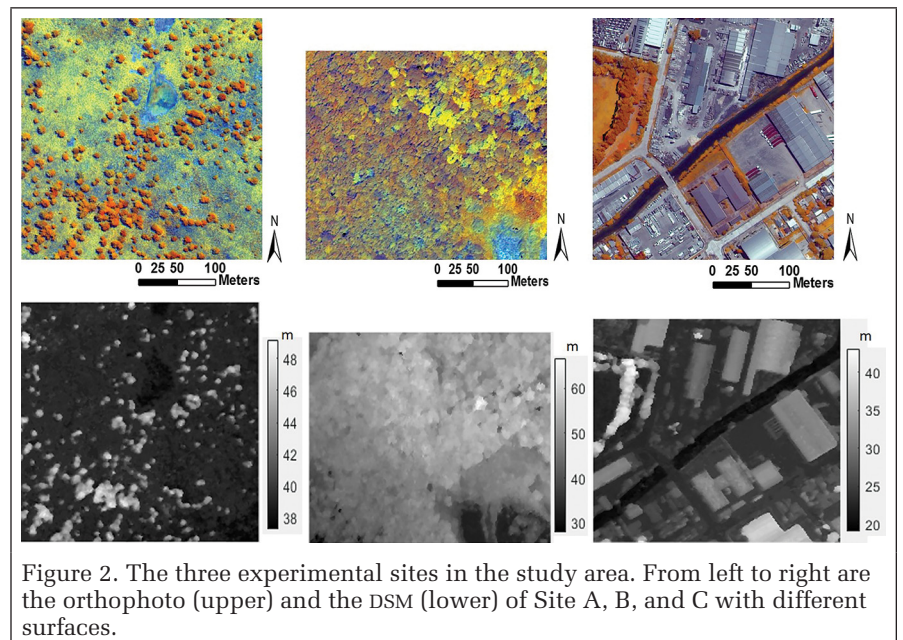


Figure 2. The three experimental sites in the study area. From left to right are the orthophoto (upper) and the DSM (lower) of Site A, B, and C with different surfaces.

different crown sizes and heights; shrubs on the street sides mixed with trees at different heights.

The satellite images in this work are from the multi-view benchmark dataset provided by John's Hopkins University Applied Physics Lab (JHUAPL) (Bosch *et al.*, 2016; Bosch *et al.*, 2017). The data contains 8 bands Worldview2/3 images with the ground resolution around 0.3 meters. To derive an accurate DSM, we selected five pairs of the on-track stereo images captured in December 2015, with the maximal off-nadir angle between 7-19 degrees and the average intersection angle between 15-21 degrees. We applied a fully automated pipeline (Qin, 2017) that consists of (1) pansharpening, (2) automatic feature matching, (3) pair-wise bundle adjustment, (4) dense matching, and (5) a bilateral-filter based depth-fusion,

to generate a high-quality DSM and subsequently true orthophoto. Comparing to the ground truth lidar data, the root-mean-square errors (RMSE) of the DSM are varying between 2.5-4 meters which is absolute accuracy at checking points which do not represent the relative accuracy of the object reconstruction. More details about the method and the accuracy evaluation can be found in Qin (2017) and Figure 2 shows the cropped orthophoto and DSM of the three experimental sites.

## Methodology

The proposed method includes several steps summarized in Figure 3: After the generation of an orthophoto and DSM, the vegetated area and terrain area are extracted to facilitate the treetop detection which is based on the local maximum of DSM through top-hat by reconstruction (THR) operation (Qin and Fang, 2014). To further improve the detection quality, we use above ground height check and non-maximum suppression with the allometric equation to eliminate the short and redundant detections. From the treetops, a modified superpixel segmentation that combines the 2D spectral and the 3D structural information is proposed to effectively delineate the tree crowns. Finally, a postprocessing for the crown refinement is used to further improve the detection accuracy.

### Vegetation and Terrain Detection

To identify the vegetation areas, we use the Normalized Difference Vegetation Index (NDVI) as the index and take the areas where their  $NDVI > \mu$  to be the vegetation area.  $\mu$  is empirically set as 0.3 leveraged based on our experiments. Digital terrain model (DTM) is a useful source for the individual tree detection, and there have been several methods proposed to extract the DTM from 3D points (Gevaert *et al.*, 2018; Hu *et al.*, 2014). Such as in Hu *et al.* (2014), they proposed an adaptive surface filter (ASF) that the threshold can vary according to the terrain smoothness to efficiently classify the airborne laser scanning data. DTM is used to offer the height information as normalized DSM (nDSM) or CHM (for forest application). However, in some densely forested areas, it may not be feasible to extract the DTM from DSM produced by images. Fortunately, the proposed method is not heavily depended on the tree height information. The treetop detection and crown delineation are mainly decided by the relative height. The absolute tree height is an extra cue to refine detections which will be discussed with more details in the experiments.

Our method does not explicitly generate the nDSM or CHM. Instead, we focus on the height gradients and estimate the above ground tree height with an effective terrain detection method. By converting the pixels in DSM map as grid point cloud, we apply the cloth simulation filter (CSF) (Zhang *et al.*, 2016) that based on the height and surrounding information to classify the points into two categories: terrain and off-terrain points. The above-ground heights of trees which are

subsequently used for crown size estimation can be estimated by subtracting the terrain height around it, and more details can be found in the next section. In the experiments, we used the open source software CloudCompare<sup>®</sup> as the segmentation tool, and an example can be found in Figure 4.

### Treetop Detection

#### Detection of Local Maximum Points

Similar to lidar-based treetop detection, we naturally assume that the local maximum in the DSM is the treetop. However, since the filter-based method requires a careful tuning of window size, we adopt the grey-level morphological top-hat by reconstruction

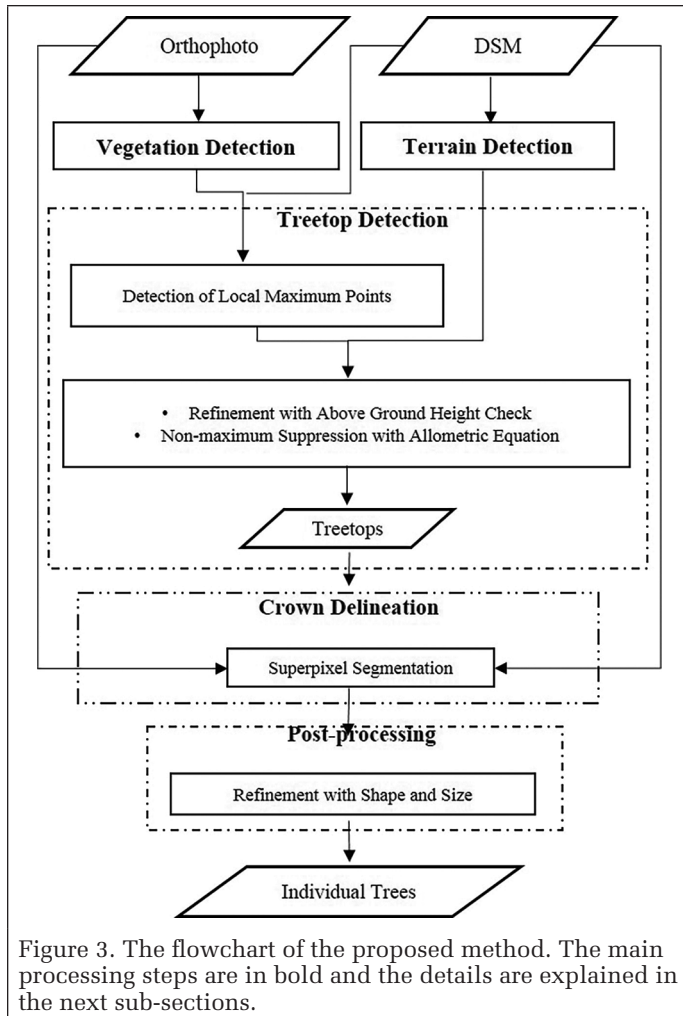


Figure 3. The flowchart of the proposed method. The main processing steps are in bold and the details are explained in the next sub-sections.



Figure 4. The vegetation and terrain detection of site C. From left to right are the 3D visualization of the textured DSM, the vegetation area, and the detected terrain area.

operator (THR) to find the local maximum, as it is an effective method of detection blob-like shapes and less sensitive to window size (Qin and Fang, 2014). In the detection, a disk-shaped structuring element (SE) is used to perform the grey-level morphology erosion on the DSM to generate a marker image  $\varepsilon(\text{DSM}, e)$ , where the erosion operation only keeps the minimum value of all the pixels in the structuring element. The morphological reconstruction mask  $B_{\varepsilon(\text{DSM}, e)}^{\text{DSM}}$  is then generated through an iterative procedure in which the dilation operation that keeps the maximum value is utilized on the marker image. Finally, by subtracting  $B_{\varepsilon(\text{DSM}, e)}^{\text{DSM}}$  from the DSM, the peaks on the DSM can be extracted as blob-shaped peak regions with respect to the local maximum.

To locate the local maximum at the pixel level, we first use the morphological opening operation to remove the weakly connected parts thus to separate a big region into several small ones. Then, for each region, we keep the highest point as the final treetop candidate. Figure 5 shows an example of the local maximum detection with two SEs (4 and 8 pixels). The detected local maximum regions with different SE sizes are shown as white and red dots (with a shift) in the rightmost image of Figure 5. As we can observe they are almost identical indicating the proposed THR operation is less sensitive to the size of SE.

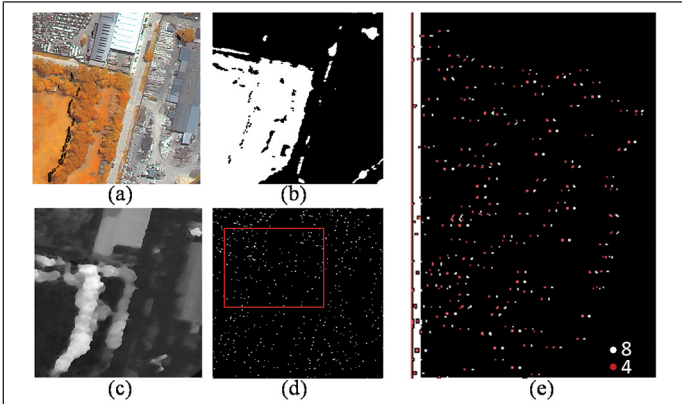


Figure 5. Illustration of the local maximum detection with different SE sizes. From image (a) to (d) are the orthophoto, the vegetated area, the DSM, and the local maximum (with 8 pixels SE). Image (e) is the non-vegetation removed results of two SEs (4 and 8 pixels) at the rectangle area in image (d).

**Refinement with Above Ground Height Check and Non-Maximum Suppression**  
To eliminate lower local maximum, we calculate per-point above ground height by subtracting its DSM height with nearby terrain height:

$$H(s) = \text{DSM}(s) - \sum_{p_i \in A_i, p_i \in T} \text{DSM}(p_i) / N, \quad (1)$$

where  $H(s)$  is the above ground height of point  $s$ ;  $\text{DSM}(s)$  and  $\text{DSM}(p)$  are the height values at point  $s$  and  $p$ .  $N$  is the total number of the terrain points in the predefined search window  $A_i$  centered at  $s$ , and  $T$  is the extracted terrain area as previously described.

To remove the redundant maximum points in one tree, a common practice is to use non-maximum filters to locate the true maximum within a window. The filter is expected to achieve the best performance when the window size is close to the crown size. However, the crown size of different types of trees may vary significantly. Given that the allometric equations describe the biological relationships between the tree

height and its crown size (Garrity *et al.*, 2012), it can be of a great value to use such cue to determine an optimal window size accountable for crown variations. While in general larger window is able to encapsulate small crowns, we consider to a type with a large crown/height ratio to obtain a good estimate as for removing non-maximum. Hence, we adopt the allometric equation for the deciduous tree (Desktop, 2011) to estimate the crown size (or filter window size)  $\chi$  for each treetop as:

$$\chi(s_i) = 3.09632 + 0.00895 * h_t(s_i)^2, \quad (2)$$

where  $h_t$  represents the above ground height of the treetop  $s_i$ . Figure 6 gives an example of the refinement of the local maximum (red dots), many (yellow circle marked) of which are not treetops to the final refined treetops (stars with a blue dot in the center). Also, in the same figure, the rectangles mark the non-maximum suppression window for each potential treetop and we can observe that they are associated with a sizeable window which is able to account for crown size variation.

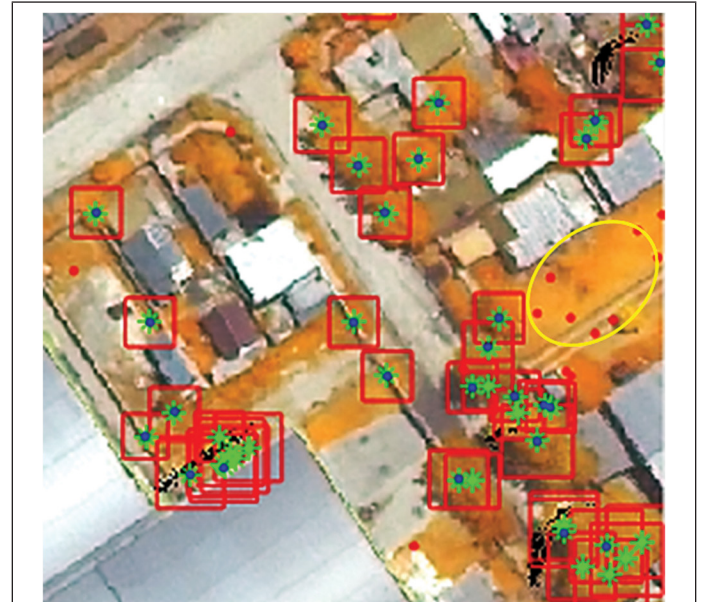


Figure 6. Treetop refinement. The initial detections are filtered by the above ground height check and non-maximum suppression with adaptive windows.

### Crown Delineation

The crown boundaries are usually indistinct in canopy density area and the texture information is normally not sufficient for the crown delineation. To utilize the 3D structure information of the DSM, we propose a modified superpixel segmentation utilizing multi-modal data to detect crown regions. The superpixel algorithm can provide a compact and homogenous representation towards all segments which naturally matches the shape of trees. In contrast to the original superpixel (Felzenszwalb and Huttenlocher, 2004), the modified version considers both 2D and 3D information in its kernel distance function:

$$D(s_i, t_j) = W_h * D_h(s_i, t_j) + W_v * D_v(s_i, t_j) + W_c * D_c(s_i, t_j) \quad (3)$$

where  $D(s_i, t_j)$  measures the spatial and spectral difference between treetop  $s_i$  and the test pixel  $t_j$ .  $D_h$ ,  $D_v$ , and  $D_c$  are both the Euclidean distance used to measure the horizontal, vertical distance and the spectral differences (8 bands) and normalized based on the statistical maximum and minimum range of tree crown size (estimated by allometric equation), tree height,

and the vegetation spectrum.  $W_h, W_v, W_c$  are the associated weights for different component which we empirically set as 0.8, 1, 0.5, emphasizing spatial distance especially the vertical one. The lower  $D(s_i, t_j)$  means higher similarity between the treetop and the test pixel, but if the smallest difference between a pixel and all the treetops is still larger than a certain threshold value  $\theta$ , the pixel will be abandoned as non-tree area. The  $\theta$  gives an extra constraint on the assignment of pixels that may not belong to trees. Smaller  $\theta$  regulates the delineated crown to be more compact and closer to the treetop, but may lose part of the true crown. On the contrary, larger  $\theta$  would reduce the restriction and let the delineation cover a larger area which may contain non-tree part. Hence, in the experiment, the  $\theta$  is carefully selected as the maximum difference value the Equation 3 could have, for example, the difference between the treetop and the leaf at the farthest crown. The idea of the revised superpixel is similar to the supervoxels (Papon *et al.*, 2013) used for full 3D data like those from terrestrial lidar. However, unlike the full 3D points, the DSM only represents 2.5 D information that only the surface points have height information. If using supervoxels, the facades (which were assumed to be cut-off planes) will be considered for segmentation which is unwanted. Besides, we have fixed the segmentation seeds at the treetops and the goal is to create a boundary delineation in the planar map. Hence, it is more appropriate to use this modified superpixel than the supervoxels.

### Postprocessing Using the Crown Shape and Size Constraints

In this study, we set two criteria to further verify the correctness of the crown's shape and size. The first criterion is that the treetop should be near the center of the crown. In the experiment, the one-third of the largest diameter of the segment is set as the maximum tolerance range. The falsely detected treetops that are far from the segment center are often the local maximum at the edge of the crowns and they are usually caused by the limited precision of the DSM. The other criterion is the coherence of the crown size. Normally, a tree and its neighbors belong to the same species and should share common biological features (e.g., the height-crown ratio). Therefore, we use the average crown size of the neighborhood as the reference crown size to remove abnormal crowns with the three-sigma rule.

## Experiments and Discussion

### Accuracy Assessment Measure

To quantitatively validate the individual tree detection and crown delineation accuracy, we use true positives (TP), false positives (FP) and false negatives (FN) to compute the detection accuracy (DA) and recall ( $r$ ), commission error ( $e_{com}$ ) and the omission error ( $e_{om}$ ):

$$r = DA = \frac{n_{TP}}{N}, \quad e_{com} = \frac{n_{FP}}{n_{TP} + n_{FP}}, \quad e_{om} = \frac{n_{FN}}{n_{TP} + n_{FN}}, \quad (4)$$

where  $n_{TP}$ ,  $n_{FN}$  and  $n_{FP}$  are the number of trees in TP, FN and FP category.  $N$  is the total number of the reference trees. Also, the precision ( $P$ ) and F-score( $F$ ) are derived as:

$$P = \frac{n_{TP}}{n_{TP} + n_{FP}}, \quad F = \frac{2rp}{r + p}. \quad (5)$$

These are normally effective in pixel-wise comparison or detection of trees in the sparsely vegetated area. However, it might be problematic when we are validating the algorithm in the densely vegetated area: one predicted tree may have

several reference trees nearby. Thus, it is hard to pair the predictions and references. To enforce a one-to-one correspondence, we wish only match the pair that has the largest overlapping area to each other. Therefore, following the measurement employed by Pascal visual object classes (VOC) challenge (Everingham *et al.*, 2010), we calculate the overlap ratio (OR) between all reference and predicted tree crowns to estimate how well they matched:

$$OR = \frac{2 * A_o}{A_r + A_p}, \quad (6)$$

where  $A_o$ ,  $A_r$ , and  $A_p$  are the size of overlapped, reference and prediction crown, respectively. However, if the corresponding trees have small overlap ratio than  $\gamma$ , we will discard this pair. We adopt  $\gamma=0.3$  as the threshold as it used in Yin and Wang (2016). For cases that: (1) one with no corresponding reference, it will be counted as a false positive; (2) one reference tree does not correspond to a predicted tree, it will be counted as a false negative. Finally, for the crown delineation accuracy, we estimate the average overlap ratio of the matched pairs:

$$CA = \frac{\sum OR(TP_i)}{n_{TP}}, \quad (7)$$

where  $CA$  is the crown accuracy,  $OR(TP_i)$  is the overlap ratio of correctly matched reference and prediction crowns.

## Results

In this work, we are limited to collect field samples and we generated the reference data by labeling the individual trees and their crowns with visual inspection as some previous studies did in their works (Zhen *et al.*, 2014). The three experimental sites variably include densely forested area, sparsely forested area, and urban area, respectively. For each site, we calculated the detection accuracy (DA), commission error ( $e_{com}$ ), omission error ( $e_{om}$ ) and crown accuracy  $CA$ , as well as the precision  $P$  and F-scores.

To demonstrate the advantage of the top-hat local maximum detector that is less sensitive to filter size, we implemented several local maximum filter based treetop detectors described in Wulder *et al.* (2000). These include fixed-window filters with sizes of 3,7,11,15,19 pixels corresponding to 1-6 meters and the filter with a variable size calculated by the slope breaks (SB) (Wulder *et al.*, 2000). In the experiment, we test these filters on the DSM in our comparative study while keeping all the other steps as the same and the final results can be found from Table 1 to Table 3.

As shown in Table 1 to Table 3, the proposed top-hat detector has the majority of highest performances across the three test sites. We believe this is due to the top-hat's characteristics of robustness and filter size insensitivity. For the fixed-window filters, the window with 7 pixels has better performance in the sparsely vegetated area, while the window with 11 pixels has better performance in the other two test sites. This shows that the performance of a fixed-window is dependent on the compatibility of the window size and the scenario. However, a suitable filter size cannot be predicted, and it is not possible to find a single filter suitable for all scenarios. And in general, the larger windows miss more small trees resulting in higher omission errors. Compared to the fixed-window detector, the proposed top-hat detector produces reliable treetop in all scenarios independent of the SE size. On the other hand, the variable-window filter based on the slope break obtains the worst results. This could be due to that the slope break distance is

sensitive to its nearby environment and cannot accurately reflect the crown size.

To understand the improvement of including 3D geometric information, we performed the treetop detection and superpixel segmentation without DSM. Following the idea in Wulder *et al.* (2000), we use the red channel

which has the best performance with the same detection processes excluding the 3D information. In Equation 3, the vertical distance is removed and the other parameters are tuned to obtain the optimal results which can be found in Table 4. Since the spectral-only based method solely considers the reflection variations of light off of trees, it is difficult to distinguish trees from other objects. Even with the help of NDVI

Table 1. The experiment results in the sparsely forested area which has total 307 reference trees. Np refers to the number of the prediction. TH is the proposed top-hat treetop detector, while F\_3, F\_7, F\_11, F\_15, and F\_19 represent the window filters with different sizes and SB stands for the variable window by slope breaks. The best numbers are bolded while other notations are the detection accuracy (DA), commission error ( $e_{com}$ ), omission error ( $e_{om}$ ) and crown accuracy (CA), precision (P) and F-scores (F).

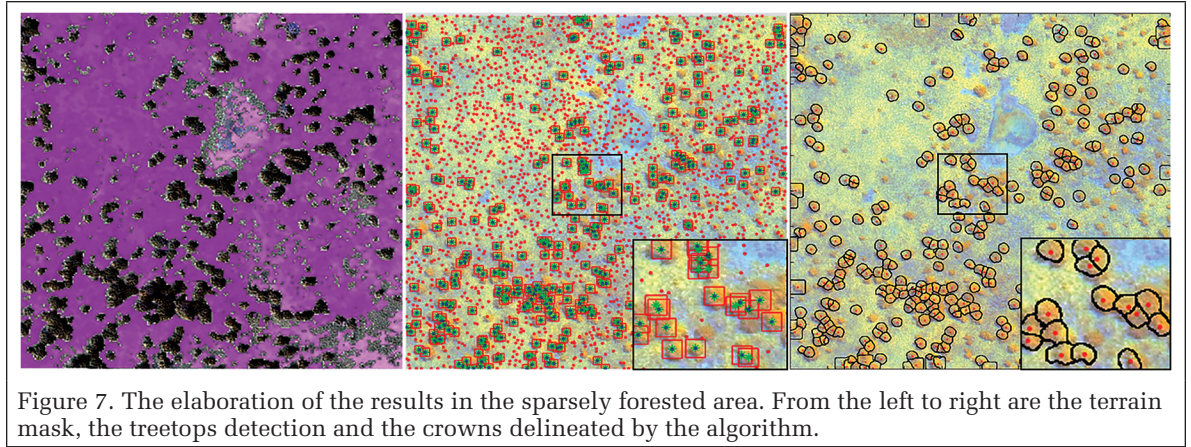
Detector	Np	DA	$e_{com}$	$e_{om}$	CA	P	F
TH	355	0.89	0.23	0.12	<b>0.64</b>	0.76	<b>0.82</b>
F_3	410	<b>0.90</b>	0.32	0.10	0.63	0.68	0.77
F_7	386	<b>0.90</b>	0.28	<b>0.09</b>	<b>0.64</b>	0.72	0.80
F_11	525	<b>0.90</b>	0.47	0.10	0.58	0.53	0.66
F_15	355	0.83	0.27	0.16	0.62	0.72	0.78
F_19	280	0.77	0.14	0.22	<b>0.64</b>	<b>0.85</b>	0.81
SB	219	0.67	<b>0.05</b>	0.32	0.56	<b>0.95</b>	0.79

Table 2. The experimental results in the densely forested area where has total 945 reference trees. The notations are the same as Table 1.

Detector	Np	DA	$e_{com}$	$e_{om}$	CA	P	F
TH	1442	<b>0.89</b>	0.41	<b>0.11</b>	<b>0.59</b>	0.58	0.70
F_3	349	0.24	0.34	0.76	0.58	0.66	0.36
F_7	1193	0.82	0.35	0.18	0.58	0.65	<b>0.73</b>
F_11	1330	0.83	0.41	0.17	0.58	0.59	0.69
F_15	1009	0.74	0.30	0.26	0.58	0.70	0.72
F_19	684	0.59	0.19	0.41	0.58	0.81	0.68
SB	543	0.51	<b>0.12</b>	0.50	<b>0.59</b>	<b>0.88</b>	0.64

Table 3. The experimental results in the urban area where has total 187 reference trees. The notations are the same as Table 1.

Detector	Np	DA	$e_{com}$	$e_{om}$	CA	P	F
TH	149	<b>0.53</b>	0.34	0.47	0.59	0.66	<b>0.59</b>
F_3	194	0.52	0.49	0.48	0.58	0.51	0.51
F_7	158	0.51	0.39	0.49	0.58	0.61	0.56
F_11	170	<b>0.53</b>	0.41	<b>0.46</b>	0.58	0.59	0.56
F_15	131	0.49	0.31	0.51	0.59	0.70	0.57
F_19	107	0.42	0.27	0.58	<b>0.61</b>	0.73	0.53
SB	69	0.29	<b>0.21</b>	0.71	<b>0.61</b>	<b>0.78</b>	0.42

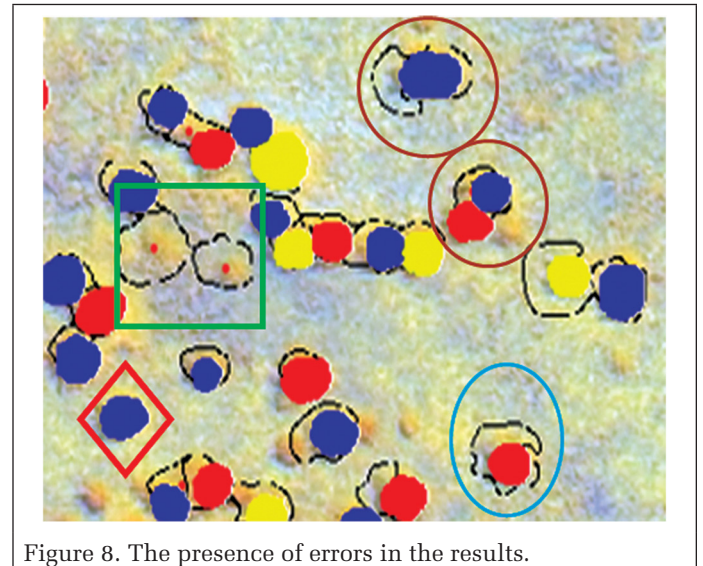


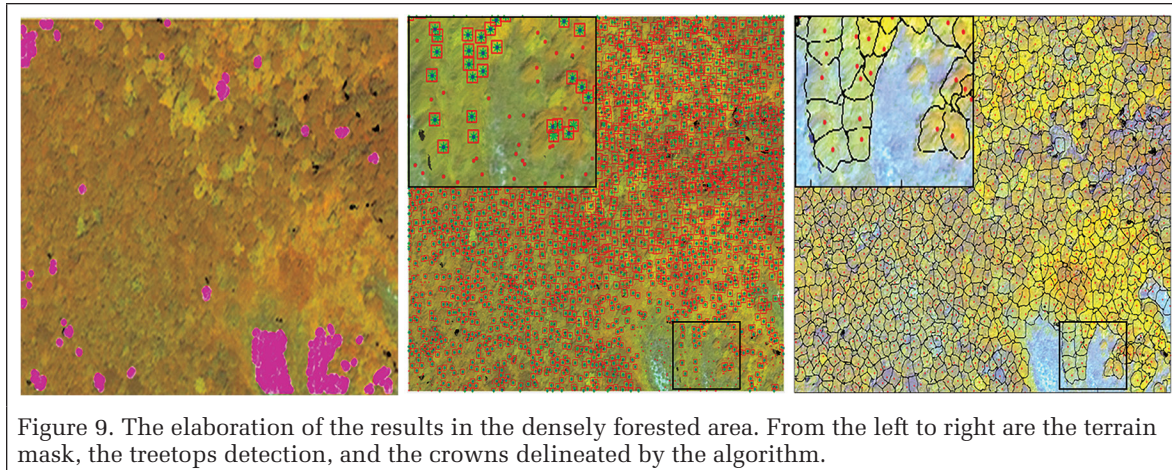
which can remove the non-vegetation area, the grassland and bushes can still be treat as part of the trees. As we can observe the results in the sparsely forested area and the urban area in Table 4, both of them have significantly high commission error ( $e_{com}$ ) due to the grasslands being identified as forests. Also, without the DSM, all the performances have significantly decreased which demonstrates the importance of including the 3D information.

As shown in Table 1 and Figure 7, at the sparsely forested area, the proposed algorithm predicted 355 trees comparing to 307 reference trees. The detection accuracy (DA) can reach as high as 0.89. For the one-to-one correctly matched trees, their average overlap is 0.64, which is better than the perfect match defined as 0.5 in Yin and Wang (2016).

Figure 8 shows examples of errors such as false negatives (diamond) and false positives (rectangle), as well as the miss-segmentations (circle), which are mainly caused by incorrectly detected treetops. The false negatives mainly exist in the short trees which are filtered by the above ground height check and non-maximum suppression that were previously described. Errors resulting in over-detection (circle in Figure 8) are mainly caused by the fact that grass near a short tree is confused as part of the crown.

In the densely forested area, the trees are highly overlapped with each other making it extremely difficult to distinguish individual crowns even by visual identification. As observed in Figure 9, the algorithm extracted the trees with a detection accuracy of 0.89 (Table 2). As compared to the sparsely





two additional tests: (1) giving a constant height, here we use 10 meters (C\_10), to all trees as an assumption., and (2) using the lowest point in the test area as the ground to calculate tree height. For the second test, we constrain the maximal tree height to avoid picking up the artifacts. Since the size of non-

forested area, the commission error ( $e_{com}$ ) is relatively large, indicating relatively more false detections. This may be due to that the dense canopies make the incorrectly detected treetops passed the postprocessing and identified as real trees. Furthermore, the low crown precision may be caused by partial detection and errors in the DSM. The partial detection refers to the detection that some branches of the tree are not included in the crown. For example, several treetops may be incorrectly detected in a large tree causing some branches could be misassigned to them. However, the post-processing may remove these incorrect detections and causes the true treetop only be assigned part of the crown. On the other hand, in the densely forested area, it is easy to mismatch feature points which are used to generate DSM from multi-view images. Hence, in this area, the 3D structure information for treetop detection may be not correct and further affect the superpixel segmentation.

One consideration in this area is that the terrain area is too limited to offer an accurate estimation of the tree height. To investigate the situation without the DTM, we conducted

maximum suppression in the treetop refinement is related to the tree height and can further affect the final detections, we evaluated two maximal tree height constraints, 13 meters (L\_13) and 15 meters (L\_15).

The results of these tests can be found in Table 5, and they show that the performances in all cases are relatively consistent (the worst decrease of DA is 0.08 of L\_15). For the constant height (C\_10), the performance of detection accuracy (DA) and omission error ( $e_{om}$ ) has even slightly increased (0.01) as this particular threshold results in more tree segments. However, some of these new trees are incorrect which increase the commission error ( $e_{com}$ ) and decrease the precision. Comparing the next two tests that set the lowest point as ground, the L\_13 has higher DA (0.07) than the L\_15. From the Table 6 which presents the number of treetops after each processing, we can find the main difference between L\_13 and L\_15 is in the non-maximum suppression step whose filter size is dynamically determined by the tree height. From the results, we can infer that by subtracting the lowest point, plenty of trees have reached the maximal tree height and a higher maximal value offers a larger non-maximum suppression size thus filtered more potential trees. Comparing the DTM based height and the assumed height, the main difference is in the above ground height check previously described. Since the DTM can offer more accurate above ground tree height estimation, some lower trees or vegetation would be removed in the height check while with the assumed heights, all the treetops are passed. However, with a suitable tree height assumption, the abnormal low treetops can be eliminated by the non-maximum suppression such as the comparable performances shown in the Table 5. Hence, we can see that the proposed algorithm is able to maintain a high performance even without accurate DTM in the densely forested area.

Table 4. The results with (S\_3D) and without (S\_2D) 3D information at the sparsely forested area (site A), densely forested area (site B), and the urban area (site C). The notations are the same as Table 1.

Site	method	Np	DA	$e_{com}$	$e_{om}$	CA	P	F
A	S_3D	355	0.89	0.23	0.12	0.64	0.76	0.82
	S_2D	2439	0.70	0.91	0.30	0.49	0.09	0.16
B	S_3D	1442	0.89	0.41	0.11	0.59	0.58	0.70
	S_2D	2053	0.84	0.61	0.16	0.52	0.39	0.53
C	S_3D	149	0.53	0.34	0.47	0.59	0.66	0.59
	S_2D	143	0.18	0.76	0.82	0.53	0.24	0.21

Table 5. The detection results in the densely forested area with/without DTM information.

	DA	$e_{com}$	$e_{om}$	CA	P	F
DTM	0.89	0.41	0.11	0.59	0.58	0.70
C_10	0.90	0.52	0.10	0.58	0.48	0.63
L_13	0.88	0.47	0.12	0.58	0.53	0.64
L_15	0.81	0.39	0.19	0.58	0.61	0.69

Table 6. The numbers of treetops after each processing step.

	Initial	Height Check	Non-Maximum Suppression	Post-Processing
DTM	2753	2491	1515	1442
C_10	2753	2753	1801	1759
L_13	2753	2753	1627	1588
L_15	2753	2753	1278	1253

At the test site C, the surface objects are complicated. However, as shown in Figure 10, the proposed algorithm still detected most of the trees even though they have different crown sizes and heights. With the help of 3D structural and spectral information, the proposed algorithm is able to distinguish the trees from confusing objects such as bushes and man-made objects. From Table 3, we can observe the  $e_{com}$  is large (0.47) and from Figure 11 we can find that the trees with small crown size or nearby buildings are not detected. We believe this is mainly caused by the limited precision of the DSM. The trees that are too thin or too close to other objects may not be completely represented in the DSM, as Figure 11 shows below.

The resolution of the DSM is critical and the 0.3 meters GSD may be insufficient to represent the details of small trees. In addition, the generation may introduce geometric errors

during the dense matching process, such as in specular reflection and textureless regions. Hence, we believe a better DSM can further improve the performance of the proposed method.

## Conclusions

In this paper, we developed a novel and automated method to fully utilize the multi-view high-resolution satellite images for ITDD. As compared to previous image-based methods, we adopt the DSM (digital surface model) derived from the multi-view satellite images and combine the multi-spectral information to identify treetops and their crowns in areas with varying canopy densities. A quantitative evaluation of three different sites shows that the proposed method is able to detect individual trees in different regions with various surface covers. The algorithm had its highest performance in the sparsely forested area with 89% detection accuracy, 0.23 commission errors and 0.12 omission errors. Even for the densely forested area, traditionally deemed as particularly challenging, the algorithm still achieved 89% detection accuracy with the slightly larger commission and omission errors.

Despite the superior results achieved by our methods, we are aware that significant vulnerabilities still exist, mainly due to the complicated surfaces of overly dense forests as well as propagated DEM errors. Detection in highly heterogeneous forests with multiple layers is challenging for even manual identification. The variations of trees and man-made objects in close proximity to the vegetation in urban areas create a very complicated scenario for individual tree detection. In the future, we plan to include dynamically adjusted tree templates of various scales in both 2D and 3D to increase the robustness to DEM errors and reduce overdetection in dense forest regions.

## Acknowledgments

The authors would like to thank John Hopkins University Applied Physics Lab for providing the Multi-view 3D Benchmark dataset used in this study. We would also thank Xing Pei and Ruopeng Wang from Lanzhou Jiaotong University for providing the tree labels. Finally, we thank jiaqiang Li from Future Cities Laboratory in Singapore-ETH Centre for the using of the CloudCompare® software for the terrain detection.

## References

Bosch, M., Kurtz, Z., Hagstrom, S., Brown, M., 2016. A multiple view stereo benchmark for satellite imagery, *Applied Imagery Pattern Recognition Workshop (AIPR)*, 2016 IEEE. IEEE, pp. 1-9.

Bosch, M., Leichtman, A., Chilcott, D., Goldberg, H., Brown, M., 2017. Metric evaluation pipeline for 3d modeling of urban scenes, *The International Archives of Photogrammetry, Remote Sensing and Spatial Information Sciences*, 42, 239.

Desktop, E.A., 2011. Release 10. Redlands, CA: *Environmental Systems Research Institute*, pp. 437-438.

Everingham, M., Van Gool, L., Williams, C.K., Winn, J., Zisserman, A., 2010. The pascal visual object classes (voc) challenge, *International Journal of Computer Vision* 88:303-338.



Figure 10. The elaboration of the results in the urban area. From the left to right are the terrain mask, the treetops detection and the crowns delineated by the algorithm.

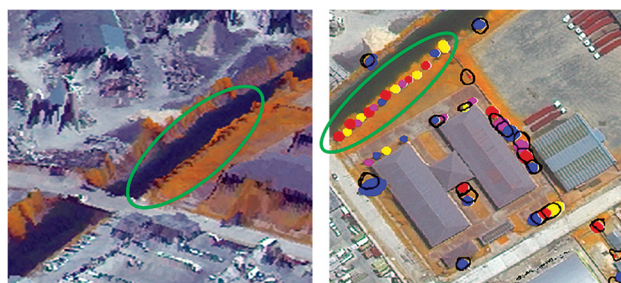


Figure 11. The mis-detection of thin trees. The left image is the 3D visualization of the test site and the right image is the detection results marked with reference trees. The ellipse marks the missing trees that only show as small bumps at the DSM.

Felzenszwalb, P.F., Huttenlocher, D.P., 2004. Efficient graph-based image segmentation. *International Journal of Computer Vision*, 59:167-181.

Ferraz, A., Saatchi, S., Mallet, C., Meyer, V., 2016. Lidar detection of individual tree size in tropical forests, *Remote Sensing of Environment* 183:318-333.

Garrity, S.R., Meyer, K., Maurer, K.D., Hardiman, B., Bohrer, G., 2012. Estimating plot-level tree structure in a deciduous forest by combining allometric equations, spatial wavelet analysis and airborne lidar, *Remote Sensing Letters*, 3:443-451.

Gevaert, C., Persello, C., Nex, F., Vosselman, G., 2018. A deep learning approach to dtm extraction from imagery using rule-based training labels, *ISPRS Journal of Photogrammetry and Remote Sensing* 142:106-123.

Gonçalves, A.C., Sousa, A.M., Mesquita, P.G., 2017. Estimation and dynamics of above ground biomass with very high resolution satellite images in pinus pinaster stands, *Biomass and Bioenergy* 106:146-154.

Gougeon, F.A., Leckie, D.G., 2006. The individual tree crown approach applied to ikonos images of a coniferous plantation area, *Photogrammetric Engineering & Remote Sensing*, 72:1287-1297.

Hu, H., Ding, Y., Zhu, Q., Wu, B., Lin, H., Du, Z., Zhang, Y., Zhang, Y., 2014. An adaptive surface filter for airborne laser scanning point clouds by means of regularization and bending energy. *ISPRS Journal of Photogrammetry and Remote Sensing* 92:98-111.

Kathuria, A., Turner, R., Stone, C., Duque-Lazo, J., West, R., 2016. Development of an automated individual tree detection model using point cloud lidar data for accurate tree counts in a pinus radiata plantation, *Australian Forestry*, 79:126-136.

Ke, Y., Quackenbush, L.J., 2011. A review of methods for automatic individual tree-crown detection and delineation from passive remote sensing, *International Journal of Remote Sensing* 32:4725-4747.

- Koch, B., Heyder, U., Weinacker, H., 2006. Detection of individual tree crowns in airborne lidar data, *Photogrammetric Engineering & Remote Sensing*, 72:357-363.
- Liu, T., Abd-Elrahman, A., 2018. Deep convolutional neural network training enrichment using multi-view object-based analysis of unmanned aerial systems imagery for wetlands classification, *ISPRS Journal of Photogrammetry and Remote Sensing*, 139:154-170.
- Liu, T., Im, J., Quackenbush, L.J., 2015. A novel transferable individual tree crown delineation model based on fishing net dragging and boundary classification, *ISPRS Journal of Photogrammetry and Remote Sensing* 110, 34-47.
- Lu, X., Guo, Q., Li, W., Flanagan, J., 2014. A bottom-up approach to segment individual deciduous trees using leaf-off lidar point cloud data, *ISPRS Journal of Photogrammetry and Remote Sensing*, 94:1-12.
- Mohan, M., Silva, C.A., Klauberg, C., Jat, P., Catts, G., Cardil, A., Hudak, A.T., Dia, M., 2017. Individual tree detection from unmanned aerial vehicle (uav) derived canopy height model in an open canopy mixed conifer forest, *Forests*, 8:340.
- Papon, J., Abramov, A., Schoeler, M., Worgotter, F., 2013. Voxel cloud connectivity segmentation-supervoxels for point clouds, *Proceedings of the IEEE Conference on Computer Vision and Pattern Recognition*, pp. 2027-2034.
- Popescu, S.C., Wynne, R.H., Nelson, R.F., 2002. Estimating plot-level tree heights with lidar: Local filtering with a canopy-height based variable window size, *Computers and Electronics in Agriculture*: 37:71-95.
- Pouliot, D., King, D., 2005. Approaches for optimal automated individual tree crown detection in regenerating coniferous forests. *Canadian Journal of Remote Sensing*, 31:255-267.
- Qin, R., 2017. Automated 3d recovery from very high resolution multi-view satellite images, *Proceedings of the ASPRS (IGTF) Annual Conference*, Baltimore, Maryland, p. 10.
- Qin, R., Fang, W., 2014. A hierarchical building detection method for very high resolution remotely sensed images combined with dsm using graph cut optimization, *Photogrammetric Engineering & Remote Sensing*:80, 873-883.
- Sousa, A.M., Gonçalves, A.C., Mesquita, P., da Silva, J.R.M., 2015. Biomass estimation with high resolution satellite images: A case study of quercus rotundifolia, *ISPRS Journal of Photogrammetry and Remote Sensing*, 101:69-79.
- Strîmbu, V.F., Strîmbu, B.M., 2015. A graph-based segmentation algorithm for tree crown extraction using airborne lidar data, *ISPRS Journal of Photogrammetry and Remote Sensing* 104:30-43.
- Véga, C., Hamrouni, A., El Mokhtari, S., Morel, J., Bock, J., Renaud, J.-P., Bouvier, M., Durrieu, S., 2014. Ptrees: A point-based approach to forest tree extraction from lidar data, *International Journal of Applied Earth Observation and Geoinformation*, 33:98-108.
- Weng, E., Malyshev, S., Lichstein, J., Farrior, C., Dybzinski, R., Zhang, T., Shevliakova, E., Pacala, S., 2015. Scaling from individual trees to forests in an earth system modeling framework using a mathematically tractable model of height-structured competition, *Biogeosciences*, 12:2655-2694.
- Wulder, M., Niemann, K.O., Goodenough, D.G., 2000. Local maximum filtering for the extraction of tree locations and basal area from high spatial resolution imagery, *Remote Sensing of Environment*, 73:103-114.
- Wulder, M.A., Coops, N.C., Hudak, A.T., Morsdorf, F., Nelson, R., Newnham, G., Vastaranta, M., 2013. Status and prospects for lidar remote sensing of forested ecosystems: *Canadian Journal of Remote Sensing* 39:S1-S5.
- Yin, D., Wang, L., 2016. How to assess the accuracy of the individual tree-based forest inventory derived from remotely sensed data: A review, *International Journal of Remote Sensing* 37:4521-4553.
- Zhang, W., Qi, J., Wan, P., Wang, H., Xie, D., Wang, X., Yan, G., 2016. An easy-to-use airborne lidar data filtering method based on cloth simulation, *Remote Sensing*, 8:501.
- Zhen, Z., Quackenbush, L.J., Zhang, L., 2014. Impact of tree-oriented growth order in marker-controlled region growing for individual tree crown delineation using airborne laser scanner (als) data, *Remote Sensing*, 6:555-579.

# SUSTAINING MEMBERS

## **Aerial Services, Inc.**

Cedar Falls, Iowa  
www.AerialServicesInc.com  
Member Since: 5/2001

## **Applanix**

**a Trimble Company**  
Richmond Hill, Ontario, Canada  
www.applanix.com  
Member Since: 7/1997

## **Ayres Associates, Inc.**

Madison, Wisconsin  
www.AyresAssociates.com  
Member Since: 1/1953

## **Bohannon Huston, Inc.**

Albuquerque, New Mexico  
www.bhinc.com  
Member Since: 11/1992

## **Cardinal Systems, LLC**

Flagler Beach, Florida  
www.cardinalsystems.net  
Member Since: 1/2001

## **Certainty 3D LLC**

Orlando, Florida  
www.certainty3d.com  
Member Since: 3/2011

## **DAT/EM Systems International**

Anchorage, Alaska  
www.datem.com  
Member Since: 1/1974

## **Dewberry**

Fairfax, Virginia  
www.dewberry.com  
Member Since: 1/1985

## **DigitalGlobe, Inc.**

Longmont, Colorado  
www.digitalglobe.com  
Member Since: 6/1996

## **Environmental Research Incorporated**

Linden, Virginia  
www.eri.us.com  
Member Since: 8/2008

## **Esri**

Redlands, California  
www.esri.com  
Member Since: 1/1987

## **GeoBC**

Victoria, Canada  
www.geobc.gov.bc.ca  
Member Since: 12/2008

## **GeoCue Group**

Madison, Alabama  
info@geocue.com  
Member Since: 10/2003

## **Geomni, Inc.**

Lehi, Utah  
Geomni.net/psm  
Member Since: 03/2018

## **GeoWing Mapping Inc.**

Oakland, California  
www.geowingmapping.com  
Member Since: 1/2017

## **Global Science & Technology, Inc.**

Greenbelt, Maryland  
www.gst.com  
Member Since: 10/2010

## **GPI Geospatial Inc.**

**formerly Aerial Cartographics of America, Inc. (ACA)**  
Orlando, Florida  
www.aca-net.com  
Member Since: 10/1994

## **Keystone Aerial Surveys, Inc.**

Philadelphia, Pennsylvania  
www.keystoneaerialsurveys.com  
Member Since: 1/1985

## **Kucera International**

Willoughby, Ohio  
www.kucerainternational.com  
Member Since: 1/1992

## **LizardTech**

Portland, Oregon  
www.lizardtech.com  
Member Since: 9/1997

## **Martinez Geospatial, Inc. (MTZ)**

Eagan, Minnesota  
www.mtzgeo.com  
Member Since: 1/1979

## **Merrick & Company**

Greenwood Village, Colorado  
www.merrick.com/gis  
Member Since: 4/1995

## **Microsoft UltraCam Team (Vexcel Imaging, GmbH)**

Graz, Austria  
www.microsoft.com/ultracam  
Member Since: 6/2001

## **Michael Baker Jr., Inc.**

Beaver, Pennsylvania  
www.mbakercorp.com  
Member Since: 1/1950

## **PCI Geomatics**

Richmond Hill, Ontario, Canada  
www.pcigeomatics.com  
Member Since: 1/1989

## **Pickett and Associates, Inc.**

Bartow, Florida  
www.pickettusa.com  
Member Since: 4/2007

## **Office of Surface Mining**

Denver, Colorado  
www.tips.osmre.gov  
Member Since: 8/2017

## **Quantum Spatial, Inc.**

Sheboygan Falls, Wisconsin  
www.quantumspatial.com  
Member Since: 1/1974

## **Robinson Aerial Survey, Inc. (RAS)**

Hackettstown, New Jersey  
www.robinsonaerial.com  
Member Since: 1/1954

## **Routescene, Inc.**

Durango, Colorado  
www.routescene.com/  
Member Since: 12/2007

## **Sanborn Map Company**

Colorado Springs, Colorado  
www.sanborn.com  
Member Since: 10/1984

## **Sidwell Company**

St. Charles, Illinois  
www.sidwellco.com  
Member Since: 11/1992

## **SkyIMD - Imaging Mapping & Data**

Richmond, California  
www.skyimd.com  
Member Since: 1/2017

## **Surveying And Mapping, LLC (SAM)**

Austin, Texas  
www.sam.biz  
Member Since: 12/2005

## **Teledyne Optech**

Toronto, Canada  
www.teledyneoptech.com  
Member Since: 1/1999

## **Terra Remote Sensing (USA) Inc.**

Bellevue, Washington  
www.terraremove.com  
Member Since: 10/2016

## **The Airborne Sensing Corporation**

Toronto, Canada  
www.airsensing.com  
Member Since: 7/2003

## **Towill, Inc.**

San Francisco, California  
www.towill.com  
Member Since: 1/1952

## **University of Twente/Faculty ITC**

Enschede, Netherlands  
www.itc.nl  
Member Since: 1/1992

## **U.S. Geological Survey**

Reston, Virginia  
www.usgs.gov  
Member Since: 4/2002

## **Woolpert LLP**

Dayton, Ohio  
www.woolpert.com  
Member Since: 1/1985

# The Potential of Multispectral Vegetation Indices Feature Space for Quantitatively Estimating the Photosynthetic, Non-Photosynthetic Vegetation and Bare Soil Fractions in Northern China

Guoxiong Zheng, Anming Bao, Xiaosong Li, Liangliang Jiang, Cun Chang, Tao Chen, and Zhihai Gao

## Abstract

Non-photosynthetic vegetation (NPV) is widely distributed in the arid and semi-arid area, especially in the sandy areas. The hyperspectral-based cellulose absorption index (CAI) is an accepted method for estimating the cover fractions of NPV. However, the spaceborne hyperspectral data currently available to us are very limited. In this study, we tried to identify one or more combinations based on the multispectral vegetation indices feature space model to quantitatively estimate the PV, NPV and bare soil fractions of the Otindag Sandy Land in northern China. Three frequently-used green vegetation indices, NDVI, EVI and OSAVI, and nine multispectral-based indices sensitive to NPV were used to examine the spatial patterns based on the field measured endmember spectra and non-growing and growing season Landsat-8 OLI image reflectance spectra. The capabilities of these different combinations were tested in this study area using mosaicked Landsat-8 OLI imagery. The results show that the feature space of different combinations based on the field measured spectra and image reflectance spectra has good consistency. The separability of feature space determines the availability of this model. The normalized difference senescent vegetation index (NDSVI) and brightness index (BI) were found to have greater potential to combine with the three selected green vegetation indices for simultaneous estimation of the fractional cover of PV, NPV, and bare soil in the Otindag Sandy Land because of their clear and separable feature space. We obtained the best and medium-precision estimates for NDVI-NDSVI ( $f_{PV}$ : RMSE=0.26;  $f_{NPV}$ : RMSE=0.17) and OSAVI-BI ( $f_{PV}$ : RMSE=0.27;  $f_{NPV}$ : RMSE=0.25) for 104 field observations.

Guoxiong Zheng is with the State Key Laboratory of Desert and Oasis Ecology, Xinjiang Institute of Ecology and Geography, Chinese Academy of Sciences, Urumqi 830011, China; University of Chinese Academy of Sciences, Beijing 100049, China; and formerly with the Key Laboratory of Digital Earth Science, Institute of Remote Sensing and Digital Earth, Chinese Academy of Sciences, Beijing 100094, China (z\_gxiong@foxmail.com).

Anming Bao, Liangliang Jiang, Cun Chang, and Tao Chen are with the State Key Laboratory of Desert and Oasis Ecology, Xinjiang Institute of Ecology and Geography, Chinese Academy of Sciences, Urumqi 830011, China.

Xiaosong Li is with the Key Laboratory of Digital Earth Science, Institute of Remote Sensing and Digital Earth, Chinese Academy of Sciences, Beijing 100094, China. lixs@radi.ac.cn

Zhihai Gao is with the Institute of Forest Resources Information Technique, Chinese Academy of Forestry, Beijing 100091, China.

## Introduction

Remote sensing of vegetation coverage and condition is needed to understand the impacts of land degradation resulting from climate change in sandy regions, which is caused by continued deterioration of dryland ecosystems characterized by a landscape mosaic of sparse trees, shrubs, and grasses co-existing at fine spatial scales (Yang *et al.*, 2012). In these regions, non-photosynthetic vegetation (NPV) is as important as photosynthetic vegetation (PV) in reducing water and soil erosion, conserving biodiversity, promoting nutrient cycles, and increasing carbon storage (Xu *et al.*, 2014). Scientifically robust and consistent information on the fractional cover of photosynthetic vegetation ( $f_{PV}$ ) and non-photosynthetic vegetation ( $f_{NPV}$ ) is critical when assessing land use and monitoring desertification processes (Guerschman *et al.*, 2015). Over large areas, e.g., on a global scale, the measurement of these fractions remains a challenge for land use managers because of the associated spatial extent and the difficulty of collecting this information in the field (Meyer and Okin, 2015). Remote sensing offers enormous potential to estimate these fractions at a large scale that might be costly, labor-intensive, and spatially discontinuous using only field measurements (Gitelson *et al.*, 2002).

Many methods have been devised to measure PV, NPV, and bare soil cover fractions in different ecological environments using remote sensing data (Asner *et al.*, 2005; Hill *et al.*, 2016; Jackson and Prince, 2016; Meyer and Okin, 2015; Verrelst *et al.*, 2007). In general, they can be classified into two categories. One tends to use specific spectral regions to detect PV, NPV, or bare soil components, and has developed many vegetation indices (VIs), such as the normalized difference vegetation index (NDVI) for green vegetation (Rouse, 1973) and the cellulose absorption index (CAI) for plant litter or crop residues (Daughtry *et al.*, 2004; Nagler *et al.*, 2003). However, these VIs only provide information on one ground cover component (Xu *et al.*, 2014). Another method, termed spectral mixture analysis (SMA), contributes to the assumption that a mixed pixel can be resolved into a group of spectral endmembers and represented as a linear or nonlinear combination of these spectral endmembers weighted by their sub-pixel fractional cover (Adams *et al.*, 1986). This method is a well-established and effective technique to address the spectral mixture problem (Somers *et al.*, 2011), but the estimation results largely depend on endmember selection and its ability to account for temporal and spatial variability (Peterson *et al.*, 2015; Somers *et al.*, 2011).

Photogrammetric Engineering & Remote Sensing  
Vol. 85, No. 1, January 2019, pp. 65–76.  
0099-1112/18/65–76

© 2019 American Society for Photogrammetry  
and Remote Sensing  
doi: 10.14358/PERS.85.1.65

On the basis of a previous study (Daughtry *et al.*, 2006), Guerschman *et al.* (2009) proposed a new unmixing method for  $f_{PV}$  and  $f_{NPV}$  estimation using the two complementary indices NDVI and CAI, and successfully applied it to the Australian tropical savannah region and also validated it in the semi-arid grasslands of northern China using EO-1 Hyperion data (Li *et al.*, 2015). In addition, Guerschman *et al.* (2009) found that a simple ratio of moderate-resolution imaging spectroradiometer (MODIS) bands 7 and 6, also termed SWIR32, could be a surrogate for CAI to resolve the fractions of PV, NPV, and bare soil in the same area of Australia. However, recent research has suggested that SWIR32 could be limited in approximating the CAI in some more sparsely vegetated savannah regions such as the Australian savannah region and more complex savannah systems such as those of southern Africa (Hill *et al.*, 2016; Zhou *et al.*, 2016).

Hyperspectral data is an ideal tool for estimating the fractional cover of PV and NPV simultaneously because the spectral resolution allows for the detection of cellulose and lignin absorption features (Peterson *et al.*, 2015), which can be used to separate NPV from PV and the bare soil background. However, hyperspectral data are still not available in most regions around the world because of the limited number of sensors and their narrow swath (Xu *et al.*, 2014). In contrast, abundant multispectral data have been collected across the Earth's surface in a long time series. How to make use of the temporal and spatial advantage of these data for estimation of  $f_{PV}$  and  $f_{NPV}$  over larger regions, particularly in sandy areas, becomes more important. Although it is still a challenge for multispectral data, several multispectral-based non-photosynthetic vegetation indices (NPVIs), such as the Landsat TM-based normalized differences senescent vegetation index (NDSVI) (Qi *et al.*, 2002), modified soil adjusted crop residue index (MSACRI) (Bannari *et al.*, 2000), ASTER-based shortwave infrared normalized difference residue index (SINDRI) (Serbin *et al.*, 2009) and MODIS-based dead fuel index (DFI) (Cao *et al.*, 2010), have been developed to extract the fraction of the NPV component.

The main purpose of this study was to identify which multispectral-based NPVI can provide the best estimation of  $f_{PV}$  and  $f_{NPV}$  in the Otindag Sandy Land by combining with three selected photosynthetic vegetation indices (PVI<sub>s</sub>). This study was divided into two parts. First, an endmember spectral library of PV, NPV, and bare soil collected from field measurements and surface reflectance data collected in the EO-1 Hyperion and Landsat-8 OLI images were used to validate whether the endmember spectral features of PV, NPV, and bare soil satisfies the assumption of the triangular linear distribution of the vegetation index feature space model.

Second, the mosaicked Landsat-8 multispectral surface reflectance imagery covering the entire Otindag Sandy Land and site data from the sampling work was used to (1) map the fractional cover of PV, NPV, and bare soil using a linear

unmixing method based on different PVI-NPVI combinations, and (2) evaluate the accuracy of the model estimation comparing it to the site data.

## Study Area

Otindag Sandy Land is among the top ten deserts of China in terms of area. It is in central-eastern Inner Mongolia in northern China (Figure 1), and occupies an area of ~ 52,000 km<sup>2</sup> with elevations of 1100 to 1400 m above sea level decreasing from southeast to northwest (Liu *et al.*, 2008; Wang *et al.*, 2014). The Otindag Sandy Land is within the East Asia monsoon climatic region. During summer, the prevailing southeasterly wind pushes humid air masses from the Pacific Ocean over the region. In contrast, the dominant wind during winter is northwesterly and frequent dust storms usually occur during spring (Gong *et al.*, 2013; Li *et al.*, 2002). The average annual precipitation is between 200 mm and 400 mm. Approximately 80 to 90% of the precipitation falls between July and September. The precipitation also shows a spatial difference in the region. The annual precipitation in the southeast part can reach 350 mm and even 400 mm, while it is only 200 mm or less in the northwest part (Zheng *et al.*, 2006). The average annual temperature is 0 to 3 °C. The average annual wind speed is 4 to 5 m/s, mainly occurring during spring (Zhou *et al.*, 2008). The average annual evaporation is 2,000 to 2,700 mm, which is 7 to 10 times the rainfall. The average annual hours of sunshine are 3,000 to 3,200 h and the cumulative time the temperature is above 10 °C is 2,400 to 2,600 h.

Vegetation species of the Otindag Sandy Land are diverse and are characterized by shrubland prairie and meadow

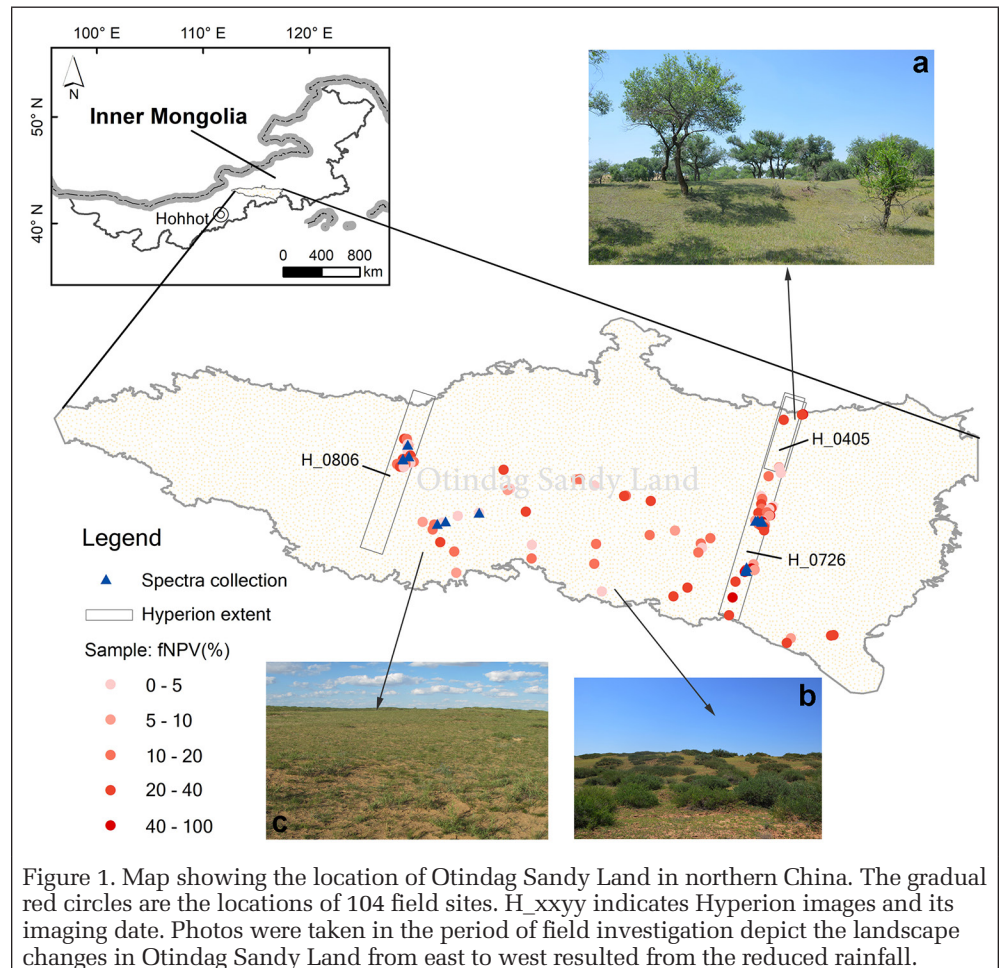


Figure 1. Map showing the location of Otindag Sandy Land in northern China. The gradual red circles are the locations of 104 field sites. H\_ xxyy indicates Hyperion images and its imaging date. Photos were taken in the period of field investigation depict the landscape changes in Otindag Sandy Land from east to west resulted from the reduced rainfall.

prairie in the east, semi-arid grassland in the central area, and desert prairie in the west. A total of 952 flowering plant species have been recorded, from 75 families and 348 genera. The two largest families are *Compositae* and *Gramineae*, with 48 genera and 150 species and 42 genera and 124 species, respectively, (Zheng *et al.*, 2006). The NPV component is prevalent in the Otindag Sandy Land because of its unique climatic conditions and geographical location (Zheng *et al.*, 2016). Dunes are mostly semi-stabilized to stabilized, and dune fields extend from the northwest to southeast, with heights ranging from 10 to 30 m. Stabilized linear dunes mainly occur in the northwest, while parabolic to barchan dunes occur in the southeast (Gong *et al.*, 2013).

## Materials and Methods

### Datasets

#### Remotely Sensed Data

Three EO-1 Hyperion images and six Landsat-8 OLI images were employed in this study (Table 1). Their acquisition time is broadly in line with the date of the field investigation. All images were downloaded from the U.S. Geological Survey (USGS) Earth Explorer website (<http://earthexplorer.usgs.gov/>). The Hyperion data were acquired on 05 April, 26 July, and 06 August, 2014. It has 242 spectral bands with a swath 185 km in length and 7.5 km in width at 30 m spatial resolution. The flight time of the selected Landsat-8 OLI images is almost the same as that of the Hyperion scenes (Table 1), and they have nine multispectral bands (with the exception of pan-chromatic and cirrus bands in this study) with the same pixel size as that of the Hyperion images, but a broader spatial extent of 185 km × 185 km. The product level is Level 1T for all with a primary precision and terrain correction. The Hyperion images are used to validate the spatial distribution of NDVI-CAI and construct other corresponding PVI-CAI feature space as a reference for multispectral index-based feature space.

The Hyperion 1–7, 58–76, and 225–242 bands were already set to values of zero when it produced (Barry, 2001), and the other bands of 121–126, 167–180, and 222–224 have severe noise because of strong water vapor absorption (Datt *et al.*, 2003). These bands were typically removed from processing at first. Then, the Hyperion images were radiometrically calibrated to spectral radiance using gain and offset information in the image header file, and further calibrated to apparent surface reflectance using the MODTRAN4 radiation transfer code (developed by Spectral Sciences, Inc.) to correct images for atmospheric water vapor, oxygen, carbon dioxide, methane, ozone absorption, and molecular and aerosol scattering. Correcting for atmospheric effects is particularly important for hyperspectral sensors. Finally, the atmospherically corrected Hyperion images were further geometrically rectified using the corresponding Landsat-8 OLI images.

Table 1. Data details used in this study: Three EO-1 Hyperion scenes and three corresponding region Landsat-8 OLI images (marked as a single asterisk) were used for the feature space analysis of the selected PVIs and NPVIs. The multispectral imagery of Otindag Sandy Land was mosaicked by the Landsat-8 OLI images acquired on 01 August 2014, and other three scenes in the list below.

Satellite & Sensor	Acquisition Time	WRS2 Path/Row	Cloud Cover (%)	Pixel Size (m)
EO-1 Hyperion	05 April 2014 02:21:06PM	124/030	0 to 9	30
	26 July 2014 02:12:10PM	124/030	10 to 19	
	06 August 2014 02:22:52PM	125/030	10 to 19	
Landsat-8 OLI	04 April 2014 02:59:06PM*	124/030	0.24	30
	25 July 2014 02:58:47PM*	124/030	8.71	
	01 August 2014 03:05:03PM*	125/030	0.01	
	04 September 2014 02:52:51PM	123/030	0.00	
	26 August 2014 02:58:59PM	124/030	0.32	
	09 September 2014 03:11:24PM	126/030	0.36	

The Landsat-8 OLI imagery was also calibrated from digital values to radiance values using the gains and offsets for each band, and further converting the radiance values to surface reflectance values. Four Landsat-8 OLI surface reflectance images acquired on 01 August, 26 August, 04 September, and 09 September, 2014, were mosaicked to cover the entire Otindag Sandy Land, and the mosaicked imagery was subsequently subset from the boundary of the Otindag Sandy Land.

#### Endmember Spectra Collection

The endmember reflectance spectra collection of PV, NPV, and bare soil was conducted on 27 July, 13 July, 07 August, and 11 August 2014, using a portable spectrometer (Analytical Spectral Devices Inc., Boulder, Colorado) at 1.4-nm intervals in the visible and near-infrared (350–1100 nm) and at 2.2-nm intervals in the near-infrared to shortwave infrared (1100–2500 nm) using a 25° sensor fore optic. Figure 1 shows the locations of the endmember reflectance spectra collection. A total of 19 reflectance spectra of PV, 8 reflectance spectra of NPV, and 10 reflectance spectra of bare soil were collected across the study area. All measurements were taken between 10:00 am and 2:00 pm of local solar noon under cloudless skies. The detector was held at 1 m above the top of the PV or NPV canopy or bare soil surface in the nadir position. Before each measurement, the spectroradiometer was calibrated to a Spectralon white reference target. Based on the spectral response function of the Landsat-8 OLI sensor, the field measured endmember spectra were resampled to Landsat-8 OLI band ranges. Figure 2 shows these resampled field reflectance spectra curves of PV, NPV, and bare soil endmember and their mean reflectance spectral curves.

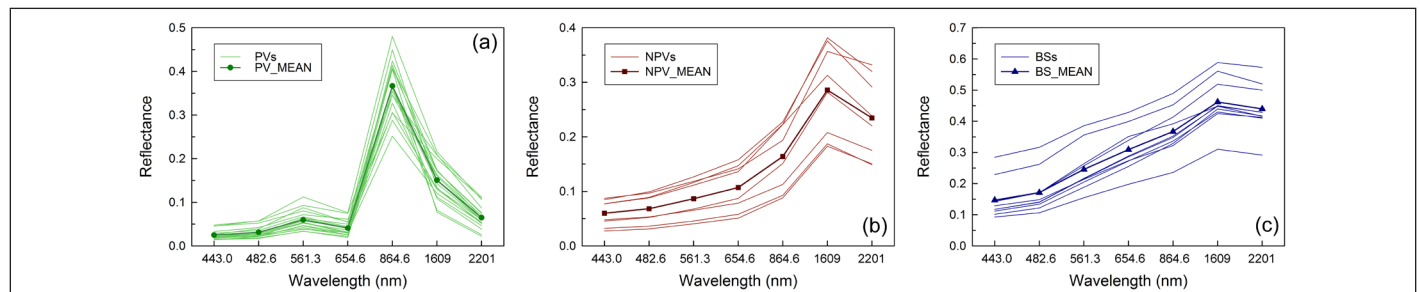


Figure 2. Field reflectance spectra of PV, NPV and bare soil endmembers collected during July and August 2014 in the Otindag Sandy Land. All of the spectra have been resampled to the Landsat-8 OLI spectral ranges using the spectral response function produced by NASA. Their average spectral curves were also plotted using simple straight line and scattered points.

### Field Measurements

Field measurements of fractional cover were obtained at 104 sites across the entire study area (Figure 1). The observations were carried out from July 26 to August 18, 2014, the maximal growing season of the Otindag Sandy Land. Sites were selected following three principles: (a) they had representative vegetation (including grassland; shrub; grassland and shrub; grassland and tree; and grassland, tree, and shrub types); (b) they had PV, NPV, and BS components as much as possible; and (c) they had percentage ground cover for vegetation (PV and NPV) classified as low, medium, and high. All sites were 30 m × 30 m to correlate with the spatial resolution of the EO-1 Hyperion and Landsat-8 OLI images. In addition, to avoid the influence of the position deviation of image pixels and plots on the results, plots that were homogeneous with the surrounding surface were selected when determining their positions. A sampling procedure of two 30 m transects intersecting at a center point distributed at 90-degree intervals, resulting in a quadratic shape, was used for field measurements. Before the measurement, a compass was used to determine due north, then a 30 m transect was established along a north-south direction using a steel ruler after another orthogonal transect was established using the same method in an east-west direction. The center point positions were recorded using a sub-meter level portable differential GPS receiver (Trimble Geo XT 3000). Along the two transects, the presence of surface land cover types (PV, NPV, and BS) was recorded at a 1 m interval directly under a thin tape. For trees and shrubs,

their cover was also recorded looking up at the meter point. To avoid measurement errors caused by subjective factors, all observations were recorded by the same person. The fractions of each type were calculated by dividing the number of counts of a particular cover type by the total number of counts (60). In addition, topography, wind and water erosion, slope and aspect, and the serial number of the digital photos from different views of each site were recorded simultaneously for later analysis and calibration.

### Methods

#### Selected Multispectral Vegetation Indices

Three multispectral-based photosynthetic vegetation indices (PVI<sub>s</sub>) including NDVI, EVI and OSAVI and nine multispectral-based non-photosynthetic vegetation indices (NPVI<sub>s</sub>) including BI, NDI<sub>5</sub>, NDI<sub>7</sub>, NDSVI, NDRI, STI, NDTI, SWIR32, and DFI were used for evaluating and testing the potential of their combinations to retrieve the fractional cover of PV, NPV and bare soil in the Otindag Sandy Land. The detailed information regarding these vegetation indices is listed in Table 2. NDVI is universally used to measure the healthy and green vegetation. However, it can saturate in dense vegetation conditions when the leaf area index (LAI) becomes high. The EVI was developed to improve the NDVI by optimizing the vegetation signal in LAI regions. It corrects soil background signals and reduces atmospheric influences by adding the blue reflectance band. The

Table 2. The photosynthetic vegetation indices (PVI<sub>s</sub>) and non-photosynthetic vegetation indices (NPVI<sub>s</sub>) used for evaluating the potential of vegetation indices feature space to estimate the fractional cover of PV, NPV, and bare soil.

Vegetation Index	Equation	Citation
Normalized difference vegetation index	$NDVI = (R_{TM4} - R_{TM3}) / (R_{TM4} + R_{TM3})$	Rouse (1973)
Enhanced vegetation index	$EVI = 2.5 \times \frac{R_{TM4} - R_{TM3}}{R_{TM4} + 6 \times R_{TM3} - 7.5 \times R_{TM1} + 1}$	Huete et al. (2002)
Optimized soil adjusted vegetation index	$OSAVI = (R_{TM4} - R_{TM3}) / (R_{TM4} + R_{TM3} + 0.16)$	Rondeaux et al. (1996)
Cellulose absorption index	$CAI = 0.5 \times (R_{2.0} + R_{2.2}) - R_{2.1}$	Daughtry (2001)
Brightness index	$BI = R_{TM1} + R_{TM2} + R_{TM3} + R_{TM4}$	Major et al. (1990)
Normalized difference index 5	$NDI5 = (R_{TM4} - R_{TM5}) / (R_{TM4} + R_{TM5})$	McNairn and Protz (1993)
Normalized difference index 7	$NDI7 = (R_{TM4} - R_{TM7}) / (R_{TM4} + R_{TM7})$	
Normalized difference senescent vegetation index	$NDSVI = (R_{TM5} - R_{TM3}) / (R_{TM5} + R_{TM3})$	Qi et al. (2002)
Normalized difference residue index	$NDRI = (R_{TM3} - R_{TM7}) / (R_{TM3} + R_{TM7})$	Gelder et al. (2009)
Soil tillage index	$STI = R_{TM5} / R_{TM7}$	van Deventer et al. (1997)
Normalized difference tillage index	$NDTI = (R_{TM5} - R_{TM7}) / (R_{TM5} + R_{TM7})$	
Shortwave infrared ratio	$SWIR32 = R_{MODIS7} / R_{MODIS6}$	Guerschman et al. (2009)
Dead fuel index	$DFI = 100 \times \left( 1 - \frac{R_{MODIS7}}{R_{MODIS6}} \right) \times \left( \frac{R_{MODIS1}}{R_{MODIS2}} \right)$	Cao et al. (2010)

Here, the wavelength ranges  $R_{2.0}$ ,  $R_{2.1}$ , and  $R_{2.2}$  are given in Table 3.  $R_{TM1}$ - $R_{TM7}$  is the reflectance value of Landsat TM bands, except for the sixth thermal infrared band, and the  $R_{MODIS1}$ ,  $R_{MODIS2}$ ,  $R_{MODIS6}$ , and  $R_{MODIS7}$  is the reflectance spectra of MODIS red (620–670 nm), near-infrared (841–876 nm) and two short-wave infrared bands (1628–1652 nm, 2105–2155 nm) respectively.

OSAVI is based on the soil adjusted vegetation index (SAVI). It can provide greater soil variation than SAVI for low vegetation cover while demonstrating increased sensitivity to vegetation cover greater than 50%. It is best used in areas with relatively sparse vegetation where the soil is visible through the canopy. BI is calculated as the sum of the first four bands of Landsat TM and is dependent on the optical properties of bare soil. NDI5, NDI7, NDSVI, NDRI, and NDTI are based on the same concept as the NDVI but using different spectral ranges. These multispectral indices introduce the shortwave infrared bands (SWIRs) which contain the spectral ranges of lignin and cellulose absorption and are prone useful to predict the percentage of crop residue cover. The STI was defined as the ratio of the Landsat TM bands 5 and 7. The SWIR32 was originally defined as the ratio of the MODIS bands 7 and 6 and was used to substitute the CAI in the NDVI-CAI model to estimate the fractional cover of PV, NPV and bare soil in the Australian tropical savanna region. DFI was designed to separate the dead fuel from green vegetation and soil background in the north of the Asian steppe area based on MODIS bands 1, 2, 6 and 7.

#### Extended PVI-NPVI Feature Space Model

In line with the assumption of the NDVI-CAI conceptual model, the PVI-NPVI feature space model also hypothesized that all pixels consist of a PV, NPV, and BS component (Guerschman *et al.*, 2009). These components can approximately form a distinguishable triangular feature space when the x-axis represents the PVI values and the y-axis represents the NPVI values of the three components. In the scatterplot of PVI and NPVI reflectance spectra, the endmembers occur at the vertexes of the approximate triangle. PV has a high PVI value and different NPVI values based on the selected vegetation index. NPV and BS have lower PVI values and different NPVI values because of their different equations. If the formed triangle is obvious and separable, the cover fractions of each component can be unmixed using the following equations:

$$P = \sum f_i P_i = f_{PV} P_{PV} + f_{NPV} P_{NPV} + f_{BS} P_{BS} \quad (1)$$

$$N = \sum f_i N_i = f_{PV} N_{PV} + f_{NPV} N_{NPV} + f_{BS} N_{BS} \quad (2)$$

$$\sum f_i = f_{PV} + f_{NPV} + f_{BS} = 100 \quad (3)$$

where  $P$  and  $N$  are the PVI and NPVI values in a given pixel and  $f_{PV}$ ,  $f_{NPV}$  and  $f_{BS}$  are the fractions of PV, NPV and bare soil, respectively, in this pixel. The  $P_{PV}$ ,  $P_{NPV}$  and  $P_{BS}$  are the PVI values of the three endmembers and the  $N_{PV}$ ,  $N_{NPV}$  and  $N_{BS}$  are the corresponding NPVI values. The sum of the cover fractions of the three components is constrained to a value of 100. The abnormalities are eliminated using the following rules:

$$N_x = 100, N_y = N_z = 0 \quad (100 < N_x \leq 120) \quad (4)$$

$$N_x = 0 \quad (-20 \leq N_x < 0) \quad (5)$$

$$N_y = N_y / (N_y + N_z) \times 100 \quad (-20 \leq N_x < 0) \quad (6)$$

$$N_z = N_z / (N_y + N_z) \times 100 \quad (-20 \leq N_x < 0) \quad (7)$$

$$N_x = N_y = N_z = 0 \quad (N_x > 120 \text{ or } N_x < -20) \quad (8)$$

where  $N_x$  is the fraction of the endmember that falls outside of 0 to 100, and  $N_y$  and  $N_z$  are the fractions of the other two endmembers. If  $N_x$  is lower than -20 or higher than 120 the corresponding three fractions are all assigned to a value of zero, which means it is an outlier.

#### Validating Estimated Cover Fractions

To validate the estimated cover fractions of PV, NPV, and bare soil, field measurements and image-estimated values were compared using the coefficient of determination ( $R^2$ ) and errors of estimate were quantified using the root mean square error (RMSE) statistic. RMSE was calculated using the following equation:

$$RMSE = \sqrt{\frac{\sum_{i=1}^n (E_i - M_i)^2}{n}} \quad (9)$$

where  $E_i$  is the estimated value of sample  $i$ ,  $M_i$  is the measured value of the sample  $i$  and  $n$  is the number of sample. The RMSE indicates the magnitude of the average error produced by a model. This error is reported in the same units as the estimated and measured values. Scatterplots displaying estimated and measured variables were also generated to help evaluate and analyze the relationship between the variables.

## Results and Analyses

### Feature Space Based on Field-Measured Endmember Reflectance Spectra

The NDVI, EVI, OSAVI, CAI, BI, NDI5, NDI7, NDSVI, NDRI, DFI, NDTI, STI, and SWIR32 values of each endmember were calculated first using field reflectance spectra based on the formulae listed in Table 2 and wavelength ranges defined in Table 3. Then, the two-dimensional scatterplots of PVI-CAI and each PVI-NPVI were plotted.

Table 3. Wavelength ranges and channel numbers used for calculating the PVI<sub>s</sub> and NPVI<sub>s</sub> with field measured, EO-1 Hyperion and Landsat-8 OLI reflectance spectra.

	Field endmember reflectance spectra (ASD) min - max [nm] and number of channels	EO-1 Hyperion min - max [nm] and number of channels	Landsat-8 OLI central wavelength [nm] and number of channels
$R_{Blue}$	465 - 475 (11)	468 (1)	483 (1)
$R_{Green}$	545 - 555 (11)	549 (1)	561 (1)
$R_{Red}$	646 - 656 (11)	651 (1)	655 (1)
$R_{NIR}$	859 - 869 (11)	864 (1)	865 (1)
$R_{SWIR1}$	1649 - 1669 (21)	1649 - 1669 (3)	1609 (1)
$R_{SWIR2}$	2193 - 2213 (21)	2193 - 2213 (3)	2201 (1)
$R_{2.0}$	2007 - 2037 (31)	2022 - 2032 (2)	
$R_{2.1}$	2088 - 2118 (31)	2093 - 2113 (3)	
$R_{2.2}$	2179 - 2208 (30)	2184 - 2204 (3)	

### PVI-CAI Feature Space

Figure 3 a1, b1, and c1 show the spatial distribution of NDVI-CAI, EVI-CAI and OSAVI-CAI with PV, NPV, and bare soil endmembers respectively. The solid black lines are linked to the three vertices denote the simulated triangular shape, which matched well with the assumption of the conceptual model (Guerschman *et al.*, 2009; Hill *et al.*, 2016). The feature space of the three models has a great similarity. PVs occur on the right side of the triangle, with a high average PVI value of 0.80, 0.58, and 0.57 for NDVI-CAI, EVI-CAI and OSAVI-CAI model, respectively, and an intermediate average CAI value of zero. NPVs are situated at the top left corner of the triangle, with a high average CAI value of 0.02 and a low average PVI value of 0.21, 0.11, and 0.13 for the three models. BSs, with a low average CAI value of -0.02 and lower average PVI value of 0.09 for NDVI-CAI and 0.7 for EVI-CAI and OSAVI-CAI, occupied the bottom left corner of the triangle.

**PVI-NPVI Feature Space**

The rest of the graphs in Figure 3 show the scatterplots of the different combinations of PVI-NPVI calculated from ground measured endmember reflectance spectra of PV, NPV, and bare soil. Similar to the PVI<sub>s</sub>-CAI, the feature space corresponding to various combinations of the three selected PVI and nine NPVI<sub>s</sub> has good similarities. The spatial distribution of PVI-BI, NDI5, NDI7, NDSVI, NDRI, and DFI, to some extent, show separability for PV, NPV, and bare soil, and form an approximately triangular shape (Figure 3a2-a7, b2-b7, and c2-c7). However, PVI-DFI may confuse NPV and bare soil because of the spectra mixing, e.g., the circles drawn in Figure 3a7, b7, and c7 show *sand sagebrush* have been mixed with bare soil. The PVI<sub>s</sub>-NDTI, STI, and SWIR32 are not in conformity with the hypothesis of the

PVI-NPVI feature space model, but they can separate PV from a mixed surface (Figure 3a8-a10, b8-b10, and c8-c10). The PVI-NDSVI feature space has the similar vertex distribution as that of the PVI-CAI feature space and PVI-BI, NDI5, NDI7, and NDRI have inverse locations to those of NPV and bare soil.

**Feature Space Based on Image Reflectance Spectra**

Figure 4a1, b1, and c1 present the pixel distribution of the NDVI-CAI, EVI-CAI and OSAVI-CAI feature space during the non-growing season (05 April 2014) and growing season (26 July 2014 and 06 August 2014). The feature space of the two growing seasons showed obvious separability with a similar spatial pattern as that measured for the spectral-based PVI<sub>s</sub>-CAI feature space. The pixels are only distributed on the left side

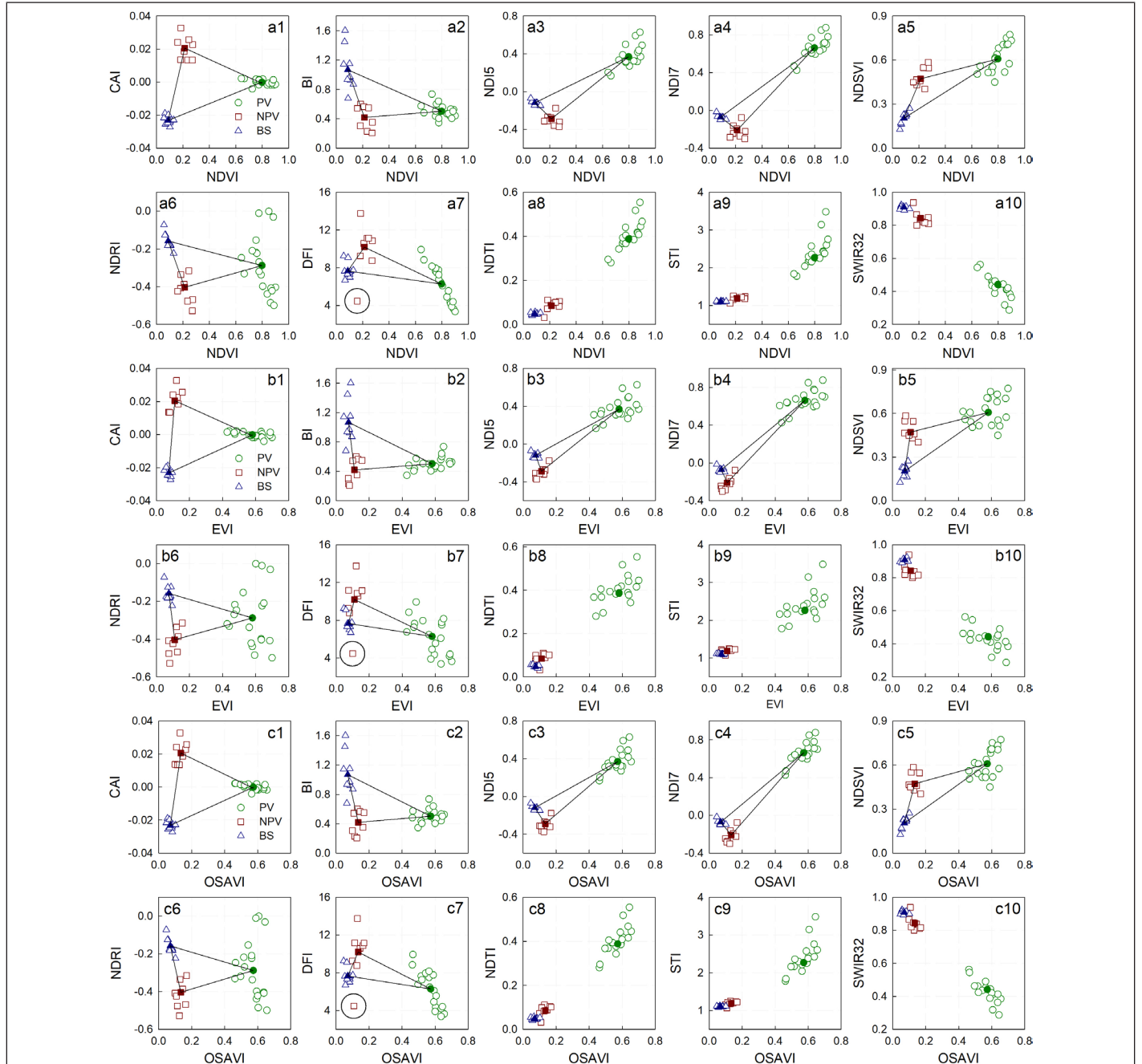


Figure 3. Spatial distribution of the PVI<sub>s</sub>-NPVI<sub>s</sub> calculated with the ground measured endmember spectra of PVs, NPVs and bare soils. The average values of PVI<sub>s</sub> and NPVI<sub>s</sub> for three endmembers were marked as solid intertinctus geometrical figures (see Table 4), and the black triangle represents the approximate spatial shape of each combination.



Table 4. The average value of selected PVIs and NPVIs corresponding to the three endmembers obtained from the ground measured reflectance spectra. The computational formulae are listed in Table 2.

	NDVI	EVI	OSAVI	CAI	BI	NDI5	NDI7	NDSVI	NDRI	DFI	NDTI	STI	SWIR32
PV	0.80	0.58	0.57	0.00	0.50	0.37	0.66	0.61	-0.29	6.28	0.39	2.27	0.44
NPV	0.21	0.11	0.13	0.02	0.42	-0.29	-0.21	0.47	-0.40	10.19	0.09	1.19	0.84
BS	0.09	0.07	0.07	-0.02	1.07	-0.12	-0.07	0.20	-0.16	7.66	0.05	1.10	0.91

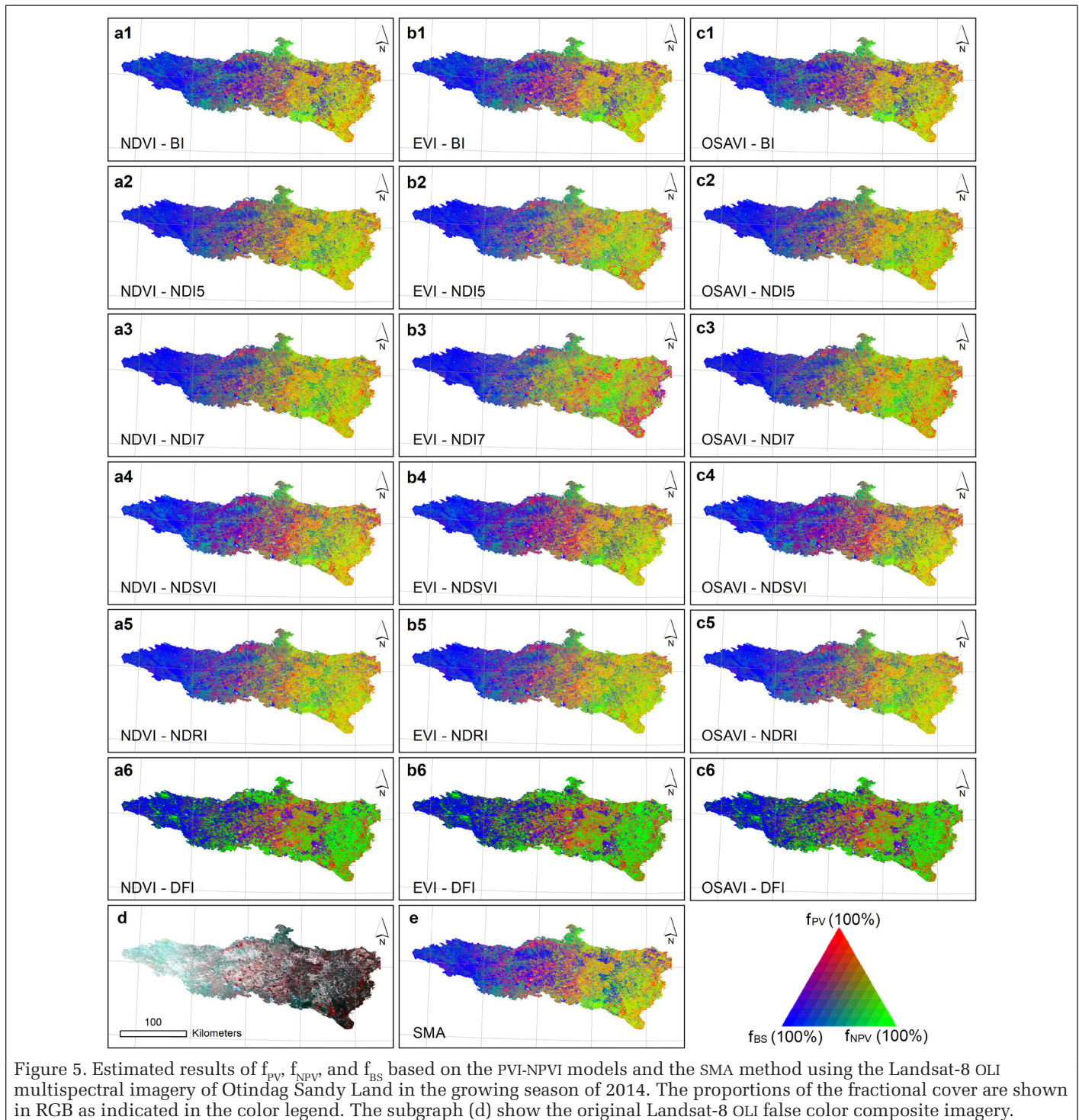


Figure 5. Estimated results of  $f_{PV}$ ,  $f_{NPV}$ , and  $f_{BS}$  based on the PVI-NPVI models and the SMA method using the Landsat-8 OLI multispectral imagery of Otindag Sandy Land in the growing season of 2014. The proportions of the fractional cover are shown in RGB as indicated in the color legend. The subgraph (d) show the original Landsat-8 OLI false color composite imagery.

## Definition of PV, NPV, and Bare Soil Endmembers for selected PVI and NPVI

The determination of PV, NPV, and BS endmember value for selected PVI and NPVI is crucial for successful model unmixing and accurate estimation of  $f_{PV}$  and  $f_{NPV}$ . In this study, the field-measured average reflectance spectrum of each endmember was used to calculate these values. The definition of three endmember values of each selected PVI and NPVI was determined using the formula listed in Table 2 and the wavelength ranges defined in Table 3, and the values were summarized in Table 4.

## Landsat-8 OLI Multispectral Unmixing

To validate the results mentioned above, we applied all combinations of the three PVI and nine NPVI to the mosaicked Landsat-8 OLI imagery of the Otindag Sandy Land. The results demonstrate that the combinations of three PVI and BI, NDI5, NDI7, NDSVI, and NDRI can separate the three components. PVI-DFI could lead to confusion regarding the NPV and BS component, and PVI-NDTI, STI, and SWIR32 were unable to distinguish between NPV and BS. The results of the fractional cover of PV, NPV, and bare soil obtained from the PVI-BI, NDI5, NDI7, NDSVI, NDRI and DFI methods are shown in Figure 5a1-c6, respectively.

Figure 5d shows the Landsat-8 OLI standard false color composite image of the study area. Visual determination of the unmixing results on a large scale shows a good match with the original satellite imagery. It presented the same trend for all of the unmixing results that were mainly covered by NPV and sandy soil in the western region and dominated by the mixed distribution of PV, NPV, and bare soil in the central and eastern regions of the Otindag Sandy Land. In addition, the RGB composite image of the three PVI-DFI models clearly shows the difference from other results and the confusion for NPV and bare soil.

## Accuracy Validation and Comparison to the SMA Method

A total of 104 field sites were used to evaluate the capacity of the selected PVI-NPVI models to estimate the fractional cover of PV, NPV, and bare soil in the Otindag Sandy Land. Figure 6a1-c6 show the validation results of the estimated  $f_{PV}$ ,  $f_{NPV}$ , and  $f_{BS}$  versus field observations. All of the methods show similar results of over-estimation of  $f_{NPV}$  and under-estimation of  $f_{PV}$ . For  $f_{PV}$ , all the combinations show a moderate and close coefficient of determination ( $R^2 \geq 0.50$ ) and RMSE (the minimum value of 0.26 for NDVI- and OSAVI-NDSVI, the maximum value of 0.31 for NDVI-NDI7) except the PVI-DFI models. For  $f_{NPV}$ , the PVI-BI and PVI-NDSVI methods have slightly better results than those of the other three methods, as the highest determination coefficient of 0.51 for NDVI-BI and lowest RMSE of 0.17 for NDVI-NDSVI. The PVI-NDSVI method has the lowest RMSE for the estimation of  $f_{NPV}$  compared to other combinations. For  $f_{BS}$ , the three PVI-BI models showed the best estimation with the highest  $R^2$  of 0.60 and the same and lowest RMSE of 0.18.

For comparison with the vegetation index-based feature space methods, the traditional SMA method was also used to retrieve the fractional cover of PV, NPV, and bare soil in the Otindag Sandy Land. The mosaicked Landsat-8 OLI surface reflectance image except for the panchromatic band and the resampled average spectra of PV, NPV, and bare soil endmember were utilized to perform the spectral mixture unmixing. Figure 5e shows the RGB composite result of the three cover fractions derived from the SMA method. It can be observed there has a similar spatial distribution to the PVI-NPVI estimates and it is approximately consistent with the true distribution of surface vegetation of the study area (Figure 5d). The accuracy validation results (Figure 6d, see next page) show that the accuracies of the  $f_{PV}$  and  $f_{NPV}$  estimates using the SMA method are near those estimated using the PVI-NPVI models. However, it has the highest coefficient of determination ( $R^2=0.61$ ) and the same and lowest RMSE as that of the PVI-BI method (RMSE=0.18) for  $f_{BS}$ .

## Discussion

This study was undertaken to evaluate the potential of multispectral remote sensing vegetation indices for quantitative estimation of the fractional cover of PV, NPV, and bare soil in the Otindag Sandy Land. The results showed that  $f_{PV}$ ,  $f_{NPV}$ , and  $f_{BS}$  can be resolved in this area by combining a linear unmixing approach with the three selected PVI and suitable NPVI. Although the estimation accuracy of  $f_{PV}$  and  $f_{NPV}$  is not high, the results indicated that these multispectral index-based feature space models have great potential for distinguishing NPV from PV and soil background in the studied sandy region.

Hyperspectral image has many advantages in discriminating different materials because of its narrow band width and abundant band numbers. The distinct absorption feature of dry plants in the 2000 to 2200 nm regions because of lignin and cellulose make hyperspectral-based CAI an ideal tool for discriminating NPV from PV and bare soil background (Nagler *et al.*, 2003; Serbin *et al.*, 2010). However, we did not have more spaceborne hyperspectral data that could be used until now. In contrast, abundant multispectral images have been collected during the past several decades. The main limitations of multispectral data are their limited sensitivity and non-ideal band width and locations in the SWIR bands (Figure 7), where the discrimination of bare soil and senescent or dry vegetation is most effective (Asner and Lobell, 2000). Therefore, the spectral resolution of satellite images plays a more important role in estimating the cover fractions of surface vegetation, especially for distinguishing between NPV and bare soil. In addition, images with higher spatial resolution can provide more features and details on surface materials and are conducive to collect purer image-based endmember spectra. However, it is more suitable for small-scale vegetation monitoring because it will result in a large amount of data and cost when it is used in a larger area due to its relatively small imaging swath and expensive price. In general, images with medium-high spatial resolution (such as Landsat, Sentinel-2, and Chinese Gaofen-1) are more appropriate for large-scale vegetation monitoring, whereas the impacts of the spatial resolution on the estimation accuracy of the fractional cover of PV, NPV, and bare soil needs further research. More advanced multispectral and hyperspectral satellites launched in recent years, such as Landsat-8 with nine multispectral bands, Sentinel-2 with 13 multispectral channels and Chinese Geofen-5 hyperspectral satellite launched on 09 May 2018 with 330 spectral channels at a spectral resolution of 5 nm for V-NIR bands and 10 nm for SWIR bands and a spatial resolution of

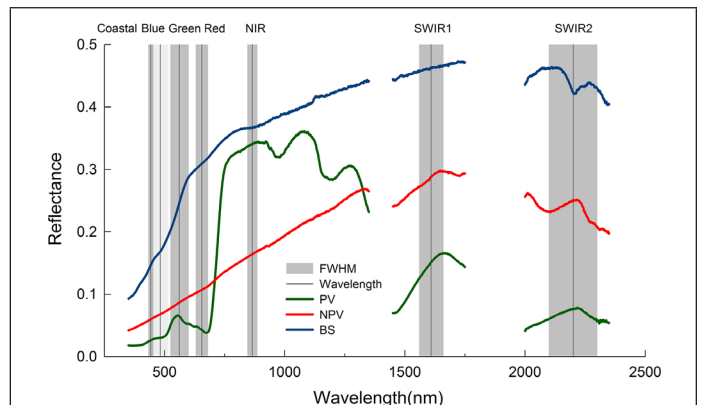
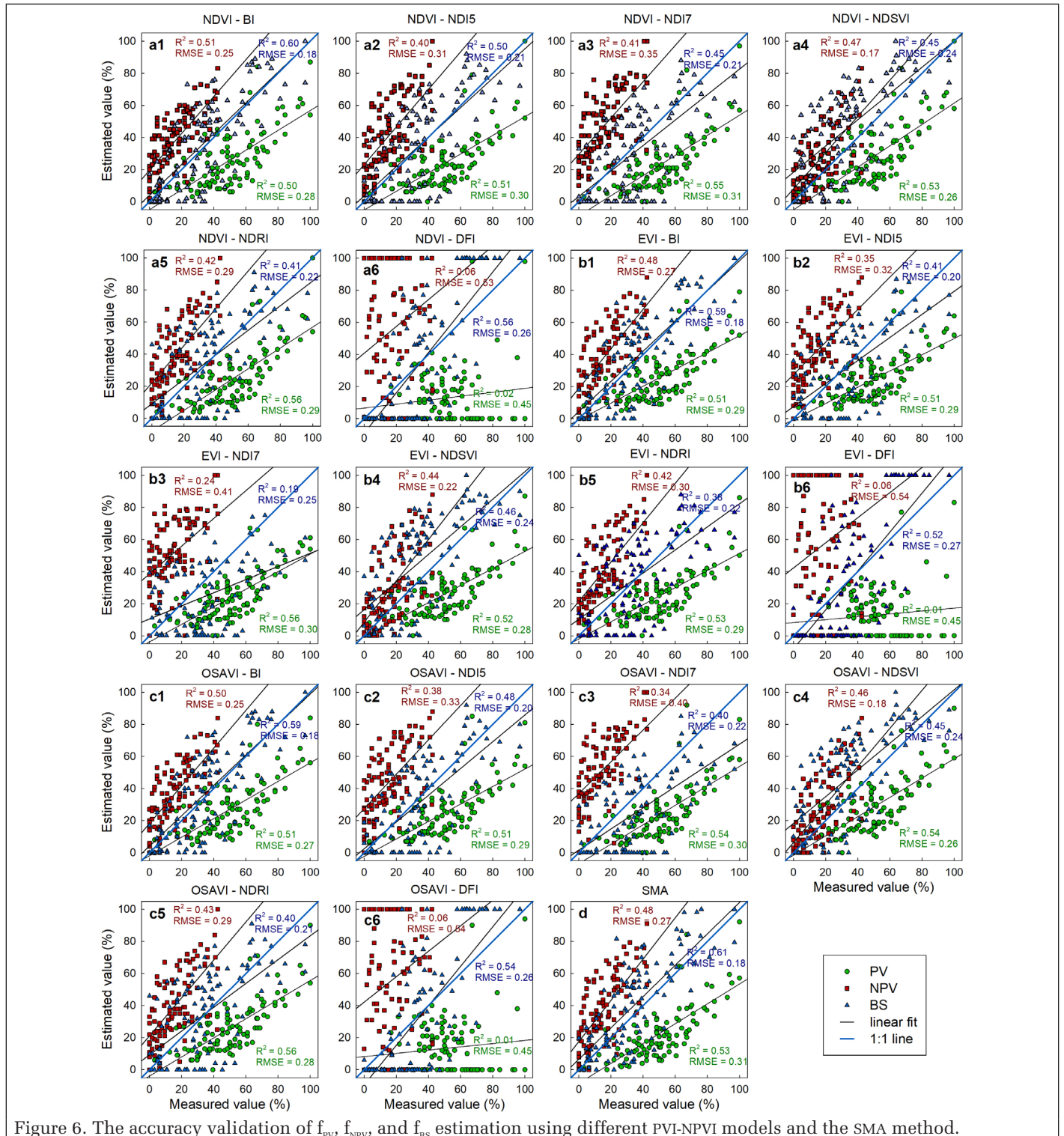


Figure 7. Field-measured mean endmember reflectance spectrum of PV, NPV, and bare soil and the wavelength ranges of Landsat-8 OLI bands that marked in grey columns. CW, FWHM represent the center wavelength and full width half maximum of Landsat-8 OLI sensor, respectively.

30 m, will provide more opportunities and great potential in detection of surface vegetation and other materials.

Proper endmember selection is one of the crucial factors to a successful and accurate estimation of  $f_{PV}$  and  $f_{NPV}$ . End-member selection involves identifying the number and type of endmembers and their corresponding spectral signatures (Somers *et al.*, 2011). The endmember spectra of selected land cover types may be derived from existing spectral libraries or obtained from field measurements using portable spectro-radiometers. Field-based endmember spectra collection

requires considerable efforts and suitable weather conditions. This approach can obtain more complete and purer spectral signatures of endmembers in a specified region. In addition, endmember reflectance spectra derived directly from the images themselves or simulated using some radiative transfer models is another commonly used method (Hill *et al.*, 2016; Zhou *et al.*, 2016). A number of advanced techniques to locate and extract endmembers from images have been proposed and applied to many studies. Image-based endmember spectra can better match the image. However, the correctness of the



endmember spectra largely depends on the technique used, and the number and the type of endmembers can be restricted due to the poor image quality.

In this study, both the PVI-NPVI models and the SMA method significantly overestimated  $f_{NPV}$  and underestimated  $f_{PV}$ . A lot of factors can result in such an estimation bias. Endmember variability and poor representation may be the main reasons. The average spectra of the selected endmembers were used to calculate the values of PVI and NPVI of the three endmembers when unmixing the pixels. If the average endmember spectra are not appropriate, it will directly lead to a deviation in the estimation results. In addition, the use of an invariant endmember to simulate all the pixels will inevitably produce an unmixing error, which will further lead to bias in the estimation results. To reduce the impacts from endmember variability, the multiple endmember spectral mixture analysis (MESMA) (Roberts et al., 1998) and automated Monte Carlo unmixing (AutoMCU; Asner and Lobell, 2000) methods were proposed based on the variable endmember selection strategies. MESMA allows both the number and the type of endmember to vary on a per-pixel basis and assigns the best-fit model (i.e., the lowest RMSE) to each pixel based on a spectral database of hundreds of spectra. Unlike MESMA, AutoMCU utilizes statistical knowledge (i.e., mean spectra) to calculate the sub-pixel fractions for each pixel by random selection of endmember spectra from a spectral library. When using the same endmember spectra to unmix the GF1-WFV images in the Otindag Sandy Land, Li *et al.* (2016) found that the SMA and MESMA methods also showed the same estimation bias of  $f_{PV}$  and  $f_{NPV}$  as the present study. This is primarily because the SMA method uses only a set of invariant endmember spectra as input, whereas the endmember spectra of bare soil in this area have large intra-variability when compared to the NPV endmember spectra and the similarity between bare soil and NPV spectra can actually lead to errors in MESMA as some NPV/BS combinations may be mistaken as combinations of other NPV/BS. The AutoMCU method can obtain more accurate estimates because of its better performance addressing endmember variability. Moreover, regardless of the fact that we have tried our best to avoid the influence of sample position and image-matching deviation, it will inevitably have an impact on the estimation results. Field measurement methods, observer bias, and time differences between field observation and image acquisition could also influence the results.

## Conclusions

In this study, we assessed the potential of multispectral vegetation indices feature space for simultaneous estimation of  $f_{PV}$ ,  $f_{NPV}$ , and  $f_{BS}$  in a sandy region of northern China, and tried to identify one or a set of multispectral-based NPVIs to combine with the selected NDVI, EVI, and OSAVI for estimating the fractional cover of PV, NPV, and bare soil. The results show that the spatial distribution of pixels defined by the three PVIs and nine NPVIs obtained from image reflectance spectra shows good consistency with that of the corresponding PVI-NPVI feature space based on field reflectance spectra of the PV, NPV, and bare soil endmembers. The feature spaces of PVI-BI, NDI5, NDI7, NDSVI, and NDRI shows the obvious spatial separability and PVI-DFI may confuse the NPV with bare soil, and PVI-NDTI, STI, and SWIR32 may not be able to separate NPV from bare soil. The clear or separable spatial pattern of PVI-NPVI plays a decisive role in model decomposability. Regarding the Otindag Sandy Land, the selected PVI-BI and PVI-NDSVI are the best models to estimate the cover fractions of PV, NPV, and, bare soil synchronously.

## Acknowledgments

This study was funded in part by the National Key Research and Development Program (Grant No. 2016YFC0500806) and the Strategic Priority Research Program of the Chinese Academy of Sciences (Grant Nos. XDA20030101 and XDA19030301).

## References

- Adams, J.B., M.O. Smith, and P.E. Johnson, 1986. Spectral mixture modeling: A new analysis of rock and soil types at the Viking Lander 1 site, *Journal of Geophysical Research Atmospheres, Solid Earth and Planets*, 91(B8):8098–8112.
- Asner, G.P., D.E. Knapp, A.N. Cooper, M.M.C. Bustamante, and L.P. Olander, 2005. Ecosystem structure throughout the Brazilian Amazon from Landsat observations and automated spectral unmixing, *Earth Interactions*, 9(7):305–319.
- Asner, G.P., and D.B. Lobell, 2000. A biogeophysical approach for automated SWIR unmixing of soils and vegetation, *Remote Sensing of Environment*, 74(1):99–112.
- Bannari, A., D. Haboudane, H. McNairn, and F. Bonn, Modified Soil Adjusted Crop Residue Index (MSACRI): A new index for mapping crop residue, *Proceedings of the Geoscience and Remote Sensing Symposium, 2000, IGARSS 2000, IEEE 2000 International, IEEE*, 2000, 7: 2936-2938.
- Barry, P., 2001. *EO-1/Hyperion Science Data User's Guide*, Redondo Beach, CA: TRW Space, Defense & Informations Systems.
- Cao, X., J. Chen, B. Matsushita, and H. Imura, 2010. Developing a MODIS-based index to discriminate dead fuel from photosynthetic vegetation and soil background in the Asian steppe area, *International Journal of Remote Sensing*, 31(6):1589–1604.
- Datt, B., T.R. McVicar, T.G. Van Niel, D.L. Jupp, and J.S. Pearlman, 2003. Preprocessing EO-1 Hyperion hyperspectral data to support the application of agricultural indexes, *IEEE Transactions on Geoscience and Remote Sensing*, 41(6):1246–1259.
- Daughtry, C.S.T., 2001. Discriminating crop residues from soil by shortwave infrared reflectance, *Agronomy Journal*, 93(1):125–131.
- Daughtry, C.S.T., P.C. Doraiswamy, E.R. Hunt, A.J. Stern, J.E. McMurtrey, and J.H. Prueger, 2006. Remote sensing of crop residue cover and soil tillage intensity, *Soil and Tillage Research*, 91(1–2):101–108.
- Daughtry, C.S.T., E.R. Hunt, Jr., and J.E. McMurtrey Iii, 2004. Assessing crop residue cover using shortwave infrared reflectance, *Remote Sensing of Environment*, 90(1):126–134.
- Gelder, B.K., A.L. Kaleita, and R.M. Cruse, 2009. Estimating mean field residue cover on midwestern soils using satellite imagery, *Agronomy Journal*, 101(3):635–643.
- Gitelson, A.A., Y.J. Kaufman, R. Stark, and D. Rundquist, 2002. Novel algorithms for remote estimation of vegetation fraction, *Remote Sensing of Environment*, 80(1):76–87.
- Gong, Z., S.-H. Li, J. Sun, and L. Xue, 2013. Environmental changes in Hunshandake (Otindag) sandy land revealed by optical dating and multi-proxy study of dune sands, *Journal of Asian Earth Sciences*, 76:30–36.
- Guerschman, J.P., M.J. Hill, L.J. Renzullo, D.J. Barrett, A.S. Marks, and E.J. Botha, 2009. Estimating fractional cover of photosynthetic vegetation, non-photosynthetic vegetation and bare soil in the Australian tropical savanna region upscaling the EO-1 Hyperion and MODIS sensors, *Remote Sensing of Environment*, 113(5):928–945.
- Guerschman, J.P., P.F. Scarth, T.R. McVicar, L.J. Renzullo, T.J. Malthus, J.B. Stewart, J.E. Rickards, and R. Trevithick, 2015. Assessing the effects of site heterogeneity and soil properties when unmixing photosynthetic vegetation, non-photosynthetic vegetation and bare soil fractions from Landsat and MODIS data, *Remote Sensing of Environment*, 161:12–26.

- Hill, M.J., Q. Zhou, Q. Sun, C.B. Schaaf, J. Southworth, N.B. Mishra, C. Gibbes, E. Bunting, T.B. Christiansen, and K.A. Crews, 2016. Dynamics of the relationship between NDVI and SWIR32 vegetation indices in southern Africa: Implications for retrieval of fractional cover from MODIS data, *International Journal of Remote Sensing*, 37(6):1476–1503.
- Huete, A., K. Didan, T. Miura, E.P. Rodriguez, X. Gao, and L.G. Ferreira, 2002. Overview of the radiometric and biophysical performance of the MODIS vegetation indices, *Remote Sensing of Environment*, 83(1):195–213.
- Jackson, H., and S. Prince, 2016. Degradation of non-photosynthetic vegetation in a semi-arid rangeland, *Remote Sensing*, 8(9):692.
- Li, S., J. Sun, and H. Zhao, 2002. Optical dating of dune sands in the northeastern deserts of China, *Palaeogeography, Palaeoclimatology, Palaeoecology*, 181(4):419–429.
- Li, T., X. Li, and F. Li, 2015. Estimating fractional cover of photosynthetic vegetation and non-photosynthetic vegetation in the Xilingol steppe region with EO-1 Hyperion data, *Acta Ecologica Sinica*, 35(11):3643–3652.
- Li, X., G. Zheng, J. Wang, C. Ji, B. Sun, and Z. Gao, 2016. Comparison of methods for estimating fractional cover of photosynthetic and non-photosynthetic vegetation in the Otindag sandy land using GF-1 Wide-Field View data, *Remote Sensing*, 8(10):800.
- Liu, H., C. Zhou, W. Cheng, E. Long, and R. Li, 2008. Monitoring sandy desertification of Otindag sandy land based on multi-date remote sensing images, *Acta Ecologica Sinica*, 28(2):627–635.
- Major, D.J., F.J. Larney, and C.W. Lindwall, Spectral reflectance characteristics of wheat residues, *Geoscience and Remote Sensing Symposium, 1990. IGARSS'90. 'Remote Sensing Science for the Nineties'.*, 10<sup>th</sup> Annual International, IEEE, 1990, 603–607.
- McNairn, H., and R. Protz, 1993. Mapping corn residue cover on agricultural fields in Oxford County, Ontario, using Thematic Mapper, *Canadian Journal of Remote Sensing*, 19(2):152–159.
- Meyer, T., and G.S. Okin, 2015. Evaluation of spectral unmixing techniques using MODIS in a structurally complex savanna environment for retrieval of green vegetation, nonphotosynthetic vegetation, and soil fractional cover, *Remote Sensing of Environment*, 161:122–130.
- Nagler, P.L., Y. Inoue, E.P. Glenn, A.L. Russ, and C.S.T. Daughtry, 2003. Cellulose Absorption Index (CAI) to quantify mixed soil-plant litter scenes, *Remote Sensing of Environment*, 87(2–3):310–325.
- Peterson, S.H., D.A. Roberts, M. Beland, R.F. Kokaly, and S.L. Ustin, 2015. Oil detection in the coastal marshes of Louisiana using MESMA applied to band subsets of AVIRIS data, *Remote Sensing of Environment*, 159:222–231.
- Qi, J., R. Marsett, P. Heilman, S. Bieden-Bender, S. Moran, D. Goodrich, and M. Weltz, 2002. Ranges improves satellite-based information and land cover assessments in southwest United States, *Eos, Transactions American Geophysical Union*, 83(51):601–606.
- Roberts, D.A., M. Gardner, R. Church, S. Ustin, G. Scheer, and R.O. Green, 1998. Mapping chaparral in the Santa Monica mountains using multiple endmember spectral mixture models, *Remote Sensing of Environment*, 65(3):267–279.
- Rondeaux, G., M. Steven, and F. Baret, 1996. Optimization of soil-adjusted vegetation indices, *Remote Sensing of Environment*, 55(2):95–107.
- Rouse, J.W., 1973. Monitoring vegetation systems in the great plains with ERTS, *Third ERTS Symposium, NASA, Washington, D.C.*, 1:309–317.
- Serbin, G., E.R. Hunt, C.S.T. Daughtry, D.J. Brown, G.W. McCarty, and P.C. Doraiswamy, 2010. Assessment of spectral indices for crop residue cover estimation, *2010 IEEE International Geoscience and Remote Sensing Symposium*, 1827–1830.
- Serbin, G., E.R. Hunt, Jr., C.S.T. Daughtry, G.W. McCarty, and P.C. Doraiswamy, 2009. An improved ASTER index for remote sensing of crop residue, *Remote Sensing*, 1(4):971–991.
- Somers, B., G.P. Asner, L. Tits, and P. Coppin, 2011. Endmember variability in spectral mixture analysis: A review, *Remote Sensing of Environment*, 115(7):1603–1616.
- van Deventer, A.P., A.D. Ward, P.H. Gowda, and J.G. Lyon, 1997. Using Thematic Mapper data to identify contrasting soil plains and tillage practices, *Photogrammetric Engineering & Remote Sensing*, 63(1):87–93.
- Verrelst, J., R. Zurita Milla, B. Koetz, J.G.P.W. Clevers, and M.E. Schaepman, 2007. Angular unmixing of photosynthetic and non-photosynthetic vegetation within a coniferous forest using CHRIS-PROBA, *Proceedings of the 10<sup>th</sup> International Symposium on Physical Measurements and Spectral Signatures in Remote Sensing (ISPMSRS'07)*, Davos, 12–14 March, 36:355–360.
- Wang, H.Y., Z.Y. Li, Z.H. Gao, J.J. Wu, B. Sun, and C.L. Li, 2014. Assessment of land degradation using time series trend analysis of vegetation indicators in Otindag sandy land, *IOP Conference Series: Earth and Environmental Science*, 17(1):012065.
- Xu, D., X. Guo, Z. Li, X. Yang, and H. Yin, 2014. Measuring the dead component of mixed grassland with Landsat imagery, *Remote Sensing of Environment*, 142:33–43.
- Yang, J., P.J. Weisberg, and N.A. Bristow, 2012. Landsat remote sensing approaches for monitoring long-term tree cover dynamics in semi-arid woodlands: Comparison of vegetation indices and spectral mixture analysis, *Remote Sensing of Environment*, 119:62–71.
- Zheng, G.X., X.S. Li, K.X. Zhang, and J.Y. Wang, 2016. Spectral mixing mechanism analysis of photosynthetic/non-photosynthetic vegetation and bared soil mixture in the Hunshandake (Otindag) sandy land, *Spectroscopy and Spectral Analysis*, 36(4):1063–1068.
- Zheng, Y.R., Z.X. Xie, C. Robert, L.H. Jiang, and H. Shimizu, 2006. Did climate drive ecosystem change and induce desertification in Otindag sandy land, China over the past 40 years?, *Journal of Arid Environments*, 64(3):523–541.
- Zhou, Q., M.J. Hill, Q.S. Sun, and C.B. Schaaf, 2016. Retrieving understory dynamics in the Australian tropical savannah from time series decomposition and linear unmixing of MODIS data, *International Journal of Remote Sensing*, 37(6):1445–1475.
- Zhou, Y., H. Lu, M. Joseph, X. Miao, S. James, and G. Ronald, 2008. Optically stimulated luminescence dating of aeolian sand in the Otindag dune field and Holocene climate change, *Science in China Series D: Earth Sciences*, 51(6):837–847.

LEARN  
DO  
GIVE  
BELONG

**ASPRS Offers**

- » Cutting-edge conference programs
- » Professional development workshops
- » Accredited professional certifications
- » Scholarships and awards
- » Career advancing mentoring programs
- » *PE&RS*, the scientific journal of ASPRS

[asprs.org](http://asprs.org)

ASPRS



# Cleared for Takeoff.

## ILMF Jan. 28th

### Space 100

 **Geomni**<sup>™</sup>  
<https://geomni.net/psm>